

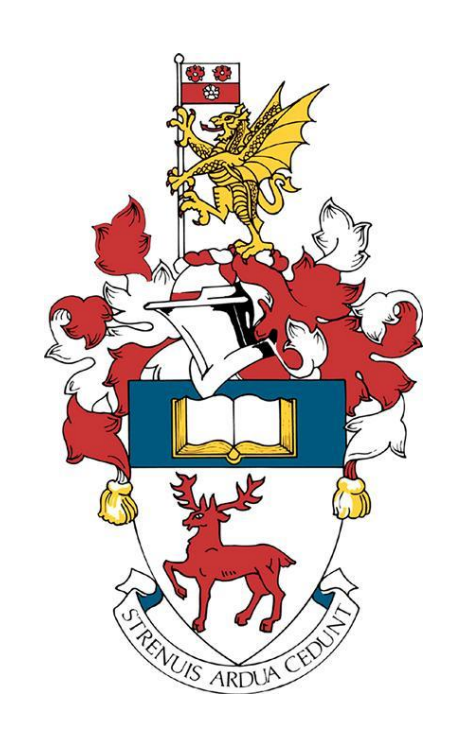
University of Southampton Research Repository

Copyright © and Moral Rights for this thesis and, where applicable, any accompanying data are retained by the author and/or other copyright owners. A copy can be downloaded for personal non-commercial research or study, without prior permission or charge. This thesis and the accompanying data cannot be reproduced or quoted extensively from without first obtaining permission in writing from the copyright holder/s. The content of the thesis and accompanying research data (where applicable) must not be changed in any way or sold commercially in any format or medium without the formal permission of the copyright holder/s.

When referring to this thesis and any accompanying data, full bibliographic details must be given, e.g.

Thesis: Author (Year of Submission) "Full thesis title", University of Southampton, name of the University Faculty or School or Department, PhD Thesis, pagination.

Data: Author (Year) Title. URI [dataset]



University of Southampton

Faculty of Medicine

School of Clinical and Experimental Sciences

A Single Gene Deficiency (*Timp3*) Affects the Regulation of Nutrition and Metabolism – Harnessing the Gut Microbiome

by

Rachel Hannah Meadows

Thesis for the degree of Doctor of Philosophy

December 2024

University of Southampton

Abstract

Faculty of medicine

Clinical and Experimental Sciences

Thesis for the Degree of <u>Doctor of Philosophy</u>

A Single Gene Deficiency (*TIMP3*) Affects the Regulation of Nutrition and Metabolism –

Harnessing the Gut Microbiome

bν

Rachel Hannah Meadows

The prevalence of metabolic syndrome (MetS) (defined as the clustering of insulin resistance, obesity, and hypertension) has sharply increased since the late 20th century and continues to rise into the present day. Metabolic syndrome leads to the development of many chronic diseases such as Type 2 Diabetes and cardiovascular diseases, the likelihood of which increases with age. Increased accessibility to high-volume, calorie dense, and highly processed foods is often pointed as the culprit for this event. However, these multifactorial conditions are known to have many genetic components and are highly influenced by the gut microbiome. As worldwide obesity and MetS rates continue to grow, the need for novel therapies to combat the problem become evermore important. This PhD project aimed to investigate the role of the gut microbiome and the extracellular matrix (ECM), via the protein TIMP3, in diet-induced obesity (DIO) and ageing mouse models.

Timp3-/- DIO mice gut had decreased abundance of short-chain fatty acid (SCFA) producing *Lachnospiraceae* bacteria, alongside decreased circulating butyrate. These mice also exhibited dysregulated energy metabolism which lead to changes in adipose tissue storage and development of obesity.

Female Timp3-/- mice have impaired aorta constriction and relaxation response, in part due to aberrant extracellular matrix remodelling and dysfunctional endothelial and vascular smooth muscle cell signalling.

This study presents a model of MetS and CVD development, via deletion of *Timp3*, within mice. The findings suggest that MetS development in the *Timp3*^{-/-} mouse is in part due to changes in the gut microbiota composition.

Table of Contents

Tab	le of (Conten	ts	i
Tab	le of ⁻	Tables.		vii
Tab	le of I	Figures		ix
Res	earch	Thesis	: Declaration of Authorship	xxv
Ackı	nowle	edgeme	ents	xxviii
Cha	pter 1	l Intr	oduction	1
1.1	Me	etabolic	Syndrome and Metabolic Disease	2
	1.1.1	. Obesi	ity	3
	1.1.2	. Туре	2 Diabetes Mellitus	6
	1.1.3	Cardi	ovascular Disease	7
	1.1.4	Non-a	alcoholic Fatty Liver Disease	8
	1.1.5	Mous	e Models in Metabolic Disease Research	8
1.2	Ke	y Conce	pts in Energy Metabolism	10
	1.2.1	. Role o	of Adipose Tissue in Energy Homeostasis	11
	1.2.2	Lipid	Metabolism and the Liver	15
	1.2.3	Role	of the Pancreas in Glucose Metabolism	18
1.3	Th	e Gut M	licrobiota	19
	1.3.1	. Overv	/iew	19
	1.3.2	? The G	Gut Microbiota and Metabolic Syndrome	20
1.4	Th	e Extrac	ellular Matrix	22
	1.4.1	. Overv	/iew	22
	1.4.2	Collag	gen	24
	1.4.3	Elasti	n	25
	1.4.4	Prote	oglycans and Fibronectin	26
	1.4.5	Matri	x Metalloproteinases	27
		1.4.5.1	Regulation of matrix metalloproteinases	28
		1.4.5.2	Matrix Metalloproteinases and Metabolic Syndrome	29
		1.4.5.3	Tissue Inhibitor of Matrix Metalloproteinases	30

Table of Contents

1.5	Tiss	ue Inhibitor of Matrix Metalloproteinase 3	31
	1.5.1	TIMP3 and inflammation	32
	1.5.2	TIMP3 and Type 2 Diabetes	33
	1.5.3	TIMP3 and cardiovascular disease	33
	1.5.4	TIMP3 and Liver Disease	34
	1.5.5	TIMP3 and the Gut Microbiota	34
1.6	Con	clusions and Knowledge Gaps	36
1.7	Proj	ect Aims and Hypothesis	36
Chap	oter 2	Materials and Methods	39
2.1	Con	trol and Experimental Groups	40
2.2	Anir	mal Work authorisation	41
2.3	Indi	rect Calorimetry	42
2.4	Tail-	-cuff Plethysmography	43
2.5	Tiss	ue sampling	43
2.6	Bloc	od Plasma Analysis	43
2.7	RNA	\ Isolation	46
2.8	Rev	erse Transcription	46
2.9	Rea	l-time Quantitative Polymerase Chain Reaction (RT qPCR)	47
	2.9.1	Primer selection and validation	47
	2.9.2	Reaction procedure	48
2.1	0 Fou	r Chamber Wire Myography	49
	2.10.1	. Myography procedure	49
2.1	1 Hist	ology Sample Processing	50
	2.11.1	Dewaxing	50
	2.11.2	Haematoxylin and Eosin Staining	50
	2.11.3	Sirius Red Staining	50
	2.11.4	Elastic Van Gieson Staining	51
	2.11.5	Sample Preparation for Second Harmonic Generation Microscopy	51
2.1	2 Brig	ht-field Imaging	51
		rised Light Field Imaging	
		ond Harmonic Generation and Two Photon Excitation Fluorescence Imaging	

	2.14.1 Syste	m Setup	52
	2.14.2 Imag	e acquisition	52
2.15	5 Analysis o	f Liver Tissue	52
2.16	5 Analysis o	f Aorta Tissue	53
	2.16.1 Aorta	Wall Measurements	53
	2.16.2 Pixel	Counting of Sirius Red Stained Collagen	53
	2.16.3 Seco	nd Harmonic Generation Image Processing	53
2.17	7 MiSeq 169	Ribosomal RNA Sequencing	54
	2.17.1 Samp	le Preparation and Sequencing	54
	2.17.2 Sequ	encing Analysis	55
2.18	3 Statistical	Methods	56
-			
Chap		velopment of Obesity in a Chronic Low-grade Inflammation	
	Mic	del, Timp3 Knockout Mice	59
3.1	Introducti	on	60
3.2		Hypothesis	
3.3			
3.4	Results		63
		ts of Diet Induced Obesity on the Phenotype of the <i>Timp3</i> Knockout	
	Mous	se	63
	3.4.1.1	Body Weight	63
	3.4.1.2	Fat Depot Weight: Gonadal, Retroperitoneal, Inguinal and Brown-	
		interscapular Fat	
	3.4.1.3	Lipid Accumulation within the <i>Timp3</i> Knockout Mouse During Obe	
	3.4.2 Effec	ts of DIO on the Energy Expenditure of the <i>Timp3-/-</i> Mouse	72
	3.4.2.1	Energy Expenditure	72
		Respiratory Exchange Ratio	
		Matrix Metalloproteinases	
		Glucose and Lipid Metabolism	
	3425	Adiponectin Receptor Expression is Decreased in the Timp3-/- Mou	ISP 91

3	3.4.2.6	Inflammation markers	93
3.4.3	Blood F	Plasma Biomarkers in <i>Timp3</i> Knockout Mou	se during Obesity95
3	3.4.3.1	Fasted Blood Glucose and Insulin Following	; 15 Weeks of High-fat Diet
			95
3.4.4	Adipon	ectin and Butyrate in the Blood	97
3.5 Dis	cussion		98
3.5.1	Adipos	ity and energy expenditure	98
3.5.2	Expres	sion of genes involved in ECM regulation	101
3.5.3	Expres	sion of genes involved in lipid and glucose i	egulation101
3.5.4	Blood b	piomarkers of insulin resistance and hyperl	ipidaemia102
3.6 Stre	engths ar	nd Limitations	103
3.7 Cor	nclusions		103
Chapter 4		gut Microbiome Profile in <i>Timp3^{-/-}</i> Mice	
	Conc	litions	105
4.1 Intr	oduction	າ	105
4.2 Aim	ns and Hy	ypothesis	106
4.3 Me	thods		107
4.4 Res	ults		
4.4.1	Initial E	xploration	109
4	4.4.1.1	Normalisation	110
4.4.2	Diversi	ty measures	111
4	4.4.2.1	Alpha Diversity	111
	4.4.2.1.1	L Observed	111
	4.4.2.1.2	2 Chao1	113
	4.4.2.1.3	3 Simpson	115
	4.4.2.1.4	Shannon	117
4	4.4.2.2	Beta Diversity	119
	4.4.2.2.1	L UniFrac	Error! Bookmark not defined.
	4.4.2.2.2	2 Weighted UniFrac	Error! Bookmark not defined.
	4.4.2.2.3	Bray-Curtis	Error! Bookmark not defined.

		4.4.2.3	Log Abundance at the Phylum Level	123
		4.4.2.4	Log Abundance at the Genus Level	124
	4.4.3	Differ	ential Abundance	126
		4.4.3.1	Combined Ages Error! Bookmark not def	ined.
	4.4.4	Differ	rential Abundance Summary	139
	4.4.5	Meas	ures of Microbial Activity within the <i>Timp3</i> -/- Mouse	141
		4.4.5.1	Expression of Toll-like Receptor 4	141
4.5	Dis	cussion		142
4.6			and limitations	
4.7			าร	
Char	oter !	5 Effe	ects of <i>Timp3</i> Deletion on Cardiovascular Function in Mice	147
5 .1			on	
5.2			Hypothesis	
5.3			, , , , , , , , , , , , , , , , , , ,	
5.4				
			ts of a high fat diet in 16-week-old <i>Timp3^{-/-}</i> female mice	
	J.4.1			51
		5.4.1.1	Effect of a high fat diet on body weight, gonadal, retroperitoneal,	.1-
			inguinal, and intrascapular brown fat in 16-week-old <i>Timp3-/-</i> fema	
		F 4 4 2	mice	151
		5.4.1.2	Effect of a high fat diet on aortic function in 16-week-old <i>Timp3-/-</i> female mice	152
	5.4.2		otype and cardiovascular function in 30-week-old <i>Timp3^{-/-}</i> female m	ice
		154		
		5.4.2.1	Comparison in body weight, gonadal, retroperitoneal, inguinal and	İ
			intrascapular brown fat between the 30- and 16-week-old chow-fe	∍d
			Timp3 ^{-/-} female mice	154
		5.4.2.2	Blood pressure and heart rate in 30-week-old <i>Timp3-/-</i> female mice	≥.156
		5.4.2.3	Aortic function in 30-week-old <i>Timp3</i> -/- female mice	157
		5.4.2.4	Comparison of aortic function between the 30- and 16-week-old	
			Timn?-/- famala mica	150

Table of Contents

5.4.3 M	lorphology and structure of the aortas taken from 30-week-old Timp3-/-
fe	male mice
5.4.	3.1 Aortic wall width160
5.4.	3.2 Measurement of collagen content within the cross-section of aortas by
	light and polarised-light microscopy161
5.4.	3.3 Measurement of collagen and elastin content within the cross-section
	of the aorta by second-harmonic generation (SHG) and two-photon-
	excitation autofluorescence (TPEF) microscopy162
5.4.4 G	ene expression in the aorta samples taken from 30-week-old <i>Timp3-/-</i>
fe	male mice
5.5 Discuss	sion171
5.6 Strengt	ths and Limitations174
5.7 Conclu	sions
Chapter 6	Conclusion
-	
Appendix A	
A.1 Supple	mentary Material
Appendix B	183
B.1 Chow [Diet Composition183
B.2 High-fa	at diet composition184
0 o oli C	4.05
Appendix C	
Appendix D	
Appendix E	
List of Refere	ences 219

Table of Tables

Table 1.1 Metab	polic syndrome diagnostic factors. Patients must exhibit abdominal obesity in
	addition to any two other factors listed, to be diagnosed with metabolic
	syndrome. Adapted from "The 2006 IDF consensus worldwide definition of the
	metabolic syndrome report" (Alberti et al., 2006)3
Table 1.2 The fo	ur major lipoprotein types and characterisation. Table adapted from
	"Introduction to Lipids and Lipoproteins" (Feingold, 2021)16
Table 1.3 Matrix	metalloproteinase categories in humans, based on substrate specificity, and a
	summary of their substrates (Birkedal-Hansen, 1995; Lu et al., 2011; Massova et
	al., 1998)27
Table 4.1 Summ	ary table of selected genera identified in differential abundance analysis.
	Genera listed are those which presented significant differences between the
	genotypes. Arrows represent increase (\spadesuit) or decrease (\blacktriangledown) in abundance. 140

Table of Figures

Figure 1.1 Over	weight and obesity trends in England, from 1993 to 2019. (a) Percentage of men
	and women in England with overweight from 1993-2019; (b) percentage of mer
	and women in England with obesity from 1993-2019; (c) average waist
	circumference of men and women in England in 1993 and 2019. Figure adapted
	from Public Health England, 20195
Figure 1.2 Life	stages of the C57BI/6 mouse and approximate comparison to humans. Figure
	taken from Flurkey et al, 20079
Figure 1.3 Sum	mary of fat depots in mice and humans. Fat depots are classified into visceral
	white adipose tissue (VAT), subcutaneous white adipose tissue (SAT) and brown
	adipose tissue (BAT). Adapted from Schoettl et al., 2018
Figure 1.4 Adip	ose tissue expansion: hyperplasia and hypertrophy. During hyperplasia, adipose
	tissue expands through increased number of adipocytes; during hypertrophy,
	adipose tissue expansion occurs through increased adipocyte size. Image taken
	from Choe et al, 201614
Figure 1.5 Sum	mary of bile acid metabolism in the liver and small intestine. The classical
	pathway is the predominant method of primary bile acid production, for which
	CYP7A1 is the rate-limiting enzyme. Secondary bile acids are produced by the
	gut microbiota. LCA and $\omega\text{-MCA}$ are excreted into faeces. Figure taken from Li
	and Chiang, 2014
Figure 1.6 Over	rview of the extracellular matrix. Taken from Dewing et al, 201923
Figure 2.1 Carto	oon diagram outlining the high-fat diet study design. Male wild-type C57BI/6J and
	knock-out <i>Timp3-/-</i> mice were fed either chow (7.4% Kcal from fat) or high-fat
	(45% Kcal from fat) diet from 5 weeks of ages. Subgroups were culled and tissue
	samples collected at ages 5, 10 and 15 weeks throughout the study duration.41
Figure 2.2 Illust	tration of the indirect calorimetry setup. Mice were housed separately in a cage
	connected to the CaloBox (PhenoSys GmbH, Germany) which was linked to
	computer where readings were automatically recorded and saved. Energy
	expenditure was measured over a 48hr period42
Figure 2.3 Exan	nple primer dissociation curve. Presenting a primer pair that produces no primer
	dimers 47

Figure 2.4 Filtering of FASTQ sequences and construction of a phyloseq object in R55		
Figure 3.1 Total	weight gain and area under the curve analysis in <i>Timp3</i> -/- mice over the study	
	duration. a) Mean values ± SEM shown for weight gain over study duration from	
	5 to 17 weeks of age in male <i>Timp3</i> -/- mice on chow (C) and high-fat (HF) diets	
	and C57BI/6J wild-type controls. b) AUC analysis of body weight gain. n= 4	
	biological samples per group. One-way ANOVA with Tukey's Comparisons was	
	used to test for differences between groups. * = $p < 0.05$, *** = $p < 0.001$, ****	
	= p < 0.000163	
Figure 3.2 Longi	itudinal representation of weight gain over the study duration, in <i>Timp3</i> -/- mice	
	on high-fat diet, and C57Bl6/J controls. Average weight gain per week ± SEM,	
	from 6 to 17 weeks of age in male <i>Timp3</i> -/- mice on chow (C) and high-fat (HF)	
	diets and C57BI/6J wild-type controls64	
Figure 3.3 Gona	dal adipose depot weight of <i>Timp3</i> -/- mice, across 5-17 weeks of age, on chow	
	(C) and high-fat (HF) diet. Mean weight expressed as a percentage of total body	
	weight \pm SEM in male $Timp3^{-/-}$ mice on chow and high-fat diet, and C57BI/6J	
	controls. n=3-10 biological samples per group. Tukey's Comparisons was used to	
	test for differences. * = p < 0.05, ** = p < 0.01, *** = p < 0.001, **** = p <	
	0.000165	
Figure 3.4 Retro	operitoneal adipose depot weight of <i>Timp3</i> ^{-/-} mice, across 5-17 weeks of age, on	
	chow (C) and high-fat (HF) diet. Mean weight expressed as a percentage of total	
	body weight \pm SEM in male $Timp3^{-/-}$ mice on chow and high-fat diet, and	
	C57BI/6J controls. n=3-10 biological samples per group. Tukey's Comparisons	
	was used to test for differences. * = p < 0.05, ** = p < 0.01, *** = p < 0.001, ****	
	= p < 0.000166	
Figure 3.5 Ingui	nal adipose depot weight of <i>Timp3^{-/-}</i> mice, across 5-17 weeks of age, on chow (C)	
	and high-fat (HF) diet. Mean weight expressed as a percentage of total body	
	weight \pm SEM in male $Timp3^{-/-}$ mice on chow and high-fat diet, and C57BI/6J	
	controls. n=3-10 biological samples per group. Tukey's Comparisons was used to	
	test for differences. * = p < 0.05, ** = p < 0.01, *** = p < 0.001, **** = p <	
	0.000167	
Figure 3.6 Inters	scapular brown adipose tissue (iBAT) depot weight of <i>Timp3</i> -/- mice, across 5-17	
	weeks of age, on chow (C) and high-fat (HF) diet. Mean weight expressed as a	

percentage of total body weight \pm SEM in male $\textit{Timp3}^{\text{-/-}}$ mice on chow and high-

	Comparisons was used to test for differences. * = $p < 0.05$, ** = $p < 0.01$, *** = p
	< 0.001, **** = p < 0.000168
Figure 3.7 Sum	total of white adipose depot weight in <i>Timp3</i> -/- mice, across 5-17 weeks of age,
	on chow (C) and high-fat (HF) diet. Mean weight expressed as a percentage of
	total body weight ± SEM in male <i>Timp3</i> -/- mice on chow and high-fat diet, and
	C57BI/6J controls. n=3-10 biological samples per group. Tukey's Comparisons
	was used to test for differences. * = $p < 0.05$, ** = $p < 0.01$, *** = $p < 0.001$, ***
	= p < 0.0001 ****69
Figure 3.8 Macr	ovesicular lipid droplet accumulation in <i>Timp3-/-</i> mouse liver samples, at 15 and
	17 weeks of age, following 10 and 12 weeks on high-fat diet respectively. a)
	Haematoxylin and eosin-stained liver sections from 15-week-old <i>Timp3-/-</i> mice
	under C and HF diets, and the C57Bl/6 controls taken at 20x magnification. Scale
	bar indicated 50µm. Black arrows indicate macrovesicles. b) Mean values and
	SEM for macrovesicular lipid droplet counts in 15 and 17-week-old <i>Timp3</i> -/- liver
	sections under chow (C) and high-fat (HF) diets, and the C57BI/6J controls. n=4-7
	biological samples per group. Tukey's comparisons was used to test differences.
	** = p < 0.01
Figure 3.9 Energ	gy expenditure of <i>Timp3</i> -/- mice, across a 24hr period at three ages, on chow (C)
	and high-fat (HF) diet. Mean energy expenditure expressed as calories per
	minute ±SEM in male <i>Timp3</i> ^{-/-} mice on chow and high-fat diet, and C57BI/6J
	controls, at 5 weeks (5a), 10 weeks (5b) and 15 weeks (5c) of age. n=4-10
	biological samples per group. Shaded area indicates the dark period within the
	animal house (from 7pm to 7am)73
Figure 3.10 Area	a under the curve of <i>Timp3</i> ^{-/-} energy expenditure. Bar chart shows area under the
	curve of energy expenditure in male <i>Timp3</i> ^{-/-} mice on chow and high-fat diet,
	and C57Bl/6J controls. Tukey's comparisons was used to test for differences.
	**** = p < 0.000174
Figure 3.11 Resp	piratory exchange ratio of <i>Timp3</i> ^{-/-} mice, across a 24hr period at three ages, on
	chow (C) and high-fat (HF) diet. Mean respiratory exchange ratio ±SEM in male
	Timp3 ^{-/-} mice on chow and high-fat diet, and C57BI/6J controls, at 5 weeks (a),
	10 weeks (b) and 15 weeks (c) of age. n=4-10 biological samples per group.

fat diet, and C57BI/6J controls. n=3-10 biological samples per group. Tukey's

	Shaded area indicates the dark period within the animal house (from 7pm to
	7am)
5: 2 42 Ave	and the control of an arise to a second of Time 2/2 arise. December to be a
Figure 3.12 Area	a under the curve of respiratory exchange ratio of <i>Timp3</i> -/- mice. Bar chart shows
	area under the curve of the respiratory exchange ratio in male <i>Timp3</i> -/- mice on
	chow and high-fat diet, and C57Bl/6J controls. Tukey's comparisons was used to
	test for differences. * = p < 0.05, **** = p < 0.000177
Figure 3.13 Mm	p8 gene expression in liver tissue of <i>Timp3</i> ^{-/-} mice, across 5-17 weeks of age, on
	chow (C) and high-fat (HF) diet. Mean fold change ± SEM (normalised to 5-
	week-old, chow-fed, C57BI/6J control samples) from RT-qPCR gene expression in
	male <i>Timp3</i> -/- liver samples on chow and high-fat diet, and C57BI/6J controls.
	n=3-10 biological samples per group. Tukey's comparisons was used to test for
	differences. Statistical analysis was conducted using ddct values, normalised to
	θ -actin and Gapdh internal control genes. ** = p < 0.0178
Figure 3.14 Mm	p9 gene expression in liver tissue of <i>Timp3</i> ^{-/-} mice, across 5-17 weeks of age, on
	chow (C) and high-fat (HF) diet. Mean fold change ± SEM (normalised to 5-
	week-old, chow-fed, C57Bl/6J control samples) from RT-qPCR gene expression in
	male <i>Timp3</i> ^{-/-} liver samples on chow and high-fat diet, and C57Bl/6J controls.
	n=3-10 biological samples per group. Tukey's comparisons was used to test for
	differences. Statistical analysis was conducted using ddct values, normalised to
	<i>B-actin</i> and <i>Gapdh</i> internal control genes. * = p < 0.05, *** = p < 0.001 79
5' 2 45 84	.42
Figure 3.15 ivim	p12 gene expression in liver tissue of <i>Timp3</i> -/- mice, across 5-17 weeks of age, on
	chow (C) and high-fat (HF) diet. Mean fold change ± SEM (normalised to 5-
	week-old, chow-fed, C57Bl/6J control samples) from RT-qPCR gene expression in
	male <i>Timp3</i> -/- liver samples on chow and high-fat diet, and C57BI/6J controls.
	n=3-10 biological samples per group. Tukey's comparisons was used to test for
	differences. Statistical analysis was conducted using ddct values, normalised to
	<i>8-actin</i> and <i>Gapdh</i> internal control genes. * = p < 0.05, *** = p < 0.001 80
Figure 3.16 Mm	p13 gene expression in liver tissue of <i>Timp3^{-/-}</i> mice, across 5-17 weeks of age, on
	chow (C) and high-fat (HF) diet. Mean fold change ± SEM (normalised to 5-
	week-old, chow-fed, C57Bl/6J control samples) from RT-qPCR gene expression in
	male <i>Timp3</i> -/- liver samples on chow and high-fat diet, and C57BI/6J controls.
	n=3-10 biological samples per group. Tukey's comparisons was used to test for

	differences. Statistical analysis was conducted using ddct values, normalised to
	θ -actin and Gapdh internal control genes. ** = p < 0.0181
Figure 3.17 Mm	p14 gene expression in liver tissue of <i>Timp3^{-/-}</i> mice, across 5-17 weeks of age, or
	chow (C) and high-fat (HF) diet. Mean fold change \pm SEM (normalised to 5-
	week-old, chow-fed, C57Bl/6J control samples) from RT-qPCR gene expression in
	male <i>Timp3</i> -/- liver samples on chow and high-fat diet, and C57BI/6J controls.
	n=3-10 biological samples per group. Tukey's comparisons was used to test for
	differences. Statistical analysis was conducted using ddct values, normalised to
	<i>β-actin</i> and <i>Gapdh</i> internal control genes. * = p < 0.0582
Figure 3.18 Mm	p19 gene expression in liver tissue of <i>Timp3^{-/-}</i> mice, across 5-17 weeks of age, or
	chow (C) and high-fat (HF) diet. Mean fold change ± SEM (normalised to 5-
	week-old, chow-fed, C57BI/6J control samples) from RT-qPCR gene expression in
	male <i>Timp3</i> ^{-/-} liver samples on chow and high-fat diet, and C57BI/6J controls.
	n=3-10 biological samples per group. Tukey's comparisons was used to test for
	differences. Statistical analysis was conducted using ddct values, normalised to
	<i>β-actin</i> and <i>Gapdh</i> internal control genes. * = p < 0.0583
Figure 3.19 Mm	p28 gene expression in liver tissue of <i>Timp3</i> -/- mice, across 5-17 weeks of age, or
	chow (C) and high-fat (HF) diet. Mean fold change ± SEM (normalised to 5-
	week-old, chow-fed, C57BI/6J control samples) from RT-qPCR gene expression in
	male <i>Timp3</i> ^{-/-} liver samples on chow and high-fat diet, and C57BI/6J controls.
	n=3-10 biological samples per group. Tukey's comparisons was used to test for
	differences. Statistical analysis was conducted using ddct values, normalised to
	<i>β-actin</i> and <i>Gapdh</i> internal control genes. * = p < 0.0584
Figure 3.20 Cyp7	7a1 gene expression in liver tissue of <i>Timp3^{-/-}</i> mice, across 5-17 weeks of age, on
	chow (C) and high-fat (HF) diet. Mean fold change ± SEM (normalised to 5-
	week-old, chow-fed, C57BI/6J control samples) from RT-qPCR gene expression in
	male <i>Timp3</i> ^{-/-} liver samples on chow and high-fat diet, and C57BI/6J controls.
	n=3-10 biological samples per group. Tukey's comparisons was used to test for
	differences. Statistical analysis was conducted using ddct values, normalised to
	θ -actin and Gapdh internal control genes. * = p < 0.05, ** = p < 0.01, *** = p <
	0.00185

Figure 3.21 Fxr gene expression in liver tissue of Timp3^{-/-} mice, across 5-17 weeks of age, on

chow (C) and high-fat (HF) diet. Mean fold change ± SEM (normalised to 5-

week-old, chow-fed, C57BI/6J control samples) from RT-qPCR gene express	ion in
male $\mathit{Timp3}^{\text{-}/\text{-}}$ liver samples on chow and high-fat diet, and C57BI/6J controls	5.
n=3-10 biological samples per group. Tukey's comparisons was used to test	for
differences. Statistical analysis was conducted using ddct values, normalised	d to
<i>β-actin</i> and <i>Gapdh</i> internal control genes. * = p < 0.05	86

- Figure 3.24 Irs2 gene expression in liver tissue of Timp3^{-/-} mice, across 5-17 weeks of age, on chow (C) and high-fat (HF) diet. Mean fold change ± SEM (normalised to 5-week-old, chow-fed, C57BI/6J control samples) from RT-qPCR gene expression in male Timp3^{-/-} liver samples on chow and high-fat diet, and C57BI/6J controls. n=3-10 biological samples per group. Tukey's comparisons was used to test for differences. Statistical analysis was conducted using ddct values, normalised to β-actin and Gapdh internal control genes. ** = p < 0.01, *** = p < 0.001.....89
- Figure 3.25 Srebf1c gene expression in liver tissue of Timp3^{-/-} mice, across 5-17 weeks of age, on chow (C) and high-fat (HF) diet. Mean fold change ± SEM (normalised to 5-week-old, chow-fed, C57Bl/6J control samples) from RT-qPCR gene expression in male Timp3^{-/-} liver samples on chow and high-fat diet, and C57Bl/6J controls.

 n=3-10 biological samples per group. Tukey's comparisons was used to test for differences. Statistical analysis was conducted using ddct values, normalised to β-actin and Gapdh internal control genes. * = p < 0.05..........................90

Figure 3.26	Adipr1 gene expression in liver tissue of Timp3 ^{-/-} mice, across 5-17 weeks of age, on
	chow (C) and high-fat (HF) diet. Mean fold change ± SEM (normalised to 5-
	week-old, chow-fed, C57BI/6J control samples) from RT-qPCR gene expression in
	male <i>Timp3</i> -/- liver samples on chow and high-fat diet, and C57BI/6J controls.
	n=3-10 biological samples per group. Tukey's comparisons was used to test for
	differences. Statistical analysis was conducted using ddct values, normalised to
	θ -actin and $Gapdh$ internal control genes. * = p < 0.05, ** = p < 0.01, *** = p <
	0.001, **** = p < 0.000191
Figure 3.27	Adipr2 gene expression in liver tissue of <i>Timp3^{-/-}</i> mice, across 5-17 weeks of age, on
•	chow (C) and high-fat (HF) diet. Mean fold change ± SEM (normalised to 5-
	week-old, chow-fed, C57BI/6J control samples) from RT-qPCR gene expression in
	male $Timp3^{-/-}$ liver samples on chow and high-fat diet, and C57BI/6J controls.
	n=3-10 biological samples per group. Tukey's comparisons was used to test for
	differences. Statistical analysis was conducted using ddct values, normalised to
	θ -actin and $Gapdh$ internal control genes. * = p < 0.05, ** = p < 0.01, *** = p <
	0.00192
Figure 3.28 <i>I</i>	1/1b gene expression in liver tissue of <i>Timp3</i> ^{-/-} mice, across 5-17 weeks of age, on
	chow (C) and high-fat (HF) diet. Mean fold change ± SEM (normalised to 5-
	week-old, chow-fed, C57BI/6J control samples) from RT-qPCR gene expression in
	male <i>Timp3</i> -/- liver samples on chow and high-fat diet, and C57BI/6J controls.
	n=3-10 biological samples per group. Tukey's comparisons was used to test for
	differences. Statistical analysis was conducted using ddct values, normalised to
	θ -actin and $Gapdh$ internal control genes. ** = p < 0.0193
Figure 3.29	Tnfa gene expression in liver tissue of Timp3 ^{-/-} mice, across 5-17 weeks of age, on
	chow (C) and high-fat (HF) diet. Mean fold change ± SEM (normalised to 5-
	week-old, chow-fed, C57BI/6J control samples) from RT-qPCR gene expression in
	male <i>Timp3</i> ^{-/-} liver samples on chow and high-fat diet, and C57BI/6J controls.
	n=3-10 biological samples per group. Tukey's comparisons was used to test for
	differences. Statistical analysis was conducted using ddct values, normalised to

Figure 3.30 Fasting blood glucose, fasting insulin and subsequent homeostatic model assessment for insulin resistance value for *Timp3-/-* mice, at 17 weeks of age, on chow (C) and high-fat (HF) diet. Mean concentration of blood glucose,

 θ -actin and Gapdh internal control genes. * = p < 0.05, ** = p < 0.01, *** = p <

0.001, **** = p < 0.0001.94

	diet, and C57BI/6J controls. n=4-5 biological samples per group. Tukey's		
	comparisons was used to test for differences. * = p < 0.05, ** = p < 0.01 95		
Figure 3.31 Bloo	d lipid profile of <i>Timp3</i> -/- mice, at 17 weeks of age, on chow (C) and high-fat (HF)		
	diet. Mean concentration of fasting blood triglycerides, low-density lipoprotein,		
	high-density lipoprotein, and total cholesterol ± SEM in male <i>Timp3</i> -/- mice on		
	chow and high-fat diet, and C57BI/6J controls. n=5 biological samples per group.		
	Tukey's comparisons was used to test for differences. ** = $p < 0.01$, *** = $p < 0.01$		
	0.001, **** p < 0.0001		
Figure 3.32 Fasti	ng blood concentration of adiponectin and butyrate within male <i>Timp3</i> -/- mice,		
	at 17 weeks old, on chow (C) and high-fat (HF) diet. a) Mean concentration of		
	adiponectin \pm SEM and b) mean concentration of butyrate \pm SEM in male $Timp3^-$		
	/- mice on chow and high-fat diet, and C57BI/6J controls. n=4-5 biological		
	samples per group. Tukey's comparisons was used to test for differences. * = $p <$		
	0.05, *** = p < 0.00		
Figure 4.1 Sampl	le read depth histograms and bar plot. a) read depth bar plot of all samples; b)		
	histogram of read depths109		
Figure 4.2 Phylu	m abundance from data sets with different normalisation methods. (a) raw		
	data; (b) rarefied data; (c) relative abundance data; (d) log-transformed data.110		
Figure 4.3 Obser	ved alpha diversity box plots of combined samples from age groups 7, 10 and		
	15 weeks using rarefied abundance data. Wilcox test was used to test for		
	differences between groups. $n = 14-15$ samples per group. $* = p < 0.05$, $** = p < 0.05$		
	0.01, *** = p < 0.001		
Figure 4.4 Chao1	Figure 4.4 Chao1 alpha diversity box plots of combined samples from age groups 7, 10 and 15		
	weeks using rarefied abundance data. Wilcox test was used to test for		
	differences between groups. n = 14-15 samples per group		
Figure 4.5 Simpson alpha diversity box plots of combined samples from age groups 7, 10 and 15			
	weeks using rarefied abundance data. Wilcox test was used to test for		
	differences between groups. $n = 14-15$ samples per group. $* = p < 0.05$, $** = p < 0.05$		
	0.01		

insulin, and HOMA-IR value ± SEM in male *Timp3*-/- mice on chow and high-fat

Figure 4.6 Shan	non alpha diversity box plots of combined samples from age groups 7, 10 and 1	15
	weeks using rarefied abundance data. Wilcox test was used to test for	
	differences between groups. n = 14-15 samples per group. ** = p < 0.01118	
Figure 4.7 PCoA	plot based on the UniFrac diversity metric, using rarefied data, for combined	
	samples from weeks 7, 10 and 15. PERMANOVA was used to test for	
	differences. Ellipses represent 95% Cl	
Figure 4.8 PCoA	plot based on the weighted UniFrac diversity metric, using rarefied data, for	
	combined samples from weeks 7, 10 and 15. PERMANOVA was used to test for	r
	differences. Ellipses represent 95% Cl	
Figure 4.9 PCoA	plot based on the Bray-Curtis diversity metric, using rarefied data, for combin	ed
	samples from weeks 7, 10 and 15. PERMANOVA was used to test for	
	differences. Ellipses represent 95% Cl	
Figure 4.10 Bar	graph displaying the top four most abundant phyla within the log-transformed	ı
	data set, for all ages combined, excluding 5 weeks. Mann-Whitney test was	
	used to test for differences between groups. n = 14-15 samples per group. * =	р
	< 0.05, *** = p < 0.001, **** = p < 0.0001123	
Figure 4.11 Hea	t map of hierarchical clustering of the 40 most abundant bacterial genera in	
	Timp3 ^{-/-} faecal samples, on chow (C) and high-fat (HF) diet, and C57BI/6 wild-	
	type controls. Heatmap colour (white to red) displays the log-transformed	
	abundance of each genus across samples125	
Figure 4.12 Volc	cano plot displaying the fold change of genera within the C57BI/6J high fat grou	qι
	compared to the C57BI/6J chow group, for all ages combined, identified by	
	DESeq2 . Grey points indicate non-significant ASVs. Red points indicate ASVs w	ith
	a p-value lower than 0.01, blue points indicate ASCVs with a Log2 fold change	
	more than +/-2 and purple points indicate ASVs that meet both these requisite	٤S.
	The 20 most significant ASVs are labelled	
Figure 4.13 Bar	plot displaying the fold change of significant genera within the C57Bl/6J high-f	at
	group compared to the C57BI/6J chow group with all ages combined, identifi	ed
	by ANCOM-BC . Significance level was set at p = 0.01128	
Figure 4.14 Ven	n diagram displaying the percentage of ASVs identified in C57BI/6J high-fat,	
	compared to C57BI/6J chow, by DESeq2 and ANCOM-BC, with common gene	ra
	between methods listed	

Figure 4.15 Volc	cano plot displaying the fold change of genera within the <i>Timp3^{-/-}</i> high-fat	group
	compared to the Timp3 ^{-/-} chow group for all ages combined, identified b	у
	DESeq2 . Grey points indicate non-significant ASVs. Red points indicate AS	SVs with
	a p-value lower than 0.01, blue points indicate ASCVs with a Log2 fold cha	ange
	more than +/-2 and purple points indicate ASVs that meet both these req	ιuisites.
	The 20 most significant ASVs are labelled	130
Figure 4.16 Bar	plot displaying the fold change of significant genera within the <i>Timp3</i> ^{-/-} hi	igh-fat
	group compared to the <i>Timp3</i> ^{-/-} chow group with all ages combined, ide	ntified
	by ANCOM-BC . Significance level was set at p = 0.01	131
Figure 4.17 Ven	n diagram displaying the percentage of ASVs identified in <i>Timp3</i> -/- high-fa	ıt,
	compared to Timp3 ^{-/-} chow, by DESeq2 and ANCOM-BC, with common g	genera
	between methods listed.	132
Figure 4.18 Volc	cano plot displaying the fold change of genera within the <i>Timp3^{-/-}</i> chow gr	oup
	compared to the C57BI/6J chow group with all ages combined, identifie	d by
	DESeq2 . Grey points indicate non-significant ASVs. Red points indicate AS	SVs with
	a p-value lower than 0.01, blue points indicate ASCVs with a Log2 fold cha	ange
	more than +/-2 and purple points indicate ASVs that meet both these req	μisites.
	The 20 most significant ASVs are labelled	133
Figure 4.19 Bar	plot displaying the fold change of significant genera within the <i>Timp3</i> ^{-/-} ch	now
	group compared to the C57BI/6J chow group with all ages combined, id	entified
	by ANCOM-BC . Significance level was set at p = 0.01	134
Figure 4.20 Ven	nn diagram displaying the percentage of ASVs identified in <i>Timp3</i> -/- chow,	
	compared to C57BI/6J chow, by DESeq2 and ANCOM-BC, with common	genera
	between methods listed	135
Figure 4.21 Volc	cano plot displaying the fold change of genera within the <i>Timp3-/-</i> high-fat	group
	compared to the C57BI/6J high-fat group at seven weeks of age, identifi	ied by
	DESeq2 . Grey points indicate non-significant ASVs. Red points indicate AS	SVs with
	a p-value lower than 0.01, blue points indicate ASCVs with a Log2 fold cha	ange
	more than +/-2 and purple points indicate ASVs that meet both these req	ιuisites.
	The 20 most significant ASVs are labelled	136

Figure 4.22 Bar plot displaying the fold change of significant genera within the <i>Timp3</i> -/- high-fat
group compared to the C57BI/6J high-fat group with all ages combined,
identified by ANCOM-BC . Significance level was set at p = 0.01137
Figure 4.23 Venn diagram displaying the percentage of ASVs identified in <i>Timp3</i> ^{-/-} high-fat,
compared to C57BI/6J high-fat, by DESeq2 and ANCOM-BC, with common
genera between methods listed138
Figure 4.24 Tlr4 gene expression in the liver of <i>Timp3</i> -/- male mice at ages 5, 10, 15 and 17 weeks
old, following high-fat diet from 5 weeks. Mean fold change ± SEM from RT-
qPCR gene expression in male <i>Timp3</i> -/- liver samples on chow (C) and high-fat (F)
diets, and C57BI/6 controls. n=3-10 biological samples per group. Data are
normalised to 5-week-old C57Bl/6 and $ heta$ -actin and Gapdh internal control genes
One-way ANOVA with multiple comparisons used to test for differences141
Figure 4.25 Tlr4 gene expression in lower colon of <i>Timp3</i> -/- male mice at ages 5, 10, 15 and 17
weeks old, following high-fat diet from 5 weeks. Mean fold change ± SEM from
RT-qPCR gene expression in male <i>Timp3-^{J-}</i> liver samples on chow (C) and high-fat
(F) diets, and C57BI/6 controls. n=3-10 biological samples per group. Data are
normalised to 5-week-old C57Bl/6 and $ heta$ -actin and Gapdh internal control genes
One-way ANOVA with multiple comparisons used to test for differences142
Figure 5.1 Body weight, heart weight and fat depot weights in 16-week-old <i>Timp3</i> -/- and
C57BI/6J female mice on either a standard chow or high fat diet. Body and
heart weights (a and b, respectively) and fat depot weights (c-f, expressed as a
percentage of total body weight) of female <i>Timp3-/-</i> and C57BI/6J control mice a
16 weeks old, on either chow (C) or high-fat (HF) diet. iBAT, intrascapular brown
adipose tissue. $n = 2-4$ per group. Values are means \pm SEM, expressed as a
percentage of total body weight. Tukey's multiple comparisons was used to test
for differences. *p<0.05, **p<0.01, ****p<0.0001152

Figure 5.2 Tension generated during myography by aortic tissues taken from 16-week-old

Timp3-/- and C57BI/6 female mice on either a standard chow (C) or high fat (HF)

diet. (a) tension generated in response to mechanical, incremental stretching;

(b) contraction generated in response to the cumulative concentration of noradrenaline (NA); (c) relaxation generated in response to the cumulative concentration of carbachol (CCh); and (d) relaxation generated in response to the cumulative concentration of sodium nitroprusside (SNP). Values are means ±

	SEM, n = 4-10 per group. Tukey's multiple comparisons was used to test for	
	differences153	
Figure 5 2 Rody	weight, heart weight and fat depot weights in 30- and 16-week-old <i>Timp3</i> ^{-/-} and	
rigule 5.5 body	C57BI/6J female mice. Total body and heart weights (a & b, respectively) and fat	
	depot weights (c-f, expressed as a percentage of total body weight) in 30 and 16-	
	week-old female <i>Timp3</i> -/- and C57Bl/6J control mice on chow diet. Values are	
	means ± SEM, n = 2-8 per group. Tukey's multiple comparisons was used to test	
	for differences between means. **p<0.01	
Figure 5.4 Heart	rate and blood pressure in 30-week-old <i>Timp3</i> ^{-/-} female mice. Mean heart rate,	
	systolic and diastolic blood pressure (a-c, respectively) in 30-week-old female	
	chow-fed <i>Timp3</i> -/- and C57BI/6J control mice measured by plethysmography.	
	Values are means ± SEM, n = 7-10 per group. Unpaired two-tailed Student t-test	
	was used to test differences between means. **p<0.01156	
Figure 5.5 Heart	weight in the 30-week-old female <i>Timp3</i> ^{-/-} mouse, as a proportion of total body	
	weight. Mean heart weight expressed as a percentage of total body weight ±	
	SEM in aged female <i>Timp3</i> -/- mice on chow diet, and C57BI/6J controls. n=7-8	
	biological samples per group. Two-tailed unpaired Student's t-test was used to	
	test for differences (p = 0.0756)	
Figure 5.6 Tensi	on generated during myography by aortic tissues taken from 30-week-old	
	female Timp3 ^{-/-} and C57BI/6 control mice on standard chow diet. (a) tension	
	generated in response to mechanical, incremental stretching; (b) contraction	
	generated in response to the cumulative concentration of noradrenaline (NA);	
	(c) relaxation generated in response to the cumulative concentration of	
	carbachol (CCh); and (d) relaxation generated in response to the cumulative	
	concentration of sodium nitroprusside (SNP). Values are means \pm SEM, n = 4-10.	
	Unpaired two-tailed Student t-test was used to test for differences. *p<0.05158	
Figure 5.7 Tension generated during myography by aortic tissue in 16- and 30-week-old female		
	Timp3 ^{-/-} and C57BI/6 female mice on chow diet. (a) tension generated in	
	response to mechanical, incremental stretching; (b) contraction generated in	
	response to the cumulative concentration of noradrenaline (NA); (c) relaxation	
	generated in response to the cumulative concentration of carbachol (CCh); and	

(d) relaxation generated in response to the cumulative concentration of sodium

	nitroprusside (SNP). Values are means \pm SEM, n = 4-10. Tukey's multiple
	comparisons was used to test for differences. *p<0.05, **p<0.01159
Figure 5.8 Total	wall width and smooth-muscle cell layer width of the aortas taken from 30-
	week-old female Timp3 ^{-/-} female and C57BI/6J control mice. (a) total aorta wall
	width; (b) tunica media width; and (c) tunica media width as a proportion of the
	total aorta wall width. Measurements taken from H&E stained aorta sections
	using ImageJ. Values are mean \pm SEM. n = 8. Unpaired two-tailed Student t-test
	was used to test for differences
Figure 5.9 Colla	gen content within Sirius Red stained aorta taken from 30-week-old <i>Timp3-/-</i>
	female mice. (a) total pixel area of stained collagen fibres in the aortas from
	Timp3 ^{-/-} and C57BI/6J WT control female mice; (b) representative images of
	Sirius Red stained aorta from 30-week-old female <i>Timp3</i> -/- and C57BI/6J control
	mice under light and polarised-light microscopes. Measurements were made
	using ImageJ. Values are mean \pm SEM. Unpaired two-tailed Student t-test was
	used to test for differences. *p<0.05161
Figure 5.10 Rep	resentative SHG and TPEF cross-section images of the aortas and individual fibre
	extraction output from CT-FIRE. Magenta signal is second-harmonic generation
	(SHG), highlighting collagen molecules (left panels). The green signal is two-
	photon-excited autofluorescence (TPEF), highlighting elastin molecules. Collager
	fibre extraction output from CT-FIRE (middle panels) is overlaid onto the SHG
	signal and red boxes indicate the section magnified within the rightmost panels.
	Within the magnified sections, in the right panels, detail of individual collagen
	fibres can be seen, identified by each coloured line163
Figure 5.11 Dist	ribution of collagen fibre parameter results from CT-FIRE analysis in cross
	sections of aortas taken from the 30-week-old female Timp3-/- aorta and
	C57BI/6J control mice. (a) collagen fibre length; (b) collagen fibre width; (c)
	collagen fibre straightness; and (d) collagen fibre angle. n = 5-6 per group. 165
Figure 5.12 Coll	agen fibre analysis of the cross-section of the aorta taken from 30-week-old
	Timp3 ^{-/-} female mice. Analysis of collagen fibre parameters in 30-week-old
	female <i>Timp3</i> -/- and C57BI/6J control mice that was measured using CT-FIRE. (a)
	fibres detected; (b) fibre width in pixels; (c) fibre length in pixels; d) fibre

straightness; (e) fibre angle; and (f) representative SHG images used in CT-FIRE

	analysis. Plots represent mean ± SEM. n = 4-6. Unpaired two-tailed Student t-
	test was used to test for differences. *p<0.05166
Figure 5.13 Total	collagen and elastin content of the cross-section of the aorta taken from 30-
	week-old <i>Timp3</i> -/- female mice. Analysis of total collagen and elastin content
	within <i>Timp3</i> ^{-/-} female mice at 30 weeks old, and C57Bl/6J controls measured
	using ImageJ. (a) total elastin pixel area; (b) total collagen pixel area; (c) elastin
	content as a proportion of total aorta area; (d) collagen content as a proportion
	of total aorta area; and (e) elastin to collagen ratio. Plots represent mean \pm SEM
	n = 4-6. Unpaired two-tailed Student t-test was used to test for differences.167
Figure 5.14 Figure	e 5.13 Correlation analysis of collagen fibre parameters within the cross-section
	of the aortas taken from <i>Timp3</i> -/- female mice. (a) fibre width and length; (b)
	fibre width and straightness; (c) fibre width and angle; (d) fibre length and angle
	(e) fibre length and straightness; and (f) fibre angle and straightness169
Figure 5.15 Mmp	2, Mmp9, Mmp12, Col1, Col3 and Glut1 gene expression in aorta tissue taken
	from 30-week-old $\textit{Timp3}^{-/-}$ female mice on chow diet. Mean fold change \pm SEM
	(normalised to aorta samples taken from 30-week-old chow-fed female C57BI/6
	control mice) from RT-qPCR gene expression in aorta samples taken from 30-
	week-old female <i>Timp3</i> -/- mice on chow diet. n=4-6 biological samples per group
	Unpaired two-tailed Student t-test was used to test for differences. Statistical
	analysis was conducted using $\Delta \Delta { m ct}$ values, normalised to $ heta$ -actin and $Gapdh$
	internal control genes. *p<0.05
Figure 5.16 Sum r	nary table of results, seen in the aged female <i>Timp3</i> ^{-/-} aorta (right column)
	compared to the WT control (left column). eNOS: Nitric oxide synthase; NO:
	Nitric oxide
Figure 6.1 propos	sed mechanism of aortic dysfunction in the timp3-/- female mice178

Research Thesis: Declaration of Authorship

Print name: Rachel Hannah Meadows

Title of thesis: A Single Gene Deficiency (*TIMP3*) Affects the Regulation of Nutrition and Metabolism – Harnessing the Gut Microbiome

I, Rachel Hannah Meadows, declare that this thesis and the work presented in it are my own and has been generated by me as the result of my own original research.

I confirm that:

- This work was done wholly or mainly while in candidature for a research degree at this University;
- 2. Where any part of this thesis has previously been submitted for a degree or any other qualification at this University or any other institution, this has been clearly stated;
- 3. Where I have consulted the published work of others, this is always clearly attributed;
- 4. Where I have quoted from the work of others, the source is always given. With the exception of such quotations, this thesis is entirely my own work;
- 5. I have acknowledged all main sources of help;
- 6. Where the thesis is based on work done by myself jointly with others, I have made clear exactly what was done by others and what I have contributed myself;
- 7. None of this work has been published before submission

Signature:	Data
Zibustiite.	Date:

Research Thesis: Declaration of Authorship

Acknowledgements

The last few years have been the most exciting and challenging times of my life. I am proud to present a thesis that reflects the incredible contributions, support, and knowledge I have received from so many people throughout this time.

Firstly, I would like to express the upmost gratitude to my primary supervisor, Dr. Sylvia Pender, without whom this thesis would not be possible. Thank you for your guidance, knowledge, and unmatched support. Thank you to my secondary supervisors Dr. Felino Cagampang and Dr. David Cleary. Dr. Cagampang, thank you for your invaluable help in understanding the cardiovascular and metabolic implications of my project. Dr. Cleary, thank you for your boundless patience in helping me to analyse my sequencing data. I really do not think I could have been gifted with a more supportive supervisory team — you have made this thesis possible for me, thank you.

I am extremely grateful for the assistance of Dr. Christopher Torrens and Dr. Sumeet Mahajan for the opportunity to use your facilities. The myography and second harmonic microscopy added exciting dimensions to my project and taught me some valuable techniques. Thank you to Eileen Li for assisting me with part of the myography and to the members of Dr. Mahajan's lab group for training me in SHG microscopy.

A great big thank you to my amazing lab members: Olivia Lee, Ahamad Alzahrani, and Murad Baabbad. Thank you for not only being great colleagues but great friends also who provided me with a lot of cakes, dates, and laughter! Thank you also to our lab manager, Regina Teo, for all your kind support.

Thank you to NOC for processing my sequencing samples. Thank you to CBAL for processing of the biochemistry assays. Thank you to the Biomedical Research Facility and Histochemistry Research

Unit for your essential help during this project.

Additionally, I would like to thank the Chinese University of Hong Kong and the University of Southampton for their funding of this project.

Finally, thank you to my family for being my rock.

Chapter 1 Introduction

This thesis investigates the role of Tissue Inhibitor of Matrix Metalloproteinase 3 (TIMP3) in the development of Metabolic Syndrome (MetS) in a mouse model, with relation to diet-induced obesity (DIO) and the gut microbiota (GM). In this introduction, key MetS concepts and driving mechanisms will be discussed. In addition, an overview of the GM, the extracellular matrix (ECM) and TIMP3 will be given and their roles in MetS progression explored.

1.1 Metabolic Syndrome and Metabolic Disease

Metabolic syndrome (MetS) describes the clustering of multiple metabolic disease risk factors, including abdominal obesity which is an essential diagnostic factor (**Table 1.1**). Chronic diseases associated with MetS such as cardiovascular disease, heart disease and type two diabetes, put a great strain on the UK and global economy. The most recent national health survey for England revealed that 65% of adults are overweight or obese (National statistics, 2019). Due to the COVID-19 pandemic, a more recent data set is not available, however pre-pandemic assessments predicted a rate of 70% by 2020 (Public Health England, 2017). Trends in overweight and obesity have also been affected by the COVID-19 pandemic. A number of studies suggest that the pandemic has worsened risk factors for overweight and obesity and is likely to contribute to increasing rates in the future (Akter et al, 2022; Daniels et al, 2022; Robinson et al, 2021). On top of this, obesity is a risk factor for severe COVID-19 and mortality (Nakeshbandi et al, 2020). Considering the role that MetS (and obesity) plays in an extensive range of diseases, it is clear that the ever-increasing rates of obesity will cause greater economic impact. It is imperative that we increase efforts to lessen the burden of MetS.

Causes of MetS are multifactorial and may have contributions from a person's genetics and environment. Environmental factors such as sedentary lifestyle and "Westernised" diet habits are large contributors to MetS, however the impact of the gut microbiota (GM) as an environmental influence and the role of genetics are becoming increasingly important in research.

Table 1.1 Metabolic syndrome diagnostic factors. Patients must exhibit abdominal obesity in addition to any two other factors listed, to be diagnosed with metabolic syndrome.

Adapted from "The 2006 IDF consensus worldwide definition of the metabolic syndrome report" (Alberti et al., 2006).

Factor	Description
Abdominal obesity	Waist circumference ≥ 102 cm in males and ≥88 cm in females
Reduced high-density lipoprotein (HDL) cholesterol	Plasma HDL cholesterol ≤ 50mg/dL in males and ≤ 40mg/dL in females
Elevated triglycerides	Plasma triglycerides ≥ 150 mg/dL
High blood pressure (BP)	Systolic BP ≥ 130 mm Hg and diastolic ≥ 85 mm Hg
Elevated fasting blood glucose	Fasted blood glucose ≥ 100 mg/dL

Metabolic syndrome risk factors underpin some of society's most prevalent metabolic diseases – cardiovascular diseases (CVDs), type 2 diabetes mellitus (T2D) and fatty liver disease. Associations with MetS are also seen in gall bladder disease, certain types of cancer, neurodegenerative diseases and coronavirus disease 2019 (COVID-19) (Costa et al., 2020). Metabolic syndrome is deeply intertwined with many important pathologies, and its prevalence among the global population only highlights further the necessity for development of novel therapies.

Within this section, I will outline the diseases encompassed within MetS and discuss the current research that surrounds them.

1.1.1 Obesity

Obesity describes a low-grade chronic inflammatory disease state. It is a medical condition wherein an individual has an abnormal or excessive amount of body fat that can result in increased risk of diseases, including CVD, T2D, and certain types of cancer. The most widely used method of classifying whether a person in obese is by calculating their body mass index (BMI). The BMI is a simple index of weight-for-height and is calculated by dividing a person's weight in kilograms by the square of their height in metres (kg/m2). A score between 18.5 to less than 25 is considered within the normal range. If the BMI score is 25 to less than 30, it falls within the overweight range, and a BMI score of 30 or higher falls within the obese range. A BMI score of 40 or higher is sometimes categorised as extremely or severely obese. The BMI cannot however

Chapter 1

distinguish between lean mass and fat mass, and cannot indicate fat distribution, therefore other methods may be used in conjunction with BMI to give a better description of a person's body fat status. Often used as an additional parameter to classify overweight and obese individuals is their waist circumference which is a marker of excess abdominal fat (Lee et al., 2008). Excess fat in this area is termed "abdominal obesity" and can be a predictor of disease risk, independent from obesity, hence its use the essential diagnostic factor in MetS (Janssen et al., 2004) (Zhang et al., 2008). Using this method, males with a waist circumference of 94 cm or greater, and females with one of 80 cm or greater are likely to have increased risk of obesity-related health problems (National Institutes of Health, 2000).

Another limitation of the BMI is that cut-offs must be altered to accommodate ethnic background. A large-scale UK study by Caleyachetty *et al* found that incidence of T2D in persons from south Asian, Arabic, Chinese or black ethnicity was equal to those of Caucasian ethnicity at a lower BMI (Caleyachetty et al., 2021). Other studies corroborate these findings and the WHO currently recommends an obesity cut-off of 27.5 for South Asian and Chinese populations, compared to 30 for white populations. Additionally, cut-off points for waist circumference also differ by ethnicity (Lear et al., 2010). The current WHO recommended wait-circumference cut-off for central obesity is 80cm and 90cm for women and men, respectively, of Asian ethnicity. Still, these guides are still not appropriate for all Asian populations. Alberti *et al* found that incidence of MetS was higher in Indonesian populations at these measures and suggested amended cut-offs at 77cm and 80cm for women and men, respectively (Alberti et al., 2009). Cut-offs for BMI and waist-circumference continue to be disputed and it is unclear whether ethnic differences are due to genetics, lifestyle factors, body composition or other factors.

Genetics factors combined with overconsumption of highly processed, high-energy foods, and increasingly sedentary lifestyles are causing global increases of obesity at an unprecedented rate. Trends in overweight, obesity and waist circumference between 1993 and 2019 in the UK can be seen in **Figure 1.1**. The increasing prevalence of obesity puts a great strain on the worldwide economy with the burden greatest in western countries, including the UK and the USA exhibiting the highest rates of obesity. If current trends in obesity continue, the cost to the UK is expected to reach £49.9 billion by 2050 (Public Health England, 2017).

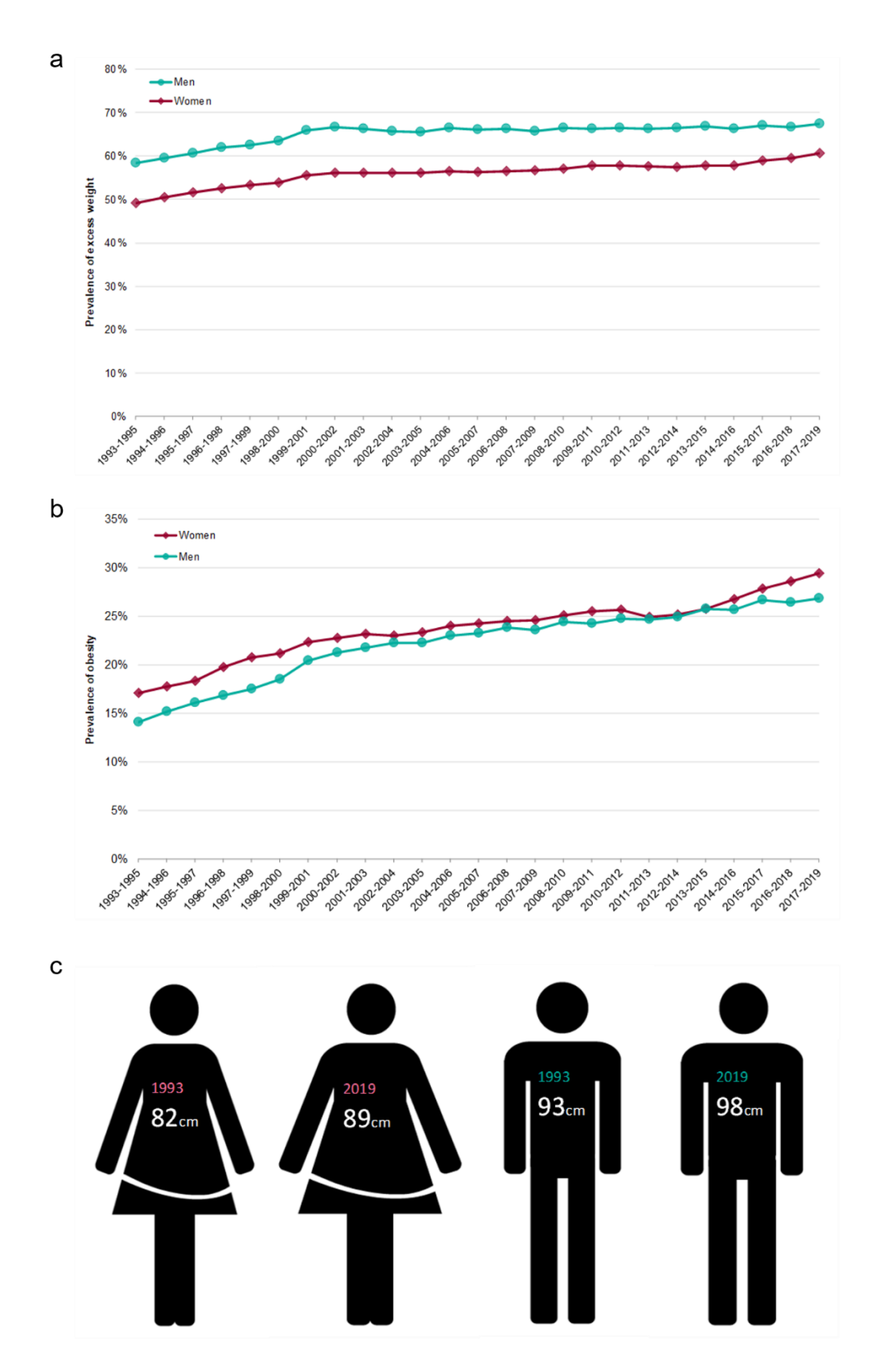


Figure 1.1 Overweight and obesity trends in England, from 1993 to 2019. (a) Percentage of men and women in England with overweight from 1993-2019; (b) percentage of men and women in England with obesity from 1993-2019; (c) average waist circumference of men and women in England in 1993 and 2019. Figure adapted from Public Health England, 2019.

1.1.2 Type 2 Diabetes Mellitus

The American Diabetes Association defines diabetes mellitus (DM) as a group of metabolic diseases characterised by hyperglycaemia (abnormally high fasting glucose) resulting from defective insulin secretion, defective insulin sensitivity or a combination of both (ADA, 2018). Diabetes is classed into two categories: type 1 where hyperglycaemia is caused by genetic defects; type 2 which is caused by lifestyle factors and accounts for around 90% of all DM cases. Type 2 diabetes is highly associated with obesity but can occur independently: 57% of obese US adults do not have DM and around 20% of type 2 diabetic US adults are not overweight (Nguyen et al., 2011). The International Diabetes Federation estimates that between 20-25% of the world's population is diabetic (Powell et al., 2010). Elevated fasting glucose is a diagnostic factor T2D and is also central factor in diagnosing MetS.

In T2D, overfeeding and therefore over-stimulation of pancreatic beta-cells leads to insulin resistance. Insulin resistance then results in an increased fasting blood glucose and decreased glucose tolerance. This therefore promotes increased release of insulin which can lead to hyperinsulinaemia (Wilcox, 2005). Hyperinsulinaemia activates certain important transcription factors, such as sterol-regulatory-element-binding protein 1c (SREBP-1c), in the liver that will promote hypertriglycerideaemia and liver steatosis or fatty liver (Haas & Biddinger, 2009; Heindel et al., 2017). Additionally, this increases the likelihood of beta-cell exhaustion (due to their overworking in the regulation of insulin) thus causing T2D. This type of conditioned insulin resistance is highly associated with abdominal obesity and adipose tissue dysfunction (Heindel et al., 2017).

1.1.3 Cardiovascular Disease

Obesity, elevated triglycerides and high blood pressure are included in the diagnostic criteria for MetS and are also risk factors for CVD (Chapman et al., 2011; Grundy, 2004; Powell et al., 2010). Type 2 diabetes also directly increases risk of CVD. Prevalence of CVD in patients with T2D is estimated at almost a third (Dokken, 2008; Einarson et al., 2018). Cardiovascular disease encompasses many diseases relating to the heart and vascular system, with major conditions being coronary heart disease, stroke, peripheral arterial disease, and aortic disease. Coronary heart disease (CHD) is the leading cause of death worldwide, followed by stroke, the risks of which and all other CVD increases with age (Dhingra and Vasan, 2012; Naghavi et al., 2017). Coronary heart disease encompasses angina, and heart failure, and is a result of coronary artery disease (CAD) – usually atherosclerosis (Sanchis-Gomar et al., 2016). Atherosclerosis is also the major risk factor for ischemic stroke, along with atrial fibrillation (Campbell et al., 2019a). Small vessel disease is another risk factor for stroke, and is associated with high blood pressure and DM, independently of CAD (Boudina and Dale Abel, n.d.; Campbell et al., 2019b; Hamby et al., 1974). Peripheral arterial disease is defined by reduced blood flow to limbs, caused by atherosclerosis and again associated with DM, age and high blood pressure (Aboyans et al., 2017; Pizzimenti et al., 2020). Aortic diseases include aneurysm, dissection and trauma (Dalman et al., 2020). The second biggest risk factor, following smoking, for aortic aneurysm (AA) is age-dependent family history, followed by high-blood pressure, elevated cholesterol and pre-existing CAD (Quintana and Taylor, 2019). Aortic aneurysm is caused due to loss of proper structure of the aortic wall, largely due to dysregulation of the extracellular matrix and vascular smooth muscle cell degeneration although other cell types are also involved (G. Li et al., 2020; Quintana and Taylor, 2019).

More recently, the importance of the gut microbiota in CVD has come to light. Processes which effect the development of CVD and related conditions, such as bile acid and short chain fatty acid metabolism are regulated by the gut microbiome, and changes in community composition are seen to negatively impact these processes (Brown and Hazen, 2018). For example, patients with atherosclerotic CVD have increased abundance Escherichia coli, Enterobacter aerogenes and Klebsiella spp. where patients of ischemic stroke were seen to have increased abundance of Lactobacillus ruminis and Atopobium genera (Brown and Hazen, 2018; Yamashiro et al., 2017).

1.1.4 Non-alcoholic Fatty Liver Disease

Non-alcoholic fatty liver disease (NAFLD) is the most common liver disease – around 25% of the global population are thought to be affected (Younossi et al., 2016). It is defined by excess fat accumulation in the liver, specifically when at least 5% of hepatocytes exhibit macrovesicular steatosis. It can be divided into sub-types: simple steatosis, a non-progressive form; or non-alcoholic steatohepatitis (NASH) which is characterised by hepatocellular ballooning, steatosis and lobular inflammation (Loomba and Sanyal, 2013). A patient with NAFLD may also develop advanced fibrosis, potentially progressing to cirrhosis (fibrosis) and increased risk of liver failure and hepatocellular carcinoma.

Obesity, elevated cholesterol, and elevated triglycerides can increase risk of NAFLD although between 10-20% of NAFLD cases occur in non-obese individuals with lower incidences of these risk factors. Patients with lean NAFLD have increased liver fibrosis and risk of cardiovascular disease (Xu et al., 2022).

1.1.5 Mouse Models in Metabolic Disease Research

The C57Bl/6 mouse is an inbred mouse strain used for models in human disease research. Being the second ever mammal to have its whole genome sequenced, it is the most popular and well characterised laboratory mouse (Marshall, 2002). The life stages of the C57Bl/6 mouse, and the approximate equivalent in humans, is shown in **Figure 1.2**.

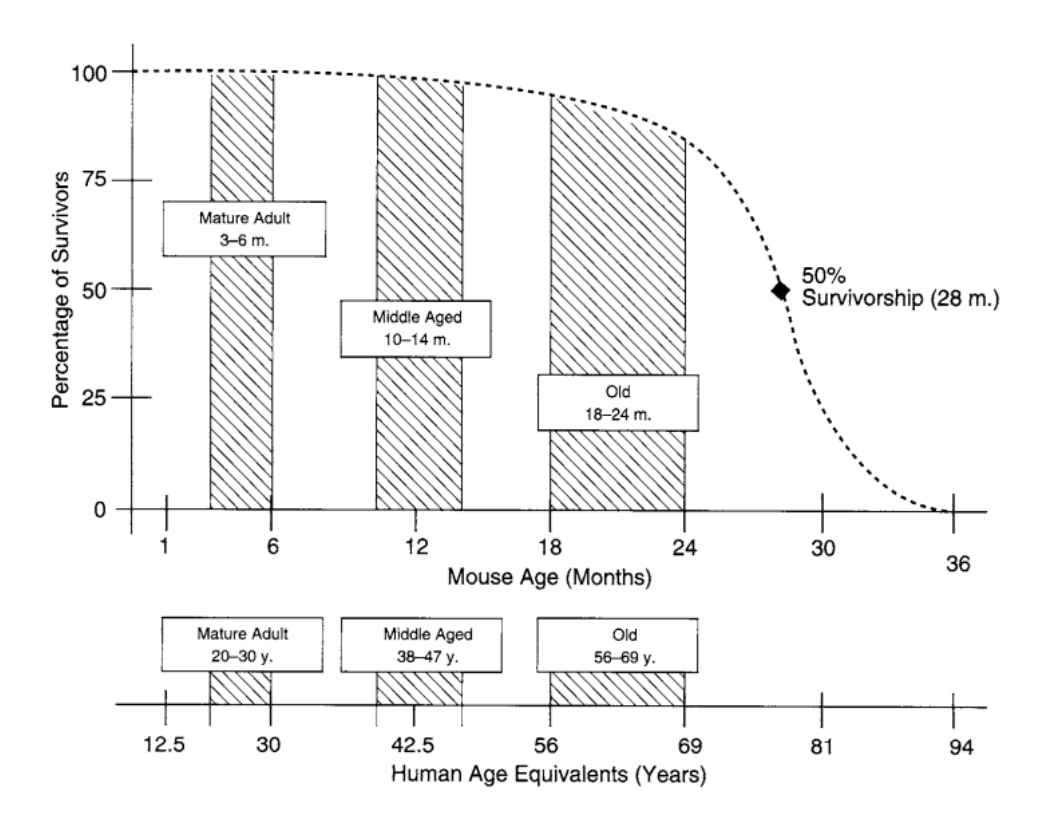


Figure 1.2 Life stages of the C57BI/6 mouse and approximate comparison to humans. Figure taken from Flurkey et al, 2007.

The C57Bl/6 mouse is susceptible to DIO, making them an ideal model for MetS research (Collins et al., 2004). Various models of obesity and metabolic disease exist. These models include genetic, chemical and nutrition modification.

The most well-established genetics-based mouse models of obesity are the ob/ob and db/db mice. The leptin-deficient obese (ob/ob) mouse was first discovered by chance in 1949, and the leptin receptor-deficient diabetic (db/db) mouse in 1959 by The Jackson Laboratory (Coleman and Hummel, 1969; Ingalls et al., 1950). Due to the interference with leptin signalling, these mice become obese due to excessive food intake and reduced energy expenditure. However, where the ob/ob mouse becomes insulin resistant, the db/db mouse develops diabetes (Suriano et al., 2021). Another well studied model of obesity and metabolic disease is the diet-induced obesity (DIO) model. The wild-type C57Bl/6 mouse is highly-susceptible to fatty liver and insulin resistance through high-fat diet feeding but remains metabolically healthy on a normal chow diet (Lang et al., 2019).

The *Timp3* knock-out mouse was first developed by Leco et al to study lung function (Leco et al., 2001). These mice exhibit low-grade, chronic inflammation have since been used to study liver inflammation, atherosclerosis and diabetes (Federici et al., 2005; Mohammed et al., 2004; Stöhr et al., 2014).

1.2 Key Concepts in Energy Metabolism

Metabolism and metabolically active tissues are regulated by the endocrine system. This system works to control appetite, satiety, adipose metabolism, and energy balance via pathways involving multiple important signalling molecules such as insulin, adiponectin, oestrogens, ghrelin, and leptin, among others (Ćirić et al., 2014; Exley et al., 2014). These, and numerous other growth factors and hormones, control pathways in the brain related to food-reward mechanisms (cravings and addiction), glucose metabolism and lipid metabolism. In this section, I will discuss the processes which regulate energy metabolism, and what may happen if these pathways are dysregulated.

1.2.1 Role of Adipose Tissue in Energy Homeostasis

The adipose tissue is an endocrine organ of major importance which regulates energy balance and nutritional homeostasis. It is classified into three types, white (WAT), brown (BAT) and beige (BeAT) adipose, and further compartmentalised into various depots around the body that can be grouped in visceral adipose tissue (VAT) and subcutaneous adipose tissue (SVT) (Schoettl et al., 2018). A summary of the various fat depots found in humans and mice is shown in Figure 3. There are distinct morphological and functional differences between the types of adipose tissue. The WAT contains large individual lipid droplets whereas the BAT possesses many small cytoplasmic ones. The WAT functions to store fat as triglycerides and release as free fatty acids, as well as secrete several hormones in order to regulate energy stores. On the other hand, the BAT functions to release energy as heat during uncoupled respiration by an uncoupling protein (uncoupling protein 1 or UCP1) found in its relatively many mitochondria (Schoettl et al., 2018; Zoico et al., 2019). Interestingly, beige fat is bi-functional and although it arises from WAT precursors or from the mature cells themselves, it is in fact thermogenic, similarly to the BAT (Harms and Seale, 2013). All adipocytes are formed from mesenchymal cells and the differentiation process is mediated by a variety of transcription factors including zinc finger protein 423 and 467 (Zfp423 and Zfp467, respectively). These, and other, transcription factors work to initially sensitise the stem cells to BMP2/4 signalling, inhibit Wnt signalling and promote perioxisome proliferator-activated receptor gamma (PPARy) expression. PPARy and CCAATenhancer-binding proteins (C/EBP) proteins work together to produce the mature, differentiated adipocyte (Heindel et al., 2017).

Chapter 1

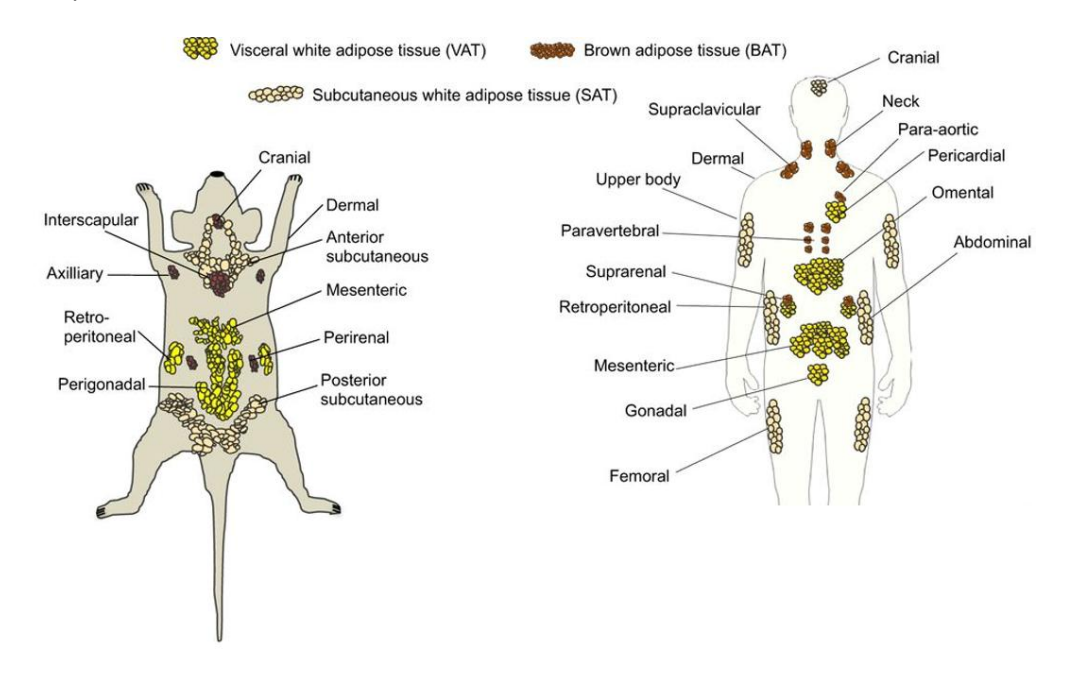


Figure 1.3 Summary of fat depots in mice and humans. Fat depots are classified into visceral white adipose tissue (VAT), subcutaneous white adipose tissue (SAT) and brown adipose tissue (BAT). Adapted from Schoettl et al., 2018.

In humans, visceral abdominal WAT is located in the abdominal cavity and surrounds the organs. It is composed of the mesenteric (surrounding the intestines), retroperitoneal (sits behind the peritoneum), pericardial (surrounds the heart) and the peritoneum (surrounds the abdominal cavity) depots (Schoettl et al., 2018). The visceral abdominal fat is highly associated with obesity, T2D and is an essential diagnostic factor for MetS (Powell et al., 2010). Conversely, subcutaneous WAT seems un-associated with or even protective against these diseases; those with a higher proportion of total fat stored in the thigh or gluteal area are at less risk of MetS and related diseases compared to their counterparts who store more fat in the abdominal area (Snijder et al., 2005). White-adipose tissue is metabolically active and uses various signals to communicate across the body, namely the leptin and adiponectin hormones. Leptin acts to reduce food intake, increase energy expenditure and its secretion is positively correlated with fat mass (an increased fat cell mass results in an increase in leptin secretion). This mechanism can be disrupted however, in obesity where a substantial, prolonged increase in leptin secretion can cause leptin resistance – the exact mechanism for which is unclear but it multifactorial including leptin receptor desensitisation and impaired leptin transport (Cui et al., 2017; Santoro et al., 2015). Adiponectin induces liver fatty acid oxidation, reduces inflammation and improves beta-cell function in the pancreas - thus it is protective against insulin resistance and obesity (Chakraborti, 2015; Folco et al., 2009; Myeong et al., 2006). Obesity is a proinflammatory condition, owing to the release of

proinflammatory cytokines by adipocytes and their immune cells. These cytokines include TNF- α and IL-6, both greatly associated with chronic systemic low-grade inflammation as well as insulin resistance (Maachi et al., 2004; Makki et al., 2013). Conversely, anti-inflammatory cytokines are preferentially secreted in healthy individuals, such as IL-10 and TGF- β (Makki et al., 2013).

Due to its role in metabolic homeostasis, adipose tissue is dynamically remodelled in response to changes in energy status, via changes in the number and size of adipocytes and changes in the number and function of the vascular cells which contribute to the maintenance of adipose function (D. Lin et al., 2016). This is known as adipose tissue remodelling. In obesity, these precise mechanisms may be disrupted, leading to abnormal tissue remodelling and dysregulation of important secretions, such as cytokines, that leads to metabolic stresses and ultimately damage other organs such as the pancreas or liver (Choe et al., 2016). The two major adipose secretions are leptin and adiponectin. Leptin binds leptin receptor beta (ObRb) in the brain to activate neural pathways which regulate appetite and glucose homeostasis. The major effect of leptin is to signal the central nervous system to reduce food intake, but it also interacts with the mesolimbic dopamine system to effect the food reward system and contributes to satiety (the feeling of being "full" after a meal). Leptin may also increase energy expenditure; in mice, it increases sympathetic nerve activity and activates thermogenesis in BAT. Obesity results in elevated circulating leptin levels which can cause brain receptors to develop resistance to the hormone, leading to interruption of appetite control inducing further excessive food intake and reduced lipid oxidation (Choe et al., 2016; Myers et al., 2010).

Extracellular matrix remodelling is essential to maintain homeostasis in response to changes in energy balance (Lackey et al., 2014). Adipose tissue expansion may be mediated by hypertrophy – an enlargement of adipocytes themselves – or hyperplasia – an increase in the number of adipocytes (Jo et al., 2009). A comparison of these processes is shown in **Figure 1.4**. These two processes are adaptive responses to nutrient excess and act as a buffer to protect other tissues from lipotoxicity. In lean human individuals, it is more favourable to possess larger adipocytes as those with smaller adipocytes will experience a worse metabolic response in a context of overfeeding (Muir et al., 2016). However, there is a threshold up until which an adipocyte size can still be considered healthy, but during obesity this point is often surpassed, resulting in abnormal lipid deposition in surrounding tissues. Extreme adipocyte hypertrophy is positively correlated with BMI and MetS in humans and mice. Excessive hypertrophy can hinder adipocyte function and may cause hypoxia when a diameter of about 100 µm is exceeded. In this case, hypoxia will lead to the activation of hypoxia response genes, causing oxidative stress, inflammation and metabolic dysfunction (Muir et al., 2016). Research suggests that, in adipose tissues, fibrosis may be beneficial in human obesity by negatively regulating adipocyte

Chapter 1

hypertrophy. Decreased adipose tissue fibrosis has been associated with increased adipocyte hypertrophy and limited hyperplasia in MetS resulting in abnormally large and metabolically impaired adipocytes (Muir et al., 2016). Additionally, decreased collagen gene expression and tensile strength in visceral WAT has been observed in obese women with T2D and MetS, compared to metabolically healthy individuals, further highlighting the connection between the ECM and MetS (Lackey et al., 2014). There is conflicting research on the relationship between the ECM and adipocyte remodelling in MetS thus further research is needed to fully elucidate the mechanism. Differences in exactly how the ECM and WAT remodels during obesity are thought to produce different outcomes in health as not all obese persons with the same BMI will suffer the same negative health consequences. Indeed, not all obese individuals will develop metabolic syndrome.

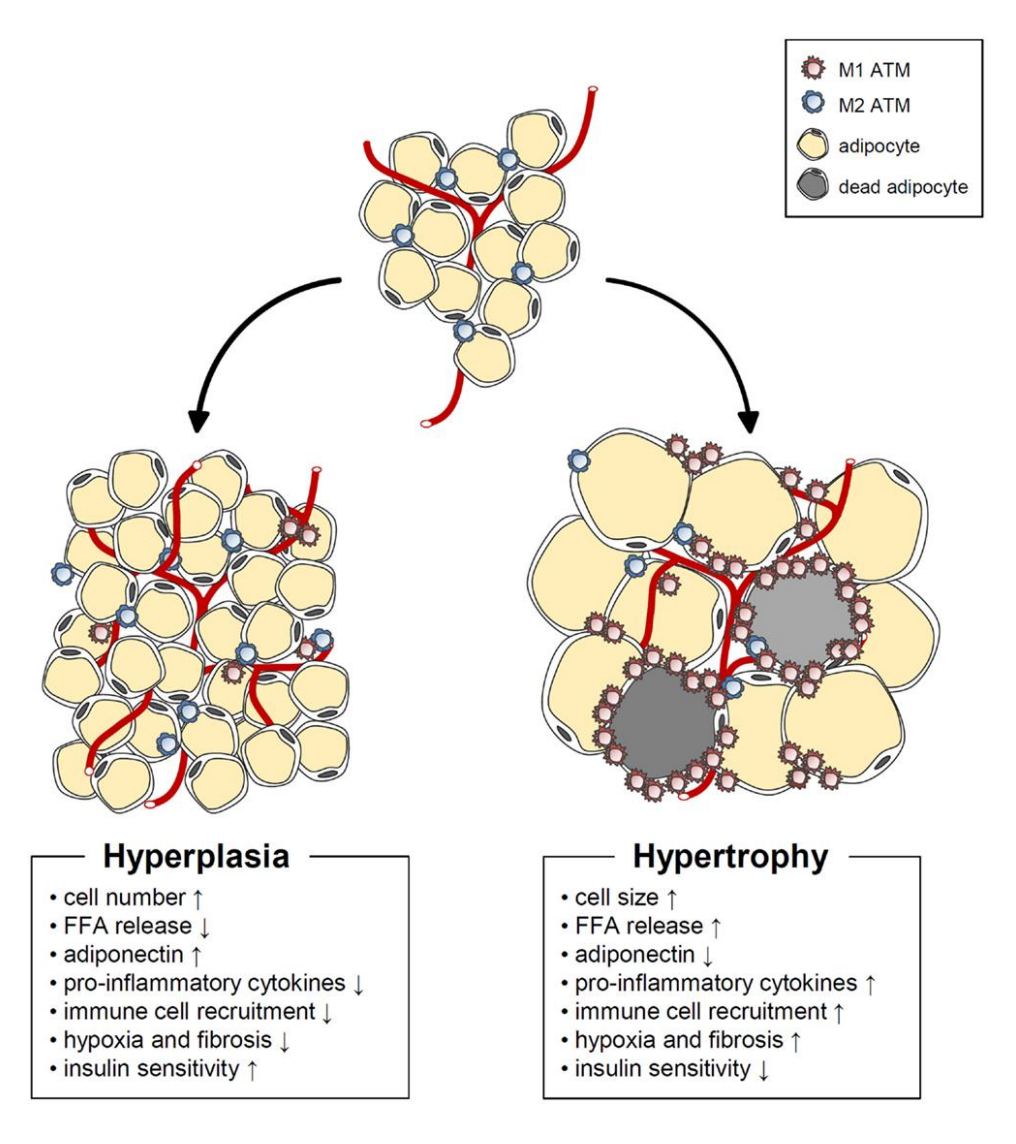


Figure 1.4 Adipose tissue expansion: hyperplasia and hypertrophy. During hyperplasia, adipose tissue expands through increased number of adipocytes; during hypertrophy, adipose tissue expansion occurs through increased adipocyte size. Image taken from Choe et al, 2016.

1.2.2 Lipid Metabolism and the Liver

The liver is central to lipid metabolism, as it is the predominant location of lipid synthesis, storage, and metabolism (Nguyen et al., 2008). The liver also produces bile which is essential for absorption of dietary lipids.

Lipids can be acquired through diet or made endogenously. Here, I will discuss triglyceride (TG) and cholesterol metabolism in specific relation to the liver. Triglycerides are esters, composed of three fatty acids (FAs) and a glycerol backbone. The FAs may be saturated, monounsaturated or poly-unsaturated (Rustan & Drevon, 2005). Most animal-derived FAs are saturated, whereas most plant-derived FAs are unsaturated. Cholesterol is a sterol, a component of the phospholipid bilayer, and is essential for the formation of steroid hormones, vitamin D and bile acids (Myant, 2014).

Since lipids are large, hydrophobic molecules which are non-soluble in water, they must be broken down into smaller molecules which can pass the intestinal membrane. This is carried out by bile in a process called emulsification (Sarkar et al., 2016). Bile, composed mainly of water and bile salts, is produced by the liver and stored in the gall bladder where it awaits release into the small intestine, upon ingestion of dietary lipids. Once in the small intestine, the bile salts break down large fat droplets into smaller ones (this aids digestion by lipases) and create micelles around the resulting cholesterols, fatty acids (FAs) and monoglycerides (micelles aid absorption of digested lipid molecules) (Sarkar et al., 2016). Bile salts are polar molecules which means that they can arrange themselves into a spherical shell, with hydrophilic tails on the outside and hydrophobic heads on the inside, that encompasses a lipid molecule (Westergaard & Dietschy, 1976). In this way, a hydrophobic lipid molecule, enclosed in a hydrophilic shell can then cross the lipid bilayer of the intestine's enterocytes.

Once inside the enterocytes, FAs and monoglycerides are transformed into triglycerides (TG). Triglycerides and cholesterols are then secreted into the plasma in the form of lipoproteins (Mansbach & Siddiqi, 2010). Lipoproteins are spherical structures of phospholipids that encase TGs and cholesterol, arranged with hydrophilic heads on the outside and hydrophobic tails on the inside, to allow for transport around the body via the blood stream. Four major types of lipoproteins transport lipids around the body (Jonas & Phillips, 2008). In order of increasing size, and decreasing density, these four types are as follows: high-density lipoprotein (HDL); low-density lipoprotein (LDL); very low-density lipoprotein (VLDL); chylomicrons. These groups and characterisations are summarised in **Table 1.2**. The chylomicrons are synthesised in the intestine and transport dietary triglycerides and cholesterol; VLDLs are produced in the liver and transport triglycerides; LDLs are derived from VLDLs and are the main transporters of cholesterol; HDLs

Chapter 1

transport cholesterol *away* from peripheral tissues and to the liver, it is for this reason that they are considered "good" cholesterol (Feingold, 2021; Jonas & Phillips, 2008). Apolipoproteins (Apo), synthesised by the liver, are proteins found on the surface of lipoproteins, which function to signpost the transport and distribution of lipoproteins around the body (Liu et al., 2021). Polymorphisms in certain Apo genes are found within the human population and can increase risk of hyperlipidaemia, atherosclerosis, and cardiovascular disease (Eichner et al., 2002).

Table 1.2 The four major lipoprotein types and characterisation. Table adapted from "Introduction to Lipids and Lipoproteins" (Feingold, 2021).

Lipoprotein class	Density (g/ml)	Size (nm)	Major lipid type	Apoproteins
HDL	1.063- 1.210	5- 12	Cholesterol	Apo A-I, Apo A-II, Apo C, Apo E
LDL	1.019- 1.063	18- 25	Cholesterol	Apo B-100
VLDL	0.930- 1.006	30-80	Triglycerides	Apo B-100, Apo E, Apo C
Chylomicron	<0.930	75-1200	Triglycerides	Apo B-48, Apo C, Apo E, Apo A-I, A-II, A-IV

Chylomicrons and VLDLs consist mainly of triglycerides and are absorbed by adipose tissue and skeletal muscle for energy storage. Any remaining triglycerides are processed by the liver and released as FAs. When plasma insulin is low, FAs are released from storage by the adipose tissues and metabolised by the liver for energy. When plasma insulin is high, and there is an excess of carbohydrates, glucose is metabolised into new FAs (this process is called *de novo* lipogenesis) (Alves-Bezerra & Cohen, 2017).

Much of the body's cholesterol is recycled, largely through bile acid metabolism. Circulating cholesterol is absorbed by the liver and used to synthesise primary bile acids cholic acid (CA) and chenodeoxycholic acid (CDCA) — in the classical pathway, this reaction is initiated by the CYP7A1 enzyme (Chiang & Ferrell, 2020). To increase their solubility and to form salts, these bile acids are conjugated with either taurine or glycine. These bile acids are secreted from the liver, into the small intestine via the gall bladder. Due to gut microbial activities, some of the primary bile acids are further metabolised to produce secondary bile acids, called deoxycholic acid (DCA) and lithocholic acid (LCA), and some are deconjugated (Ridlon et al., 2006). Both primary and

secondary bile acids can be absorbed through the small intestine and re-circulated in the plasma as cholesterol, ready to be metabolised again by the liver. Excess cholesterol is excreted from the body in faeces – approximately 50% of excreted cholesterol is in the form of bile acids (Kruit et al., 2006). A summary of bile acid metabolism in the liver and small intestine can be seen in **Figure 1.5**.

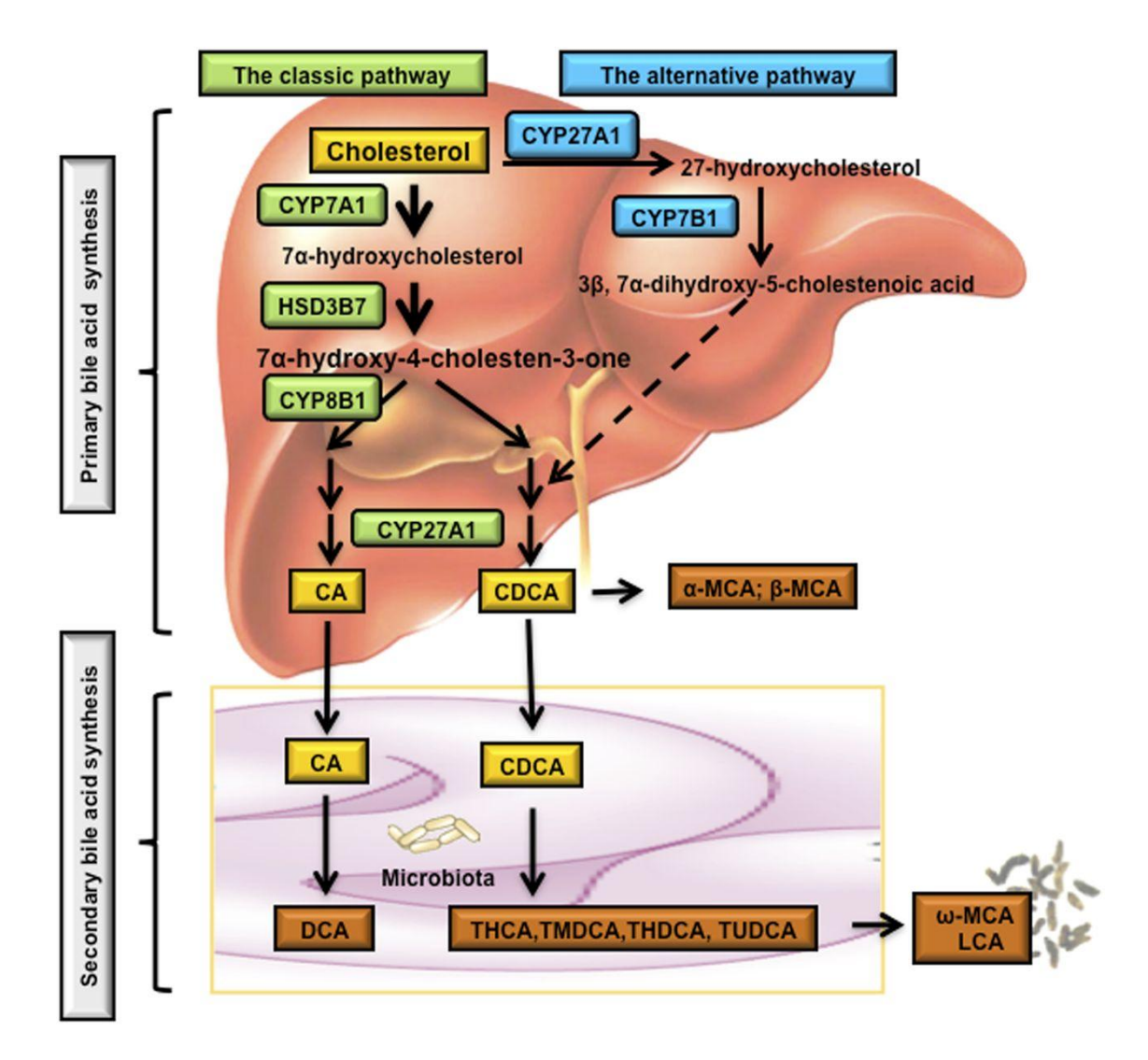


Figure 1.5 Summary of bile acid metabolism in the liver and small intestine. The classical pathway is the predominant method of primary bile acid production, for which CYP7A1 is the rate-limiting enzyme. Secondary bile acids are produced by the gut microbiota. LCA and ω -MCA are excreted into faeces. Figure taken from Li and Chiang, 2014.

1.2.3 Role of the Pancreas in Glucose Metabolism

The pancreas releases insulin upon detecting an increase in blood glucose concentration, thereby promoting tissue uptake of glucose. Additionally, the pancreas will release glucagon in response to low blood glucose, thus stimulating gluconeogenesis (synthesis of glucose from non-carbohydrate sources) and glycogenolysis (catalysis of glycogen to form glucose) in the liver to raise blood glucose levels.

The pancreas is comprised of a dorsal and ventral section with two separate tissue types: exocrine and endocrine where the former functions as a duct system, through which the digestive fluid it produces drains into the intestine, and the latter which comprises groups of pancreatic islets or "islets of Langerhans" that contain multiple cell types that secrete essential hormones (Jennings et al., 2015). The predominant cell type in the islets of Langerhans is the beta-cell (in humans, these cells make up 50% of the islets of Langerhans) which releases insulin. There also reside alpha-cells responsible for glucagon secretion, delta-cells that release somatostatin, epsilon-cells that release ghrelin and gamma-cells that secrete pancreatic polypeptide (Heindel et al., 2017; Jennings et al., 2015). Beta-cell replication seldom occurs in adult humans but may occur in response to physiological challenges such as high blood glucose, peripheral insulin resistance and pancreatic injury (Heindel et al., 2017). Upon uptake and metabolism of glucose by beta-cells, an increase in the ATP:ADP ratio (the concentration of ATP and ADP across the mitochondrial inner membrane) causes certain plasma membrane channels to close thus resulting in depolarisation of the cell and insulin release. The insulin then of course binds receptors of target cells to initiate their glucose uptake and metabolism. Within skeletal muscle and WAT, insulin promotes the recruitment of glucose transporter type 4 (GLUT4) to the plasma membrane to increase glucose uptake and metabolism to store as triglycerides (and in addition, for skeletal muscle, glycogen) (Heindel et al., 2017). In the cases of DM, autoimmune destruction of beta-cells causes type 1 diabetes (T1D) and beta-cell dysfunction resulting from persistent increased insulin demand causes T2D (Heindel et al., 2017). In response to low blood glucose levels, pancreatic beta-cells will secrete glucagon in order to stimulate gluconeogenesis and glycogenolysis in the liver thus raising the blood glucose. Once a certain threshold is reached (high enough for insulin production to be activated), glucagon release is halted (Quesada et al., 2008).

1.3 The Gut Microbiota

A microbiota is defined as the entire collection of microorganisms within a specific niche. The human gut microbiota (GM) is physiologically important and is increasingly being linked to major disorders such as inflammatory bowel syndrome, asthma and MetS (Berg et al., 2020; Nishida et al., 2018; Sokolowska et al., 2018). This section will discuss the GM and its role in MetS.

1.3.1 Overview

Our intestine is one of the largest interfaces through which host-microbiota interactions can occur and is adapted for bi-directional exchange between microbe and host across a membrane of one epithelial cell thick. Within the human GM exist trillions of microorganisms, the majority of which are bacterial. These microorganisms play a vital role in the extraction of energy and nutrients during digestion and interact with the immune system to protect the body against pathogens (Carding et al., 2015; Thursby and Juge, 2017). The development of the GM begins at birth, with the type of delivery (vaginal or caesarean section) and diet (breast milk or formula) having significant impacts on the composition and function of the microbiome (Bäckhed et al., 2015). Between the ages of 3 and 5 years old, the configuration of the GM closely resembles the mature, adult microbiome (Rodríguez et al., 2015). During adulthood, the microbiome remains generally stable but may be impacted by events such as long-term diet alteration, antibiotic treatment, infection, surgery and other lifestyle changes (Rodríguez et al., 2015). Sequencing analyses suggest there is a common microbial "core" conserved across the human population between 40% and 50% conservation between individuals is predicted. Overall, the major GM phyla are the Firmicutes and Bacteroidetes; many studies suggest that the ratio of these two phyla are an important risk factor for obesity with increased ratios seen in obese patients compared to their healthy counterparts (Koliada et al., 2017; Riva et al., 2017). However, the relevance of this ratio is disputed with recent research suggesting it has little significance (Magne et al., 2020). Many groups have adopted the term "gut dysbiosis" to describe unfavourable shifts in gut microbiome composition, although the usefulness of this term is debateable as much is still unknown about the gut microbiome and what truly defines a healthy one.

1.3.2 The Gut Microbiota and Metabolic Syndrome

Dietary changes are shown to account for up to 52% of GM changes (Zhang et al., 2018). High consumption of dietary fibre is associated with various health benefits (such as prevention of diet-induced obesity) through increase of short-chain fatty acids (SCFAs), beneficial alteration of GM and an increase in g-protein coupled receptor activity (GPRs) (Zhang et al., 2018). Indeed, the GPR43 (also known as FFAR2) receptor for SCFAs has been indicated in the promotion of the beneficial gut bacteria Bifidobacterium spp, the suppression of Helicobacter hepaticus (linked to cancers and colitis) and suppression of colon cancers (Fox et al., 2011; Sivaprakasam et al., 2016). Other studies have demonstrated that the gut bacteria family Protovella has a beneficial role in glucose metabolism and were found in increased abundance in those supplementing with dietary fibre (Kovatcheva-Datchary et al., 2015). Some groups have also found that dietary fibre supplementation prevents common symptoms of MetS in mice — namely dyslipidaemia, insulin resistance and liver lipotoxicity (Han et al., 2015).

High fat diets are seen to cause changes in gut microbiome composition and may even propagate its effects via diurnal variations in GM (Leone et al., 2015). Western diets (high fat and high sugar) typically include an excessive proportion of animal-derived fats (long-chain fatty acids). These kinds of fats have long been linked to inflammation, obesity and CVD, whereas short chain fatty acids such as the omega-3 fatty acids (found in plant foods and oily fish) are associated with reduced weight gain and inflammation in obese subjects via modulation of the gut microbiome. Mice fed a lard-based diet presented increased WAT inflammation and impaired insulin sensitivity compared to those fed fish oils, through altered GM and increased activation of TLR4 – a receptor that initiates the NF-kB signalling pathway and inflammatory cytokine production (Caesar et al., 2015; Kim et al., 2012). The GM are also able to alter the mouse epigenome via SCFAs, and other metabolites yet to be elucidated, but the effects they have on chromatin packaging seem to be supressed when the mouse is fed a high-fat high-sugar diet (Krautkramer et al., 2016).

Bile acids and the GM have a complex relationship that regulates mechanisms of metabolism. Farsenoid X receptor (FXR) is expressed in many tissues, though largely in the liver and intestine, and regulates bile acid homeostasis, alongside glucose and lipid metabolism. This nuclear receptor is primarily activated by primary bile acids cholic acid (CA) and chenodeoxycholic acid (CDCA), and the secondary bile acid deoxycholic acid (DCA) (Sato et al., n.d.; Sun et al., 2018). Secondary bile acids are produced by anaerobic intestinal bacteria after deconjugating glycine and taurine and subsequently alternatively metabolising the primary bile acids (Wahlström et al., 2017). Increased activation of FXR was seen to reverse insulin resistance and protect against

weight gain in genetically obese rats (fa/fa rats were administered CDCA) (Cipriani et al., 2010). In healthy volunteers, suppression of bile acid synthesis increased the population of Gram-positive bacteria in the small intestine and in mice given the same supressing agent, an increase in Firmicutes (the majority of which are also gram-positive) proportions in the small intestine was seen (Friedman et al., 2018). Increased microbial metabolism of bile acids and their conjugates results in a smaller, hydrophobic bile acid pool. This is because the secondary bile acids seldom or do not at all activate FXR (Ridlon et al., 2014). In rats fed bile acids, increased CA intake resulted in increased representation of Firmicutes from 54% to over 90% of the GM (Ridlon et al., 2014). This therefore resulted in an increased Bacteroidetes:Firmicutes ratio which is associated with obesity. The importance of the relationship between bile acid metabolism and the GM is clear but the exact mechanism is not.

1.4 The Extracellular Matrix

The extracellular matrix (ECM) is vital to the execution of many processes and behaviours of cells in the body, and thus must be maintained in homeostasis. The following section will describe the components of the ECM, their roles and regulation.

1.4.1 Overview

The extracellular matrix (ECM) is a network of non-cellular macromolecules, present in all tissues, composed of H2O and various proteins and polysaccharides. These molecules are secreted by the cells themselves to create and provide a physical and physiological scaffolding which supports, with specificity, the mechanical and biochemical functions of tissues (Clause and Barker, 2013; Hynes, 2009). These functions include regulation of cell density, organisation, ligand attachment, differentiation, and modulation of growth factors, signalling molecules and pH among various others which form a plastic microenvironment that can be remodelled in response to stimuli (Berardi, 2018; Clause and Barker, 2013).

Water and negatively charged proteoglycan (PG) polymers form the hydrating-gel which houses other components of the ECM. This includes a network of fibrous proteins and adhesive glycoproteins such as collagens and fibrinogen (Berardi, 2018; Hynes, 2009). Collagens provide tensile strength to tissues and are the most abundant proteins (namely, collagen I) in the mammalian ECM with 28 types having been identified (Berardi, 2018; Hynes, 2009). To confer tissue-specific structure, collagens have sustained, complex interactions with other structural ECM proteins. One such protein is elastin – one of the most durable human proteins, regulated by PGs (Berardi, 2018). Fibronectin is able to bind simultaneously to multiple ECM components such as collagens and PGS, thus supporting communication between molecules (Berardi, 2018). It is important in tissue development, morphogenesis and cell adhesion, and can also bind important growth factors including VEGF and hepatic growth factor (HGF) (Berardi, 2018). Throughout its evolution, diversification of the ECM has occurred alongside major evolutionary events such as the development of a closed circuit vascular system and the neural crest (gives rise to the peripheral nervous system and various other cell types) – indicating its role in conferring structural and functional specificity to different tissues (Naba et al., 2016). An overview of the ECM and its various components is shown in Figure 1.6.

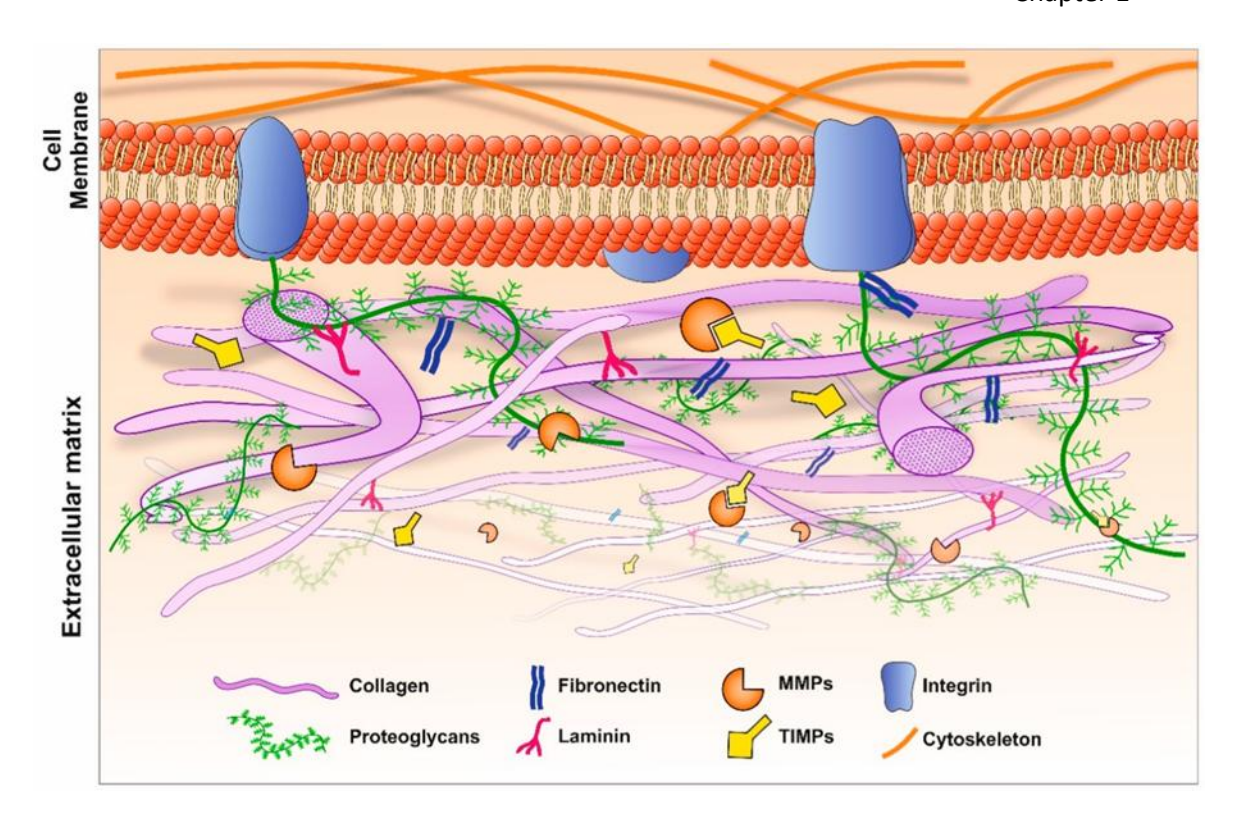


Figure 1.6 Overview of the extracellular matrix. Taken from Dewing et al, 2019.

Disturbance of ECM homeostasis (often resulting in excess deposition or degradation of ECM components) can lead to numerous diseases, either genetic, acquired or combination. In coronary heart disease for example, plaque formation is caused by a build-up of lipids trapped by components of the vascular ECM (Chistiakov et al., 2013). Further, altered vascular ECM can also lead to stiffening of the arteries and thus hypertension (Berk et al., 2007).

1.4.2 Collagen

Collagen amounts for one third of total protein in humans and is the most abundant protein in the ECM. The primary structure of collagen is comprised of repeating glycine-Xaa-Yaa units where Xaa and Yaa are often (2S)-proline and (2S, 4R)-4-hydroxyproline (pro and hyp, respectively), comprising about 10% of all collagen triplets. From these triplets, three strands together form a left-handed polyproline helix. The tertiary structure, tropocollagen, is formed with the assembly of three of the polyproline helices, each staggered by one residue, into a right-handed triple helix which is stabilised by hydrogen bonding. The tropocollagen can be either homo- or hetero-trimeric where polyproline helices are either all identical or have one or more non-identical strands (Shoulders and Raines, 2009). From this, the collagen can assemble into various complex quaternary structures. Quaternary collagen fibrils can be traced back 500 million years ago to mammalian organisms (Kadler et al., 1996).

The multi-layered and complex assembly of collagen provides strength, resistance to proteolytic cleavage and configuration for protein interactions. As quaternary structures, collagens can be classified into 5 sub-families: fibrillar, short-chain, fibril-associated with interrupted triple-helices (FAITs), membrane-associated with interrupted triple helices (MAITs), and multiple triple-helix domains and interruptions (multiplexins). The most abundant collagens in humans are fibrillar. Type I collagen, for example, is an interstitial collagen found in connective and embryonic tissues, the tropocollagen of type I collagens are unstable at body temperature and the process of assembly into fibrils allows stabilisation if the triple helix. Firstly, although the c-terminal peptides of the tropocollagen are essential for triple helix formation, they prevent fibirillogenesis and must be removed to leave telopeptides (Amar et al., 2017). These telopeptides initiate self-assembly into fibrils, interacting with neighbouring telopeptides within the microfibrils, to form covalently-bonded cross-links (mediated by lysyl oxidase). This process provides stabilisation for the quaternary structures and greatly increases resistance to proteolysis by matrix metalloproteinsases (MMPs, enzymes which regulate the turnover of ECM components). The telopeptides must be once again cleaved before the collagen can be targeted by an MMP. In the mature fibrils, the telopeptides possess lysyl side chains which form hydroxyl pyridinoline and lysyl pyridoline crosslinks between lysine and hydroxylisines, thus creating an additionally layer of stability. Excessive cross-linking of the fibrils, however, causes brittleness – a characteristic of aging.

1.4.3 Elastin

Elastic fibres within the ECM are comprised 90% of elastin and the remainder of microfibrils, with elastin providing the structural support and elastic recoil that defines the protein. The stretch properties of the elastic fibres are essential in soft tissues which are continually stretching and recoiling in response to forces (Vindin et al., 2019).

Similarly to collagen, elastin forms cross-links to assemble into the quaternary structures of elastin fibres. Cells which include fibroblasts, endothelial cells, and smooth muscle cells, secrete elastin in the form of tropeoelastin, an asymmetric monomer (Wise et al., 2014). Tropeoelastin has a structure of alternating hydrophobic and hydrophilic domains with lysine and alanine rich domains forming cross-links. Alternate splicing determines the length of the molecule then after secretion, the molecules self-aggregate onto the surface of the cell and undergo elastinogenesis. The microfibrils which form fibres with elastin include fibrillin-1, fibrillin-2 and microfibrilassociated glycoprotein-1 (MAGP-I). Secreted tropeoelastin associates with the microfibril scaffold after oxidation by lysyl oxidase and then with numerous other secreted and oxidised tropeoelastin molecules (through the process of coacervation) to form the elastic fibre. Coacervation occurs due to interactions between the hydrophobic domains – interactions cause increased temperature and therefore aggregation. In this process, the tropeoelastin assembles in a head-to-tail fashion, where the order of deposition into the growing fibre is coordinated by the c-terminal region. This process will only occur if optimal environmental conditions within the ECM are met. Transglutaminase crosslinks form between fibrillin-1 and tropeoelastin to stabilise the fibre, driven by the oxidation of lysine residues (lysl oxidase reduces lysine residues to form allysine). Coacervation increases the entropy of the fibre, and these changes in entropy grant elastic properties; stretching causes a decrease in entropy and the subsequent recoil Is a reaction which brings fibres back to their maximum entropy (Hoeve and Flory, 1974; Vrhovski and Weiss, 1998). There are multiple models which attempt to describe the exact sequence of how change in entropy is achieved, with the actual process still uncertain. The highly specific structure of elastin is clearly essential for its function which requires elasticity and strength. The half-life of elastin is about 70 years, due to the extensive crosslinking within the fibre network. Improper formation, remodelling or degradation of elastin occurs with aging, injury and disease and has great impacts on function of elastin. For example, abnormal elastin fibres are found in aortic aneurysms and atherosclerosis, causing impaired distension and increased stiffness in blood vessels (Lee et al., 2001). In the case of aging, the cause of elastin degradation is due to elastase activity. Elastases may belong to one of four protease classes: metalloproteinase, serine, aspartic and cysteine. The degradation products of elastin can induce processes such as cell proliferation and migration, and ECM protein synthesis and deposition.

1.4.4 Proteoglycans and Fibronectin

Other important components of the ECM are proteoglycans (PG) and fibronectin.

The PG classes which exist within the ECM are the chondroitin containing (CSPGs), dermatan sulphate containing (DSPGs) and small leucine rich PGs (SLRPs) (lozzo & Schaefer, 2015). The CSPGs and DSPGs retain water, providing the viscoelastic gel which acts in maintaining osmotic pressure, and aid in proper collagen formation. The SLRPs are expressed in the majority of the ECM and are the largest PG family, its basic structure consisting of a protein core encompassing a centre of leucine rich repeats (LRR). Providing structural properties to the ECM and also act as signalling molecules, SLRPs influence processes such as cell migration, proliferation, apoptosis and other essential pathways. The SLRPs also serve to function as physical barriers to collagen fibril cleavage sites, thus preventing collagenase activity. An extensively studied PG is decorin. Decorin abnormalities have roles in various human diseases such as diabetic nephropathy, tubulointerstitial fibrosis and hepatic fibrosis, and the transcription of the decorin gene can be supressed by TNF- α . As well as interactions with collagens, decorin has many direct and indirect interactions with important proteins such as TGF β , VEGF, TIMPs and MMPs.

Fibronectin is an adhesive glycoprotein, most well-known for its association with fibrin during blood clotting. It is essential for collagen fibril formation, using a process called "fibrillogenesis" to extend collagen molecules into fibres.

1.4.5 Matrix Metalloproteinases

The composition and topology of the ECM is highly specific to each tissue type and is constantly being remodelled. This precise homeostasis of the ECM allows maintenance of the differential properties of each tissue or organ. Dysregulation of the ECM results in either excess tissue degradation or collagen deposition – the latter resulting in fibrosis – and can contribute to a multitude of illnesses such as chronic ulcers, cancer and arthritis(Serra, 2020). To maintain the precise ECM turnover, enzymes are employed which degrade specific components. These enzymes are "matrix metalloproteinases" (MMPs). Thus far, over 60 MMPs are known – 24 of which are found in humans. With slight variations in domain lengths, MMPs are generally comprised of an 80 amino acid-long peptide chain, a 170 amino acid-long catalytic domain, a variable length linker peptide and a 200 amino acid-long hemopexin domain (Massova et al., 1998). Variations in structure and substrate specificity enable the MMPs to be classified into categories (Birkedal-Hansen, 1995; Lu et al., 2011; Massova et al., 1998). These categories in humans can be seen in **Table 1.3**. Some MMP names are redundant, for example membrane type MMP4 is also known as MMP 17, and nomenclature differs slightly in mice, for example human MMP1 is known as MMP13 in mice.

Table 1.3 Matrix metalloproteinase categories in humans, based on substrate specificity, and a summary of their substrates (Birkedal-Hansen, 1995; Lu et al., 2011; Massova et al., 1998).

Category	Members	Function
Collagenases	1, 8, 13, 18	Cleave triple helical interstitial collagens, type I, II, III and X
Gelatinases	2, 9	Cleave collagen type IV and digested collagens
Stromelysins	3, 10, 11, 12, 19, 20, 27	Cleave proteoglycans, fibronectin, elastin and some collagen pro-domains
Membrane- type	14, 15, 16, 17, 24, 25	Various cleavage substrates, poorly characterised
Matrilysins	7, 26	Broad substrate range including proteoglycans, gelatin, fibronectin, and some collagen types
Furin- containing	28	Poorly characterised, plays a role in colon and heart homeostasis

1.4.5.1 Regulation of matrix metalloproteinases

The activities of MMPs have downstream effects on cell-matrix and cell-cell interactions as they directly breakdown ECM and cell-surface components, such as growth factors, that could affect processes such as cell growth, cell differentiation, apoptosis and inflammatory processes to name a few. The broad implications of MMPs calls for highly controlled and precise regulation of their activities.

Regulation firstly occurs at the transcriptional level, where MMP gene expression is tissuespecific and controlled by a variety of cytokines such as interleukins, TNF- α and TGF- β (Overall et al., 1991; Vincenti and Brinckerhoff, 2002; Yeo et al., 2020). At the post-transcriptional level, MMPs are secreted into the ECM as zymogens, and only become active upon proteolysis of their amino terminal domain (Massova et al., 1998). The zymogen possesses a catalytic domain with a cysteine-zinc organisation that prevents water (essential for MMP catalytic activity) from binding the zinc atom (Rowsell et al., 2002). To add a further level of regulation, MMPs may be endogenously inhibited by tissue inhibitors of matrix metalloproteinases (TIMPs) or α 2macroglobin. The α 2-macroglobin works to inhibit MMPs by trapping the enzymes, and the subsequent complex is cleaved by endocytosis TIMPs inhibit MMPs mainly by direct binding to their active site. There are 4 known mammalian TIMPs and these inhibit activated MMPs by binding directly to the MMP active site to remove the catalytically-essential H2O molecule. The Nterminus of the TIMP binds the MMP active site cleft, allowing the TIMP cysteine 1 residue to chelate the MMP zinc anion. This binding forms H bonds between an MMP carboxylate O cation and its catalytic glutamate residue. Subsequently, this causes the zinc anion to lose its essential water molecule and results in a blocked MMP active site (Brew and Nagase, 2010; NAGASE et al., 2006)

1.4.5.2 Matrix Metalloproteinases and Metabolic Syndrome

As discussed previously, MetS is the presence of particular CVD and T2D risk factors centred around obesity, a chronic low-grade inflammatory state. The cytokine TNFa plays a key role in the regulation of inflammation and is known to activate MMP gene transcription. One such MMP gene targeted by TNFa is Mmp1 (Yeo et al., 2020). The MMP1 enzyme, also known as interstitial collagenase, targets collagen, gelatin and the MMP9 zymogen. In human subjects with obesity or MetS, MMP1 gene expression and blood plasma levels are associated with increased blood pressure, and BMI (Boumiza et al., 2021; Fourti et al., 2020).

The MMP8, also known as neutrophil collagenase, is another collagenase implicated in MetS. Its plasma levels are highly associated with inflammation and obesity in human subjects, independent of other markers (Belo et al., 2009; Carbone et al., 2022; Gonçalves et al., 2009; Hoseini et al., 2015; Lauhio et al., 2016).

Macrophage metalloelastase, MMP12, is a stromelysin that is expressed in macrophages and digests elastin. The MMP12 is a known regulator of adipose tissue remodelling. Its expression is highly increased in obese adipose tissue and is seen to modulate inflammation and increase insulin resistance in mouse models of obesity (Chavey et al., 2003; Lee et al., 2014; Niu et al., 2016). In rats, MMP12 is also related to increased arterial stiffens and hypertension (Soler et al., 2018).

The MMP19 is another stromelysin which is highly expressed in obese mouse adipose tissue and mice lacking the enzyme were shown to be more susceptible to DIO (Chavey et al., 2003; Pendás et al., 2004). The MMP19 also has a role in liver fibrosis, where MMP19^{-/-} mice are protected against CCl4-induced fibrosis (Jirouskova et al., 2012).

The gelatinases, MMP2 and MMP9, break down type IV collagen. In mouse models MMP9 is required for regulation of smooth muscle cells (Cho and Reidy, 2002). In human subjects, serum MMP2 and MMP9 is associated with hypertension and arterial stiffening (Yasmin et al., 2005). The MMP9 gene is upregulated in human subjects with coronary artery disease and the MMP2 gene is associated with aortic aneurysm (Crowther et al., 2000; Goodall et al., 2002; Wang et al., 2020).

The MMP28, also known as epilysin, is thought to regulate homeostasis in a range of tissues including the colon intestine and heart (Illman et al., 2008). Overexpression of the MMP28 gene in human cell lines resulted in increased MMP19 and TIMP3 messenger RNA (Rodgers et al., 2009). In female mice, MMP28 deletion causes increased inflammation of cardiac tissue (Ma et al., 2012). In the Pender lab group, Clinical and Experimental Sciences, Faculty of Medicine, University of Southampton, MMP28^{-/-}mice are naturally obese and have impaired insulin sensitivity.

Chapter 1

The MMP14 has a wide substrate range including collagen types I-III, PGs and fibronectin. It is involved in adipose tissue remodelling and atherosclerosis in humans and mouse models (Chun et al., 2010; Johnson et al., 2014; X. Li et al., 2020; Melin et al., 2021).

1.4.5.3 Tissue Inhibitor of Matrix Metalloproteinases

Despite being integral regulators of the ECM, MMP activity is generally very low in healthy adult tissues. The four known TIMPs are termed TIMP-1 to -4 and all but TIMP-3 are secreted enzymes (TIMP-3 remains within the ECM). The general structure of TIMPs is conserved, with each comprising a 125 amino acid-long N-terminus, 65 amino acid-long C-terminus and a variable Cys - x - Cys domain, stabilised by 3 disulphide bonds (Apte et al., 1995; Brew & Nagase, 2010). Interestingly, the TIMP N-terminus on its own has been shown to form an active MMP inhibitor in vitro (Murphy et al., 1991). The TIMP secondary structure comprises an OB-fold (a closed or partially open, 5-stranded β -barrel with a Greek key motif) and at least one α -helix (Brew & Nagase, 2010).

All TIMPs inhibit all MMPs but have varying binding affinities for different types and in vitro activities do not necessarily translate to activity in the natural physiological state. The TIMP3 may be the most important regulator of MMPs due to wide ranging roles in cell processes and diseases – it is the only TIMP to inhibit ADAM17 a.k.a. TACE (TNF α converting enzyme), for example.

1.5 Tissue Inhibitor of Matrix Metalloproteinase 3

TIMP3 is the only TIMP that is bound to the ECM and has the largest substrate range, acting and associating with MMP-9, -14, proMMP-9, -2 and members of the ADAM and ADAMTS families, including ADAM17 (also known as TACE) – a sheddase (sheddases cleave the extracellular domains of transmembrane proteins) which activates the inflammatory cytokine Tumour Necrosis Factor alpha (TNF-α) (Brew & Nagase, 2010). TIMP3 is commonly known for its role in Sorsby's Fundus Dystrophy (SFD) – a degenerative macular disease – however, it is increasingly being implicated in pathologies relating to bone health, cancers, and metabolic diseases. Sorsby's Fundus Dystrophy is caused by mutations in the TIMP3 gene and has an onset around 40 years of age. It is characterised by deposition of drusen (extracellular proteins, lipids and cell-debris) within the retina, followed by choroidal neurovascular membrane formation and macular degeneration. This culminates in severe visual impairment unless treated with anti-VEGF injections to prevent the formation of aberrant blood vessels (Clarke et al., 2001; Langton et al., 2005; Qi et al., 2019). A functioning TIMP3 protein ordinarily works to inhibit VEGF action. Agerelated macular degeneration is also associated with TIMP3 mutations and presents similarly to SFD (Dewing et al., 2019; Kamei & Hollyfield, 1999). In addition to AMD, the TIMP3 protein has other roles in aging. During Alzheimer's, TIMP3 has an indirect role in the regulation of betaamyloid (Ab) deposition in the brain and altered TIMP3 levels are seen in patients with this disease. At least 70% of Alzheimer's patients exhibit Cerebral amyloid angiopathy (CAA) where Ab protein accumulates within the cerebral blood vessels. Cerebral amyloid angiopathy is also present in up to 50% of the elderly population. This disorder causes weakening of the vessel walls and can lead to haemorrhages. Blood vessel rupture is linked to increased activity of MMP9 and TIMP3 (Jäkel et al., 2020).

In this section, I will explore the current literature on TIMP3 in its relation to MetS and the gut microbiota.

1.5.1 TIMP3 and inflammation

Tissue inhibitor of matrix metalloproteinase 3 (TIMP3) is unique out of the four TIMPs in that it exhibits strong inhibition of tumour necrosis factor alpha-converting enzyme (TACE), also known as ADAM17 (Amour et al., 1998). Tumour necrosis factor alpha-converting enzyme is a transmembrane disintegrin metalloproteinase and thus is a member of the A disintegrin and metalloproteinase (ADAM) family (Killar et al., 1999). The TACE is responsible for proteolytic cleavage of certain cell surface proteins including cytokines and receptors (Müllberg et al., 1993; Reddy et al., 2000). Perhaps most importantly, TACE cleaves pro-TNFa to produce its active from (Moss et al., 1997). Given the hugely significant role that the pro-inflammatory cytokine TNFa plays in inflammation and immune response regulation, TACE and thus TIMP3 are also medically important proteins.

It has long been known that TNFa is systemically and chronically elevated in obesity, expressed by adipocytes, and has many adverse effects for example on the cardiovascular system and the liver (Hotamisligil et al., 1993). Following studies have shown that the interplay between TIMP3 and TACE is key to inflammation during metabolic disease. For example, inhibition of TACE in ob/ob mice protects against insulin resistance, and TACE deficiency in mice causes reduced fat mass and increased energy expenditure (Gelling et al., 2008; Meijer et al., 2011). In addition, overexpression of *Timp3* in the macrophages of LDL-receptor-deficient mice reduces inflammation and alleviates atherosclerosis (Casagrande et al., 2012). In humans, dysregulation of TACE and TIMP3 is seen in the skeletal muscle of obese patients – TIMP3 protein levels are decreased, TACE activity is increased, and this is accompanied by increased expression of TNFa (Monroy et al., 2009).

1.5.2 TIMP3 and Type 2 Diabetes

Early research investigating the links between T2D and TIMP3 saw the increased activation of ADAM17, due to a reduced expression of *Timp3* in the liver, induced hyperglycaemia and inflammation in a mouse model (Federici et al., 2005). Patients with T2D commonly suffer with obesity, accelerated atherosclerosis and hyperglycaemia. In these patients, increased MMP and ADAM activities are observed in atherosclerotic plaques, and this is thought to be related to altered *Timp3* expression. In those whose first relatives are type-2 diabetic, reduced monocyte *Timp3* mRNA was accompanied by increased insulin resistance, atherosclerosis, and increased TACE activity (Cardellini et al., 2011). In addition, a reduction in insulin receptor substrate 2 (Irs2) expression was accompanied by reduced TIMP3 levels and increased ectodomain shedding activity – caused by the resultant increase in MMP activity (Cardellini et al., 2011). Further, in mouse models, the *Timp3* gene has been identified through quantitative trait loci (QTL) analysis as correlating with dyslipidaemia and diabetes (Cardellini et al., 2009).

1.5.3 TIMP3 and cardiovascular disease

It has previously been shown that loss of or reduced *Timp3* expression results in increased inflammation and oxidative stress markers in vascular tissues and circulation in mice (Stöhr et al., 2015). This was seen alongside increased accumulation of atherosclerotic plaques and decreased life span, which was exacerbated by a high-fat diet (Stöhr et al., 2014, 2015). The suggested mechanism indicates regulation of inflammation and lipid metabolism by TIMP3 via apelin (an adipose-specific cytokine). These findings are supported by the observation of reduced TIMP3 but increased ADAM17 and MMP9 activity in atherosclerotic plaques in human T2D patients (Cardellini et al., 2009). Liver diseases can lead to inappropriate iron metabolism thus increased iron absorption from dietary sources and eventually iron overload. Iron overload in turn can cause heart failure – the likelihood of which is seen to increase in *Timp3*-/-mice, alongside abnormalities in systolic and diastolic blood pressures (Zhabyeyev et al., 2018). These mice also exhibited increased expression of MMP2 and MMP9 in heart tissue with increase myocardial fibrosis, suggesting TIMP3 regulates the heart ECM to protect against iron-induced cardiomyopathy (Zhabyeyev et al., 2018).

1.5.4 TIMP3 and Liver Disease

Non-alcoholic fatty liver disease (NAFLD) is commonly associated with obesity, T2D and insulin resistance. Due to excess lipids in the hepatocytes, oxidative stress and lipotoxicity occurs, promoting the development of inflammation (Casagrande et al., 2017). It is not surprising therefore that TNF-α is a predictor of NAFLD and increased levels of this pro-inflammatory cytokine are associated with advanced stages of NAFLD (Casagrande et al., 2017). A reduction in *Timp3* expression is implicated in the development of NAFLD and hepatic inflammation. In accordance with these observations, an overexpression of *Timp3* in macrophages was seen to rescue NASH symptoms in mouse models of insulin resistance. In transgenic mice overexpressing *Timp3* in macrophages and fed a high fat diet, *Timp3* overexpression improved liver inflammation, insulin sensitivity among other factors relating to MetS (Menghini et al., 2012). The effect of TIMP3 was mediated via adipose remodelling and altered signalling pathways involved in inflammation and oxidative stress (Menghini et al., 2012).

1.5.5 TIMP3 and the Gut Microbiota

TIMP3 interacts with apolipoproteinE (ApoE), where *ApoE^{-/-}* mice are hypercholesterolemic and there is increased immune activity when these mice are also *Timp3^{-/-}* (Stöhr et al., 2015). In these double knock-out mice, alterations in gut microbiome metabolites were seen compared to the WT and single *ApoE^{-/-}* groups, including changes in the levels of serotonin, N-acetyltryptophan and 3-indoxyl sulphate, suggesting TIMP3 interacts with gut microbiome to effect metabolism and cardiovascular health (Stöhr et al., 2015). The *Timp3/ApoE* double knock-out mice also exhibited increased lipid droplets and lipid accumulation within the heart, along with reduced lipid oxidation and expression of the enzymes involved in this process (Stöhr et al., 2015). A reduction in apelin was also seen. Apelin is an adipose-specific cell-surface receptor protein that regulates migration of cell progenitors which differentiate into cardiomyocytes (the contractile cells of the heart) and stimulates cardiac contractility in the adult heart cells (Perjés et al., 2014).

Timp3^{-/-} mice fed a high-fat diet exhibit gut dysbiosis, accompanied by liver steatosis, insulin resistance and increased branched chain amino acids – an increase which is associated with impaired insulin signalling (Mavilio et al., 2016; Newgard et al., 2009). The negative effects of the high-fat diet were seen to improve when given antibiotic treatment, thus highlighting the role of the gut microbiome; this study identified a potential pathway of microbiome-induced insulin resistance, via increased IL-6 signalling and regulated by TIMP3 (Mavilio et al., 2016).

Research elucidating the exact relationship between TIMP3, the gut microbiome and metabolic syndrome is limited but suggests TIMP3 could be a potential target to improve metabolic syndrome and possibly via modulation of the gut microbiome (Basu et al., 2012; Federici et al., 2005; Hanaoka et al., 2014; Mavilio et al., 2016; Menghini et al., 2012; Stöhr et al., 2014)

1.6 Conclusions and Knowledge Gaps

The mechanisms underlying the development of obesity and MetS are complicated, owing to the elaborate interactions between genetics, nutrition, and the gut microbiota. The importance of the gut microbiota was realised, in relative terms, only recently and therefore is poorly understood. Current treatment of MetS relies primarily on diet and exercise interventions, but the continuing increase of its prevalence only emphasises the need for novel treatments, particularly those which address the gut microbiota.

TIMP3 is an important regulator of the ECM, implicated in the development of T2D, fatty liver and cardiovascular disease in mouse models and humans. The *Timp3*-/-mice are genetically susceptible to obesity and MetS, through a process that may involve the gut microbiota. The mechanism linking TIMP3 to the gut microbiota remains unclear but, if elucidated, could reveal important insights into the development of MetS.

1.7 Project Aims and Hypothesis

This study aimed to examine the role of TIMP3 in the development of metabolic disease and diet-induced obesity within a mouse model, focusing on the liver, the gut microbiota, and the aorta. I hypothesised that the composition of the gut microbial species would be altered in *Timp3*-mice, would be exacerbated in response to a high-fat diet, and that these changes would cause the mice to be more susceptible to obesity and metabolic diseases. The study hoped to broaden our understanding of mechanisms that bring about the development of metabolic syndrome, within the context of the gut microbiota.

To achieve this aim, I set three main objectives:

- 1. Characterise the development and progression of metabolic syndrome and obesity within the *Timp3*-/-mouse.
- 2. Analyse the species composition of the gut microbiota within *Timp3-¹⁻*mice, and in response to a high fat diet.
- 3. Investigate the impact of the *Timp3*^{-/-}on the integrity and function of the aorta.

Chapter 2 Materials and Methods

2.1 Control and Experimental Groups

The C57Bl/6 strain is used in this study. This strain is highly susceptible to diet-induced obesity (DIO). Whilst this strain remains lean on a chow diet, it will become obese when fed a HF diet, and although this effect is associated with hyperphagia, it can also be independent of increased caloric intake (Collins et al., 2004; Petro et al., 2004). This DIO is accompanied by hypertension, hyperinsulinemia and hyperglycaemia which are criteria for metabolic syndrome (MetS) (Collins et al., 2004; Alberti et al., 2006). Other C57 mouse strains such as the C57Bl/KsJ are not as vulnerable to HF diet-induced obesity (Collins et al., 2004). The C57Bl/6 therefore allows us to study the effect of altering environmental factors (namely, changing to a HF diet) on obesity and related diseases – this may mimic the development of these diseases in the human population where increasing prevalence of obesity is largely put down to changes to diets containing high amounts of fat.

The C57Bl/6 mouse strain was used for wild-type (WT) controls and the *Timp3*-/- mice were in a C57Bl/6 background. The *Timp3*-/- mouse was a gift from Professor Hideaki Nagase (Kennedy Institute of Rheumatology, Oxford, UK) and originated from the colony in Professor Rama Khokha's lab (Ontario Cancer Institute, Toronto). Quantitative real-time pcr (q RT-PCR) was used in a subset of samples to test *Timp3* expression in the knockout mice to confirm the gene was absent (**Appendix D**).

All mice used in this project were bred in the Biomedical Research Facility at the University of Southampton and maintained in a specific pathogen free (SPF) area in individually ventilated cages (IVC), with ad libitum access to food and water. The WT and *Timp3*^{-/-} controls were fed a control diet (standard chow diet, 7.4% kcal fat; RM1-SDS diet; Special Dietary Services UK) from weaning at 5 weeks of age.

To investigate metabolism and the gut microbiome, male mice were given a high fat diet (HF; 45% kcal fat; SDS 824053; Special Dietary Services UK) from 5 weeks of age, until culling and sampling at 17 weeks old, the study end point. These mice were used in indirect calorimetry experiments at 5, 10 and 15 weeks of age. Additional subgroups were culled at select ages of 5, 7, 10 and 15 weeks old for tissue and colon content sampling. High fat diet was also administered to these mice, expect the newly weaned 5 week old group.

To investigate vascular function, female *Timp3*-/-and WT mice on chow diet were used at 16 and 30 weeks old with subgroups in the 16-week-old group given high-fat diet diet from 5 weeks of age until culling at 16 weeks.

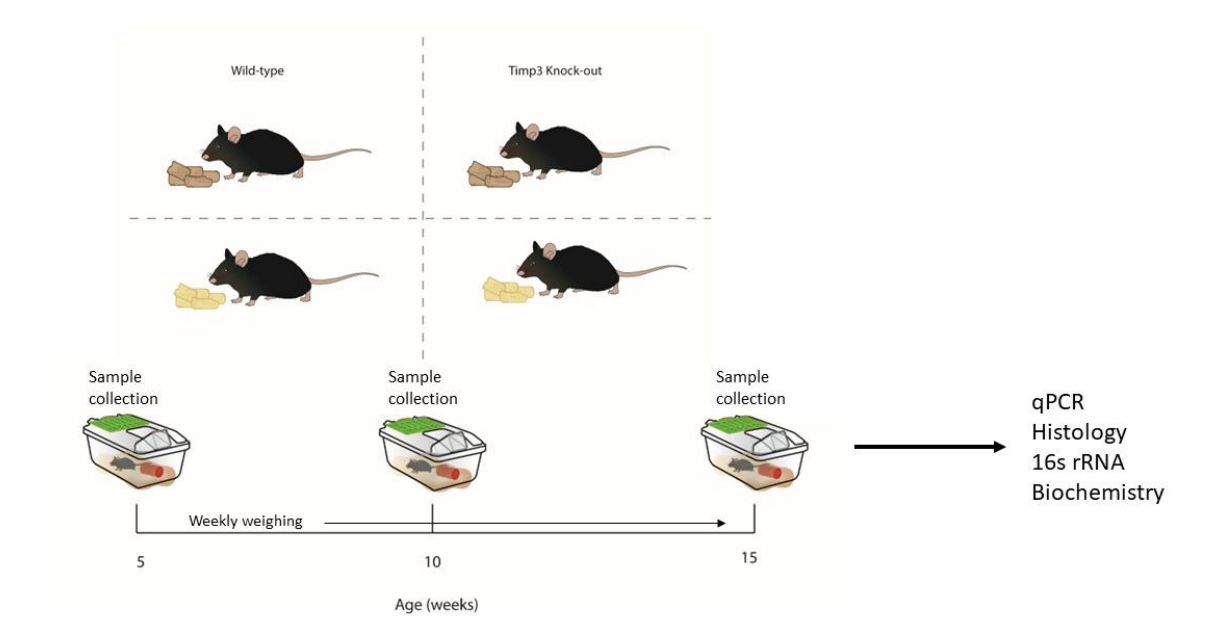


Figure 2.1 Cartoon diagram outlining the high-fat diet study design. Male wild-type C57Bl/6J and knock-out *Timp3*-/- mice were fed either chow (7.4% Kcal from fat) or high-fat (45% Kcal from fat) diet from 5 weeks of ages. Subgroups were culled and tissue samples collected at ages 5, 10 and 15 weeks throughout the study duration.

2.2 Animal Work authorisation

All mice were bred and maintained in Biomedical Research Facilities, University of Southampton in accordance with the United Kingdom Animals (Scientific Procedures) Act 1986. This study has ethical approval from the local ethics committee AWERB and operates under an existing Home Office animal project licence (PFE11A5B5). The regulated protocols were performed according to the ARRIVALS guidelines and in compliance with the 3R policy set by the Home Office.

2.3 Indirect Calorimetry

Energy expenditure was measured using an indirect calorimetry instrument (CaloBox, PhenoSys, PhenoSys GmbH, Berlin, Germany) wherein *Timp3*-/- and WT mice were separately housed and measured for 48hrs. Initial readings taken in the first 1hr of recording were discarded for potential unreliability due to mouse acclimatisation to new cage environment. Energy expenditure is calculated using the respiratory quotient (VCO2/VO2) and is a measure of total energy used for the maintenance of vital bodily functions, metabolism of food and physical activity. Illustration of the indirect calorimetry setup is shown in **Figure 2.2.**



Figure 2.2 Illustration of the indirect calorimetry setup. Mice were housed separately in a cage connected to the CaloBox (PhenoSys GmbH, Germany) which was linked to computer where readings were automatically recorded and saved. Energy expenditure was measured over a 48hr period.

2.4 Tail-cuff Plethysmography

Non-invasive blood pressure was measured by tail-cuff plethysmography, using an IITC blood pressure monitor (229 model; Linton Instruments, Diss, Norfolk, UK) in the WT and *Timp3*-/-female between the ages of 25 and 28 weeks old.

2.5 Tissue sampling

All sampling was carried out in the morning following an overnight fasting. Blood was collected via cardiac puncture, under terminal anaesthesia and plasma was extracted for future analysis. Heart and fat depots (retroperitoneal, gonadal and interscapular brown adipose tissue (iBAT)) were dissected weighed. Other organs and tissues were also collected (liver, duodenum, pancreas, cecum, colon, colon content, skeletal muscle, brain and aorta) and snap frozen for RT qPCR analysis. Liver and gonadal fat samples were fixed in 10% neutral buffered formalin for 24hrs preceding paraffin embedding (Histochemistry Research Unit, University of Southampton) for future histological analysis.

2.6 Blood Plasma Analysis

Blood plasma samples were sent to the Core Biochemical Assay Laboratory (Cambridge University Hospitals NHS Foundation Trust, Cambridge, UK) for analysis. Assays were selected to measure mouse lipid profile, insulin levels and butyrate levels.

2.6.1 Beta Hyrdoxybutyrate assay

Beta hydroxybutyrate (3-OH Butyrate) was measured using the Stanbio Beta Hydroxybutyrate Liquicolour kit (EKF Diagnostics, Cardiff, UK) as par the manufacturer's protocol. Per sample, 10μl of plasma was used.

In this assay, 3-OH Butyrate and NAD are converted to acetoacetate and NADH, in a reaction catalysed by D-3 Hydroxybutyrate dehydrogenase. Then, diaphrose catalyses a reaction between NADH and INT to produce NAD and INT. This reaction produces a blue colour which absorbs at 505 nm. This absorbance is directly proportional to the concentration of 3-OH Butyrate within the sample.

2.6.2 Insulin assay

Insulin was measured using the Mescoscale Discovery (MSD) Mouse Metabolic Kit (Meso Scale Diagnostics, Maryland, USA) according to manufacturer's protocol. Per sample, $10\mu l$ of plasma was used.

In this assay, mouse monoclonal anti-insulin capture antibodies were bound to a 4-spot MSD assay plate. To this plate, the sample and mouse monoclonal antibody to insulin were added and incubated for 2 hours. During incubation, insulin within the sample binds to the capture antibodies and the detection antibodies bind to the insulin. The plate is subsequently washed and MSD read buffer is added for electrochemiluminescence. The plate is loaded into MSD s600 instrument where a voltage is applied, causing labels bound to the electrode surface to emit light. The intensity of the light emission is measured, and insulin concentration is calculated using MSD software.

2.6.3 Triglycerides assay

Triglycerides were measured using an automated enzymatic assay on the Siemens Dimension EXL analyser. Per sample, 4µl of plasma was used.

In this assay, triglycerides are converted into glycerol and fatty acids by lipoprotein lipase. Glycerol is phosphorylated by ATP, catalysed by glycerol kinase, to produce glycerol-3-phosphate. Glycerol-3-phosphate is oxidised to dihydroxyacetone phosphate and hydrogen peroxide by glycerol-3-phosphate oxidase. Quinoneimine is then produced from hydrogen peroxide, aminoantipyrine and 4-chlorophenol, catalysed by peroxidase. The change of absorbance due to quinoneimine is measured and is directly proportional to the quantity of glycerol and/or glycerol precursors within the sample. Absorbance is measured as a bichromatic endpoint at 510 nm and 700 nm. (Hagen and Hagen, 2011)

2.6.4 Total Cholesterol assay

Total cholesterol was measured using an automated enzymatic assay on the Siemens Dimension EXL analyser. Per sample, $3\mu l$ of plasma was used.

In this assay, cholesterol esters are hydrolysed by cholesterol esterase, to produce free cholesterol. Free cholesterol is oxidised by cholesterol oxidase to produce hydrogen peroxide and cholest-4-ene-3-one. The hydrogen peroxide is used to oxidise DEA-HCL/AAP to produce a coloured product which absorbs at 540 nm. The absorbance of the product is directly proportional to the cholesterol concentration within the plasma sample. Absorbance is measured as a polychromatic endpoint at 452 nm, 540 nm and 700 nm. (Rautela and Liedtke, 1978)

2.6.5 High-density Lipoprotein assay

High-density lipoprotein (HDL) was measured using an automated homogenous accelerator selective detergent assay on the Siemens Dimension RxL analyser. Per sample, $3\mu l$ of plasma was used.

In this assay, non-HDL un-esterfired cholesterol undergoes an enzymatic reaction which produces peroxide. A peroxidase reaction with DSBmT is then used to produce a colourless product from the peroxide. Then, HDL is solubilised by a detergent, and cholesterol oxidase plus a chromogenic coupler develop colour in the reaction. The amount of colour produced is directly proportional to the HDL concentration within the sample.

2.6.6 Low-density Lipoprotein calculation

From the measured triglyceride, cholesterol and HDL concentrations, low-density lipoprotein (LDL) concentration can be calculated using the Friedwald formula. (Nauck et al., 2002)

The Friedwald formula is as follows:

$$LDL = Cholesterol - HDL - (\frac{Trigylcerides}{2.2})$$

2.7 RNA Isolation

All steps were performed on wet ice. Tissue samples were placed into 1.5ml tubes with 0.5g beads and 1ml TRIzol (Invitrogen Life Technologies) reagent, then vortexed for 20-30 seconds before being cooled on ice for 120 seconds. Samples were transferred to new 1.5ml tubes, leaving beads behind. To separate sample, chloroform (Sigma-Aldrich) was added at a 5:1 ratio, TRIzol to chloroform. Samples were then vortexed for 10 seconds then rested on ice for 5 minutes. Samples were then centrifuged at 12000 x g at 4°C for 30 minutes. Following this, the aqueous phase was transferred to fresh 1.5ml tubes and ice-cold isopropanol was added at 2:1 ratio, aqueous phase to isopropanol. Glycogen was then added at a ratio of 100:1, aqueous phase to glycogen. Samples were then vortexed for 20 seconds before storage at -80°C for a minimum of 2 hours or overnight. Samples were defrosted and immediately centrifuged at 12000 x q at 4°C for 30 minutes to pellet RNA. The isopropanol layer was removed, leaving RNA pellet behind, and 1ml 70% ice-cold ethanol (molecular biology grade, Sigma-Aldrich) was added for washing steps. Samples were then briefly vortexed, left on ice for 10 minutes then centrifuged at $12000 \times g$ at 4°C for 30 minutes. Ethanol suspension was removed, leaving behind RNA pellets which were airdried before being resuspended in 30 μl RNAse-free H₂O. Concentration and quality of RNA was validated using Nanodrop ND-1000 spectrophotometer (Thermo Fisher Scientific). Good quality RNA has an absorbance at 260/280 nm of around 2.00 (Wilfinger et al, 1997).

2.8 Reverse Transcription

Applied Biosystems High-Capacity cDNA Reverse Transcription Kit was used as per manufacturer's protocol, using a concentration of total RNA of $500 \text{ng/}\mu\text{l}$. Reverse transcription was performed using Bio-Rad MJ Research Tetrad2 thermocycler with steps as follows: 37°C for 60 minutes, 90°C for 5 minutes.

2.9 Real-time Quantitative Polymerase Chain Reaction (RT qPCR)

2.9.1 Primer selection and validation

Primers were selected to measure target genes involved in extracellular matrix remodelling, inflammatory pathways, and those implicated in metabolic syndrome. Prior to use, a dissociation curve was produced and analysed for each primer pair. A dissociation curve with multiple peaks indicates the presence of primers dimers which would produce a false positive in the RT qPCR reaction. Primer pairs that produced primer dimers were therefore discarded.

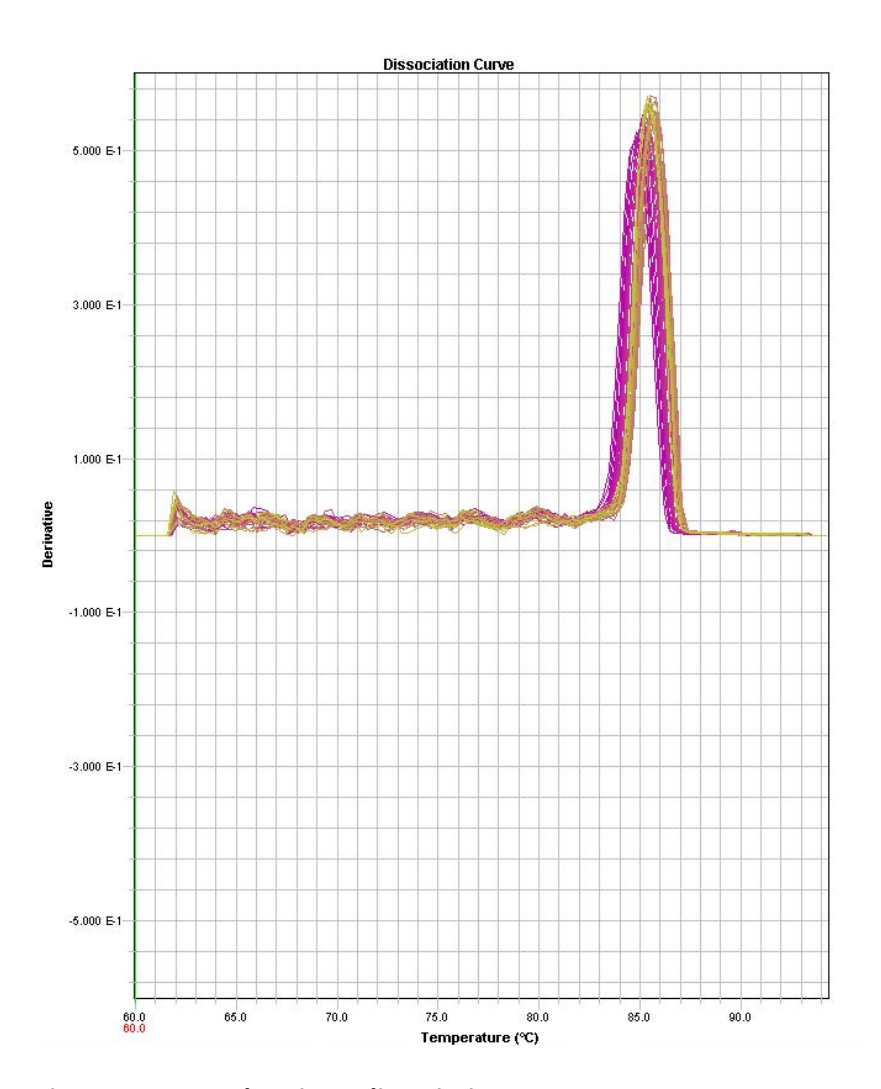


Figure 2.3 Example primer dissociation curve. Presenting a primer pair that produces no primer dimers.

2.9.2 Reaction procedure

Gene expression was measured with SYBR-green gene detection method using SDS v2.4 software for the 7900HT Fast Real Time PCR System (Applied Biosystems, California, USA). The qPCR master mix per well was as follows: 0.25 μ l of each forward and reverse primers (100 μ M), 4.5 μ l diluted cDNA, 5 μ l Power Up SYBR Green Master Mix (Fisher Scientific). Primer- , cDNA- and SYBR- only controls were used to control for contamination. Thermocycle steps were as follows: 50°C for 2 minutes, 95°C for 10 minutes, then 40 cycles of 95°C for 15 seconds and 60°C for 1 minute.

Fold change was calculated using the Comparative C_T method as follows:

$$\Delta C_T = C_T(target\ gene) - C_T(reference\ gene)$$

$$\Delta \Delta C_T = \Delta C_T(experimental\ sample) - \Delta C_T(control\ sample)$$
 Fold change = $2^{-\Delta\Delta C_T}$

Gene expression was normalised to θ -actin and Gapdh housekeeping genes as these are the most frequently used reference genes in qPCR experiments in metabolic disease studies in mice (Almeida-Oliveira et al., 2017).

2.10 Four Chamber Wire Myography

A four-chambered wire myograph was used in this study. Wire myography is an ex vivo method to assess the function of endothelial cells and vascular smooth muscle cells in isolated arteries, in response to vasoconstrictors and vasodilators (Spiers and Padmanabhan, 2005; del Campo and Ferrer, 2015).

2.10.1 Myography procedure

Myograph baths (5 ml volume, containing Ca2+ free physiological salt solution (PSS)) and buffers (PSS and potassium-physiological salt solution (KPSS)) were kept at 37°C. Myograph baths were gassed at 95% O2 and 5% CO2.

Aorta from each mouse was dissected, washed, and cut into a section of at least 5 mm in length which was mounted in one channel of the myograph with the assistance of Dr. Christopher Torrens (Human Development and Health, Faculty of Medicine, University of Southampton). Samples were normalised to their appropriate tension (sample dependent) then their functionality tested by draining the myograph baths before adding KPSS and recording the response after two minutes. Following this, baths were drained again and replenished with PSS – this was repeated as necessary until tissue returned to its resting state.

Tissue was initially subjected to passive stretching. In this method, the aorta is stretched mechanically using the myograph dial in increments of equal amount every 2 minutes and recorded until a measure of around 14 kPa is reached. The aorta is then returned to resting state and left for around 10 minutes to allow its acclimatisation.

For the active measurements, three drugs were tested: noradrenaline (NA), carbachol (Cch) and Sodium Nitroprusside (SNP). In each experiment, each drug was added cumulatively, resulting in bath concentrations ranging from 1 nM to 100 nM, every 2 minutes for NA, and 0.1 nM to 10 nM every 2 minutes for Cch and SNP. The response curve was recorded, and measurements taken every 2 or 1 minute, depending on type of drug. For the Cch and SNP experiments, 5 μ l of 100 uM thromboxane was added to each bath beforehand to constrict the tissue. Between each experiment, baths were repeatedly drained and replenished with PSS buffer until tissue returned to rest.

2.11 Histology Sample Processing

Prior to staining, all paraffin embedded tissues were sectioned at 4um thick using a microtome. Sections were placed onto aminopropyltriethoxysaline (APES) coated slides and left to dry at 37°C for 24 hours.

2.11.1 Dewaxing

Tissue sections were dewaxed in Tissue-Tek Tissue Clear twice for 10 minutes each then rehydrated in two graded alcohols for 5 minutes each. Before submersion in 70% ethanol for 5 minutes.

2.11.2 Haematoxylin and Eosin Staining

The haematoxylin and eosin (H&E) stain is one of the most widely used tissue stains. Eosin stains the extracellular matrix and organelles pink, whilst haematoxylin stains nuclei blue (Chan, 2014).

Following dewaxing, slides were washed under filtered running water for 5 minutes, then immersed in Mayer's haematoxylin for 5 minutes. Next, slides were washed under running tap water for 5 minutes then immersed in eosin for 5 minutes. After this, slides were briefly rinsed in tap water before dehydration in 100% ethanol and absolute alcohol twice, each for 1 minute. Finally, slides were immersed in three xylene baths for 3 minutes each before being mounted with DPX and allowed to dry.

2.11.3 Sirius Red Staining

Sirius red stain is used to stain collagen fibres red. Due to the absorbance of the dye, Sirius red stained collagen fibres can be visualised under polarised light (Lattouf et al, 2014).

Following dewaxing, slides were submerged in distilled H_2O twice for 5 minutes each, before immersion in 0.2% phosphomolybdic acid for 5 minutes. Slides were then submerged in Picro-Sirius red for 2 hours. After 2 hours, slides were briefly washed with 0.01% HCL then distilled in H2O before being submerged in Mayer's haematoxylin for 2 minutes. Further, sections were "blued" under running tap water (approximately 5 minutes) before dehydration in 70% alcohol, absolute alcohol twice, and two xylene baths, respectively, all for 5 minutes each.

2.11.4 Elastic Van Gieson Staining

Elastic Van Gieson stain is used to stain elastin fibres black. Cell nuclei are also stained black, collagen is stained red and other components stained yellow (Kazlouskaya et al, 2012).

Following dewaxing, sections were stained in Verhoff solution for 30 minutes (until tissue turned black). Slides were then rinsed briefly in tap water before differentiation in 2% ferric chloride for 2 minutes. After this, slides underwent multiple brief rinses in tap water until elastin fibres could be seen against a grey background, under a light microscope. Then, slides were washed with 5% sodium thiosulphate for 1 minute and running tap water for 5 minutes before counterstaining with Van Gieson stain for 3 minutes. Slides were blotted dry before dehydration in 100% ethanol and absolute alcohol twice, each for 1 minute. Finally, slides were immersed in three xylene baths for 3 minutes each.

2.11.5 Sample Preparation for Second Harmonic Generation Microscopy

Aorta section slides were submerged in two rounds of Tissue-tek Tissue Clear for 10 and 5 minutes, respectively, then in absolute alcohol twice for 5 minutes each. Following this, slides were submerged in three graded alcohols, 70% EtOH, 50% EtOH then 20% EtOH for 5 minutes each before immersion is deionised H₂O for 5 minutes. Samples were then blotted dry, and a cover slip was applied using clear nail polish, ensuring samples were water tight.

2.12 Bright-field Imaging

Images of stained aorta and liver tissue were acquired using an Olympus BX51 microscope with Olympus CC12 microscope camera.

2.13 Polarised Light Field Imaging

Images of Sirius red stained aorta sections, visualised under polarised light, were acquired using a Nikon Eclipse 80i microscope by a summer project student from CUHK, Eileen Yu.

2.14 Second Harmonic Generation and Two Photon Excitation Fluorescence Imaging

Second harmonic generation (SHG) microscopy was used to investigate the composition of collagen fibres within a contact tissue. Collagen fibres are very strong emitters of SHG signal due to their fibrillar structure (Chen et al., 2012).

2.14.1 System Setup

A custom-built multiphoton imaging setup was used for second harmonic generation (SHG) and two-photon excitation fluorescence (TPEF) imaging (Bionanophotonics group, Institute for Life Sciences, University of Southampton, UK). The setup consisted of a tunable femtosecond pulsed laser (MaiTai, Spectra Physics) coupled to a Leica DRMB upright microscope. Laser scanning was performed by a Galvo Scanner (Cambridge Technology 6220H), and the SHG and TPEF signals were detected by separate PMTs (Hamamastu H10722-20 and H10722-01, respectively). Laser settings were adjusted via the software Spectra System and laser wavelength was set to 800 nm.

2.14.2 Image acquisition

The microscope objective used for all images was 63x/1.2 water. A standard sample for SHG signal was imaged at the beginning of each session. Image acquisition parameters were controlled via ScanImage 2016b software (Vidrio technologies). Parameters were set to 8000ns exposure time, 160 scan phase and 512 pixels per image. Using a script in MATLAB, written by a previous member of the Biononaphotonics group and set to run in ScanImage, tiled images were taken. In short, after setting stage limits on the x and y axis, images are acquired sequentially along the x. When the limit of the x axis is reached, the stage returns to the initial x co-ordinate and moves along the y axis. Movements along the x axis are then restarted, and this process is repeated until the y limit is reached. The tiled images are later stitched together during analysis in Fiji.

2.15 Analysis of Liver Tissue

Haematoxylin & Eosin stained liver sections were visualised and imaged at 20x magnification. Samples were analysed using a NAFLD scoring system developed by Kleiner et al (Kleiner et al, 2005). Per liver sample, at least 5 locations were analysed.

2.16 Analysis of Aorta Tissue

2.16.1 Aorta Wall Measurements

Haematoxylin and eosin stained aorta tissue sections were visualised and imaged at 10 and 20x magnification preceding analysis in ImageJ. Total aorta width and tunica media width was measured at least 12 separate points along the section. One section was analysed per mouse and 3 mice were analysed per group.

2.16.2 Pixel Counting of Sirius Red Stained Collagen

Image analysis of Sirius Red stained collagen was performed by visiting summer student, Eileen Yu, from CUHK. Images were captured at 400x magnification and processed in ImageJ. Images were converted into a black and white format, and the black area was quantified into pixel area. Colour signals were quantified using Metamorph (version 7.0) and threshold sensitivity set to 5 (the most stringent). Ares with desired colour were selected manually and quantified into integrated optical densities.

2.16.3 Second Harmonic Generation Image Processing

A custom-built multiphoton imaging setup was used for second harmonic generation (SHG) and two-photon excitation fluorescence (TPEF) imaging (Bionanophotonics group, Institute for Life Sciences, University of Southampton, UK). Details can be found in section 2.14. The microscope objective used for all images was 20x/0.5. The tiled images were acquired using Scanlmage 2016b and were later stitched together during analysis in Fiji. Using Fiji, SHG images were thresholded using the Triangle method and TPEF using the default method. Pixel area of collagen and elastin within each section was quantified for analysis.

Individual collagen fibre extraction and analysis was performed using CT-FIRE v3.0 (Laboratory for Optical and Computational Instrumentation, LOCI) (Bredfeldt et al., 2014). This program identifies four fibre properties. Width is the average width along the fibre length in pixels. Angle is the fibre angle with respect to the horizontal axis (ranging between 0-180 degrees). Length is the distance of the fibre from end to end in pixels. Straightness is the distance between the two end points of the fibre divided by the fibre length, and ranges between 0-1.

2.17 MiSeq 16S Ribosomal RNA Sequencing

Sequencing of the 16S ribosome is a widely used technique that allows for phylogenetic and taxonomic classification of bacterial species without the need of culturing them (Weisburg et al, 1991). Sequencing was used in this study to investigate bacteria within the mouse gut.

2.17.1 Sample Preparation and Sequencing

Snap-frozen colon content samples and blank control samples were sequenced at The National Oceanography Centre, Southampton. Extraction of DNA from faecal samples was performed using QIAamp PowerFecal DNA Kit as per manufacturer's protocol. Samples were then prepared as per protocol for the Illumina MiSeq system found in "16S Metagenomic Sequencing Library Preparation" manual. Sequencing was performed using Illumina MiSeq Reagent Kit v3 (600-cycle) (cat no. MS-102-3003), where pooled library was loaded at a concentration of 8 pM with a 5% PhiX spike. The V3-V4 region of the 16s ribosomal RNA gene was sequenced with primers pro341F (5'-CCTACGGGNBGCASCAG-3') and pro805R (5'-GACTACNVGGGTATCTAATCC-3') (Takahashi et al., 2014).

2.17.2 Sequencing Analysis

Raw FASTQ sequence data was processed in R v.4.0 using the workflow described by Callahan et al and sequences matched to the SILVA database v.138.1 (Figure 2.4) (Ben J. Callahan et al., 2016; Quast et al., 2013; R Studio Team, 2020). To summarise, the sequences were filtered and clustered into ribosomal sequence variants (RSVs) using the dada2 package to remove errors from the data (Benjamin J. Callahan et al., 2016). Following this, a sequence table was constructed, and chimeras removed before comparison with the SILVA reference database. To account for variation in sequence depth, data were log transformed for downstream analysis. Using the vegan package, the alpha diversity was estimated using Shannon and Simpson indices and tested using Wilcoxon ranked Sum (Jari Oksanen, F. Guillaume Blanchet, Michael Friendly et al., 2019). The beta diversity was estimated using Bray-Curtis distance and principal coordinates analysis, tested using the vegan package adonis function (Jari Oksanen, F. Guillaume Blanchet, Michael Friendly et al., 2019). Abundance data were tested using Wilcoxon ranked sum or unpaired two-tailed Student's t-test with significance set at p<0.05, presented as means ± SEM. Differential abundance analysis was conducted using the statistical frameworks DESeq2 and ANCOM-BC in R (H. Lin & Peddada, 2020; Love et al., 2014).

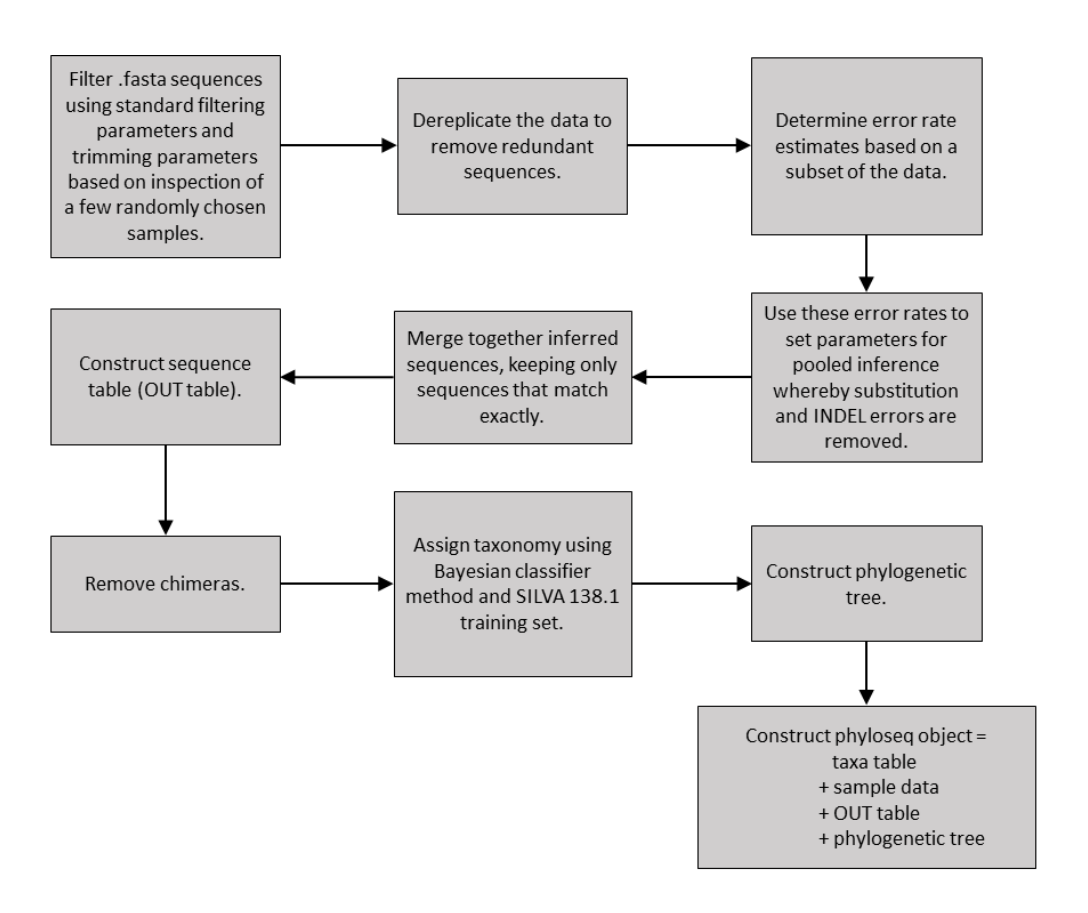


Figure 2.4 Filtering of FASTQ sequences and construction of a phyloseq object in R.

2.18 Statistical Methods

Unless otherwise specified, statistical analysis (two- and one-way ANOVA with multiple comparisons, and unpaired, two-tail Student's t-test, dependent on experimental design) was conducted and figures generated using GraphPad Prism v8.0.2. Sample size was determined using G*Power software, with significance set to 0.5 and power 0.8 (Faul et al., 2007, 2009). Data are expressed at means with ±SEM where applicable with significance set to p<0.05. Outliers were removed from the data set if they were due to factors such as sampling or measurement error.

Chapter 3 Development of Obesity in a Chronic Lowgrade Inflammation Model, *Timp3* Knockout Mice

3.1 Introduction

Chronic inflammation, characterised by excessive body fat, measured using BMI or body fat percentage (Maachi et al., 2004; Makki et al., 2013; Powell et al., 2010). High-fat diet implications in obesity have been well studied in mice, where it is seen to contribute to excessive body weight, fatty liver, and diabetes even independently from excess calorie consumption (Collins et al., 2004; Elahi et al., 2009; Petro et al., 2004; Surwit et al., 1988).

It is well known that in the obese state, the expression of inflammatory cytokines is increased in adipose and liver tissues (Maachi et al., 2004; Makki et al., 2013). In the liver, this altered gene expression in obesity is often accompanied by lipid accumulation and in extreme cases, fibrosis (Velázquez et al., 2019). Increased energy expenditure is also seen in obesity studies in humans (Carneiro et al., 2016).

Previous groups have investigated the energy expenditure of the *Timp3*-/- model under standard chow diet, and the effect of a high-fat diet in C57BI/6J mice separately (Hanaoka et al., 2014; Mavilio et al., 2016). However, the manifestation of obesity, and its related pathologies, during *Timp3*-/- mouse development has not been established. Therefore, this chapter aims to investigate the role of *TIMP3* in the development of obesity in a *Timp3*-/- mouse model, from juvenile to adult.

3.2 Aims and Hypothesis

The aim of this study was to characterise the development and progression of metabolic syndrome and obesity within the *Timp3*-/- mouse, in comparison to sex- and age-matched C57BI/6J controls.

The hypothesis of this study was that absence of *TIMP3* in male mice would impact the development of obesity and exacerbate the effects on metabolic syndrome risk factors such as fatty liver, insulin resistance and dyslipidaemia. This would be mediated via changes in expression of matrix metalloproteinase genes and genes involved in lipid and glucose metabolism.

To achieve this aim, HFD was administered from 5 weeks to 17 weeks of age in *Timp3*^{-/-} and C57BI/6 mice, and these groups were matched to diet controls. The following objectives were set:

- 1. Monitor body weight and weight of selected fat depots
- 2. Monitor energy expenditure during the development of obesity
- 3. Measure blood biomarkers of insulin resistance, hyperglycaemia, and hyperlipidaemia
- 4. Examine expression of MMPs and MetS-related genes within the liver
- 5. Examine lipid accumulation and inflammation in the liver

3.3 Methods

In this study, body weight and adiposity measurements, histology, indirect calorimetry, blood plasma assays and RT-qPCR were used to investigate the development and mechanisms of obesity within the *Timp3*-/- mouse.

Male mice were fed high-fat diet from 5 weeks old until the study endpoint of 17 weeks old when adipose, liver and blood samples were collected. Subgroups were sampled at 5, 7, 10 and 15 weeks old and tissue samples collected. Mice were also weighed at a regular time weekly to determine the pattern of weight gain.

Indirect calorimetry (CaloBox, PhenoSys, PhenoSys GmbH, Berlin, Germany) was used to measure energy expenditure at 5, 10 and 15 weeks old. Individual mice were temporarily housed for a period of 48hrs for measurements. Light period within the animal house spanned 07:00-18:59, dark period spanned 19:00-06:59.

Hepatic steatosis was measured using H&E-stained liver sections. Sections were visualised and imaged at 20x magnification. Lipid droplet analysis was carried out using the Kleiner et al scoring system (Kleiner et al, 2005).

Blood plasma samples were sent to the Core Biochemical Assay Laboratory (Cambridge University Hospitals NHS Foundation Trust, Cambridge, UK) for analysis. Assays were selected to measure mouse lipid profile, insulin levels and butyrate levels. Details of specific assays can be found in Chapter 2.6.

Gene expression was measured using RT-qPCR. Primers were selected to measure target genes involved in extracellular matrix remodelling, inflammatory pathways, and those implicated in metabolic syndrome. Full methods can be seen in **Chapter 2.9**.

Unless otherwise specified, statistical analysis (two- and one-way ANOVA with multiple comparisons, and two-tailed unpaired Student's t-test, depending on experimental design) was conducted and figures generated using GraphPad Prism v8.0.2. Data are expressed at means with ±SEM where applicable with significance set at p<0.05.

3.4 Results

3.4.1 Effects of Diet Induced Obesity on the Phenotype of the *Timp3* Knockout Mouse

3.4.1.1 Body Weight

To determine the phenotypic effects of *TIMP3* absence and HF diet on mouse body weight, weight was measured at regular weekly intervals across the study duration. Total weight gain and AUC analysis is shown in **Figure 3.1**. Both HF diet groups gained significantly more weight over the 12 weeks, compared to their chow-fed controls (p < 0.0001). Additionally, both $Timp3^{-/-}$ chow and HF diet groups gained less weight than their C57Bl/6J counterparts (p < 0.05 and p < 0.001, respectively).

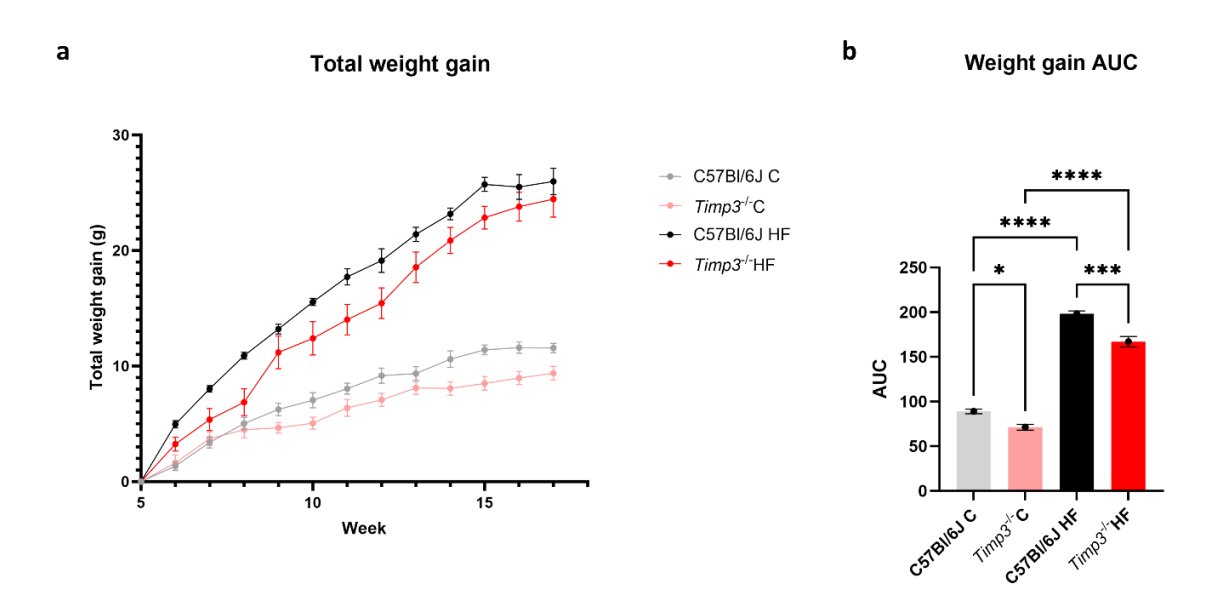


Figure 3.1 Total weight gain and area under the curve analysis in $Timp3^{-/-}$ mice over the study duration. a) Mean values \pm SEM shown for weight gain over study duration from 5 to 17 weeks of age in male $Timp3^{-/-}$ mice on chow (C) and high-fat (HF) diets and C57BI/6J wild-type controls. b) AUC analysis of body weight gain. n= 4 biological samples per group. One-way ANOVA with Tukey's Comparisons was used to test for differences between groups. * = p < 0.05, *** = p < 0.001, **** = p < 0.0001.

Chapter 3

To examine the rate of weight gain across the study, weight difference between each week is presented in a line graph and bar plots in **Figure 3.2**. Both chow-fed groups had a peak weight gain at 7 weeks old, during middle adolescence, which subsequently followed a sigmoidal pattern of gain. Weight gain in the C57BI/6J HF group was highest at the start of the study (6 weeks), and steadily decreased over the duration. Interestingly, the *Timp3*-/- HF did not follow either pattern of weight gain. The largest peak was at 9 weeks, in late adolescence, which was followed by a second smaller peak at 13 weeks when the mice had reached maturity.

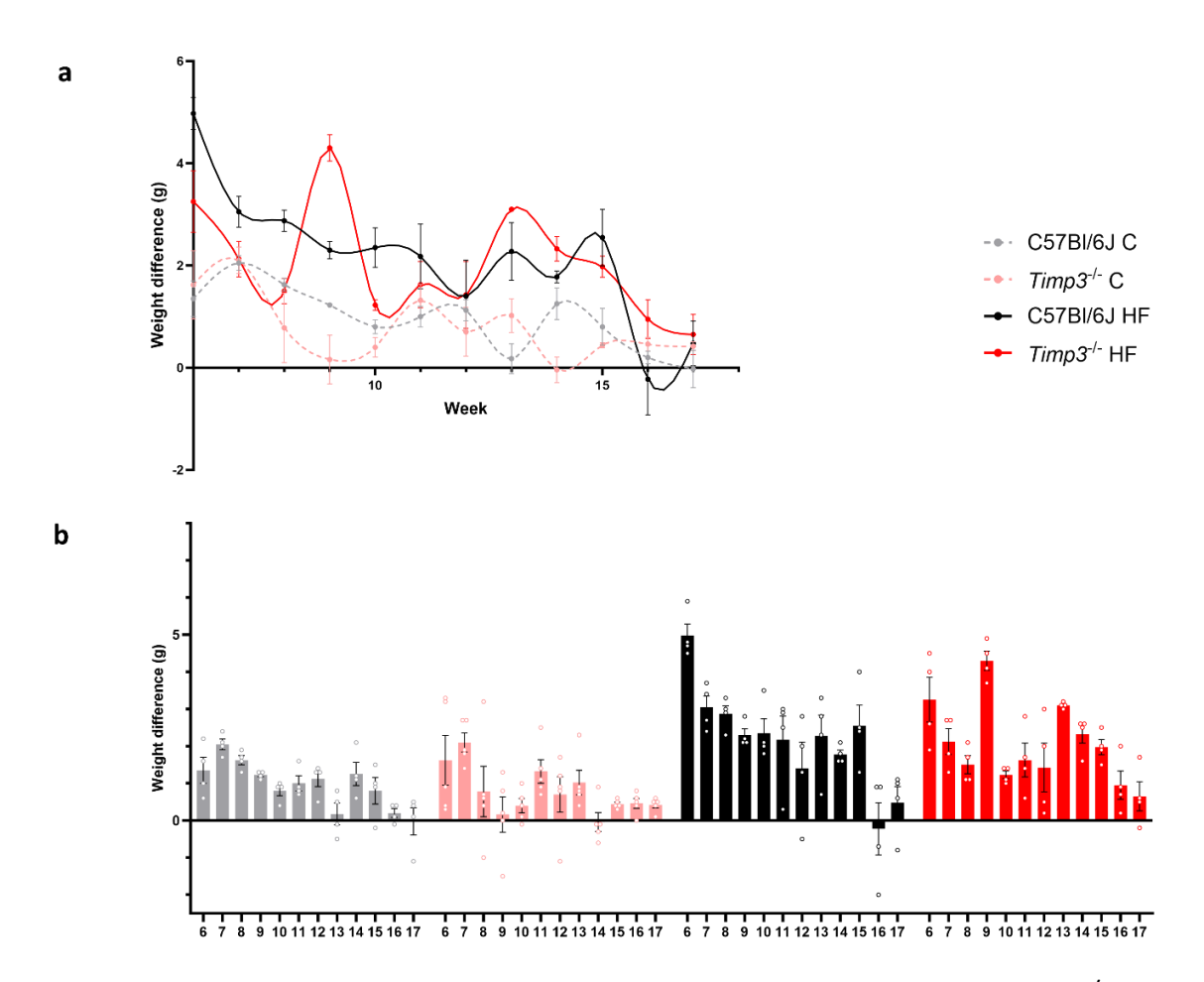


Figure 3.2 Longitudinal representation of weight gain over the study duration, in *Timp3*-/- mice on high-fat diet, and C57Bl6/J controls. Average weight gain per week ± SEM, from 6 to 17 weeks of age in male *Timp3*-/- mice on chow (C) and high-fat (HF) diets and C57Bl/6J wild-type controls.

3.4.1.2 Fat Depot Weight: Gonadal, Retroperitoneal, Inguinal and Brown-interscapular Fat

Various fat depot weights (expressed as a percent of total body weight) of *Timp3*. male mice at 5, 7, 10, 15 and 17 weeks old on chow (C) and high-fat (HF) diets, and their C57Bl/6J controls, are shown in **Figures 3.3-3.7**.

The addition of high-fat diet caused significant increases in relative gonadal fat weight in $Timp3^{-/-}$ mice at ages 7, 10, 15 and 17 weeks (**Figure 1**, p < 0.05, p < 0.01 and p < 0.0001, respectively). This was also seen in the C57Bl6J mice at 7, 15 and 17 weeks (**Figure 1**, p < 0.05, p < 0.0001, and p < 0.0001, respectively). Between the two genotypes, the gonadal weight was significantly increased within the $Timp3^{-/-}$ HF group, compared to C57Bl6J HF, at 7 weeks of age only (**Figure 1**, p < 0.05).

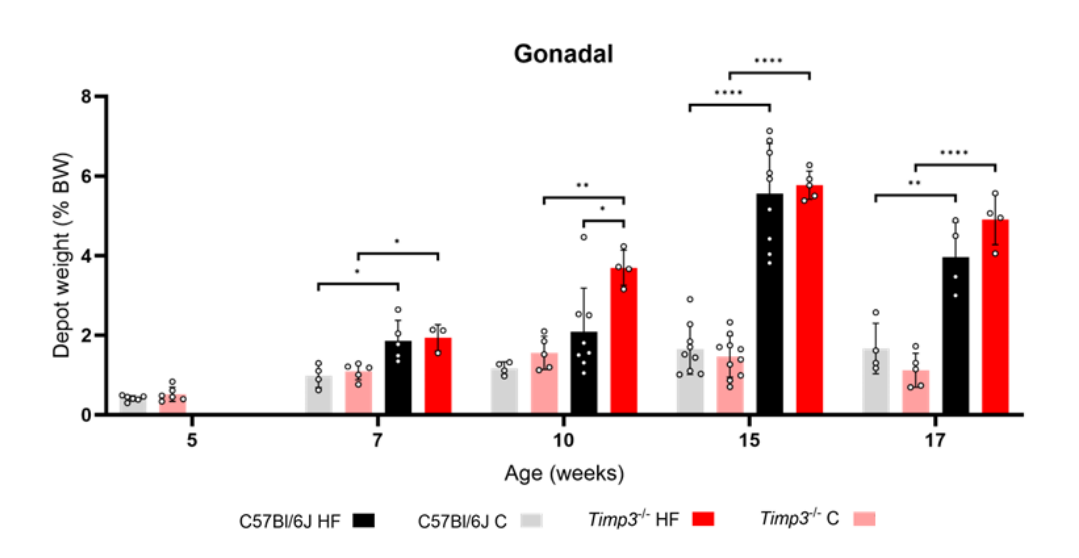


Figure 3.3 Gonadal adipose depot weight of $Timp3^{-/-}$ mice, across 5-17 weeks of age, on chow (C) and high-fat (HF) diet. Mean weight expressed as a percentage of total body weight \pm SEM in male $Timp3^{-/-}$ mice on chow and high-fat diet, and C57BI/6J controls. n=3-10 biological samples per group. Tukey's Comparisons was used to test for differences. * = p < 0.05, ** = p < 0.01, *** = p < 0.001, *** = p < 0.0001.

Chapter 3

Similarly, addition of high-fat diet caused significant increases in relative retroperitoneal fat weight in $Timp3^{-/-}$ mice at ages 7, 15 and 17 weeks (**Figure 3.3**, p < 0.01 and p < 0.0001, respectively). Also, within C57Bl6J mice at 7, 15 and 17 (**Figure 3.4**, p < 0.01, p < 0.0001 and p < 0.01**, respectively) weeks, high-fat diet caused increased fat depot weight. Between the two genotypes, the gonadal weight was significantly increased within the $Timp3^{-/-}$ HF group, compared to C57Bl6J HF, at 15 and 17 weeks of age (**Figure 3.4**, p < 0.01).

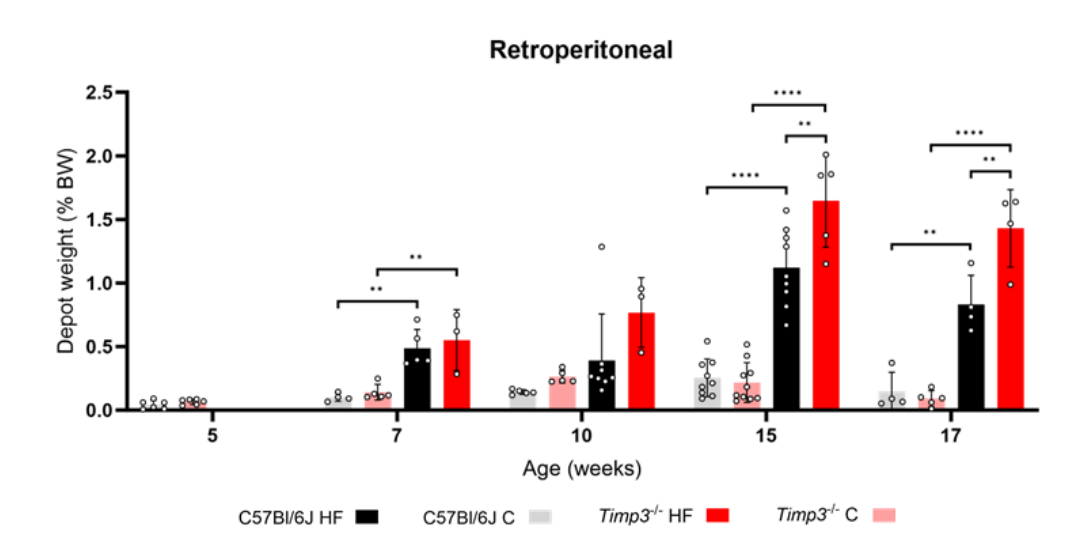


Figure 3.4 Retroperitoneal adipose depot weight of $Timp3^{-/-}$ mice, across 5-17 weeks of age, on chow (C) and high-fat (HF) diet. Mean weight expressed as a percentage of total body weight \pm SEM in male $Timp3^{-/-}$ mice on chow and high-fat diet, and C57BI/6J controls. n=3-10 biological samples per group. Tukey's Comparisons was used to test for differences. * = p < 0.05, ** = p < 0.01, *** = p < 0.001, **** = p < 0.0001.

The same pattern was seen when examining the inguinal fat depot (**Figure 3.5**). High-fat diet significantly increased the inguinal fat weight in both $Timp3^{-/-}$ (ages 7, 10, 15 and 17 weeks; p < 0.001 and p < 0.0001, respectively) and C57Bl6J groups (ages 7, 15 and 17; p < 0.01 and p < 0.0001, respectively). Between the two genotypes, increased depot weight was seen in $Timp3^{-/-}$ compared to C57Bl6J at 10 weeks of age only (p < 0.01).

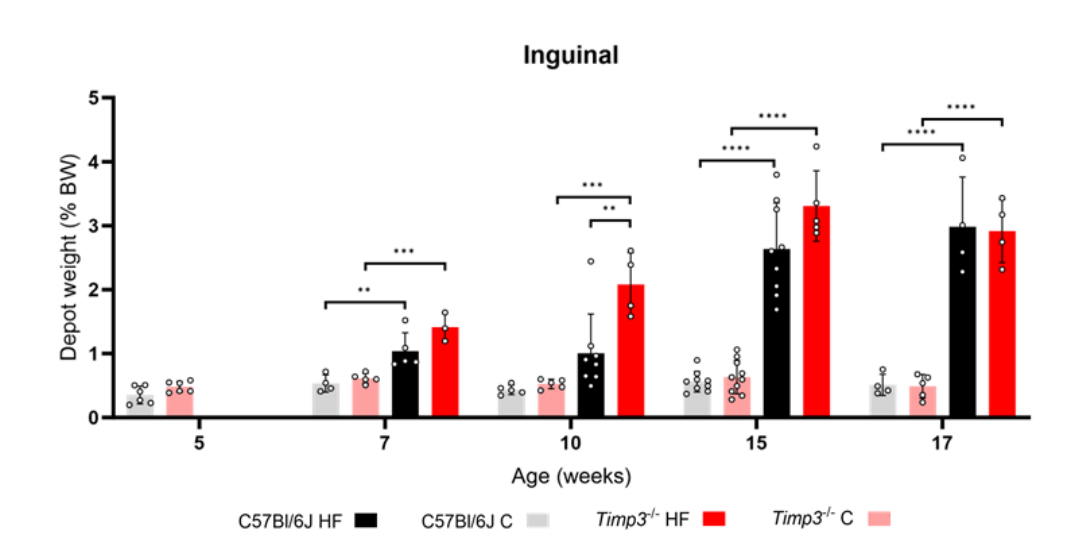


Figure 3.5 Inguinal adipose depot weight of $Timp3^{-/-}$ mice, across 5-17 weeks of age, on chow (C) and high-fat (HF) diet. Mean weight expressed as a percentage of total body weight \pm SEM in male $Timp3^{-/-}$ mice on chow and high-fat diet, and C57Bl/6J controls. n=3-10 biological samples per group. Tukey's Comparisons was used to test for differences. * = p < 0.05, ** = p < 0.01, *** = p < 0.001, **** = p < 0.0001.

Chapter 3

Compared to the white adipose depots, more subtle changes were seen within the brown adipose tissue sampled, iBAT. Significant increases in iBAT weight upon addition of high-fat diet were seen in the later ages of 15 and 17 weeks only, in both genotypes (**Figure 3.6**, p < 0.05 and p < 0.01 within the C57Bl6J, respectively; p < 0.05 and p < 0.0001 within the $Timp3^{-/-}$, respectively). Only at 15 weeks of age was the $Tiimp3^{-/-}$ HF iBAT weight significantly heavier than the C57Bl6J HF (p < 0.05 *).

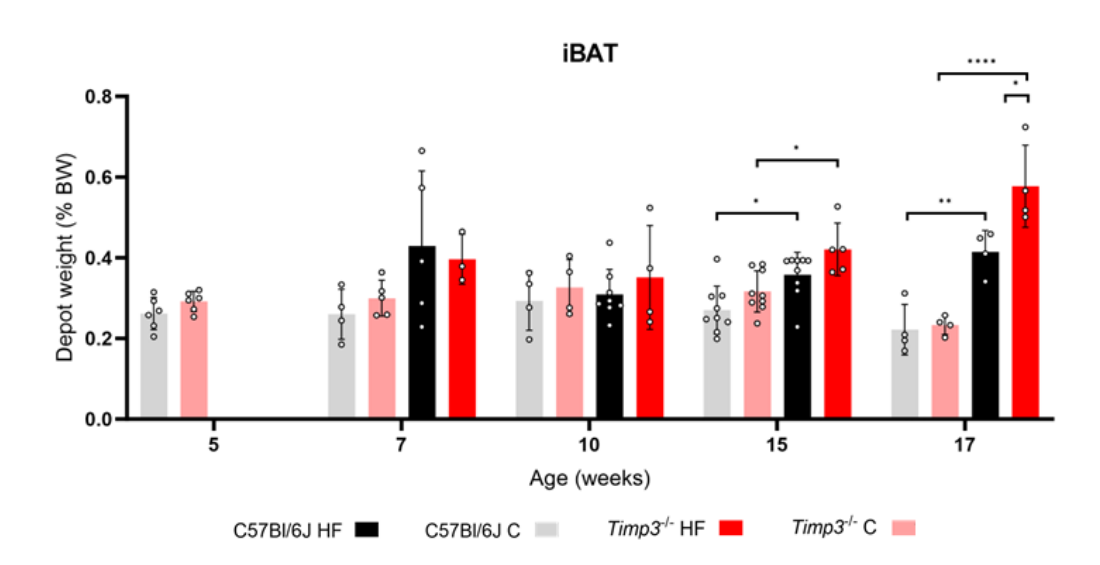


Figure 3.6 Interscapular brown adipose tissue (iBAT) depot weight of $Timp3^{-/-}$ mice, across 5-17 weeks of age, on chow (C) and high-fat (HF) diet. Mean weight expressed as a percentage of total body weight \pm SEM in male $Timp3^{-/-}$ mice on chow and high-fat diet, and C57BI/6J controls. n=3-10 biological samples per group. Tukey's Comparisons was used to test for differences. * = p < 0.05, ** = p < 0.01, **** = p < 0.001.

The total sum of white adipose depot weights measured in this study is shown in **Figure 3.7**. At each age, *Timp3*^{-/-} HF total depot weight is significantly heavier than that in the *Timp3*^{-/-} chow group. The same is true for C57BI/6J HF, compared to the chow-fed controls, at ages 7, 15 and 17. No significant differences were seen between the genotypes.

Total White Adipose Depot

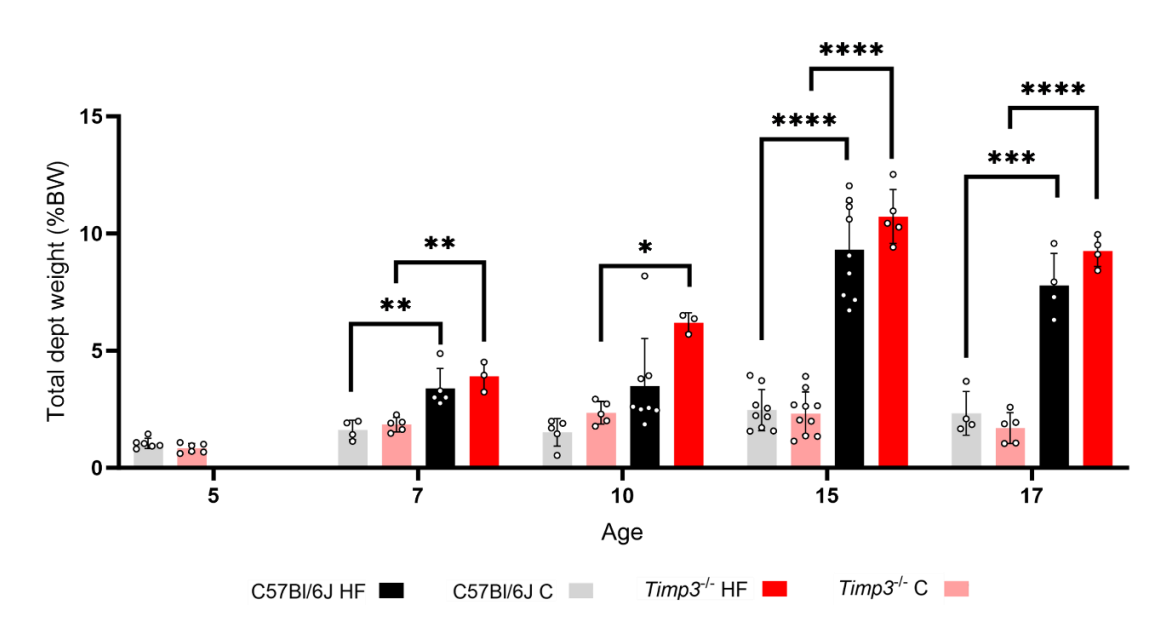
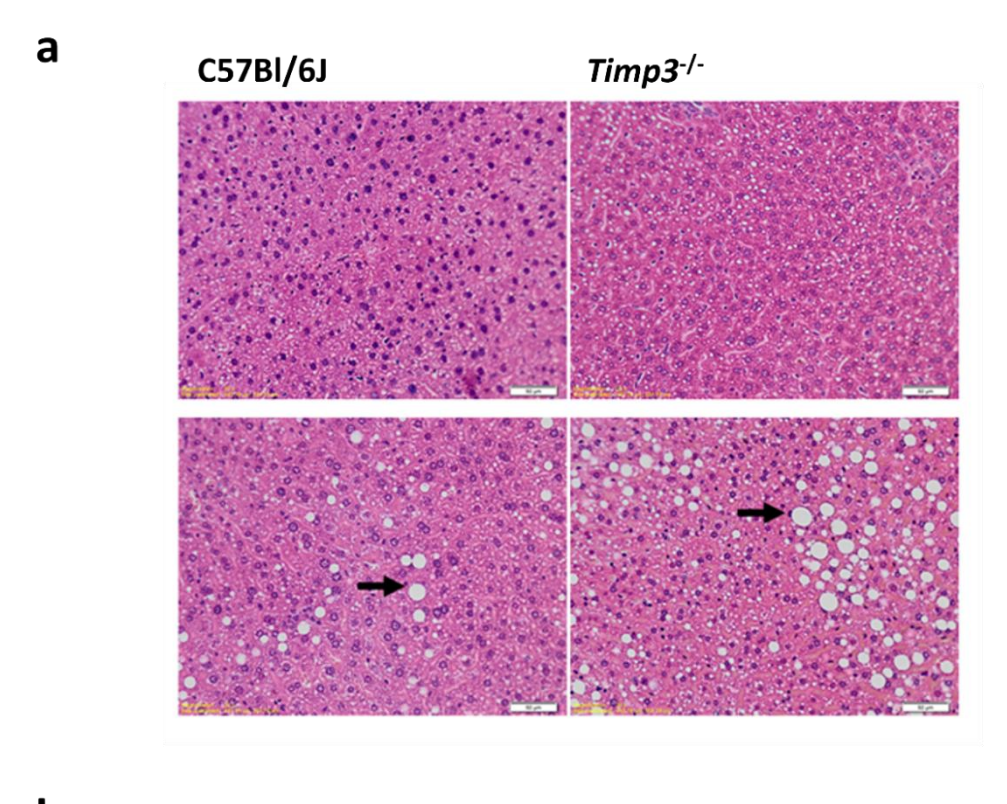


Figure 3.7 Sum total of white adipose depot weight in $Timp3^{-/-}$ mice, across 5-17 weeks of age, on chow (C) and high-fat (HF) diet. Mean weight expressed as a percentage of total body weight \pm SEM in male $Timp3^{-/-}$ mice on chow and high-fat diet, and C57BI/6J controls. n=3-10 biological samples per group. Tukey's Comparisons was used to test for differences. * = p < 0.05, ** = p < 0.01, *** = p < 0.001, *** = p < 0.0001 ****.

3.4.1.3 Lipid Accumulation within the *Timp3* Knockout Mouse During Obesity

Metabolic syndrome is known to increase the risk of hepatic steatosis due to excessive consumption of high-fat foods and dysregulation of lipid storage and metabolism. To examine the effect of HF diet within the *Timp3*^{-/-} mouse, presence of macrovesicular lipids was quantified using the Kleiner scoring system at 15 and 17 weeks old, following 10 and 12 weeks of HF diet, respectively. Macrovesicular steatosis is defined as lipid droplets within the hepatocyte that are so large, they displace the cell nucleus.

Outcome of Kleiner scoring and example liver sections are shown in **Figure 3.8**. Black arrows highlight selected macrovesicles (**Figure 3.8a**). Both genotype groups on chow diet showed little or no presence of lipid accumulation within the liver, and scores were not significantly different from each other. The $Timp3^{-/-}$ HF group had significantly increased lipid accumulation compared to the chow-fed control group at both 15 and 17 weeks old (p < 0.01 and 0.001, respectively). Statistically significant increased score in the C57Bl/6J HF group, compared to chow, was only seen at 15 weeks, however (p < 0.05).



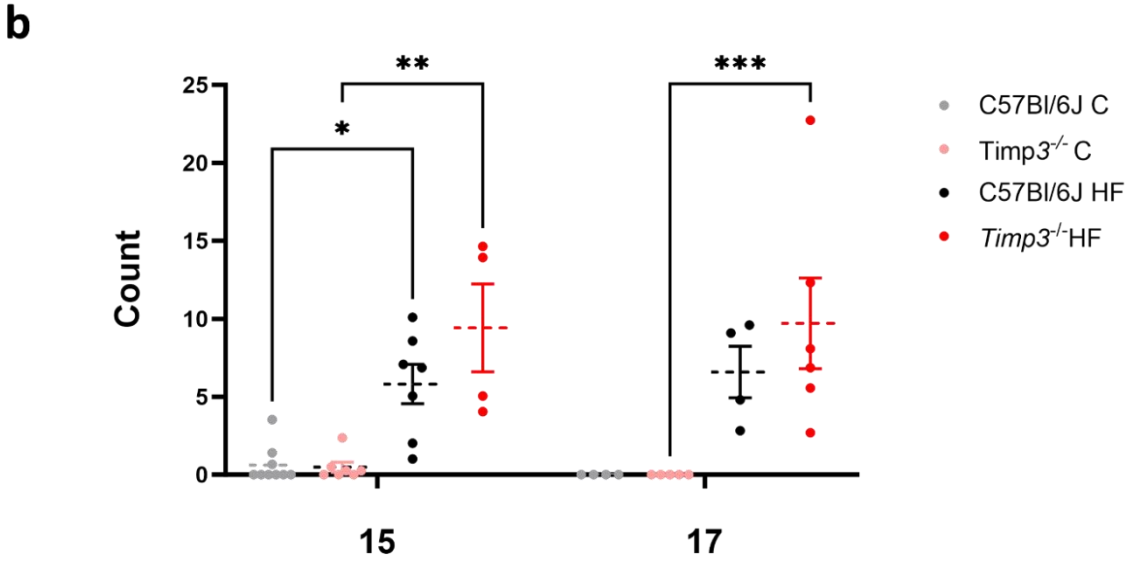


Figure 3.8 Macrovesicular lipid droplet accumulation in *Timp3*-/- mouse liver samples, at 15 and 17 weeks of age, following 10 and 12 weeks on high-fat diet respectively. a)

Haematoxylin and eosin-stained liver sections from 15-week-old $Timp3^{-/-}$ mice under C and HF diets, and the C57Bl/6 controls taken at 20x magnification. Scale bar indicated 50µm. Black arrows indicate macrovesicles. b) Mean values and SEM for macrovesicular lipid droplet counts in 15 and 17-week-old $Timp3^{-/-}$ liver sections under chow (C) and high-fat (HF) diets, and the C57Bl/6J controls. n=4-7 biological samples per group. Tukey's comparisons was used to test differences. ** = p < 0.01.

3.4.2 Effects of DIO on the Energy Expenditure of the *Timp3*^{-/-} Mouse

3.4.2.1 Energy Expenditure

Energy expenditure of *Timp3*-/- mice was measured at three ages of 5, 10 and 15 weeks old, following 0, 5 and 10 weeks feeding of high-fat diet, respectively (**Figure 3.9**). Area under the curve (AUC) of the energy expenditures are shown in **Figure 3.10**. At 5 weeks old, the chow fed *Timp3*-/- group have a significantly lower energy expenditure compared to their C57Bl6J counterparts. Additionally, there is also less variation within this group and changes between the light and dark periods is less apparent (dark period indicated by shaded area). At 10 weeks old, following 5 weeks on a high-fat diet, the C57Bl6J HF group have significantly increased energy expenditure compared to their chow-fed and *Timp3*-/- counterparts. The *Timp3*-/- HF group, however, have a significantly decreased energy expenditure compared to their chow-fed control group. At 15 weeks old, there is much less variation between the groups and only the *Timp3*-/- have significantly higher energy expenditure compared to the C57Bl6J and chow-fed control groups. Change between the light and dark periods is also more apparent in this group.

5 Week EE longitudinal а EE (cal/min) Time 10 Week EE longitudinal b C57BI/6J HF EE (cal/min) C57BI/6J C Timp3^{-/-} HF Timp3^{-/-} C 15 Week EE longitudinal C EE (cal/min)

Figure 3.9 Energy expenditure of *Timp3*-/- mice, across a 24hr period at three ages, on chow (C) and high-fat (HF) diet. Mean energy expenditure expressed as calories per minute ±SEM in male *Timp3*-/- mice on chow and high-fat diet, and C57Bl/6J controls, at 5 weeks (5a), 10 weeks (5b) and 15 weeks (5c) of age. n=4-10 biological samples per group. Shaded area indicates the dark period within the animal house (from 7pm to 7am).

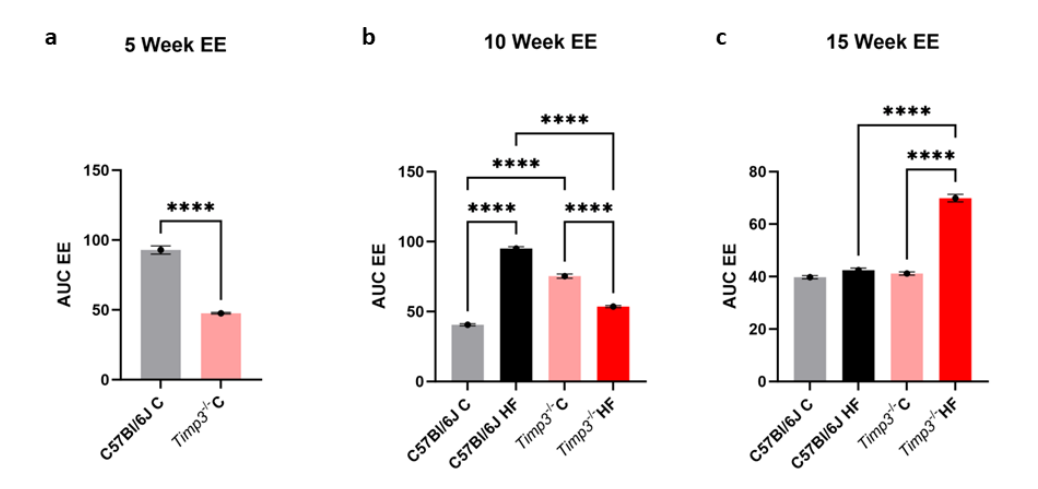
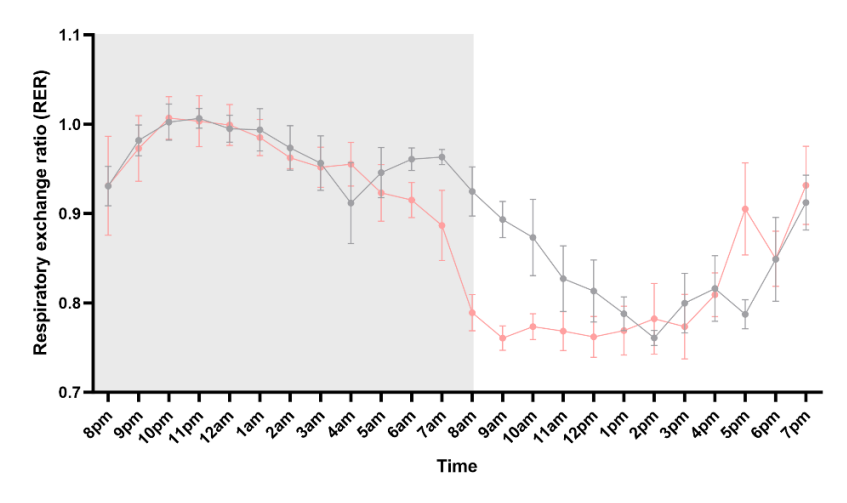


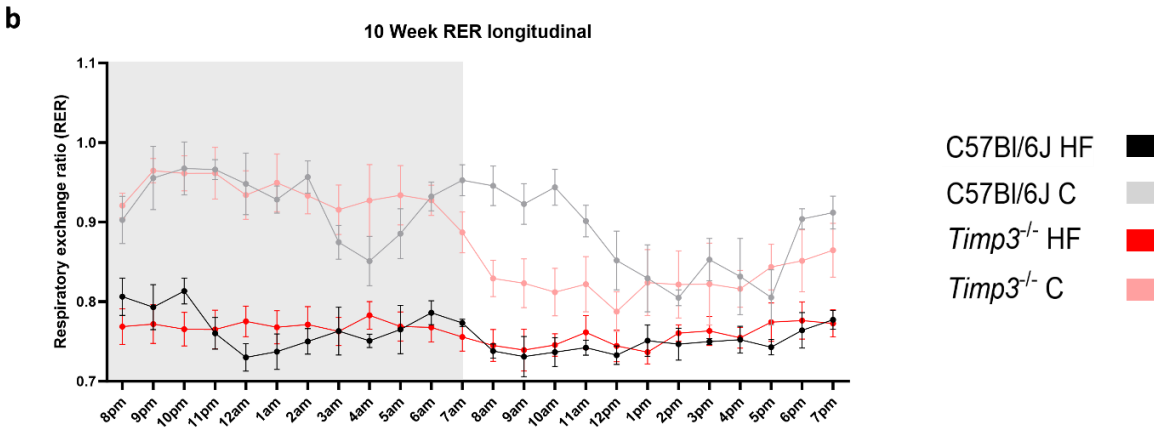
Figure 3.10 Area under the curve of $Timp3^{-/-}$ energy expenditure. Bar chart shows area under the curve of energy expenditure in male $Timp3^{-/-}$ mice on chow and high-fat diet, and C57BI/6J controls. Tukey's comparisons was used to test for differences. **** = p < 0.0001.

3.4.2.2 Respiratory Exchange Ratio

The ratio of oxygen consumption to carbon dioxide production can be expressed at the respiratory exchange ratio (RER) where a ratio of 0.7 indicates that fats are the main substrate for metabolism and 1.0 indicates carbohydrates as the main substrate. At the baseline of 5 weeks old, the *Timp3*-/- chow group overall have a slightly significant favour towards fats for energy metabolism compared to the controls, and both groups show a favour towards carbohydrate metabolism during the dark period when the mice are most active. At the later ages of 10 and 15 weeks old, both HF groups use fats predominantly as a fuel source. This is significantly different to their chow-fed controls who have a preference for carbohydrates, which is expected due to the distinctly different food sources. At these ages, the *Timp3*-/- chow-fed group is seen to maintain the initial discrepancy between light and dark periods where dark periods utilise carbohydrate as the primary fuel source. However, the other three groups do not have such a clear trend, particularly as the HF groups lean more toward fat metabolism during both light and dark.







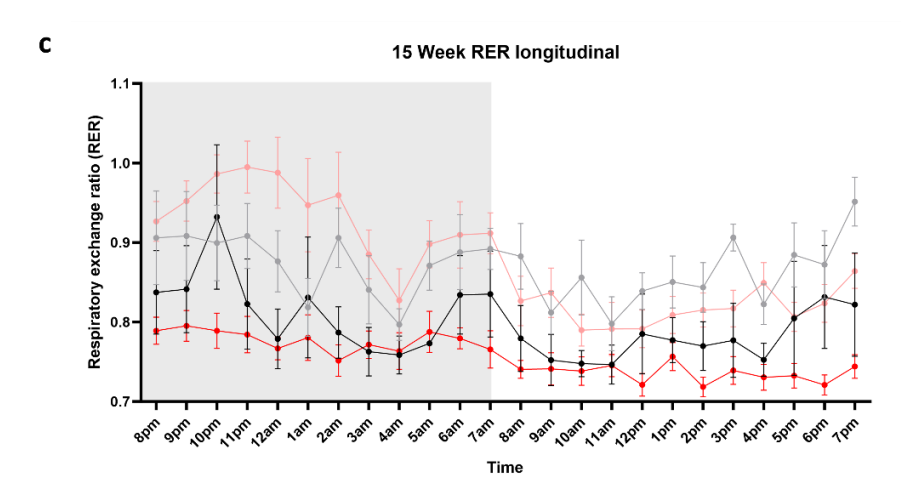


Figure 3.11 Respiratory exchange ratio of *Timp3*-/- mice, across a 24hr period at three ages, on chow (C) and high-fat (HF) diet. Mean respiratory exchange ratio ±SEM in male *Timp3*-/- mice on chow and high-fat diet, and C57BI/6J controls, at 5 weeks (a), 10 weeks (b) and 15 weeks (c) of age. n=4-10 biological samples per group. Shaded area indicates the dark period within the animal house (from 7pm to 7am).

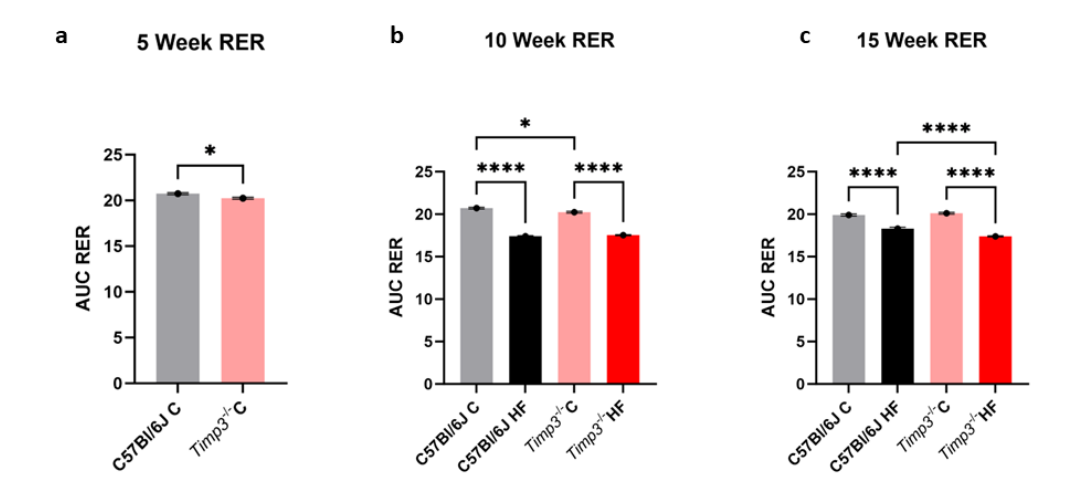


Figure 3.12 Area under the curve of respiratory exchange ratio of $Timp3^{-/-}$ mice. Bar chart shows area under the curve of the respiratory exchange ratio in male $Timp3^{-/-}$ mice on chow and high-fat diet, and C57Bl/6J controls. Tukey's comparisons was used to test for differences. * = p < 0.05, **** = p < 0.001.

3.4.2.3 Matrix Metalloproteinases

Components of the extracellular matrix (ECM) are regulated by matrix metalloproteinases (MMPs) and TIMP3 is an inhibitor of many of these enzymes. To examine the effect of TIMP3 absence on the regulation of the ECM, gene expression of selected MMPs were measured in the HF *Timp3*^{-/-} liver and controls.

MMP8

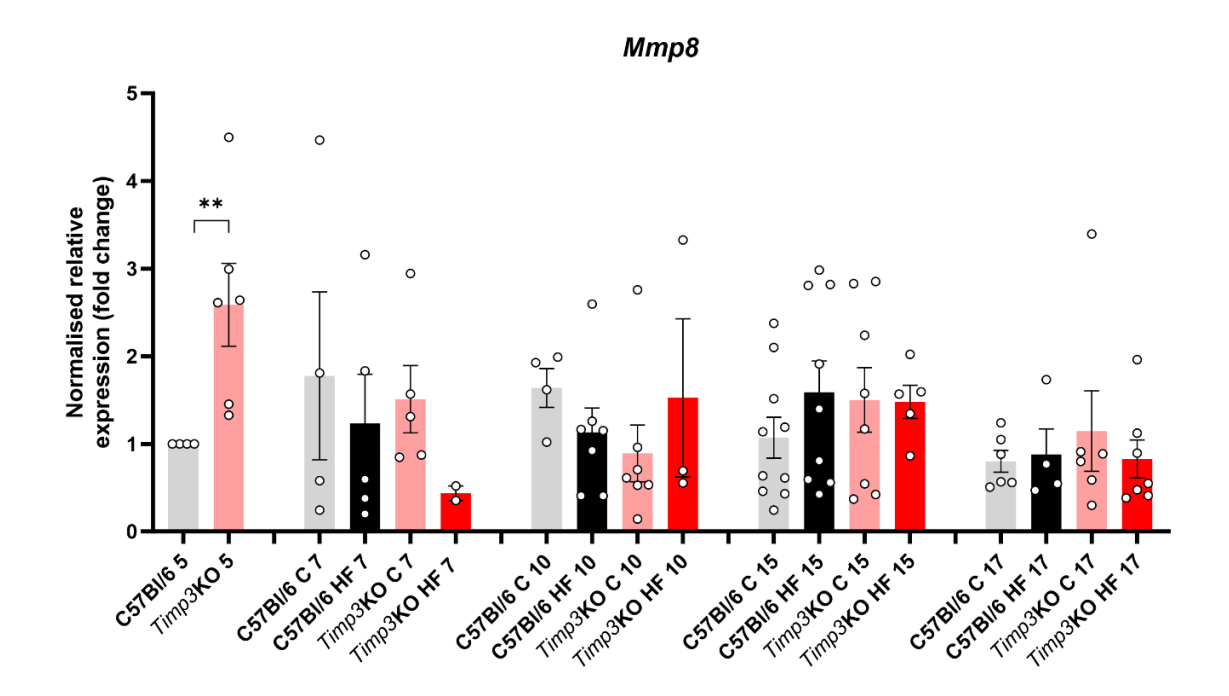


Figure 3.13 Mmp8 gene expression in liver tissue of $Timp3^{-/-}$ mice, across 5-17 weeks of age, on chow (C) and high-fat (HF) diet. Mean fold change \pm SEM (normalised to 5-week-old, chow-fed, C57Bl/6J control samples) from RT-qPCR gene expression in male $Timp3^{-/-}$ liver samples on chow and high-fat diet, and C57Bl/6J controls. n=3-10 biological samples per group. Tukey's comparisons was used to test for differences. Statistical analysis was conducted using ddct values, normalised to θ -actin and Gapdh internal control genes. ** = p < 0.01.

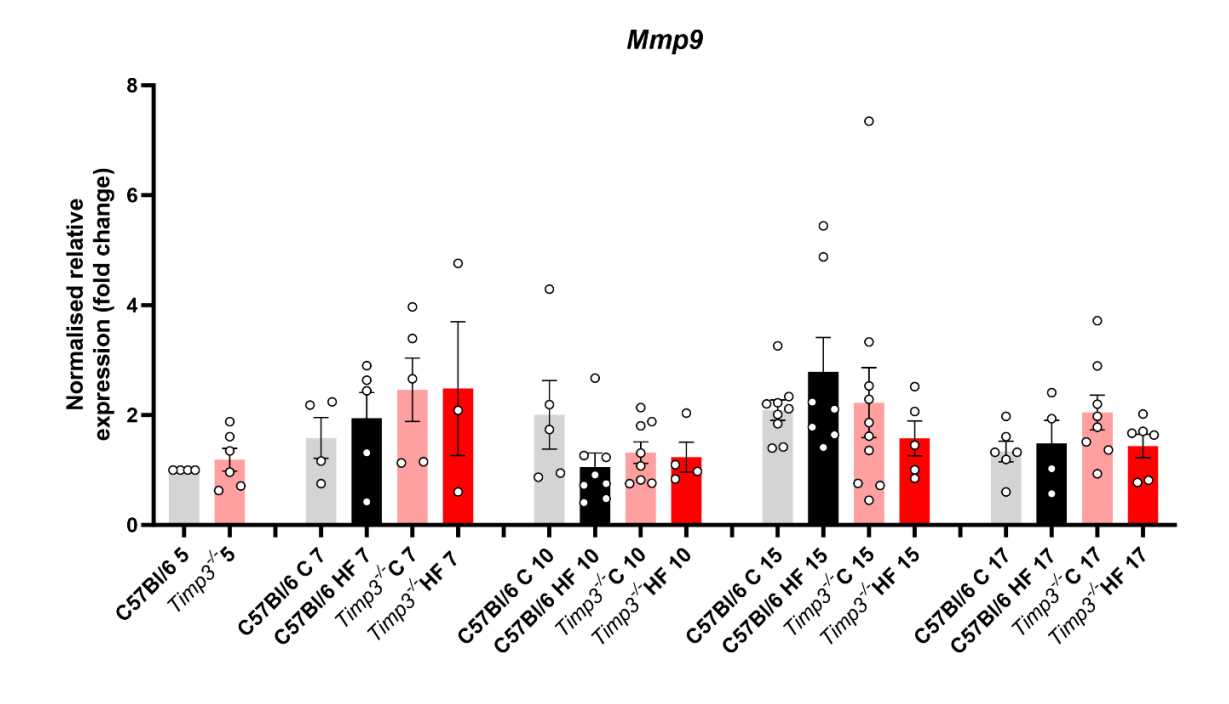


Figure 3.14 Mmp9 gene expression in liver tissue of $Timp3^{-/-}$ mice, across 5-17 weeks of age, on chow (C) and high-fat (HF) diet. Mean fold change \pm SEM (normalised to 5-week-old, chow-fed, C57Bl/6J control samples) from RT-qPCR gene expression in male $Timp3^{-/-}$ liver samples on chow and high-fat diet, and C57Bl/6J controls. n=3-10 biological samples per group. Tukey's comparisons was used to test for differences. Statistical analysis was conducted using ddct values, normalised to θ -actin and Gapdh internal control genes. * = p < 0.05, *** = p < 0.001.

Macrophage metalloelastase, Mmp12, expression was increased in the HF diet groups compared to their chow controls at ages 15 and 17 weeks (**Figure 3.19**). These changes were significant at 17 weeks (p < 0.001 and p < 0.05 for C57Bl/6J and $Timp3^{-/-}$, respectively). At the 5-week-old baseline, Mmp12 expression in the $Timp3^{-/-}$ groups was increased compared to controls (p < 0.05).

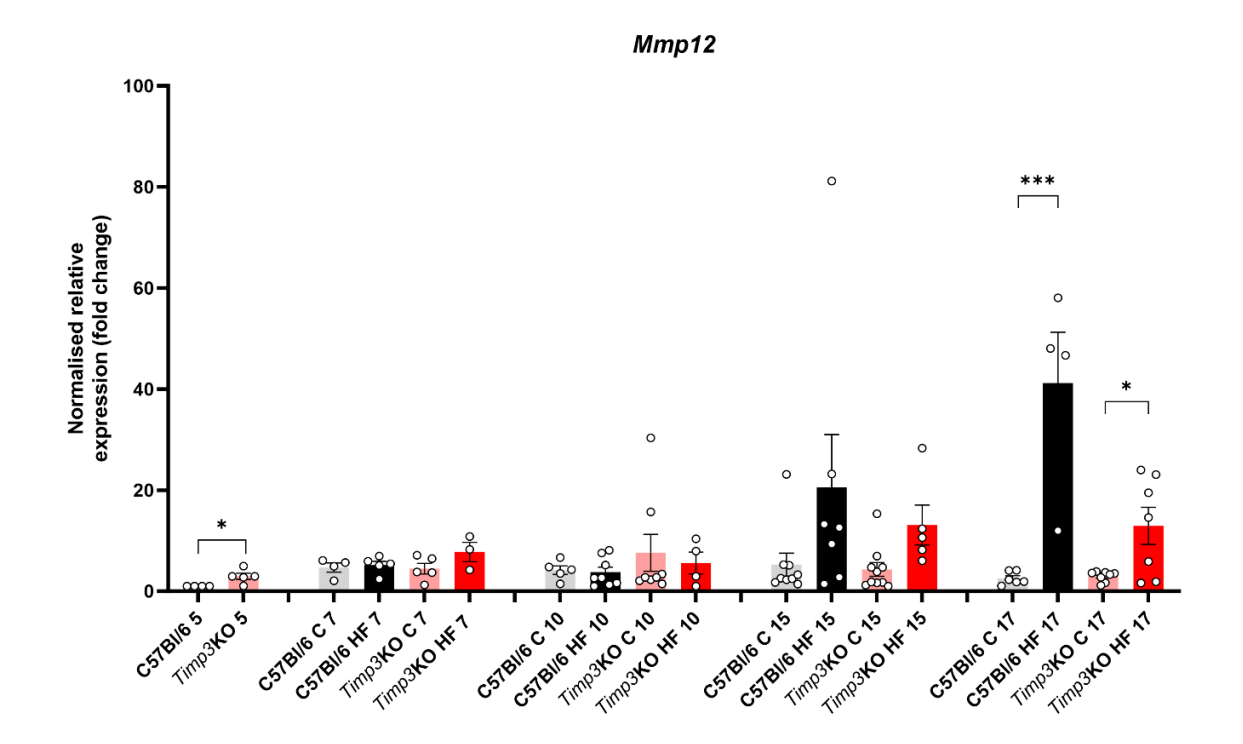


Figure 3.15 Mmp12 gene expression in liver tissue of $Timp3^{-/-}$ mice, across 5-17 weeks of age, on chow (C) and high-fat (HF) diet. Mean fold change \pm SEM (normalised to 5-week-old, chow-fed, C57Bl/6J control samples) from RT-qPCR gene expression in male $Timp3^{-/-}$ liver samples on chow and high-fat diet, and C57Bl/6J controls. n=3-10 biological samples per group. Tukey's comparisons was used to test for differences. Statistical analysis was conducted using ddct values, normalised to θ -actin and Gapdh internal control genes. * = p < 0.05, *** = p < 0.001.

Expression of *Mmp13* was significantly increased in the C57Bl/6J HF group compared to the chow group at ages 15 and 17 weeks (**Figure 3.20**, p < 0.01). This pattern was not matched with the *Timp3*-/- groups. Expression was also elevated in *Timp3*-/- at 5 weeks, though this trend was not seen at older ages (p < 0.01).

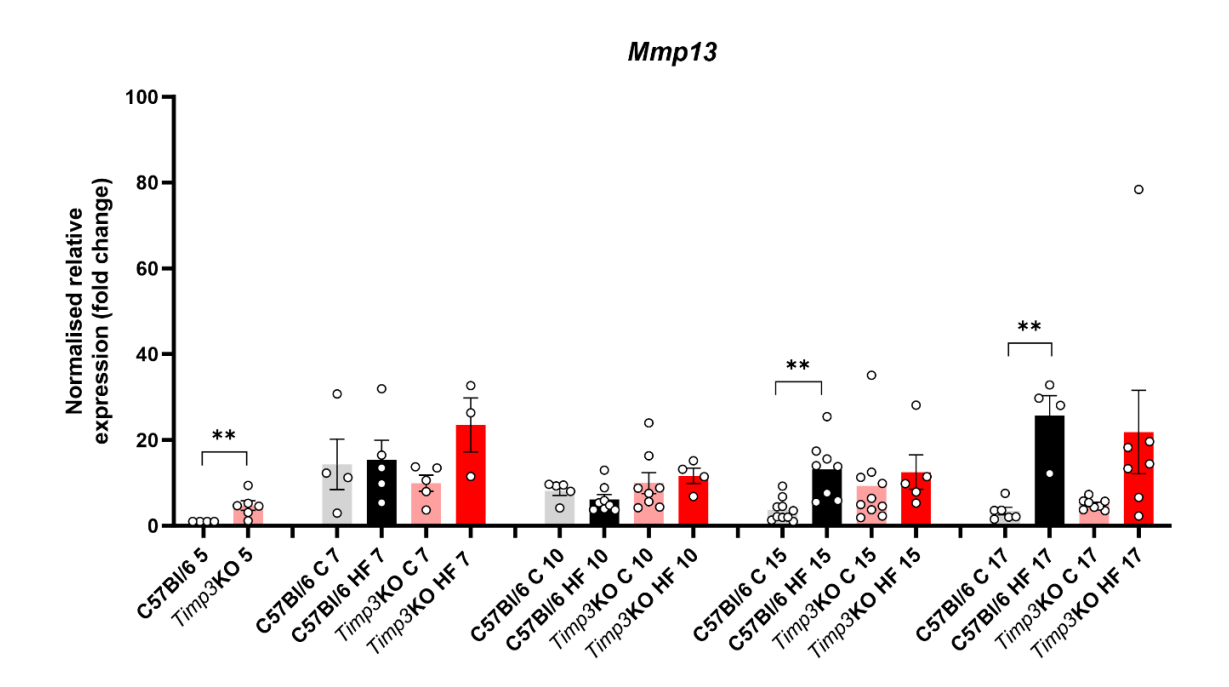


Figure 3.16 Mmp13 gene expression in liver tissue of $Timp3^{-/-}$ mice, across 5-17 weeks of age, on chow (C) and high-fat (HF) diet. Mean fold change \pm SEM (normalised to 5-week-old, chow-fed, C57Bl/6J control samples) from RT-qPCR gene expression in male $Timp3^{-/-}$ liver samples on chow and high-fat diet, and C57Bl/6J controls. n=3-10 biological samples per group. Tukey's comparisons was used to test for differences. Statistical analysis was conducted using ddct values, normalised to θ -actin and Gapdh internal control genes. ** = p < 0.01.

At 5 weeks, $Timp3^{-/-}$ mice also showed increased expression of Mmp14 (**Figure 3.21**, p < 0.05). Both HF groups showed decreased expression at 17 weeks, compared to their chow controls (p <0.05). This trend was seen at the younger ages but not significant.

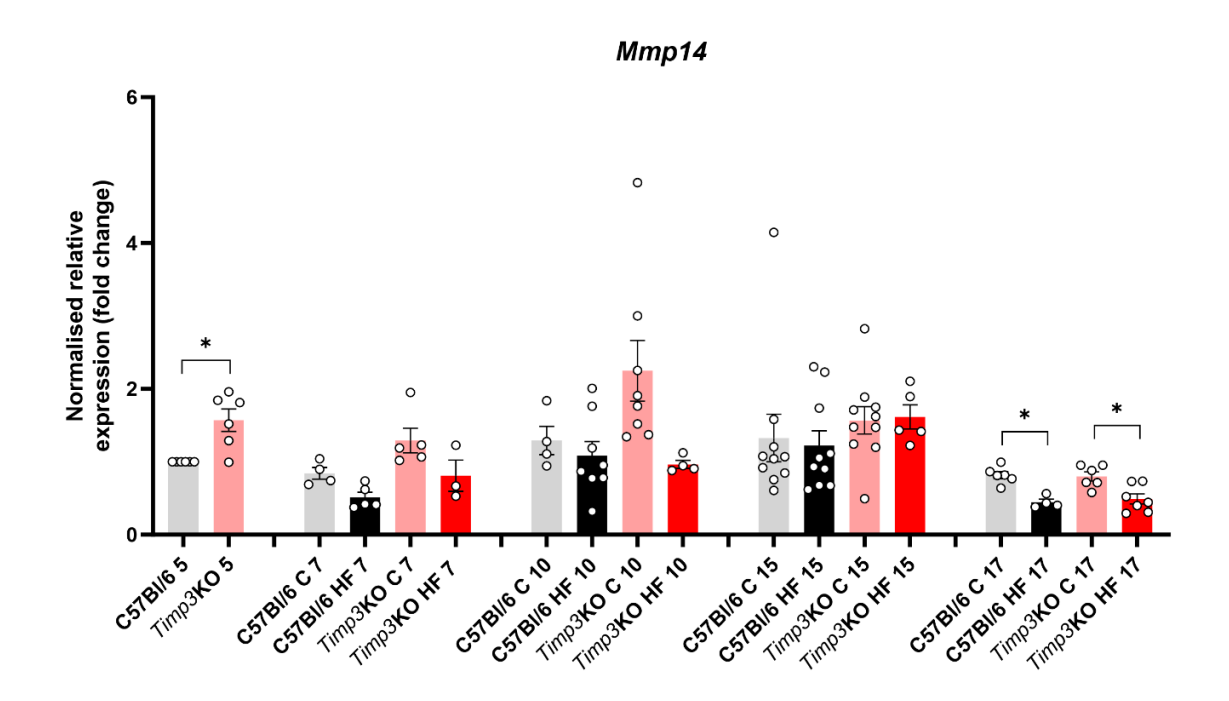


Figure 3.17 Mmp14 gene expression in liver tissue of $Timp3^{-/-}$ mice, across 5-17 weeks of age, on chow (C) and high-fat (HF) diet. Mean fold change \pm SEM (normalised to 5-week-old, chow-fed, C57Bl/6J control samples) from RT-qPCR gene expression in male $Timp3^{-/-}$ liver samples on chow and high-fat diet, and C57Bl/6J controls. n=3-10 biological samples per group. Tukey's comparisons was used to test for differences. Statistical analysis was conducted using ddct values, normalised to θ -actin and Gapdh internal control genes. * = p < 0.05.

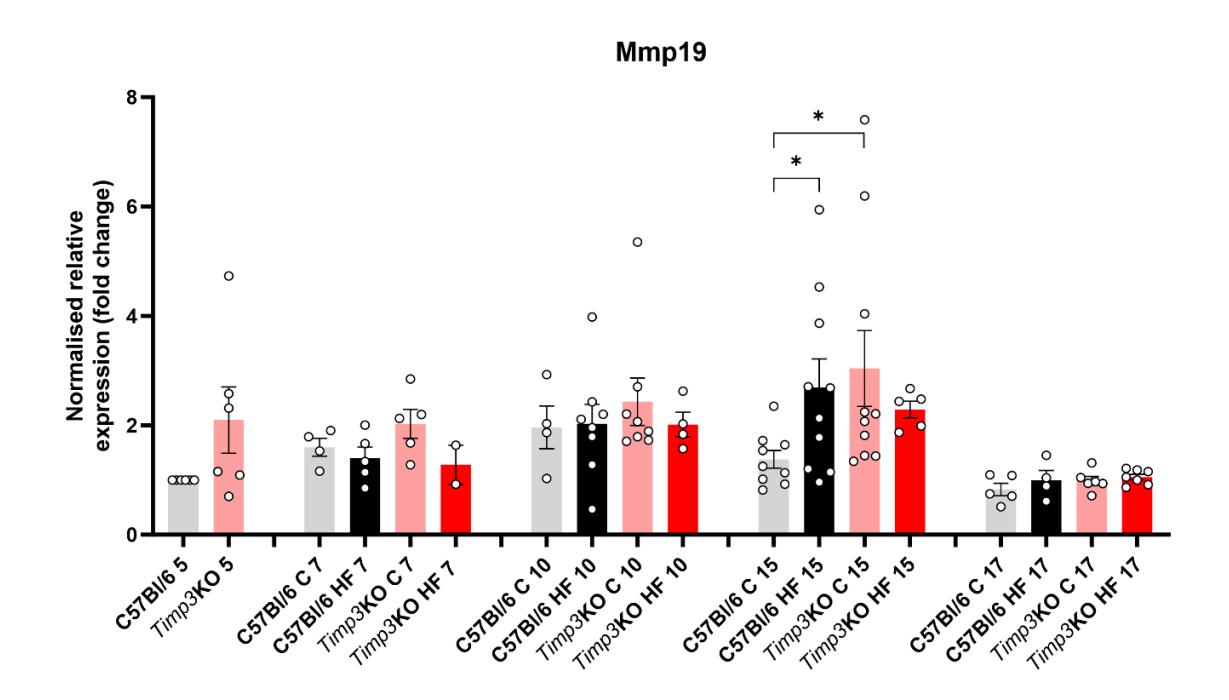


Figure 3.18 Mmp19 gene expression in liver tissue of $Timp3^{-/-}$ mice, across 5-17 weeks of age, on chow (C) and high-fat (HF) diet. Mean fold change \pm SEM (normalised to 5-week-old, chow-fed, C57Bl/6J control samples) from RT-qPCR gene expression in male $Timp3^{-/-}$ liver samples on chow and high-fat diet, and C57Bl/6J controls. n=3-10 biological samples per group. Tukey's comparisons was used to test for differences. Statistical analysis was conducted using ddct values, normalised to θ -actin and Gapdh internal control genes. * = p < 0.05.

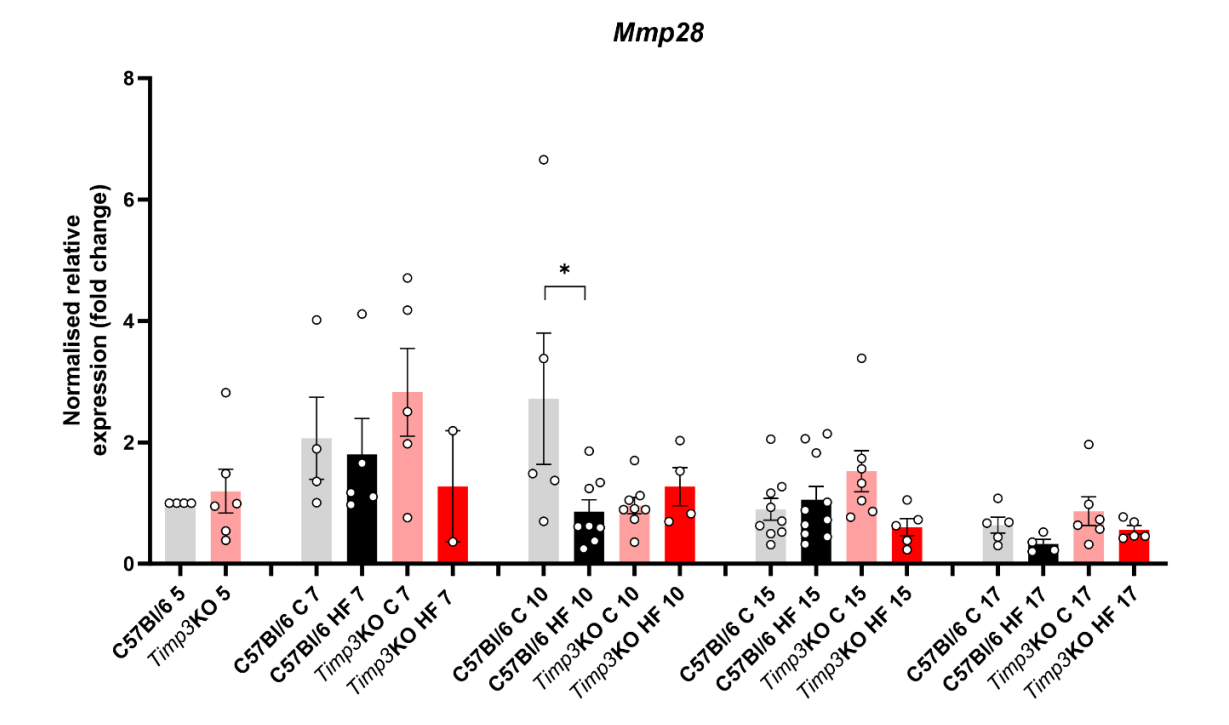


Figure 3.19 Mmp28 gene expression in liver tissue of $Timp3^{-/-}$ mice, across 5-17 weeks of age, on chow (C) and high-fat (HF) diet. Mean fold change \pm SEM (normalised to 5-week-old, chow-fed, C57Bl/6J control samples) from RT-qPCR gene expression in male $Timp3^{-/-}$ liver samples on chow and high-fat diet, and C57Bl/6J controls. n=3-10 biological samples per group. Tukey's comparisons was used to test for differences. Statistical analysis was conducted using ddct values, normalised to θ -actin and Gapdh internal control genes. * = p < 0.05.

3.4.2.4 Glucose and Lipid Metabolism

To evaluate the effect of high-fat diet and *TIMP3* absence on lipid and glucose metabolism within the liver, selected genes involved in these processes were measured (**Figure 19**).

The *Fxr* and *Cyp7a1* genes are essential in bile acid metabolism and are affected by gut microbial activities. When measured in the liver, no significant differences in *Cyp7a1* expression were seen across groups.

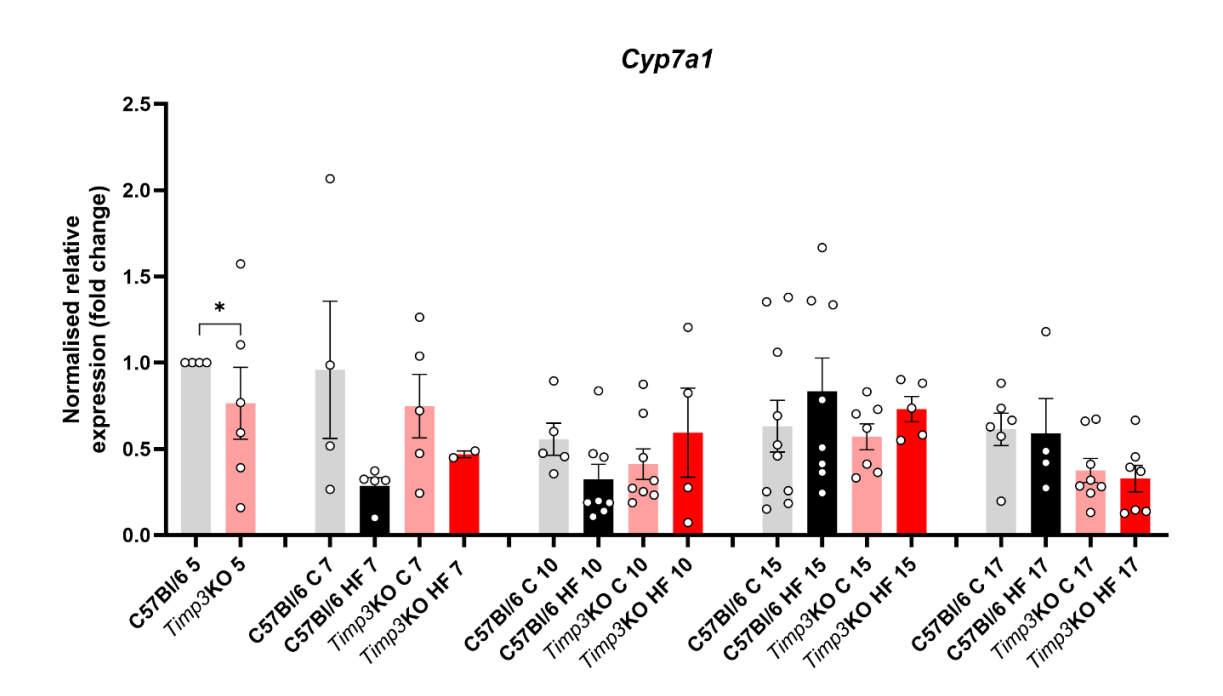


Figure 3.20 Cyp7a1 gene expression in liver tissue of $Timp3^{-/-}$ mice, across 5-17 weeks of age, on chow (C) and high-fat (HF) diet. Mean fold change \pm SEM (normalised to 5-week-old, chow-fed, C57Bl/6J control samples) from RT-qPCR gene expression in male $Timp3^{-/-}$ liver samples on chow and high-fat diet, and C57Bl/6J controls. n=3-10 biological samples per group. Tukey's comparisons was used to test for differences. Statistical analysis was conducted using ddct values, normalised to θ -actin and Gapdh internal control genes. * = p < 0.05, ** = p < 0.01, *** = p < 0.001.

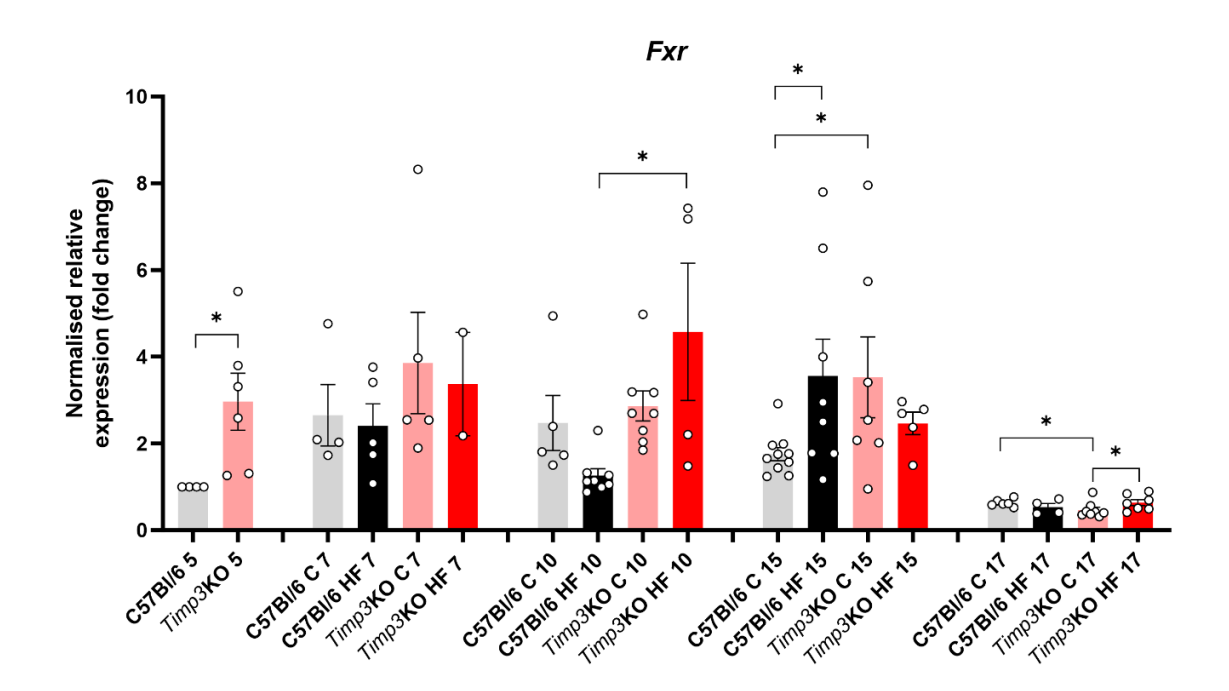


Figure 3.21 Fxr gene expression in liver tissue of $Timp3^{-/-}$ mice, across 5-17 weeks of age, on chow (C) and high-fat (HF) diet. Mean fold change \pm SEM (normalised to 5-week-old, chow-fed, C57Bl/6J control samples) from RT-qPCR gene expression in male $Timp3^{-/-}$ liver samples on chow and high-fat diet, and C57Bl/6J controls. n=3-10 biological samples per group. Tukey's comparisons was used to test for differences. Statistical analysis was conducted using ddct values, normalised to θ -actin and Gapdh internal control genes. * = p < 0.05.

Within the liver, *Glut2* is the major glucose transporter. When measured in this study, no significant differences were seen across groups (**Figure 3.26**).

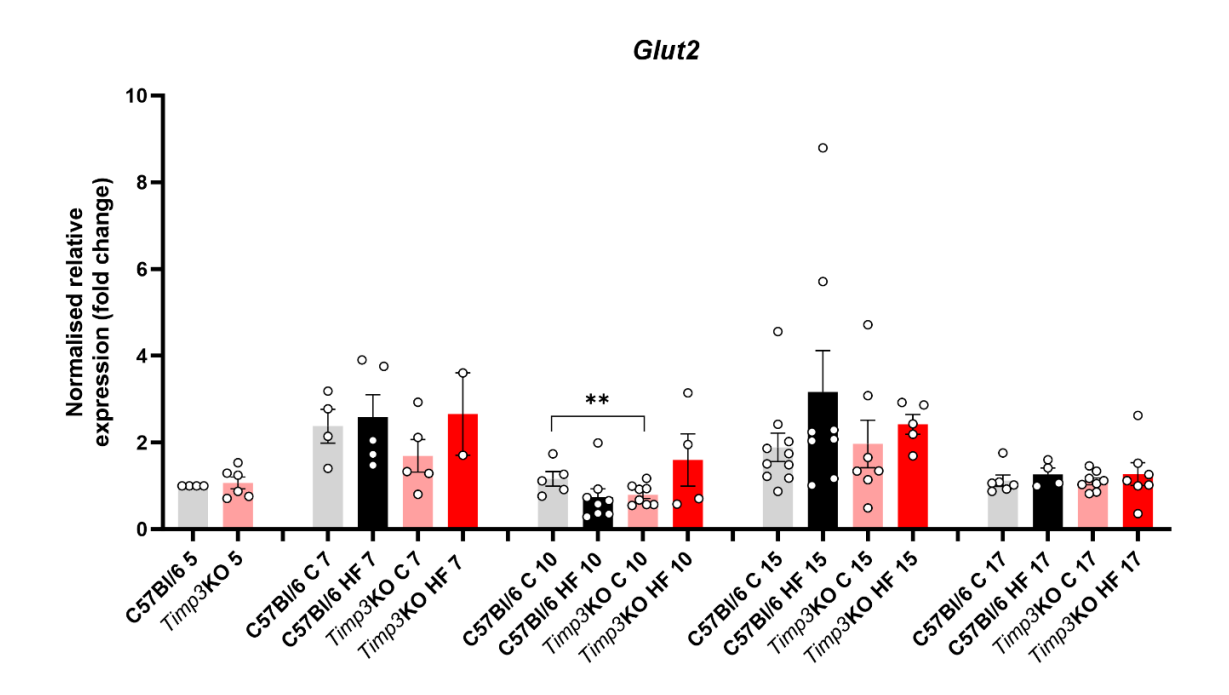


Figure 3.22 *Glut2* gene expression in liver tissue of *Timp3*^{-/-} mice, across 5-17 weeks of age, on chow (C) and high-fat (HF) diet. Mean fold change \pm SEM (normalised to 5-week-old, chow-fed, C57Bl/6J control samples) from RT-qPCR gene expression in male *Timp3*^{-/-} liver samples on chow and high-fat diet, and C57Bl/6J controls. n=3-10 biological samples per group. Tukey's comparisons was used to test for differences. Statistical analysis was conducted using ddct values, normalised to *\theta*-actin and *Gapdh* internal control genes. ** = p < 0.01.

Insulin receptor substrates 1 and 2 are integral to insulin signalling and glucose metabolism. Here, no changes were seen in *Irs1* expression across groups (Figure 22). However, *Irs2* expression was significantly decreased in the HF groups compared to their chow-fed counterparts at age 17 weeks (**Figure 23**, p < 0.01 and p < 0.001 for C57Bl6J and $Timp3^{-/-}$ respectively). This trend was also seen at younger ages, but only significant at 10 weeks of age between the C57Bl/6J groups (p < 0.01 **).

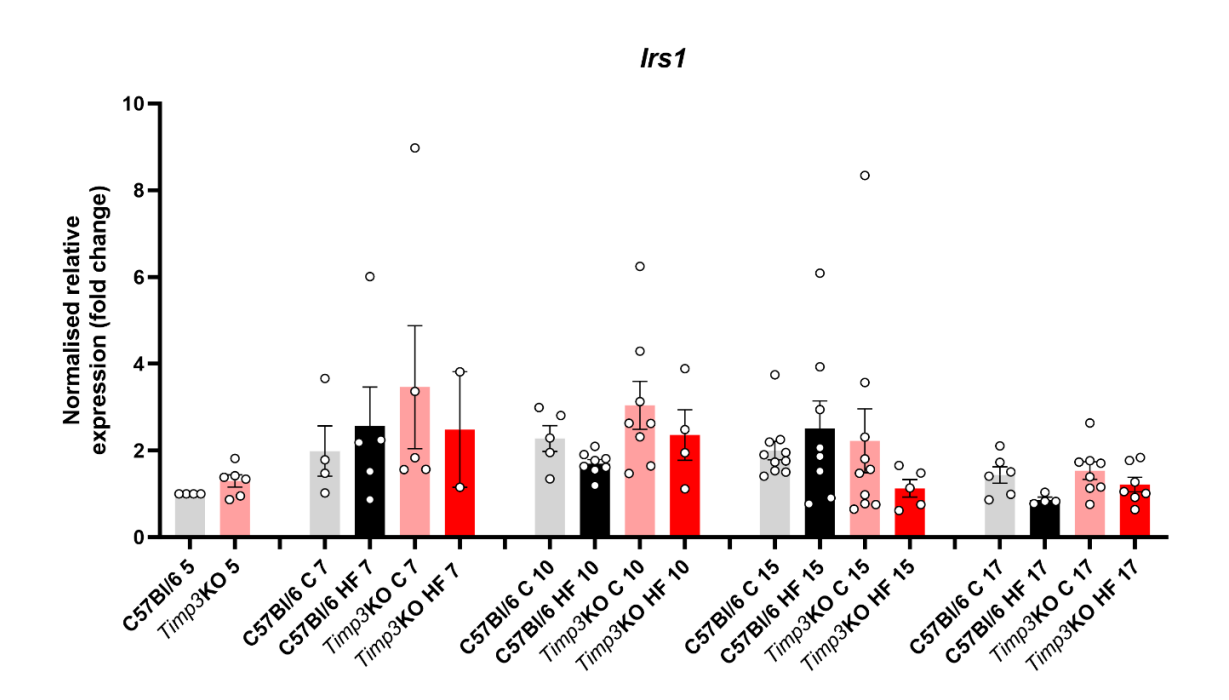


Figure 3.23 *Irs1* gene expression in liver tissue of *Timp3*-/- mice, across 5-17 weeks of age, on chow (C) and high-fat (HF) diet. Mean fold change ± SEM (normalised to 5-week-old, chow-fed, C57Bl/6J control samples) from RT-qPCR gene expression in male *Timp3*-/- liver samples on chow and high-fat diet, and C57Bl/6J controls. n=3-10 biological samples per group. Tukey's comparisons was used to test for differences. Statistical analysis was conducted using ddct values, normalised to *β-actin* and *Gapdh* internal control genes.

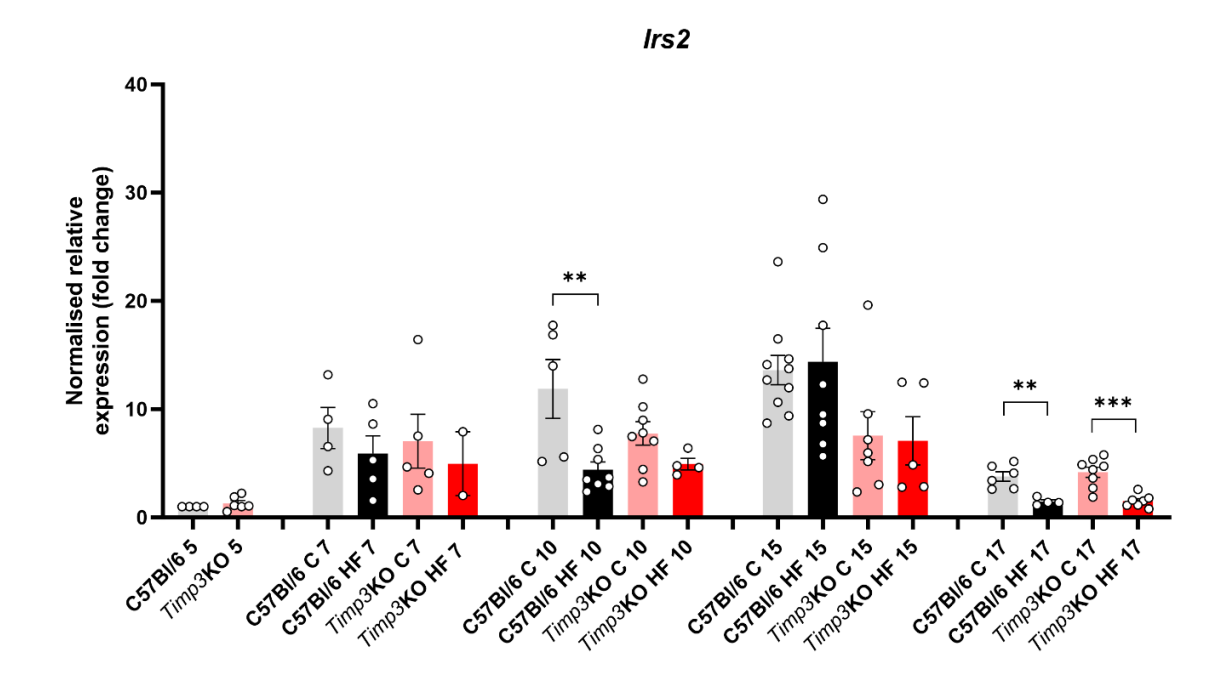


Figure 3.24 Irs2 gene expression in liver tissue of $Timp3^{-/-}$ mice, across 5-17 weeks of age, on chow (C) and high-fat (HF) diet. Mean fold change \pm SEM (normalised to 5-week-old, chow-fed, C57Bl/6J control samples) from RT-qPCR gene expression in male $Timp3^{-/-}$ liver samples on chow and high-fat diet, and C57Bl/6J controls. n=3-10 biological samples per group. Tukey's comparisons was used to test for differences. Statistical analysis was conducted using ddct values, normalised to θ -actin and Gapdh internal control genes. ** = p < 0.01, *** = p < 0.001.

The *Srebf1c* gene encodes a transcription factor which binds LDL receptors and is important for cholesterol metabolism. A trend of increased expression was seen within the HF groups compared to their chow-fed controls, but this was only significant at age 15 weeks between the C57B7/6J groups (**Figure 3.29**, p < 0.05 *). At 17 weeks, expression was also increased in the $Timp3^{-/-}$ chow group compared to C57Bl/6J chow – a trend also seen at 15 weeks (**Figure 3.29**, p < 0.05 *).

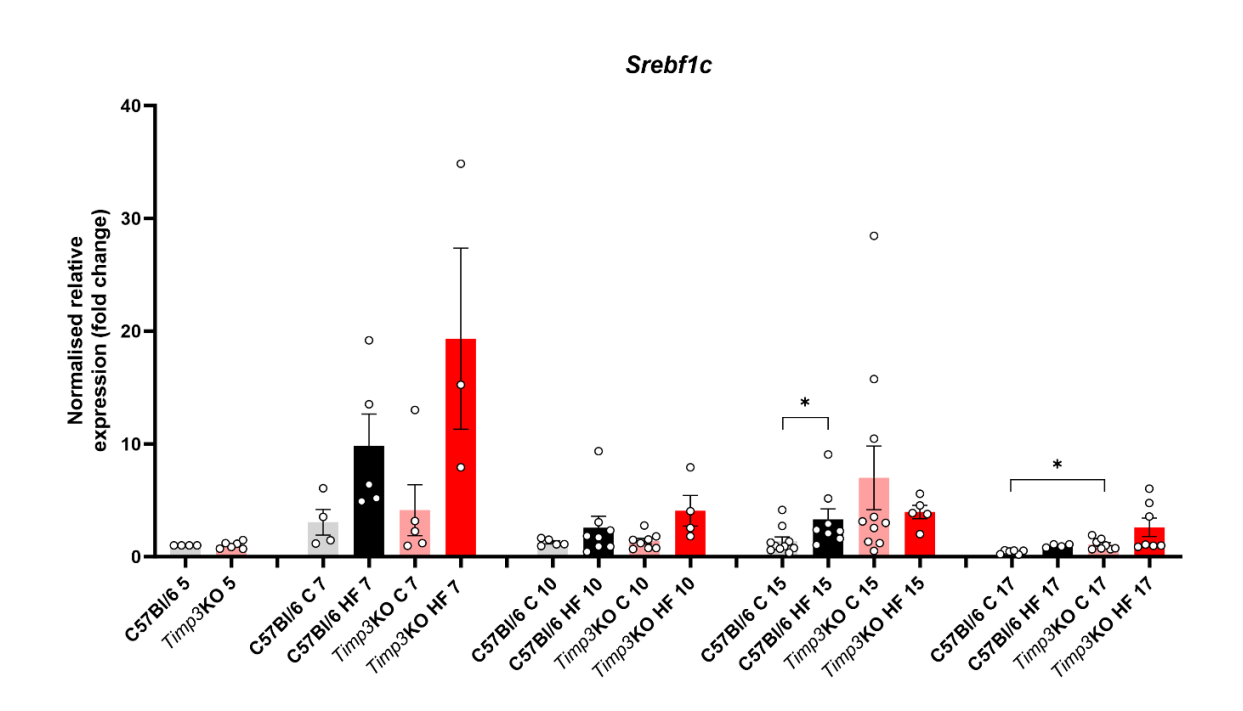


Figure 3.25 *Srebf1c* gene expression in liver tissue of *Timp3*^{-/-} mice, across 5-17 weeks of age, on chow (C) and high-fat (HF) diet. Mean fold change \pm SEM (normalised to 5-week-old, chow-fed, C57Bl/6J control samples) from RT-qPCR gene expression in male *Timp3*^{-/-} liver samples on chow and high-fat diet, and C57Bl/6J controls. n=3-10 biological samples per group. Tukey's comparisons was used to test for differences. Statistical analysis was conducted using ddct values, normalised to *\theta*-actin and *Gapdh* internal control genes. * = p < 0.05.

3.4.2.5 Adiponectin Receptor Expression is Decreased in the *Timp3*-/- Mouse

Adiponectin is a signalling molecule produced by adipose tissue which regulates insulin sensitivity. To further examine the effect of TIMP3 absence on insulin regulation, adiponectin receptor expression within the liver was measured.

Adiponectin receptor 1 expression (**Figure 3.30**) was seen to decrease in the HF groups, compared to their chow-fed controls, at ages 10 (p < 0.01, p < 0.05 for C57Bl6/J and $Timp3^{-/-}$ respectively) and 17 weeks (p < 0.001 and p < 0.0001 for C57Bl6/J and $Timp3^{-/-}$ respectively). Expression was also significantly lower in the $Timp3^{-/-}$ HF group compared to the C57Bl/6J HF group at 17 weeks (p < 0.05).

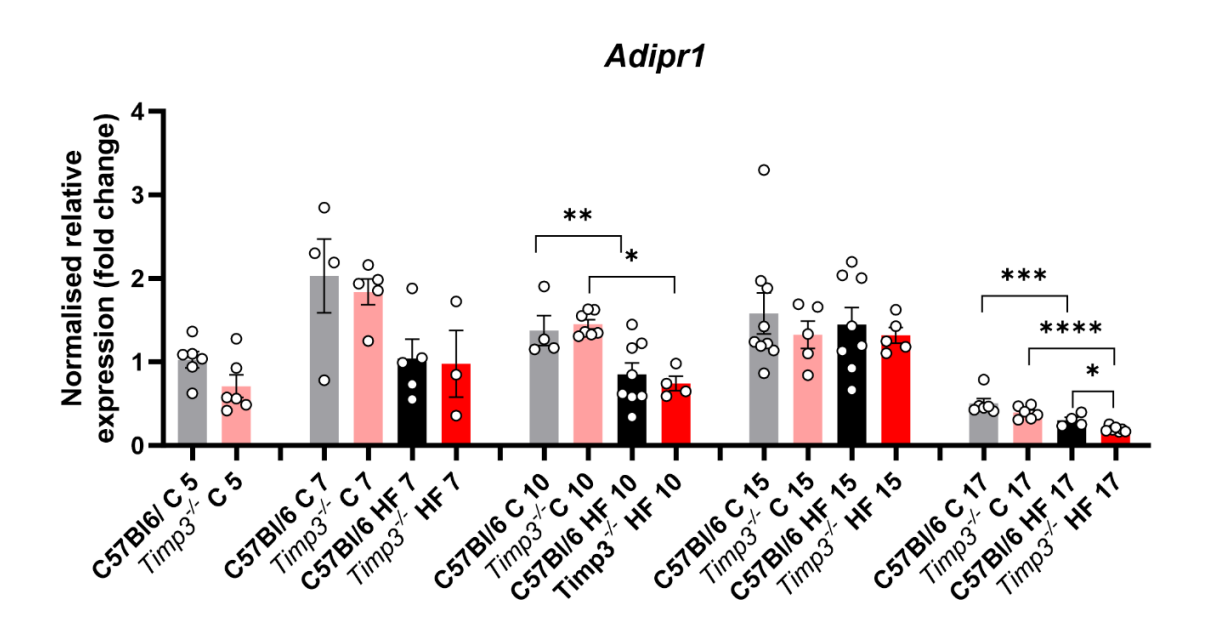


Figure 3.26 Adipr1 gene expression in liver tissue of *Timp3*^{-/-} mice, across 5-17 weeks of age, on chow (C) and high-fat (HF) diet. Mean fold change ± SEM (normalised to 5-week-old, chow-fed, C57Bl/6J control samples) from RT-qPCR gene expression in male *Timp3*^{-/-} liver samples on chow and high-fat diet, and C57Bl/6J controls. n=3-10 biological samples per group. Tukey's comparisons was used to test for differences. Statistical analysis was conducted using ddct values, normalised to *β-actin* and *Gapdh* internal control genes. * = p < 0.05, ** = p < 0.01, *** = p < 0.001, **** = p < 0.0001.

Similarly, at 10 and 17 weeks, *Adipr2* expression is decreased in the *Timp3*-/- HF group compared to the chow controls (**Figure 3.31**, p < 0.01 and p < 0.001, respectively). Between the C57Bl/6J groups, decreased expression with HF diet was only seen at 17 weeks (p < 0.05). Additionally, at 5 weeks, expression in *Timp3*-/- is also significantly decreased compared to the C57Bl/6J group (p < 0.05).

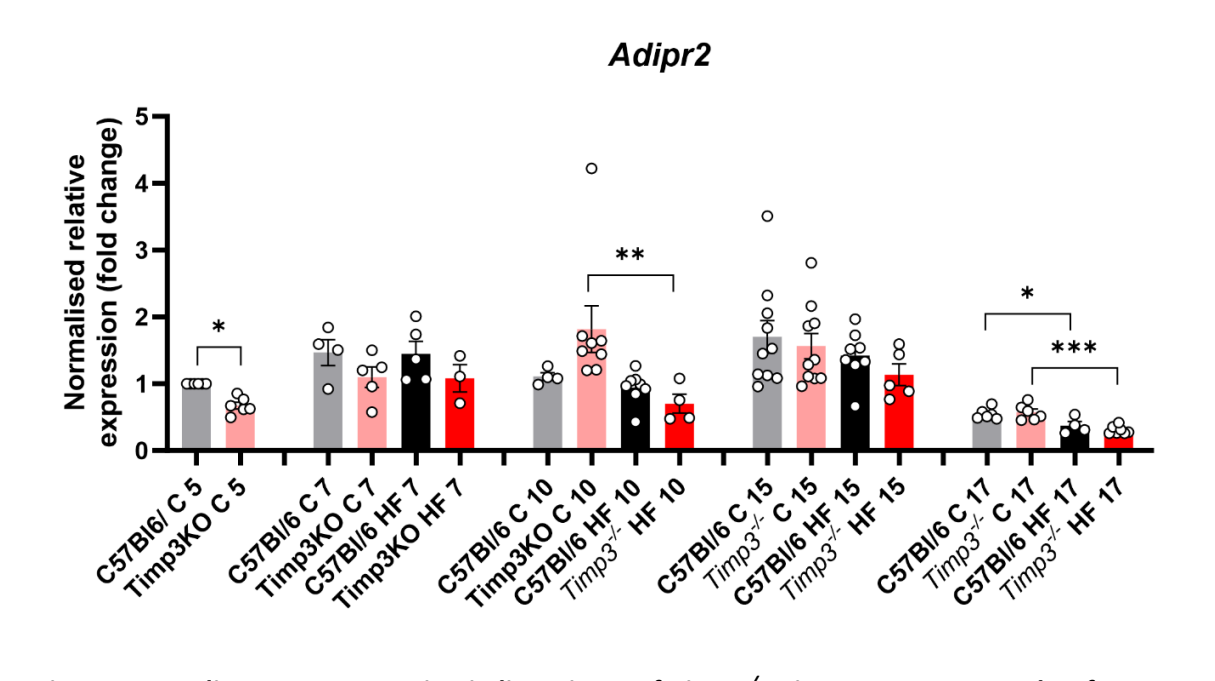


Figure 3.27 Adipr2 gene expression in liver tissue of $Timp3^{-/-}$ mice, across 5-17 weeks of age, on chow (C) and high-fat (HF) diet. Mean fold change \pm SEM (normalised to 5-week-old, chow-fed, C57Bl/6J control samples) from RT-qPCR gene expression in male $Timp3^{-/-}$ liver samples on chow and high-fat diet, and C57Bl/6J controls. n=3-10 biological samples per group. Tukey's comparisons was used to test for differences. Statistical analysis was conducted using ddct values, normalised to θ -actin and Gapdh internal control genes. * = p < 0.05, ** = p < 0.01, *** = p < 0.001.

3.4.2.6 Inflammation markers

Obesity is a characterised by low-grade chronic inflammation. The *Timp3*-/- mouse model is also a known model of inflammation due to the *TIMP3* role in regulation of ADAM17/TACE which directly regulates TNFa. In this study, gene expression of inflammatory markers *Tnfa* and *II1b* were measured in the liver at ages 5-17 (**Figures 3.32** and **3.33**). Within the 17-week-old groups, II1b expression was significantly reduced in the *Timp3*-/- HF group, compared to the *Timp3*-/- chow group. Although at the later age groups, Tnfa expression trends higher within the HF groups, its expression was only significantly higher within the *Timp3*-/- chow at the baseline age of 5 weeks.

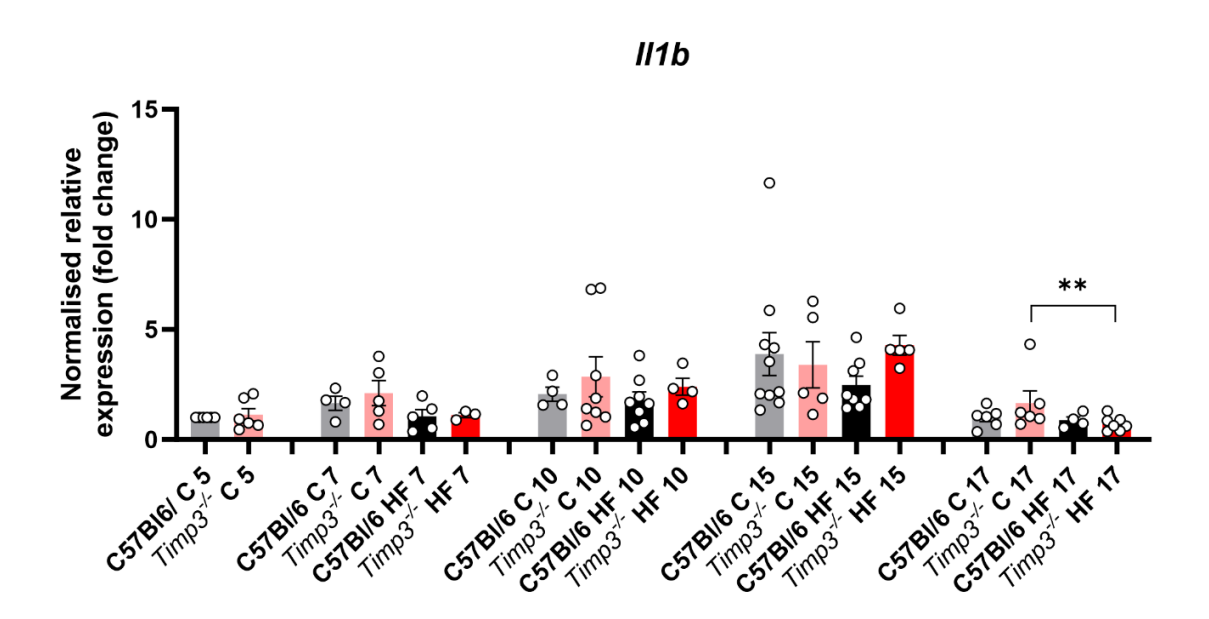


Figure 3.28 *Il1b* gene expression in liver tissue of *Timp3*^{-/-} mice, across 5-17 weeks of age, on chow (C) and high-fat (HF) diet. Mean fold change \pm SEM (normalised to 5-week-old, chow-fed, C57Bl/6J control samples) from RT-qPCR gene expression in male *Timp3*^{-/-} liver samples on chow and high-fat diet, and C57Bl/6J controls. n=3-10 biological samples per group. Tukey's comparisons was used to test for differences. Statistical analysis was conducted using ddct values, normalised to *\theta*-actin and Gapdh internal control genes. ** = p < 0.01.

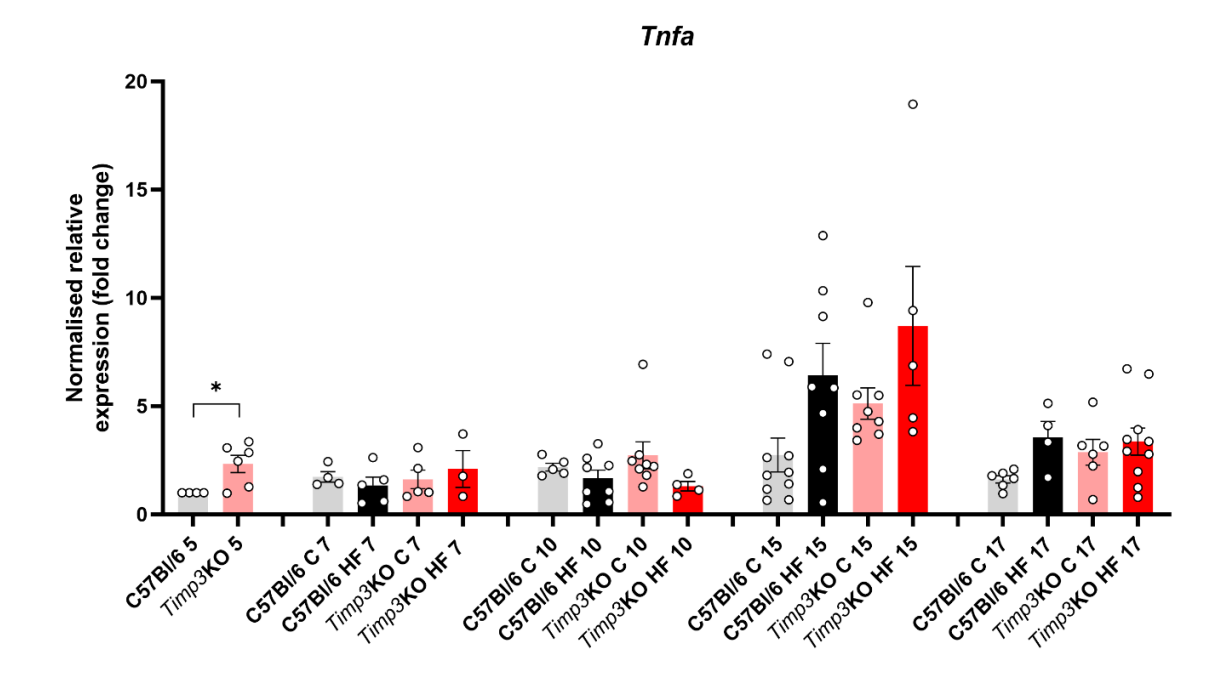


Figure 3.29 *Tnfa* gene expression in liver tissue of *Timp3*^{-/-} mice, across 5-17 weeks of age, on chow (C) and high-fat (HF) diet. Mean fold change \pm SEM (normalised to 5-week-old, chow-fed, C57Bl/6J control samples) from RT-qPCR gene expression in male *Timp3*^{-/-} liver samples on chow and high-fat diet, and C57Bl/6J controls. n=3-10 biological samples per group. Tukey's comparisons was used to test for differences. Statistical analysis was conducted using ddct values, normalised to θ -actin and Gapdh internal control genes. * = p < 0.05, ** = p < 0.01, *** = p < 0.001, **** = p < 0.0001.

3.4.3 Blood Plasma Biomarkers in *Timp3* Knockout Mouse during Obesity

3.4.3.1 Fasted Blood Glucose and Insulin Following 15 Weeks of High-fat Diet

As expected, fasting blood glucose within the high-fat diet groups was significantly elevated compared to their controls. Fasting insulin and HOMA-IR measures were also elevated, however not significant. No significant differences were seen between the two genotypes, although the $Timp3^{-/-}$ HF group showed a trend to decrease compared to the C57Bl6J, across all three parameters.

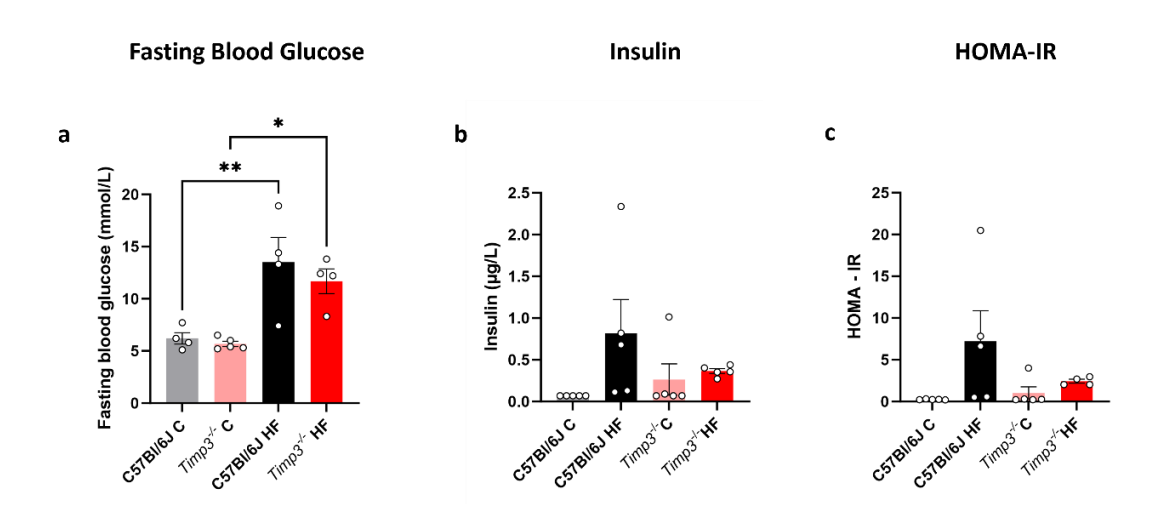


Figure 3.30 Fasting blood glucose, fasting insulin and subsequent homeostatic model assessment for insulin resistance value for *Timp3*-/- mice, at 17 weeks of age, on chow (C) and high-fat (HF) diet. Mean concentration of blood glucose, insulin, and HOMA-IR value ± SEM in male *Timp3*-/- mice on chow and high-fat diet, and C57Bl/6J controls. n=4-5 biological samples per group. Tukey's comparisons was used to test for differences. * = p < 0.05, ** = p < 0.01.

3.4.3.2 Lipid Profile Following 15 Weeks of High-fat Diet

Fasting blood lipid concentrations were measured at 17 weeks old. Triglyceride levels were elevated within the C57Bl6J chow group compared to all other groups, though this was only significantly different compared to its HF counterpart. As expected, high-fat fed groups had higher LDL and total cholesterol concentrations compared to the chow-fed controls, though no differences were seen in HDL levels.

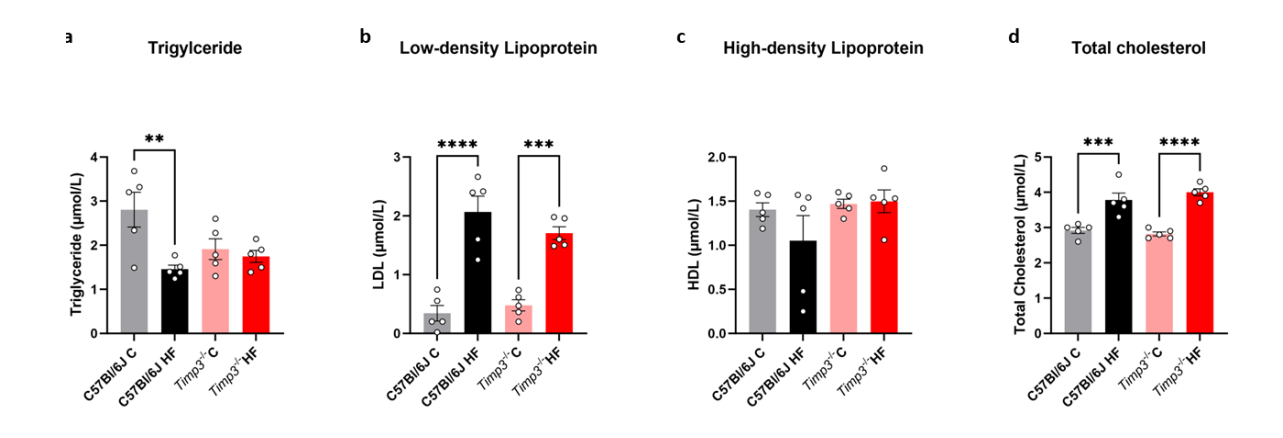


Figure 3.31 Blood lipid profile of *Timp3*-/- mice, at 17 weeks of age, on chow (C) and high-fat (HF) diet. Mean concentration of fasting blood triglycerides, low-density lipoprotein, high-density lipoprotein, and total cholesterol ± SEM in male *Timp3*-/- mice on chow and high-fat diet, and C57BI/6J controls. n=5 biological samples per group. Tukey's comparisons was used to test for differences. ** = p < 0.01, *** = p < 0.001, **** p < 0.0001.

3.4.4 Adiponectin and Butyrate in the Blood

Adiponectin and butyrate are signalling molecules involved in metabolic homeostasis. Adiponectin is produced exclusively by adipocytes, and butyrate by gut microbiota as a byproduct of fermentation.

Here, at 17 weeks old, circulating adiponectin is increased within both high-fat groups compared to their chow-fed counterparts. On standard chow diet, *Timp3*-/- mice have naturally lower circulating adiponectin. The *Timp3*-/- mice on high fat diet also have lower circulating butyrate compared to the C57Bl/6J high-fat and *Timp3*-/- chow groups.

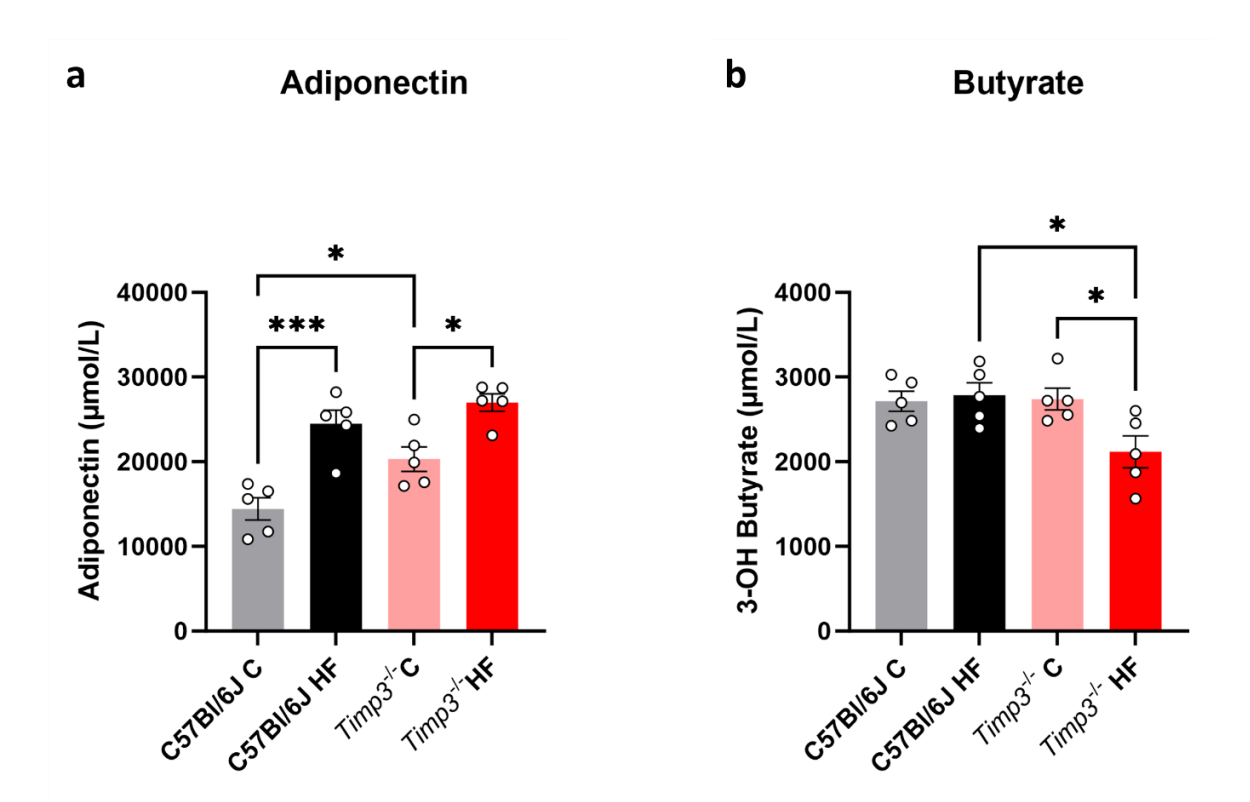


Figure 3.32 Fasting blood concentration of adiponectin and butyrate within male *Timp3*-/- mice, at 17 weeks old, on chow (C) and high-fat (HF) diet. a) Mean concentration of adiponectin ± SEM and b) mean concentration of butyrate ± SEM in male *Timp3*-/- mice on chow and high-fat diet, and C57BI/6J controls. n=4-5 biological samples per group. Tukey's comparisons was used to test for differences. * = p < 0.05, *** = p < 0.00

3.5 Discussion

3.5.1 Adiposity and energy expenditure

Diet-induced obesity is a widely used method in obesity research. The wild-type C57BI/6 mouse is susceptible to high-fat diet feeding where they have increased likelihood of insulin resistance and fatty liver. This is a model widely used in obesity and metabolic disease research.

In this study, the HF diet induced obesity within the C57Bl/6J mice and negatively impacted markers of metabolic health, including fasting blood glucose and insulin, and blood lipids. The same effects were seen within the *Timp3*-/- mice, though to a lesser extent. The *Timp3*-/- mice naturally weigh less than the C57Bl/6J wild-type and remain lighter than the control on HF diet. both chow diet groups followed a sigmoidal pattern of weight gain which peaked at 7 weeks old. The C57Bl/6J HF gained the most weight at 6 weeks old and gain steadily decreased over the study duration. The *Timp3*-/- HF peak was much later than the C57Bl/6J HF peak, at 9 weeks old during late adolescence. This group also had a smaller peak at 13 weeks, once the mice had reached maturity. This suggests that the absence of *TIMP3* effects the regulation of body weight and pattern of gain. The *Timp3*-/- mice were less "obese" than the WT on HFD, and the development of obesity did not follow the same pattern (**Figure 3.2**). Both HF groups showed decrease in weight gain at later ages, which may be indicative of negative regulation in response to the DIO.

In line with excessive body weight in the HF groups, gonadal and retroperitoneal fat depots were significantly increased compared to the chow fed controls. Gonadal depot weight in *Timp3*-/- HF group was only significantly higher than the C57Bl/6J HF group at 10 weeks. This may be reflective of the weight gain peak at 9 weeks. Retroperitoneal weight within this group was also higher that the C57Bl/6J chow at 15 and 17 weeks. This trend was also seen at earlier ages. In humans and mice, retroperitoneal fat contributes to the visceral fat depot which is implicated in obesity and is a diagnostic factor for (MetS), independent of obesity (Bjorntorp, 1990; Chusyd et al., 2016; Després & Lemieux, 2006; Yki-Järvinen, 2014). The largest fat pad, the inguinal depot, was also significantly heavier in the hf groups compared to chow controls. At 10 weeks old, the *Timp3*-/- HF inguinal depot weight was significantly heavier than that in the C57Bl/6J HF group which may again be reflective of the weight gain peak at 9 weeks.

Significant changes to the iBAT weight in HF groups were only seen at the later ages, 15 and 17 weeks old. This correlates with the slowed body weight gain of both HF groups towards the study endpoint, particularly within the C57bl/6J HF group which showed a sharp decrease at 15 weeks 9Figure 2). Conversely to the aforementioned WAT depots, which function as lipid stores,

brown adipose tissue is thermogenic and these increases would therefore result in increased energy loss in the mice via heat. This could therefore contribute to the slower weight gain at later ages within the HF groups. at 17 weeks, the *Timp3*-/- HF group had heavier iBAT fat depots compared to the C57bl/6J counterpart, correlating with the presence increased retroperitoneal fat.

No differences in weight of any fat depots between the two chow groups were seen. This illuminates the compounding effect of the absence of TIMP3 *and* HF diet. Additionally, when summed, no changes were seen in the overall WAT depot weight between the genotypes. Although the HF diet effect was still present. Therefore, in this study, the absence of TIMP3 did not affect the total lipid storage within these fat depots, but crucially the *location* of lipid storage where *Timp3*-/- HF tended to store more fat in the retroperitoneal and iBAT depots.

On chow diet, neither genotype showed evidence of hepatic steatosis. The HF diets both exhibited macrovesicular steatosis, though these groups were not significantly different to each other despite higher mean values in the *Timp3*-/- HF mice. At the baseline of 5 weeks old, the C57Bl/6J had consistently higher EE, VO2 and VCO2 values (VO2 and VCO2 plots can be seen in **Appendix D**). At these ages, both groups lean towards lipid metabolism during the light period (in sleep), and carbohydrate metabolism during the dark period (awake). Although *Timp3*-/- utilise more lipids overall. This may account for the lower body weight within the Timp3-/- mice. Additionally, whilst the C57Bl/6J group metabolic parameters show a clear circadian rhythm, the *Timp3*-/- mice do not show any obvious disparity between the light and dark cycles.

At 10 weeks, late adolescence, *Timp3*-/- chow metabolic parameters are higher than the C57Bl/6J chow group. This "swap" is also mirrored in the body weight gain, where *Timp3*-/- C initially was gaining more weight than the C57Bl/6J C group but at 10 week was gaining less. Between the HF groups, C57Bl/6J has higher metabolic parameters than *Timp3*-/- HF also at a point where the weight gain of C57Bl/6J was higher. Additionally, the RER of both chow groups maintains a ratio between 0.8-1, however the HF groups both have ratios closer to 0.8 which is reflective of the HF diet.

By 15 weeks of age, all groups aside from *Timp3*-/- HF have the same EE and O2/CO2. Thimp3-/- HF has significantly increased EE, O2/CO2 compared to the chow control and C57Bl/6J counterparts. This is mirrored in the weight gain as *Timp3*-/- HF group gain is higher at ages 15-17 weeks. The RER in these groups is more variable compared to 10 weeks but still show an overall higher ratio within the chow groups and lower in the HF groups. Even more so, the *Timp3*-/- HF group leans further towards lipid metabolism than C57Bl/6J HF. During adolescence, *Timp3*-/- C

had a lower ratio than the controls, but this discrepancy was diminished once maturity was reached.

The wild-type C57Bl/6J C mouse exhibits an overall RER pattern which shifts towards carbohydrate fuel utilisation during the dark phase and lipid utilisation in during the light phase. This fits nicely with in line with the sleep-wake cycle where carbohydrates will be the preferred energy source in the active wake period. At precisely 4am, the wild-type chow mouse experiences a sharp decrease in RER, preceding the light phase, shifting towards lipid utilisation. The trough is followed by gently ascending RER going into the light phase. This pattern is exhibited at all measured ages, at exactly 4am. The *Timp3*-/- C mouse follows the wild type RER pattern very neatly, until 4am where instead of an RER trough, *Timp3*-/- RER peaks, denoting an increase in carbohydrate utilisation. The peak is followed by a gentle RER decline going into the light phase. This pattern is seen at 5 and 10 weeks. By age 15 weeks, the *Timp3*-/- C RER pattern marries almost perfectly with the wild type. The RER displays a clear circadian rhythm, coupled to the light/dark cycle. The stark deviation of energy source in the juvenile *Timp3*-/- suggests that *Timp3* is involved in regulation of fuel utilisation by the circadian clock.

The circadian clock refers to an internal 24hr rhythm that physiological processes abide by, corresponding to the light/dark cycle. The key genes involved in regulation of the circadian clock are circadian locomotor output cycles kaput (CLOCK) and basic helix-loop-helix ARNT-like protein 1 (BMAL1) which work with PER and CRY to create a regulatory feedback loop (Cox & Takahashi, 2019). The circadian clock influences the timing of many important cell functions.

The TIMP genes are targets of clock genes in humans and mice. For example, in human keratinocytes, downregulation of *TIMP3* expression by CLOCK caused inflammation alongside increased expression of *MMP1* and *TNFa* (Park et al., 2018). Further, in a mouse model of abdominal aortic aneurysm (AAA), *Timp3* expression was supressed by the deletion of *Bmal1* in smooth muscle cells, whilst expression of *Timp4* was increased (Lutshumba et al., 2018). High fat diet impairs circadian rhythms and *Clock*-deficient mice develop obesity and metabolic syndrome (Kohsaka et al., 2007; Turek et al., 2005).

3.5.2 Expression of genes involved in ECM regulation

Expression of select MMP genes was measured in the liver to assess effects of *TIMP3* absence and DIO on ECM remodelling.

Collagenases *Mmp8* and *Mmp13* were measured in this study. MMPs in this group cleave collagens type I, II, III and X. Both MMPs had increased gene expression within the *Timp3*-/- mouse on chow at 5 weeks old. At later ages, there were no differences in *Mmp8* expression, however Mmp13 expression was higher in the C57BI/6J HF group compared to its chow control in the mature mouse. These two collagenases have roles in NAFLD and DIO.

Stromelysins Mmp12 and 19 were measured. Macrophage metalloelastase (Mmp12) expression followed a trend of increased expression within the HF diet groups, which became more significant in the mature mouse. Published literature also shows that Mmp12 expression is upregulated in obesity and regulates adipose remodelling (Chavey et al., 2003; J.-T. Lee et al., 2014). Mmp19 shows increased expression in the mature C57Bl/6J HF and *Timp3*-/- C group compared to the C57Bl/6J chow control.

Expression of *Mmp28* showed no significance but was generally higher in chow groups compared to HF, suggesting decreased *Mmp28* is associated with obesity. This corroborates unpublished data from the Pender lab group (University of Southampton), which shows that *Mmp28*-/- mice are naturally obese. Mmp28 is also associated with liver disease (Zhou et al., 2019).

3.5.3 Expression of genes involved in lipid and glucose regulation

Cyp7a1 and Fxr are important enzymes in bile acid (BA) synthesis. Expression of Fxr was highly varied throughout adolescence but in the mature mice expression showed a more defined patter. Expression was decreased in the Timp3^{-/-} mice but seemed to be restored under HF diet. Here, the Timp3^{-/-} microbiota profile and HF diet can be seen to have a direct impact in BA synthesis. Increased expression of Fxr is associated with improved metabolic outcomes. This suggests that HF diet may have a beneficial effect of restoring BA homeostasis within the Timp3^{-/-} mouse. No differences were seen in the expression of Cypa71, suggesting that this step in BA synthesis is unaffected despite Fxr modulation. Bile acid synthesis is a multi-step process however and other genes involved should be investigated to elucidate the full effect of TIMP3 absence. Additionally, Fxr can bind multiple different BAs and therefore changes within the BA pool cannot

be inferred from this data. Variation in *Fxr* expression during adolescent ages may be indicative of a developing microbiome which stabilises in the mature mouse.

The *Cyp7a1* enzyme is rate-limiting in the primary pathway of BA synthesis, but not the secondary pathway. In this study, enzymes involved in the secondary BA synthesis pathway were not investigated and therefore could be included in future studies to see how gene expression differs to *Cyp7a1*.

The *Irs1* gene expression is correlated with obesity. Here, expression of *Irs1* was decreased with obesity in the mature mouse. There were no significant differences at younger ages, suggesting the effect of high-fat diet takes some time to develop.

The expression of adiponectin receptor genes, *Adpr1* and *Adpr2* were decreased in the mature mice on HF diet. Expression of *Adpr1* was also decreased in the *Timp3*-/- mouse compared to the C57BI/6J at 17 weeks. This was accompanied by increased circulating adiponectin in the high-fat groups and *Timp3*-/- chow (compared to C57BI/6J) at 17 weeks. This suggests that the *Timp3*-/- mouse is naturally less sensitive to adiponectin than the C57BI/6J wild-type.

3.5.4 Blood biomarkers of insulin resistance and hyperlipidaemia

The HF diet increased insulin resistance within both genotypes, however the effect in the *Timp3*-/- was smaller than that seen in the C57BI/6J group, suggesting that DIO has a reduced effect on glucose homeostasis within the knockout. A similar pattern was seen in measures of blood lipids – HF diet increased LDL and total cholesterol levels in both genotypes, but not difference was seen between the genotypes. The *Timp3*-/- mice had naturally lower triglyceride levels which matched that of the C57BI/6J under HF diet. This effect remained unchanged under HF diet conditions.

3.6 Strengths and Limitations

Here, the use of a longitudinal study allowed the examination of the development of obesity within the *Timp3*-/- mouse. However, to maintain alignment with the three Rs of animal research (replacement, reduction, and refinement), sample number was kept to a necessary minimum. Due to the variability of mouse development during adolescence, some effects of the *TIMP3* gene were more difficult to elucidate. Future experiments with an increased sample size would help to confirm the results seen in this study. The gene expression measurements within this study helped draw a picture of the underlying mechanisms involved in obesity within the *Timp3*-/- mouse, however expression regulation is one of many levels of regulation of gene products. Gene expression may not directly correlate to enzyme activity. Future studies to assess enzyme activity would be useful to paint a broader picture of the mechanisms at play.

3.7 Conclusions

In this study, the *Timp3*^{-/-} mouse on high-fat diet has an altered development of obesity compared to the C57BI/6J control. This is evidenced by differing patterns of weight gain and energy expenditure accompanied by irregular storage of lipids in the abdominal retroperitoneal fat pad. Independent of HFD, the respiratory exchange ratio exhibits and altered circadian rhythm in the *Timp3*^{-/-} mouse, suggesting a role of *Timp3* in the circadian clock regulation of energy utilisation.

In addition, changes in the expression of adiponectin receptor genes and circulating adiponectin suggest that the *Timp3*-/- mouse is naturally less sensitive to adiponectin, an important regulator in lipid homeostasis.

Changes in the concentration of circulating butyrate and *Fxr* expression suggest that the alternative development of obesity presented by the *Timp3*-/- mouse may be in-part due to the gut microbiota.

Chapter 4 The gut Microbiome Profile in *Timp3*-/- Mice, Under High-fat diet Conditions

4.1 Introduction

The incidence of metabolic syndrome (MetS) is highly influenced by our environment. The gut microbiome (GM) is increasingly becoming one of the most important factors in pathology. The GM has been shown to play a pivotal role in the development of obesity, diabetes mellitus and cardiovascular disease (Brown and Hazen, 2018; Koliada et al., 2017). The composition of the gut microbiome is not only influenced by other environmental factors such as diet and lifestyle but also our genetics (Bäckhed et al., 2015; Zhang et al., 2018).

Recently, TIMP3 has been implicated in the regulation of the gut microbiome in mouse models of hypercholesterolemia and diet-induced obesity (DIO). However, the *Timp3*-/- mouse gut microbiome has not been characterised. Therefore, this chapter aims to determine the composition of the *Timp3*-/- GM and the effect of the absence of TIMP3 during DIO.

4.2 Aims and Hypothesis

The overall aim of this experiment was to investigate the *Timp3*-/- male mouse gut microbiome at multiple stages of development (five, seven, ten and fifteen weeks of age) in response to a high-fat diet, in comparison to the age-matched C57Bl/6 wild-type. The hypothesis was that the composition of the gut microbiome would be altered in *Timp3*-/- mice, compared to the wild-type, and this would be exacerbated in response to a high-fat diet. Specific objectives were as follows:

- 1. Characterise the gut microbiome diversity of high-fat fed C57BI/6 and *Timp3*-/- mice at ages five, seven, ten and fifteen weeks
- 2. Identify differentially abundant taxa in high-fat fed C57Bl/6 and *Timp3*-/- mice at ages five, seven, ten and fifteen weeks
- 3. Compare findings from the high-fat diet groups to the control diets
- 4. Compare findings from the *Timp3*^{-/-} to the C57BI/6 controls.

4.3 Methods

All analyses were conducted in R v 4.2.1. As described in **Chapter 2.18**, sequence reads and metadata were combined into a phyloseq object for downstream analysis (McMurdie and Holmes, 2013). Data were analysed as normalised abundances using the following methods: rarefaction, relative abundance and log10 transformations. Alpha diversity (estimates of within sample species richness and evenness) was estimated using Observed species, Chao1, Shannon and Simpson indices with the vegan R package (reference and version number needed) and tested using Wilcoxon ranked Sum (Jari Oksanen, F. Guillaume Blanchet, Michael Friendly et al., 2019).

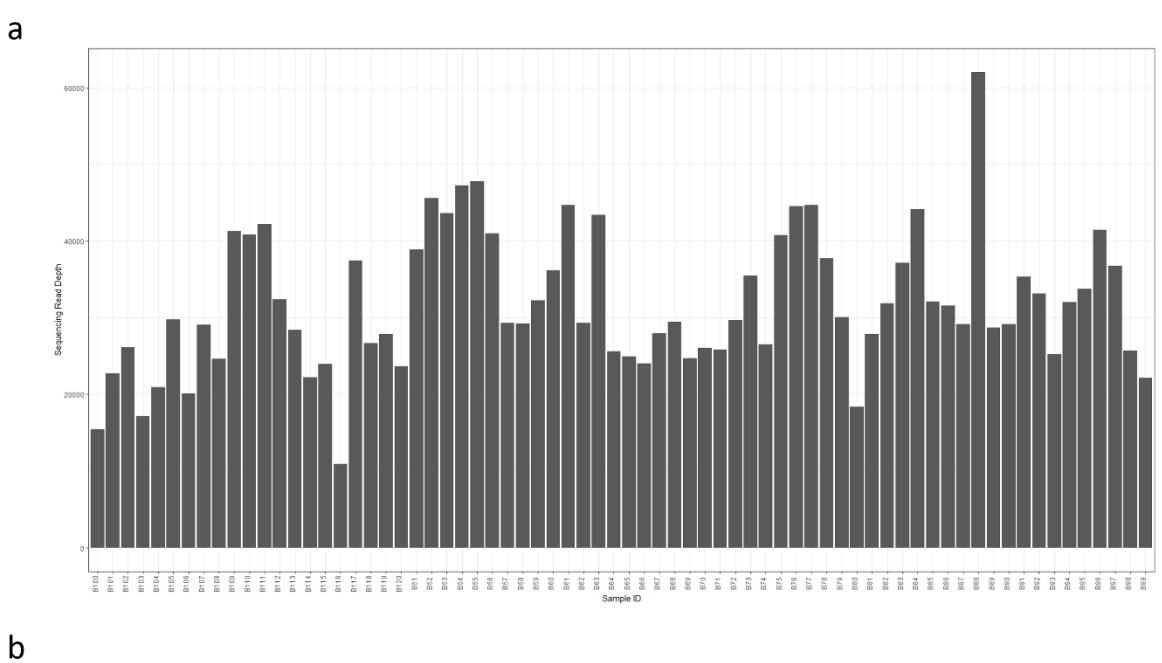
Using the vegan package, the Beta diversity (a measure of between sample species diversity) was also estimated using UniFrac (weighted and unweighted) and Bray-Curtis dissimilarity. The UniFrac method identifies differences between communities by measuring the distance between taxa within a phylogenetic tree (Lozupone & Knight, 2005). Unlike the unweighted UniFrac, weighted also considers the abundance of ASVs as a factor. The Bray-Curtis method differs in that it doesn't use assumptions based on phylogenetic relationships and only measures whether an ASV is present or not (Bray & Curtis, 1957). Beta diversity was visualised with principal coordinates analysis (PCoA) plots and tested using PERMANOVA also with the vegan package (Jari Oksanen, F. Guillaume Blanchet, Michael Friendly et al., 2019).

Differential abundance analysis was conducted at the genus level, using DESeq2 and ANCOMBC packages (Lin and Peddada, 2020; Love et al., 2014; Martin et al.,)

4.4 Results

4.4.1 Initial Exploration

Sample read depth is illustrated in **Figure 4.1**. Uncharacterised and low-frequency taxa were removed (see Appendix for list of those removed).



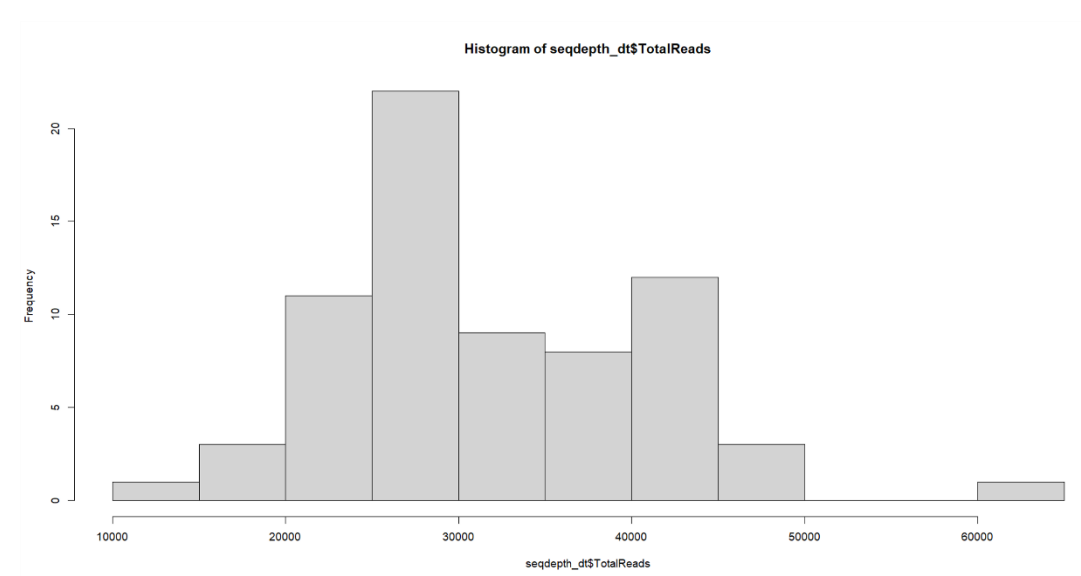


Figure 4.1 Sample read depth histograms and bar plot. a) read depth bar plot of all samples; b) histogram of read depths.

4.4.1.1 Normalisation

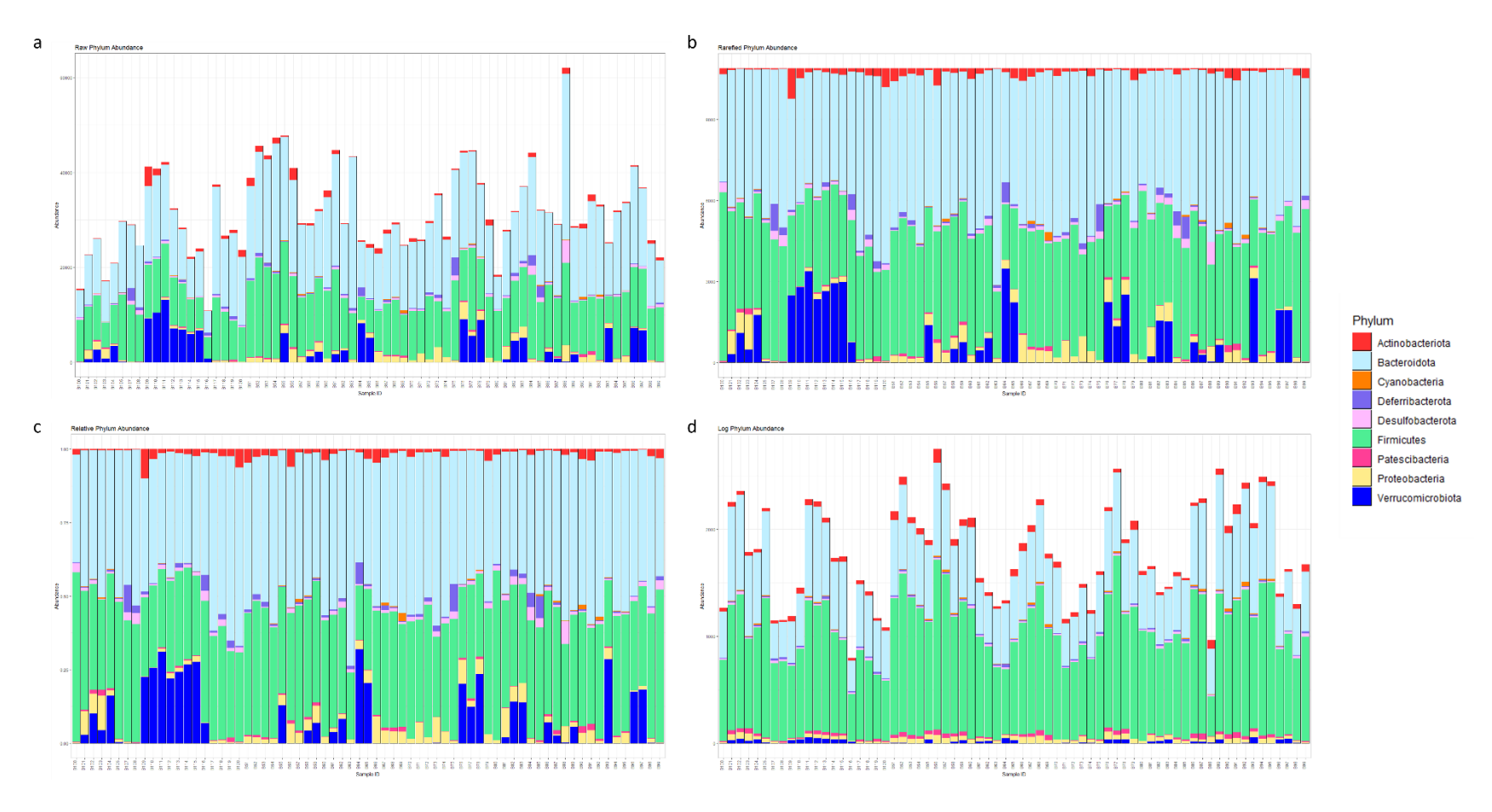


Figure 4.2 Phylum abundance from data sets with different normalisation methods. (a) raw data; (b) rarefied data; (c) relative abundance data; (d) log-transformed data.

4.4.2 Diversity measures

4.4.2.1 Alpha Diversity

Alpha diversity describes the species diversity within a particular sample. Four different indices were used to measure alpha diversity (observed and chao1 indices of richness, and Simpson and Shannon indices of diversity and evenness, respectively) in rarefied abundance data. Rarefaction was used here for data transformation as other methods such as log-transformation and relative abundance can affect species evenness, amplify differences in rare taxa and quash differences between dominant taxa – features which alpha diversity metrics rely on. Each age group was analysed independently, however, as few differences were seen due to aging, data are presented here with all age groups combined.

4.4.2.1.1 Observed

The Observed alpha diversity index for rarefied abundance data is presented in **Figure 4.3**. Observed diversity is a simple count of the number of different species seen within a sample. The $Timp3^{-/-}$ mouse exhibited a naturally decreased diversity compared to the wild-type (WT) (p < 0.01). Under high fat diet (HFD) conditions however, despite a further decrease in $Timp3^{-/-}$ microbiota diversity, there was no distinction from the WT.

Observed Diversity Plot for Rarefied Data Combined Ages Observed *** 1200-Alpha Diversity Measure 600 400-**□** C57BI/6 HF iii Timp3⁻/⁻ C **iii** Timp3⁻/⁻ HF

Figure 4.3 Observed alpha diversity box plots of combined samples from age groups 7, 10 and 15 weeks using rarefied abundance data. Wilcox test was used to test for differences between groups. n = 14-15 samples per group. * = p < 0.05, ** = p < 0.01, *** = p < 0.001.

4.4.2.1.2 Chao1

As with the Observed index, Chao1 also measures species richness but additionally considers the counts of rare taxa. Chao1 index for rarefied abundance data is presented in **Figure 4.4**. Again, gut microbiota richness is decreased naturally in the $Timp3^{-/-}$ mouse compared to the WT (p < 0.05) but this distinction is abolished under HFD.

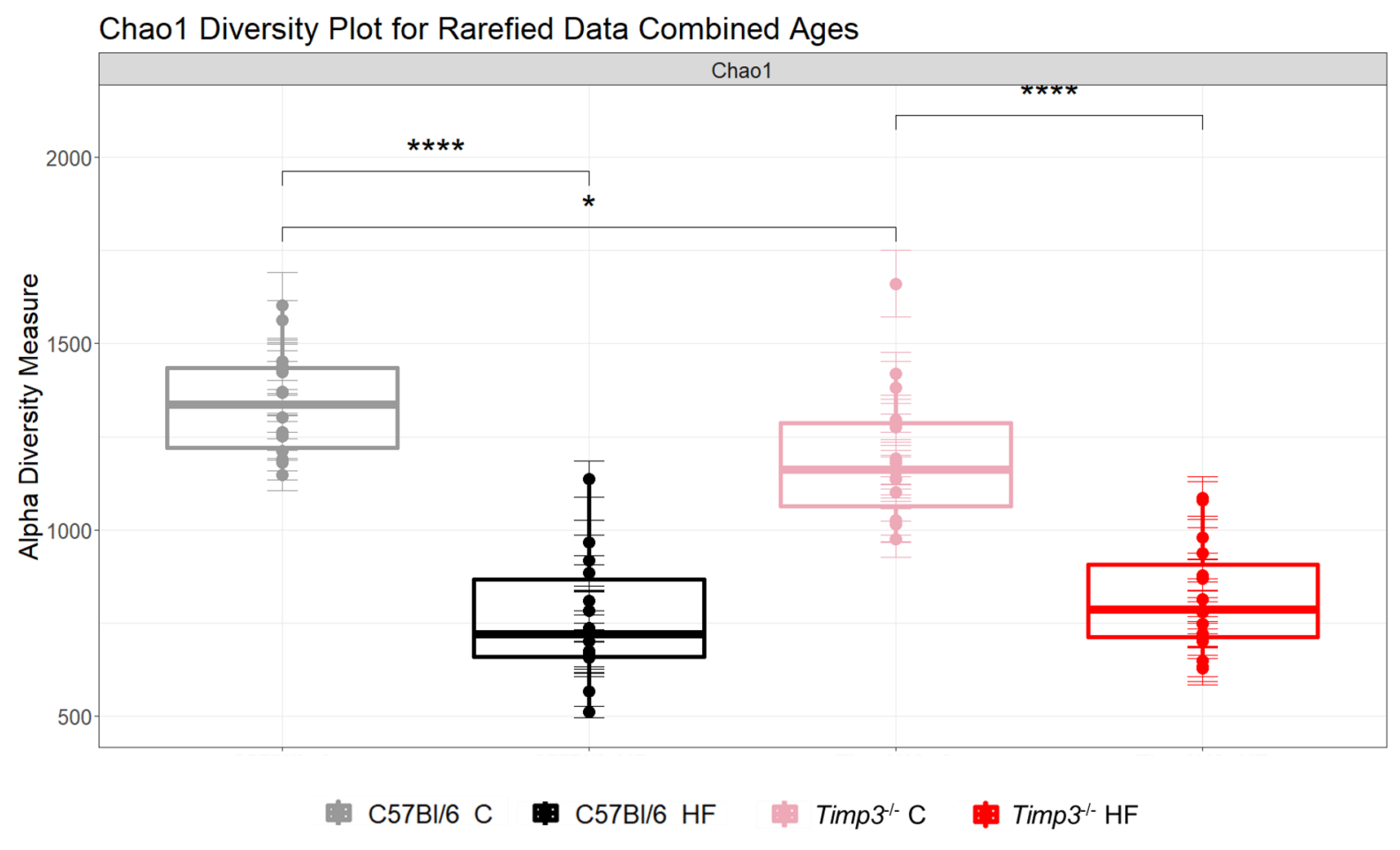


Figure 4.4 Chao1 alpha diversity box plots of combined samples from age groups 7, 10 and 15 weeks using rarefied abundance data. Wilcox test was used to test for differences between groups. n = 14-15 samples per group.

4.4.2.1.3 Simpson

Simpson index is a measure of the probability that two randomly selected species form the same sample will be identical. A lower value indicates decreased probability and therefore increased diversity. It gives more weighting to the dominant species within a sample.

Visualised in **Figure 4.5**, no significant differences in Simpson diversity were seen between the genotypes in either diet condition. High fat diet seemed to increase diversity in both groups, but this change was only significant within the $Timp3^{-/-}$ mouse (p < 0.001).

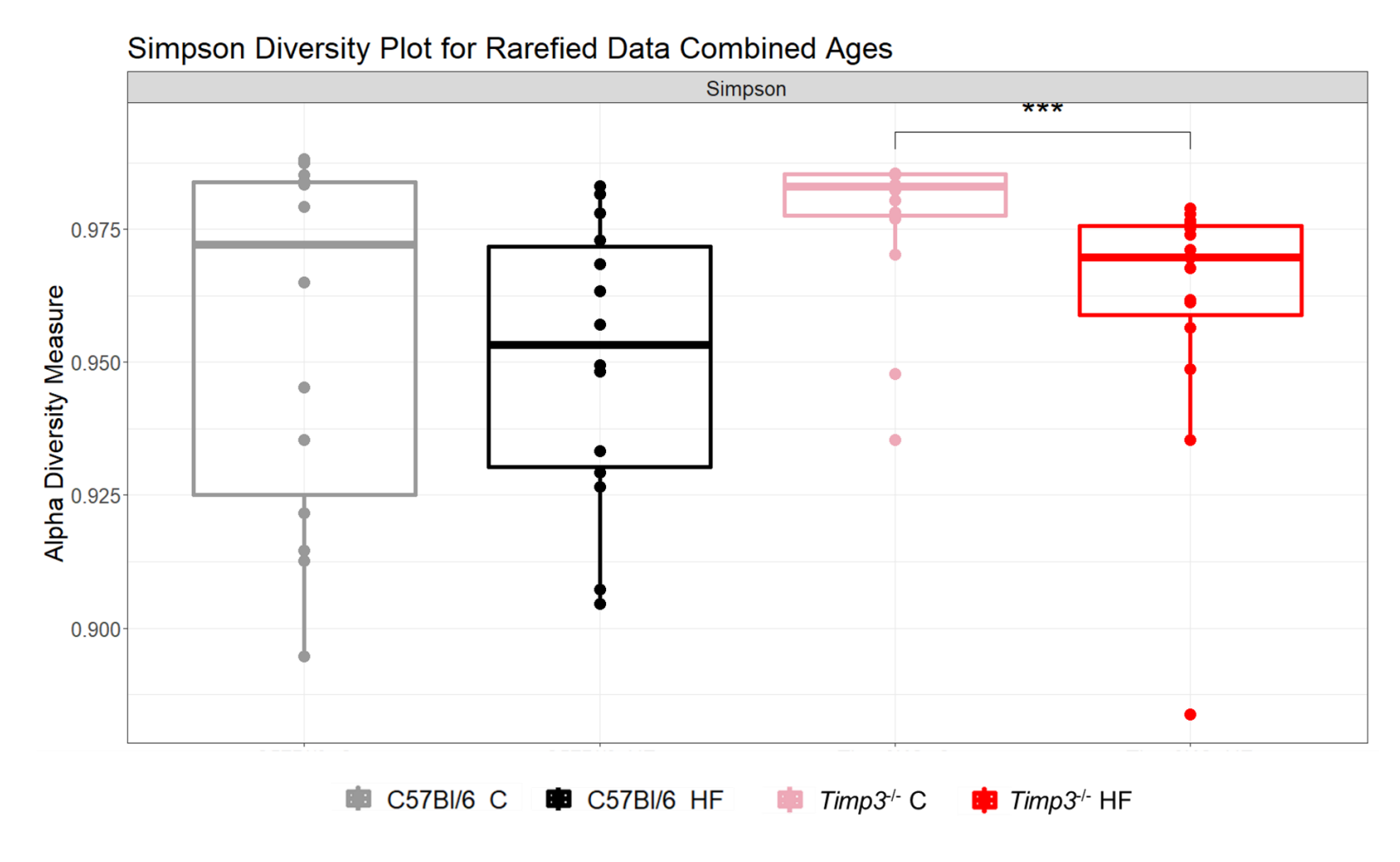


Figure 4.5 Simpson alpha diversity box plots of combined samples from age groups 7, 10 and 15 weeks using rarefied abundance data. Wilcox test was used to test for differences between groups. n = 14-15 samples per group. * = p < 0.05, ** = p < 0.01.

4.4.2.1.4 Shannon

The Shannon index measures the proportions of single species' within a sample. Presented in **Figure 4.6**, we can see that HFD causes a significant decrease in species evenness in both genotypes (p < 0.001 and p < 0.0001 in the WT and $Timp3^{-/-}$ mice, respectively), but no genotype specific variations are seen.

Shannon *** Alpha Diversity Measure □ C57BI/6 C □ C57BI/6 HF Timp3⁻/⁻ C **i** Timp3⁻/⁻ HF

Shannon Diversity Plot for Rarefied Data Combined Ages

Figure 4.6 Shannon alpha diversity box plots of combined samples from age groups 7, 10 and 15 weeks using rarefied abundance data. Wilcox test was used to test for differences between groups. n = 14-15 samples per group. *** = p < 0.001; **** = p < 0.0001.

4.4.2.2 Beta Diversity

Beta diversity was estimated using UniFrac (weighted and unweighted) and Bray-Curtis dissimilarity. The UniFrac method identifies differences between communities by measuring the distance between taxa within a phylogenetic tree (Lozupone & Knight, 2005). Weighted UniFrac also considers the abundance of ASVs as a factor. The Bray-Curtis method doesn't use assumptions based on phylogenetic relationships and only measures whether an ASV is present or not (Bray & Curtis, 1957). Beta diversity was visualised with principal coordinates analysis (PCoA) plots and significance tested with PERMANOVA.

As with alpha diversity, ageing contributed only a small amount of variation in microbial diversity and therefore the following results are presented using all age groups combined. Beta diversity measurements by age can be found in **Appendix E**.

Across all three methods (**Figures 4.7-4.9**), diet was responsible for a significant amount of the variation observed. The *Timp3*^{-/-} genotype produced small significant variation, and the combined effect of diet and genotype was negligible.

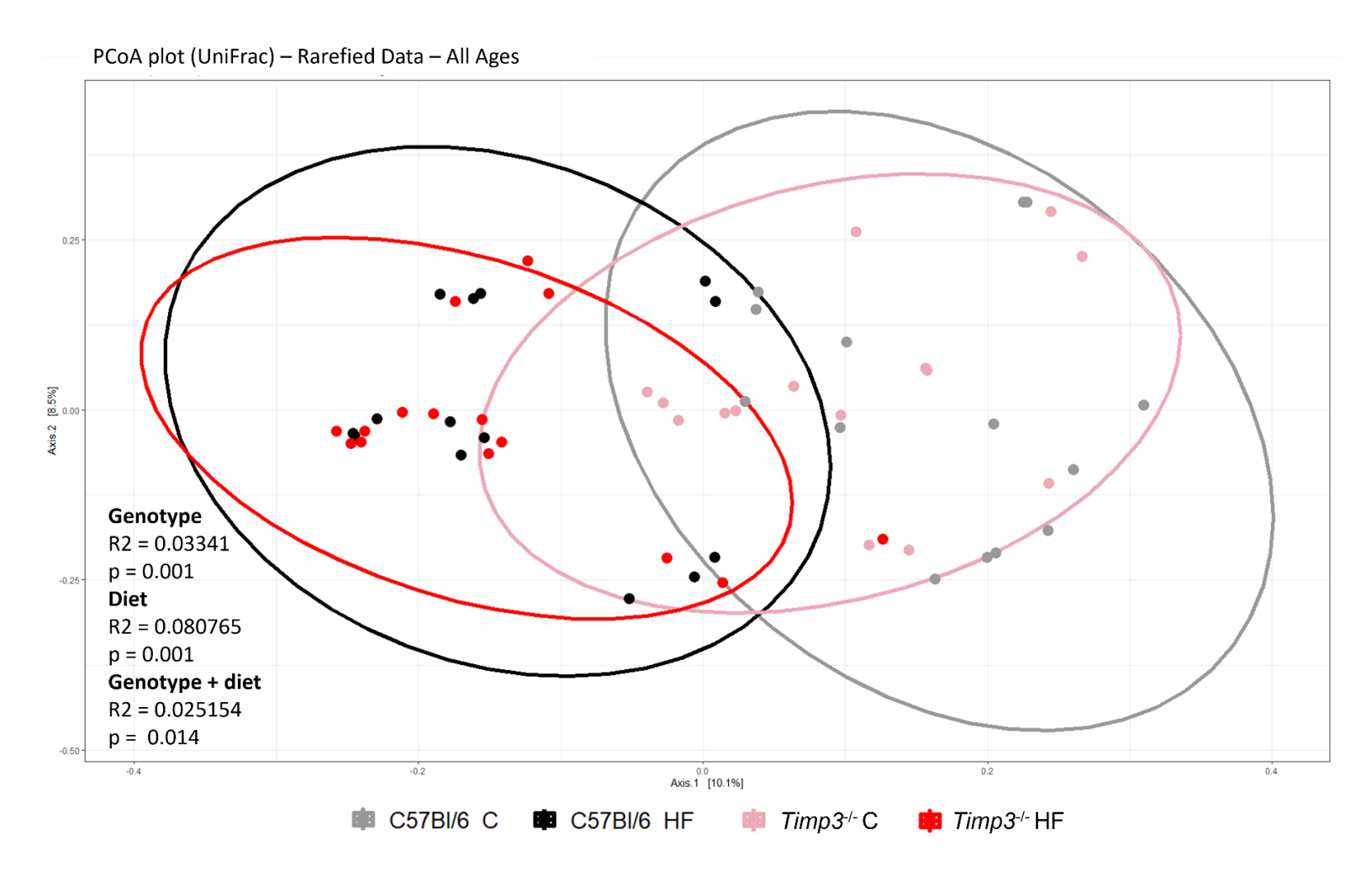


Figure 4.7 PCoA plot based on the UniFrac diversity metric, using rarefied data, for combined samples from weeks 7, 10 and 15. PERMANOVA was used to test for differences. Ellipses represent 95% CI

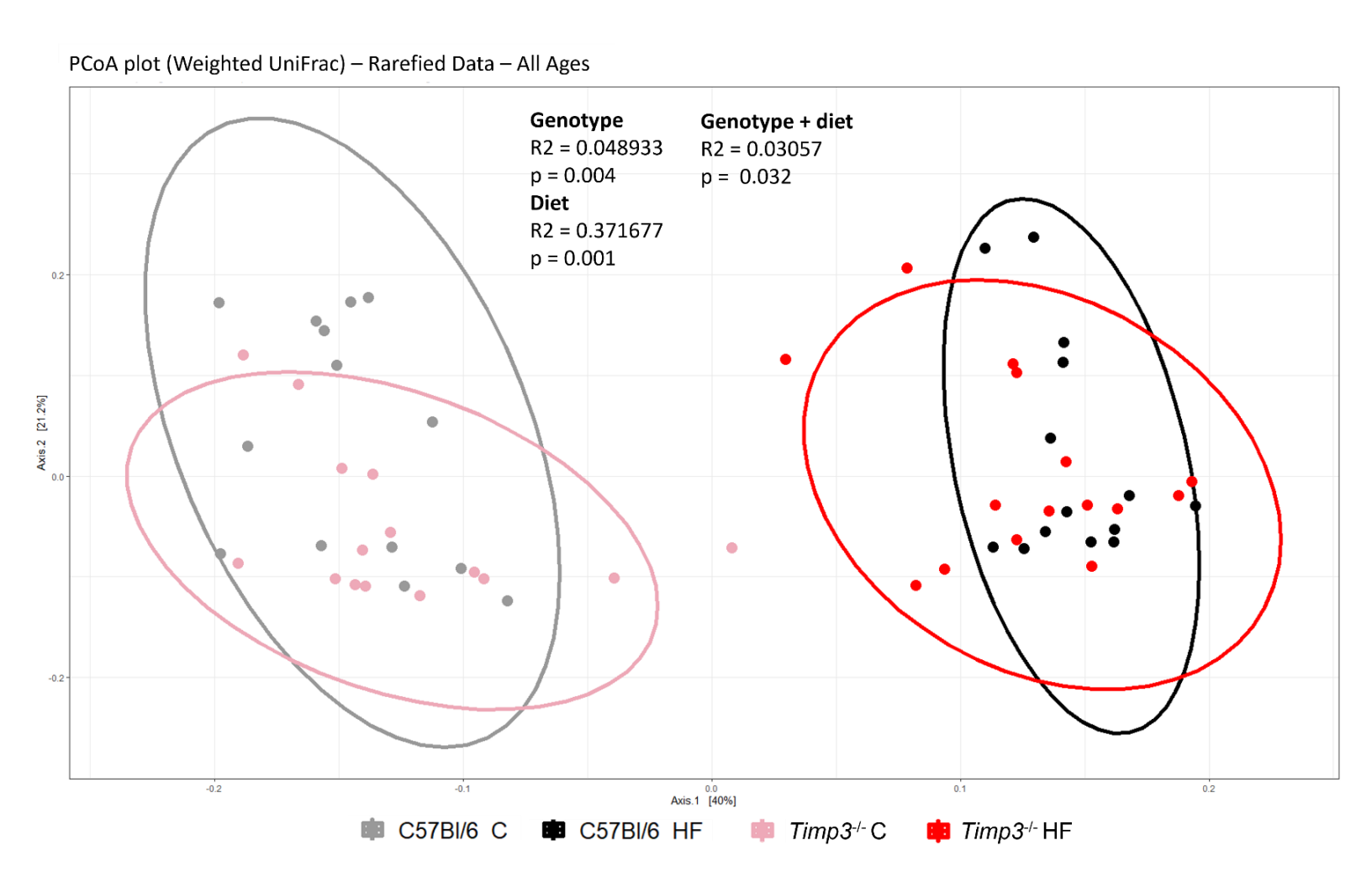


Figure 4.8 PCoA plot based on the weighted UniFrac diversity metric, using rarefied data, for combined samples from weeks 7, 10 and 15. PERMANOVA was used to test for differences. Ellipses represent 95% CI.

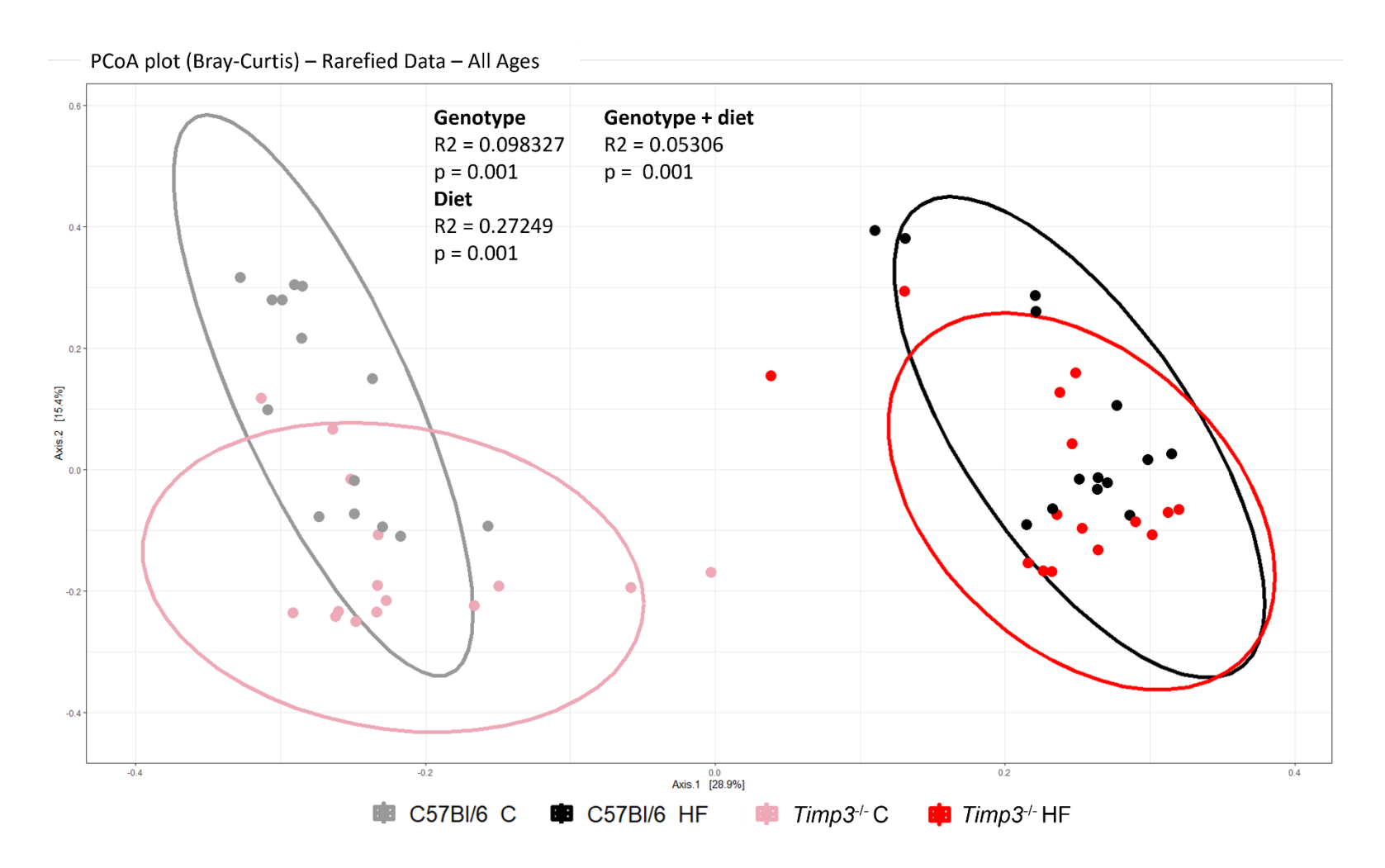


Figure 4.9 PCoA plot based on the Bray-Curtis diversity metric, using rarefied data, for combined samples from weeks 7, 10 and 15. PERMANOVA was used to test for differences. Ellipses represent 95% CI.

4.4.2.3 Log Abundance at the Phylum Level

The four most abundant phyla within the log abundance data set are shown in **Figure 4.10**. The HFD groups have significantly decreased abundance of Bacteroidota, Firmicutes and Proteobacteria compared to their chow-fed counterparts. This trend is also seen between the $Timp3^{-/-}$ groups for Actinobacteria abundance, but abundance within the C57Bl/6J HF group is decreased compared to its chow control. On chow diet, $Timp3^{-/-}$ mice had increased abundance of Actinobacteriota and Bacteroidota compared to the C57Bl/6J controls. On HF diet, the $Timp3^{-/-}$ mice had decreased Firmicutes abundance and increased Proteobacteria abundance.

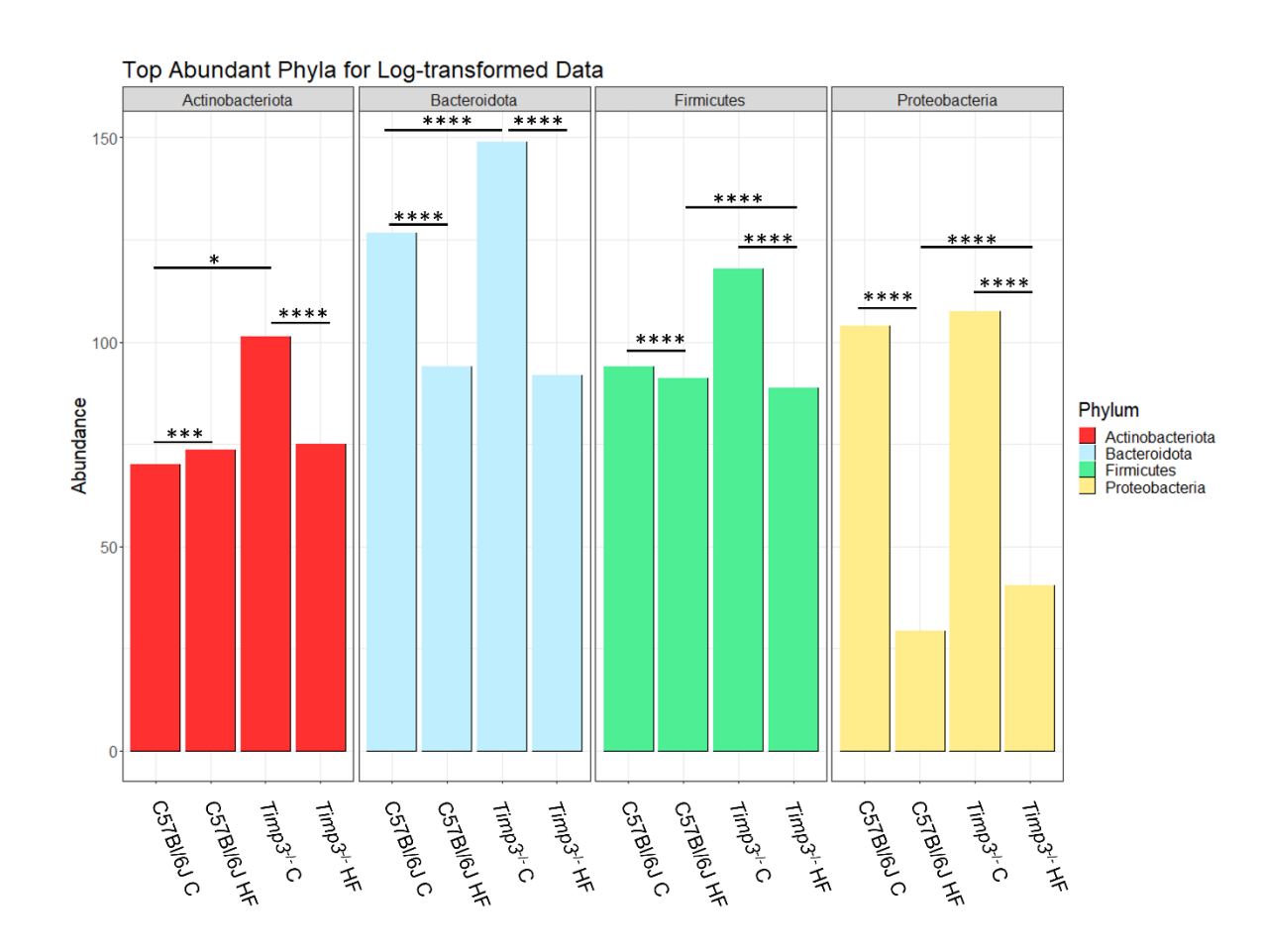


Figure 4.10 Bar graph displaying the top four most abundant phyla within the log-transformed data set, for all ages combined, excluding 5 weeks. Mann-Whitney test was used to test for differences between groups. n = 14-15 samples per group. * = p < 0.05, *** = p < 0.001, **** = p < 0.0001.

4.4.2.4 Log Abundance at the Genus Level

The top 20 most abundant genera across all samples are represented by a heatmap in **Figure 4.11**. Heatmap colour indicates high (red) or low (white) log-transformed abundance. The five most enriched genera are the *Lachnospiraceae* NK4A16 group, *Oscillibacter*, *Alistipies*, *Colidextribacter* and *Rikenellaceae* RC9 gut group.

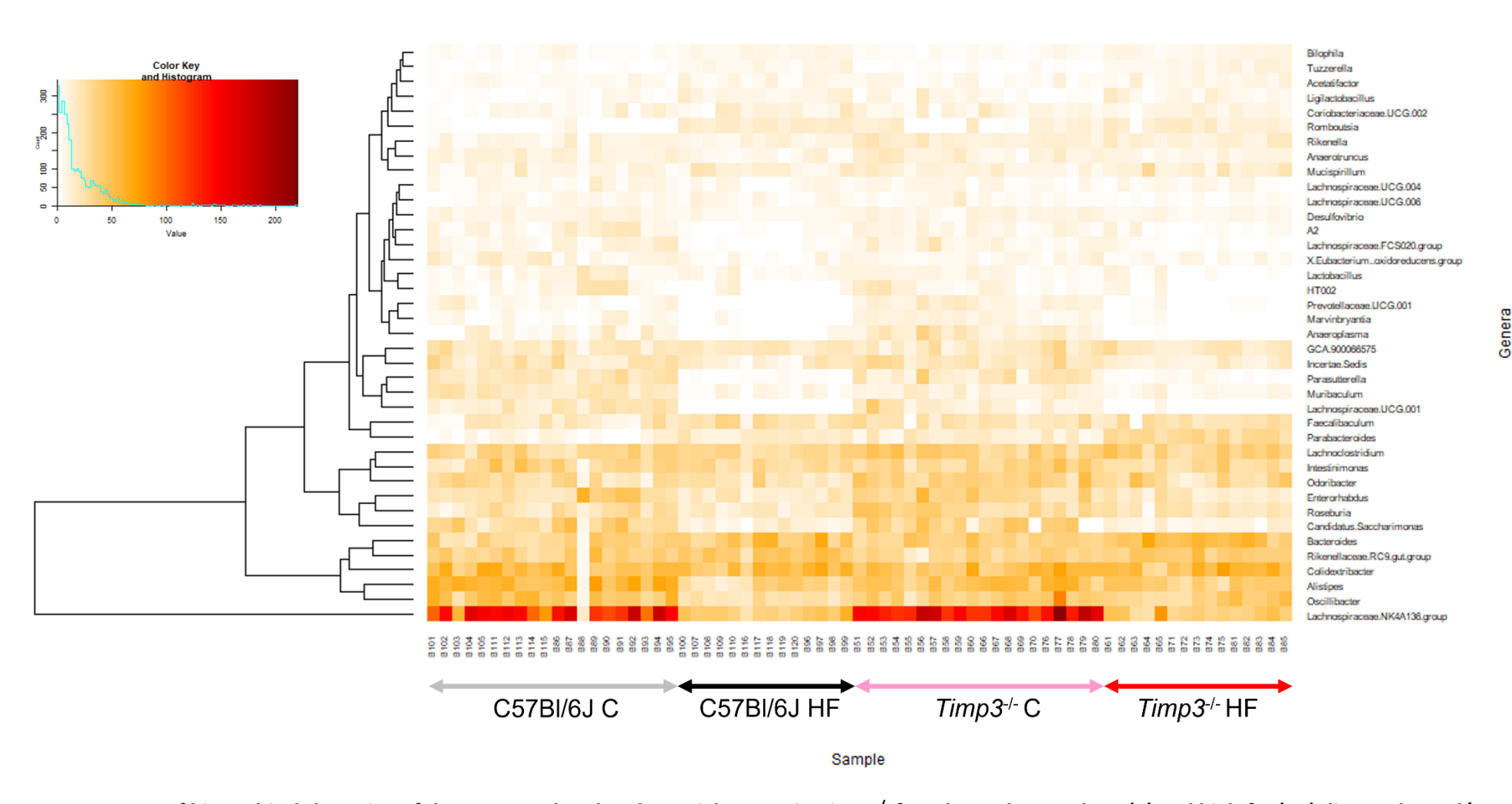


Figure 4.11 Heat map of hierarchical clustering of the 40 most abundant bacterial genera in *Timp3*-/- faecal samples, on chow (C) and high-fat (HF) diet, and C57BI/6 wild-type controls. Heatmap colour (white to red) displays the log-transformed abundance of each genus across samples.

4.4.3 Differential Abundance

Two different methods were employed to test for differential abundance of genera between experimental groups: DESeq2 and ANCOMBC. The following results combine all ages in each experimental group but results by age group can be found in **Appendix E**.

Differentially abundant ASVs in the C57Bl6/J and *Timp3*-/- groups are presented in **Figures 4.12 -4.23**, accompanied by Venn diagrams to highlight the commonly identified bacteria from each method. Similarly to the Alpha and Beta diversity measures, most variation was seen in response to diet. Even so, many genera were differentially abundant in the *Timp3*-/- mouse on chow diet, compared to WT. The fewest ASVs were identified within the *Timp3*-/- mouse on HFD, in comparison to the HFD WT group.

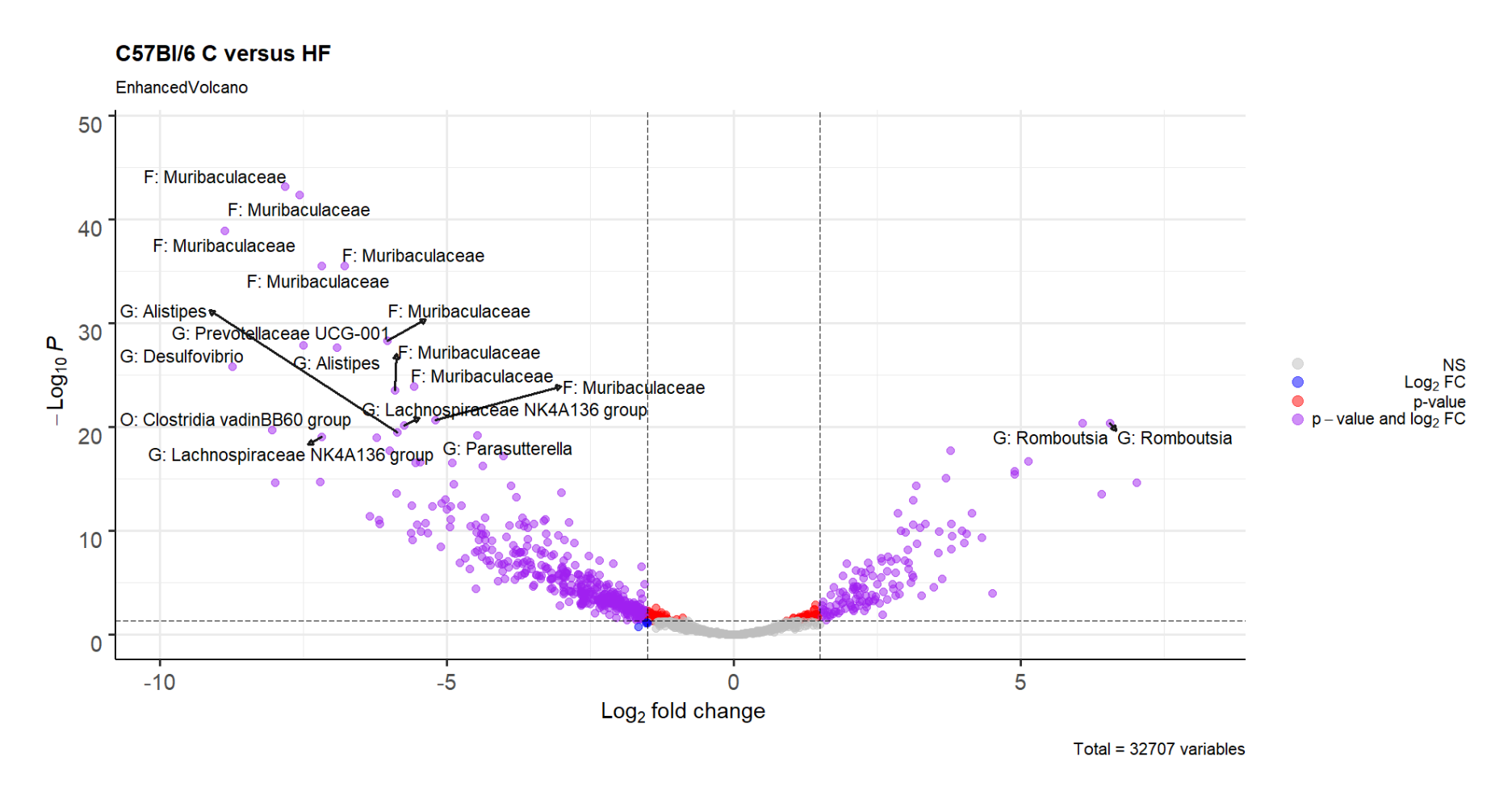


Figure 4.12 Volcano plot displaying the fold change of genera within the C57Bl/6J high fat group compared to the C57Bl/6J chow group, for all ages combined, identified by DESeq2. Grey points indicate non-significant ASVs. Red points indicate ASVs with a p-value lower than 0.01, blue points indicate ASCVs with a Log2 fold change more than +/-2 and purple points indicate ASVs that meet both these requisites. The 20 most significant ASVs are labelled.

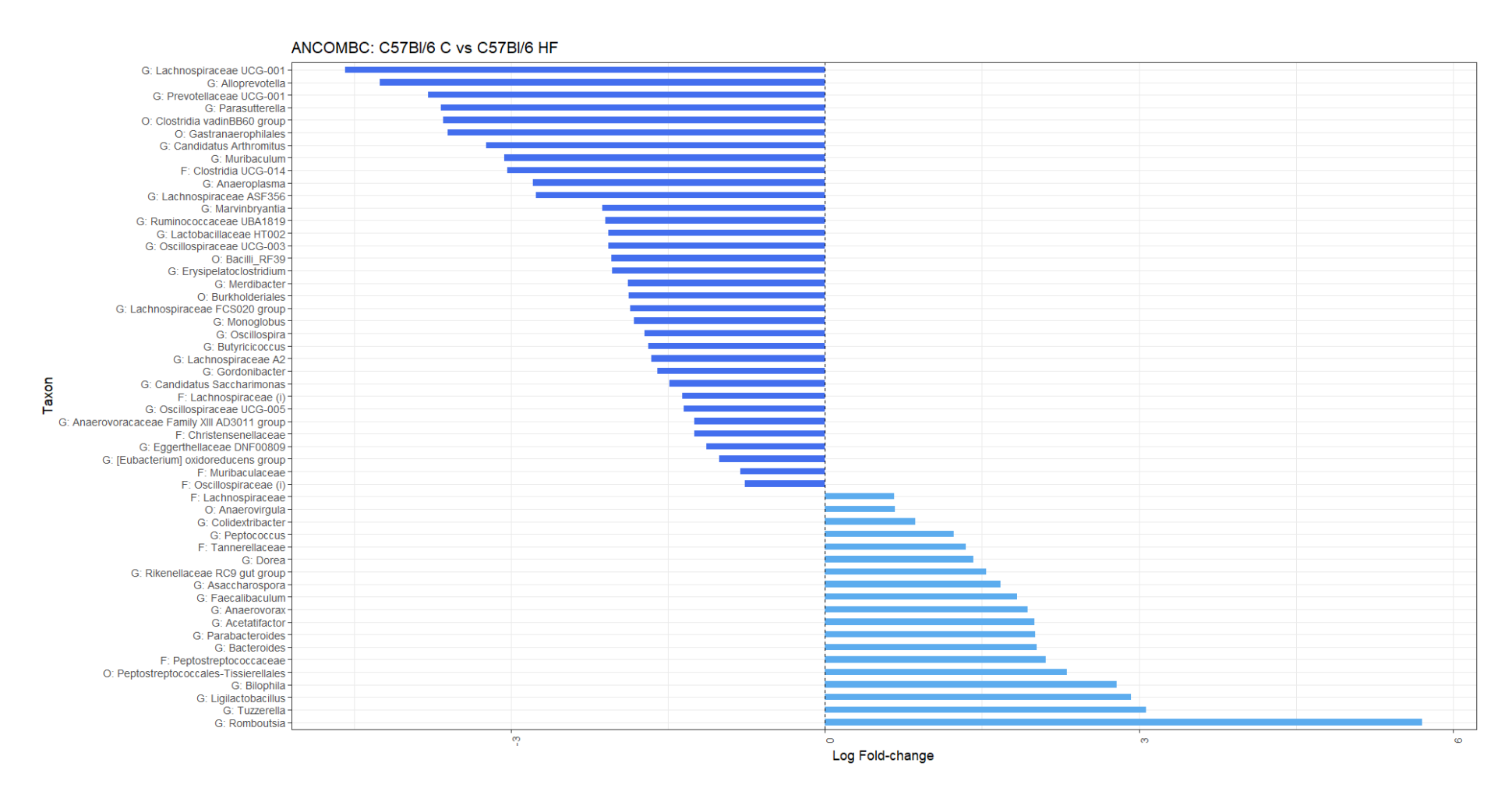


Figure 4.13 Bar plot displaying the fold change of significant genera within the C57Bl/6J high-fat group compared to the C57Bl/6J chow group with all ages combined, identified by ANCOM-BC. Significance level was set at p = 0.01.

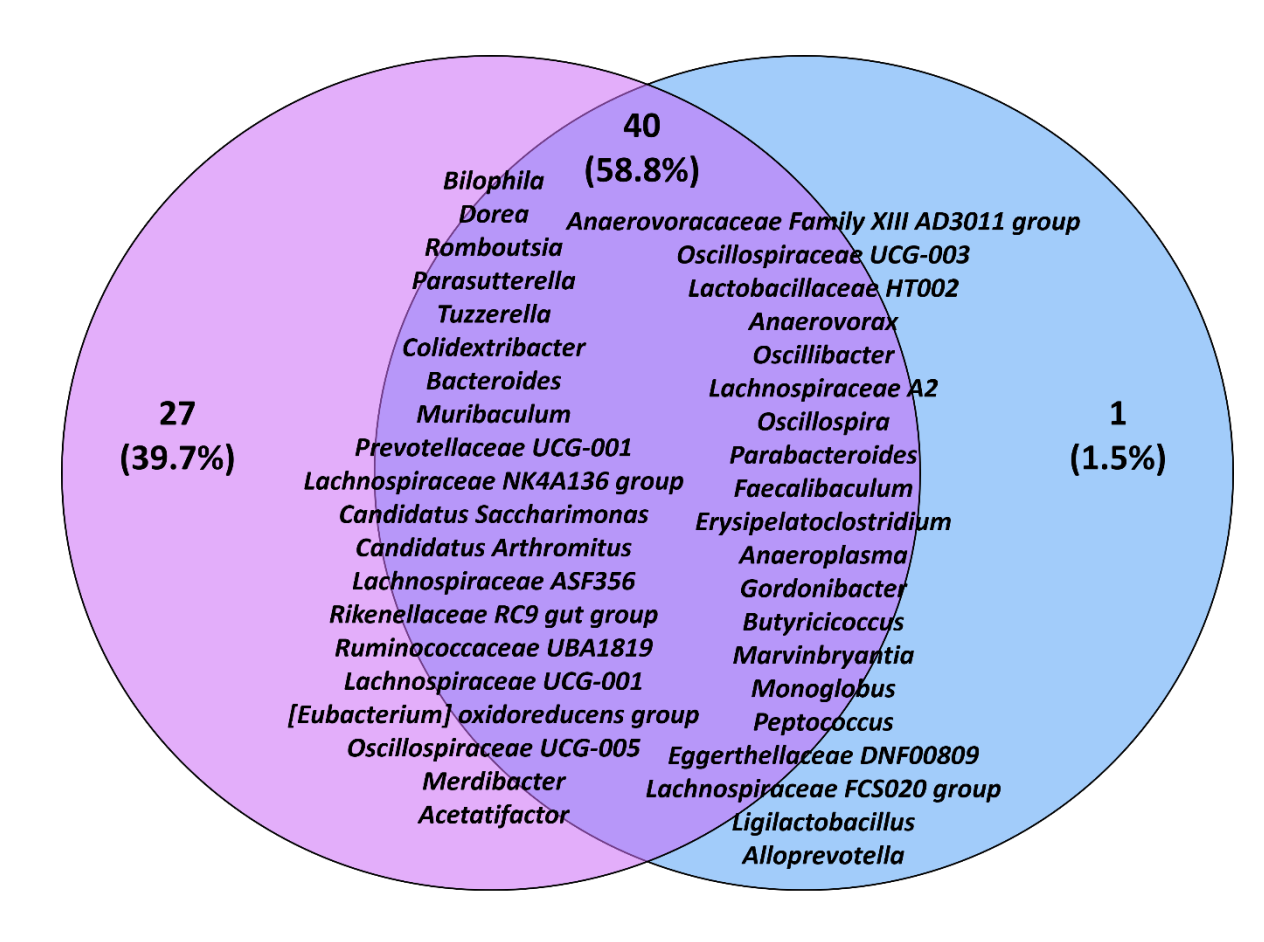


Figure 4.14 Venn diagram displaying the percentage of ASVs identified in C57BI/6J high-fat, compared to C57BI/6J chow, by DESeq2 and ANCOM-BC, with common genera between methods listed.

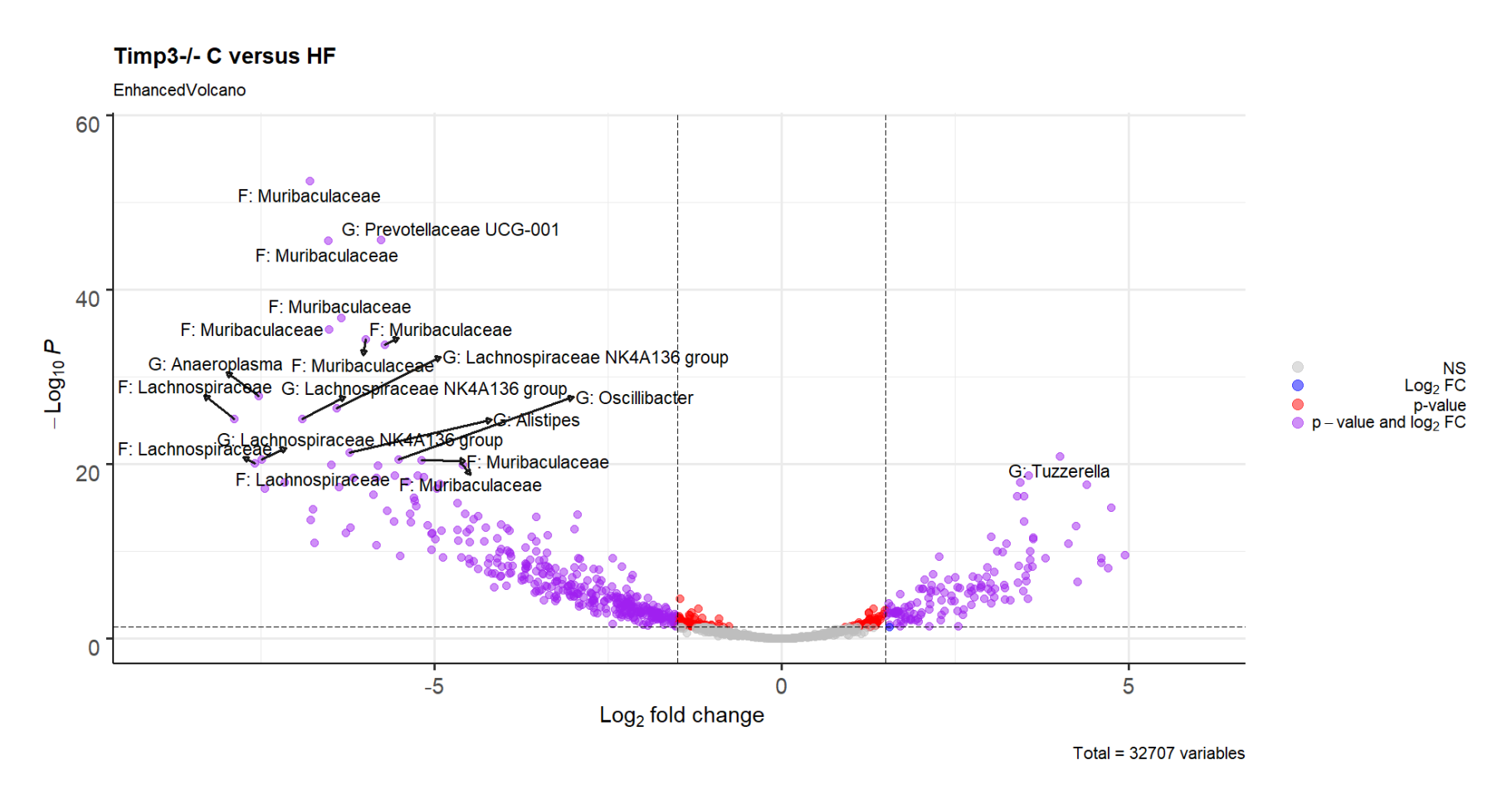


Figure 4.15 Volcano plot displaying the fold change of genera within the *Timp3*^{-/-} high-fat group compared to the *Timp3*^{-/-} chow group for all ages combined, identified by DESeq2. Grey points indicate non-significant ASVs. Red points indicate ASVs with a p-value lower than 0.01, blue points indicate ASCVs with a Log2 fold change more than +/-2 and purple points indicate ASVs that meet both these requisites. The 20 most significant ASVs are labelled.

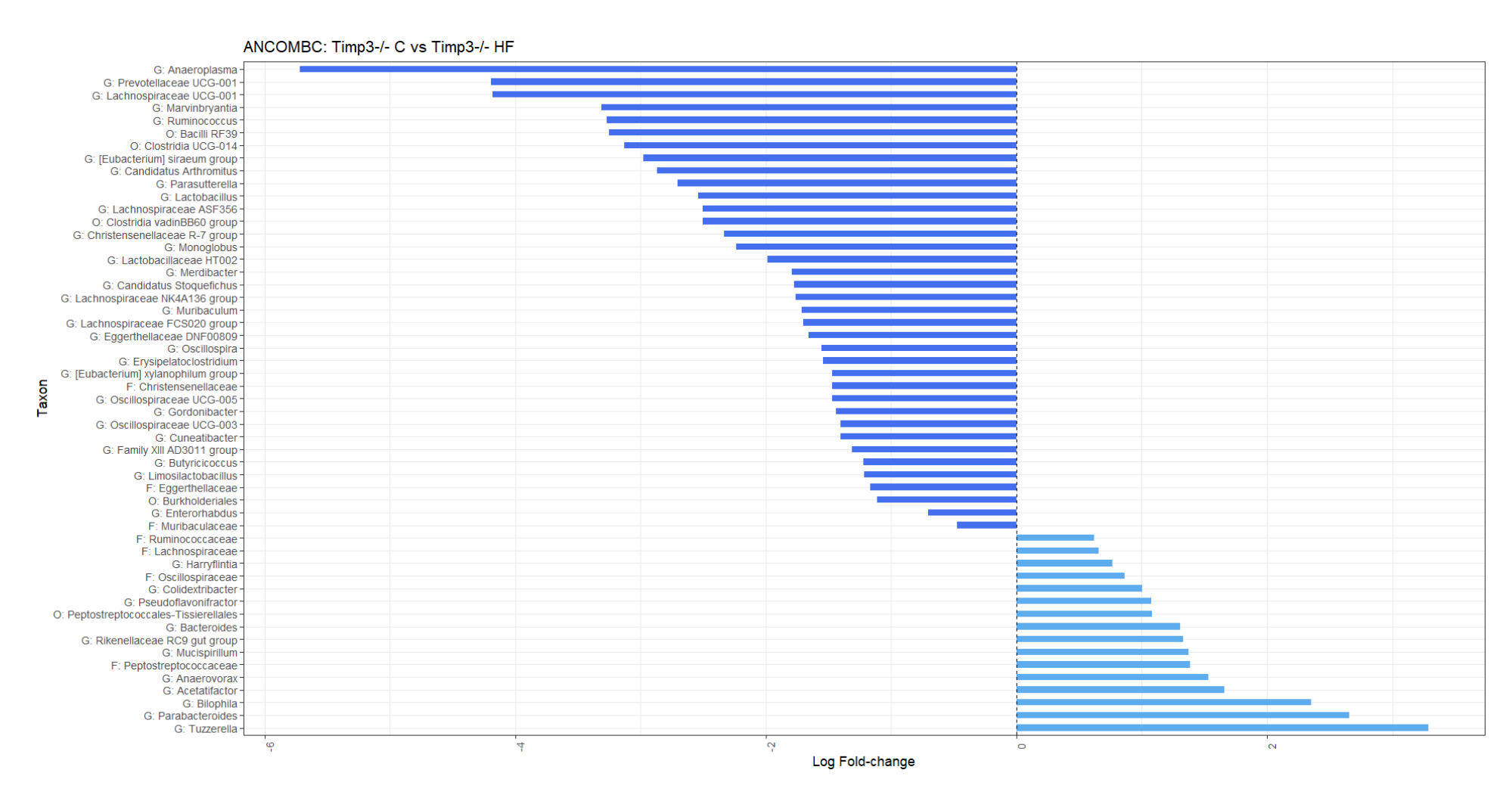


Figure 4.16 Bar plot displaying the fold change of significant genera within the *Timp3*-/- high-fat group compared to the *Timp3*-/- chow group with all ages combined, identified by ANCOM-BC. Significance level was set at p = 0.01.

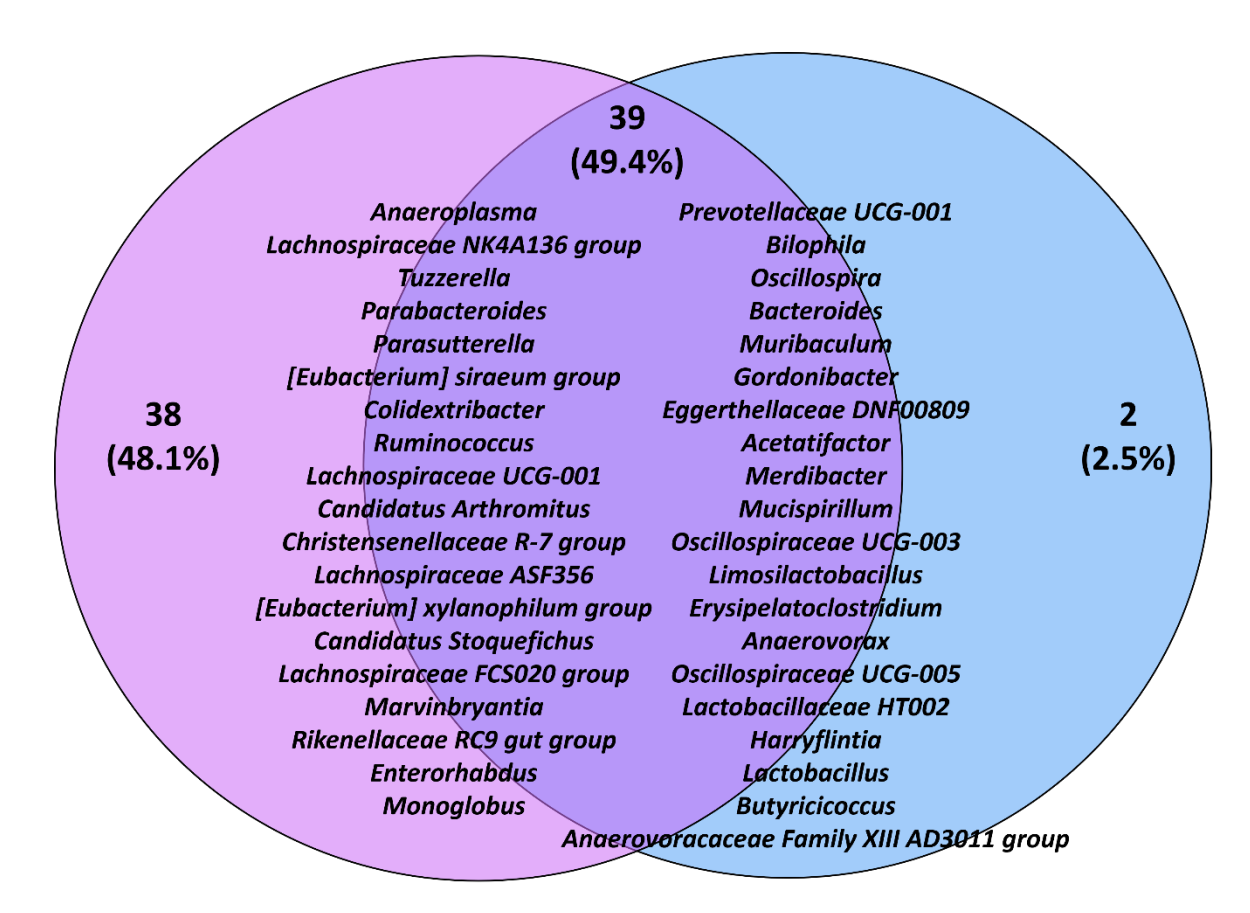


Figure 4.17 Venn diagram displaying the percentage of ASVs identified in *Timp3*-/- high-fat, compared to *Timp3*-/- chow, by DESeq2 and ANCOM-BC, with common genera between methods listed.

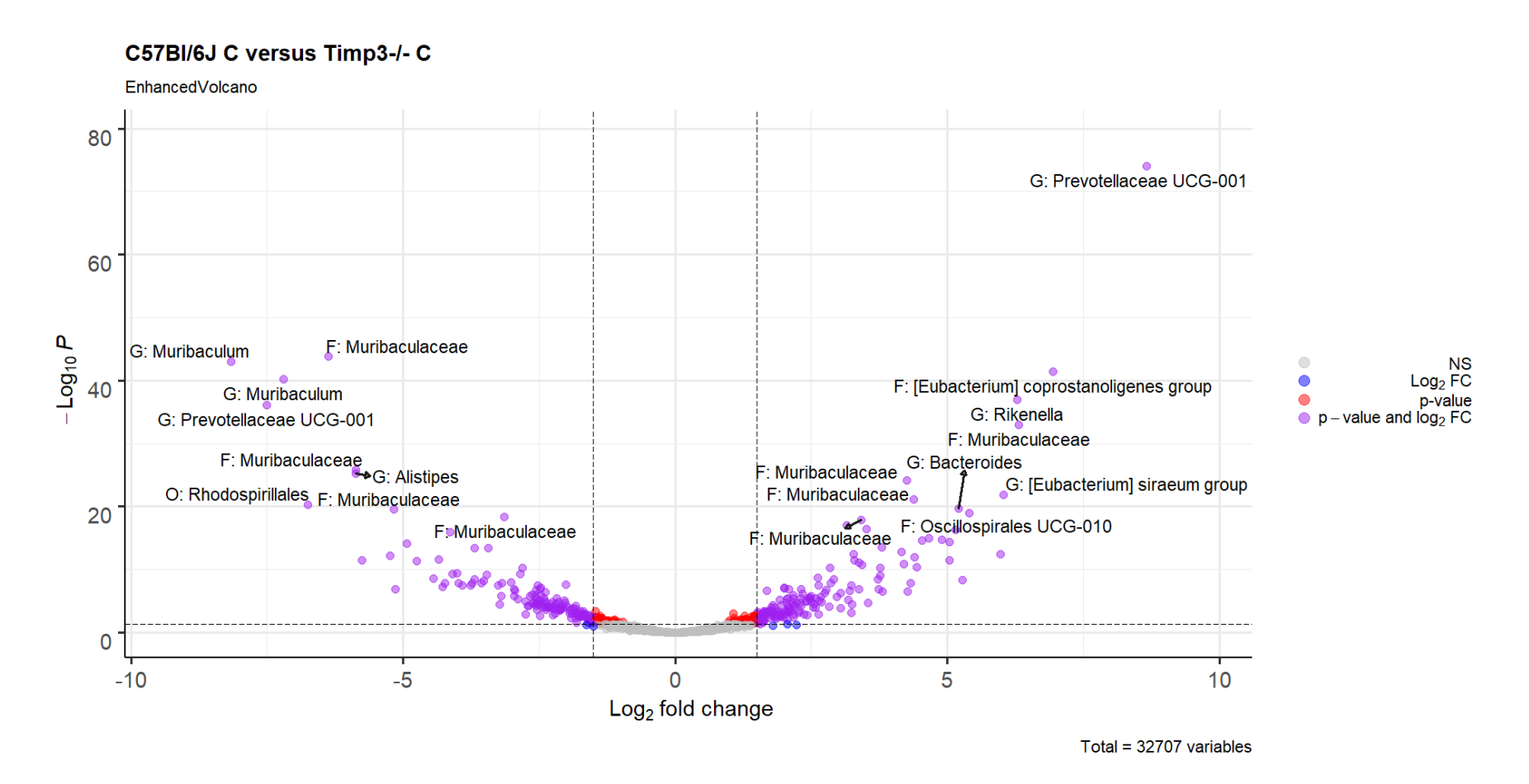


Figure 4.18 Volcano plot displaying the fold change of genera within the *Timp3*-/- chow group compared to the C57Bl/6J chow group with all ages combined, identified by DESeq2. Grey points indicate non-significant ASVs. Red points indicate ASVs with a p-value lower than 0.01, blue points indicate ASCVs with a Log2 fold change more than +/-2 and purple points indicate ASVs that meet both these requisites. The 20 most significant ASVs are labelled.

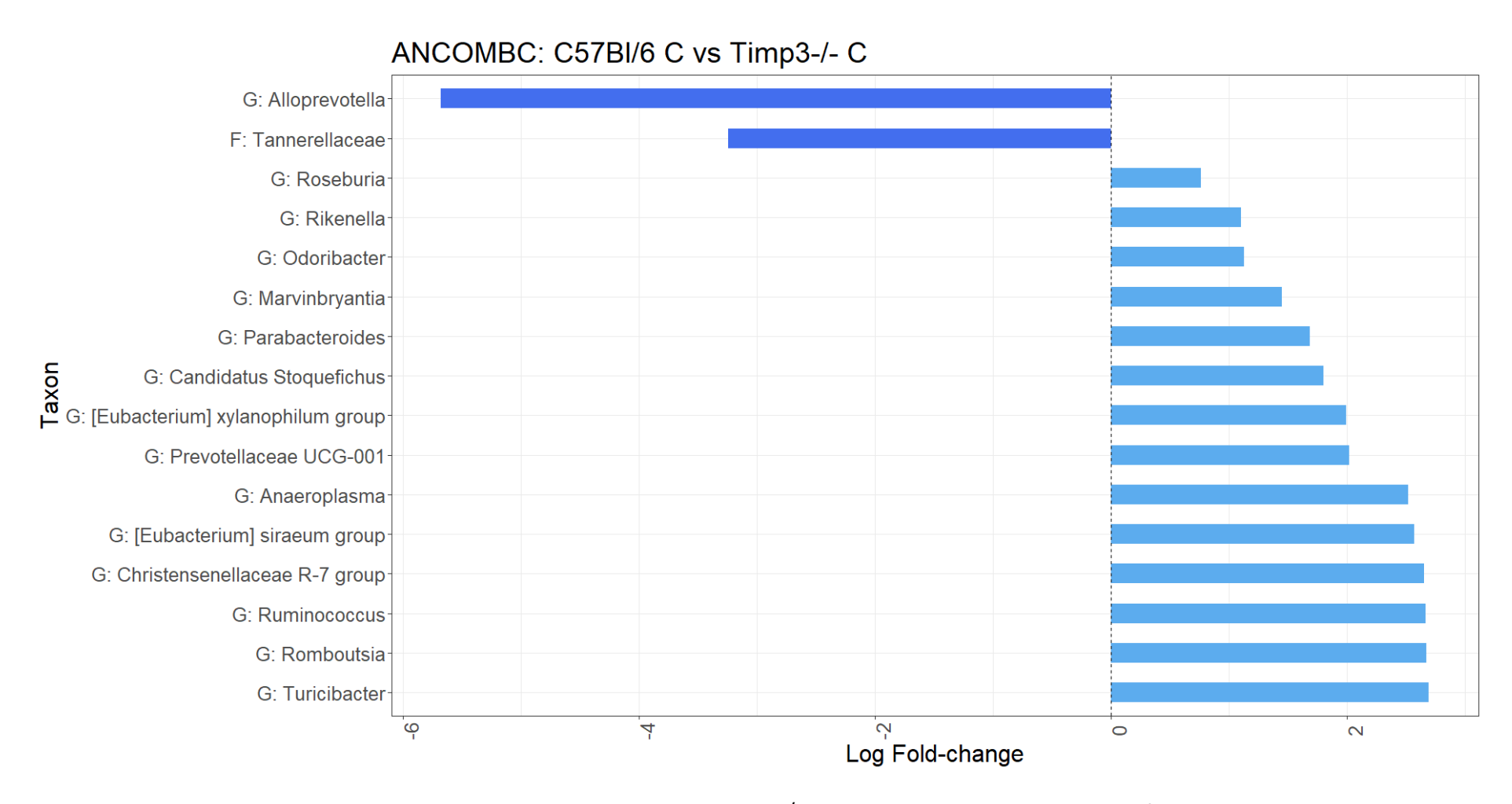


Figure 4.19 Bar plot displaying the fold change of significant genera within the *Timp3*-/- chow group compared to the C57BI/6J chow group with all ages combined, identified by ANCOM-BC. Significance level was set at p = 0.01.

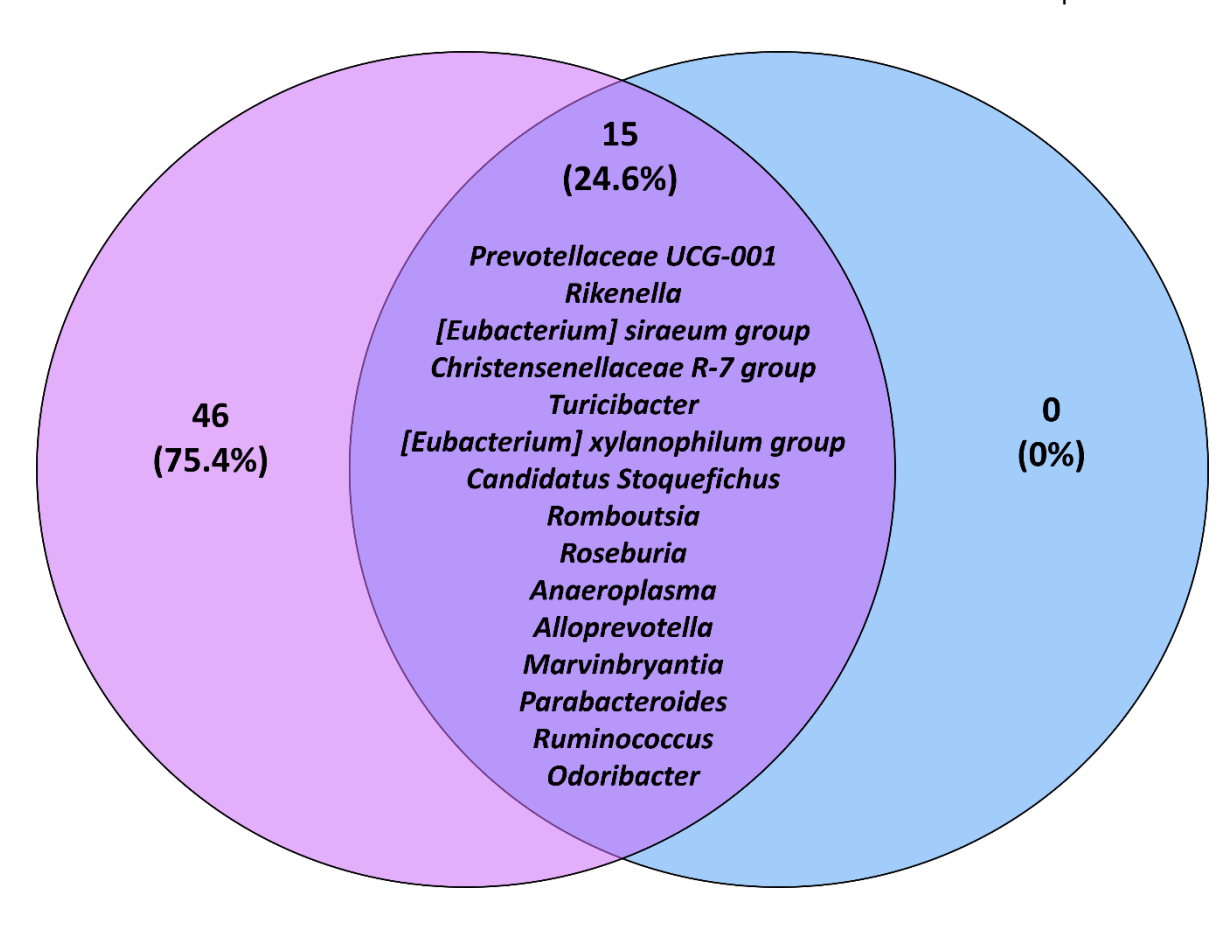


Figure 4.20 Venn diagram displaying the percentage of ASVs identified in *Timp3*-/- chow, compared to C57BI/6J chow, by DESeq2 and ANCOM-BC, with common genera between methods listed.

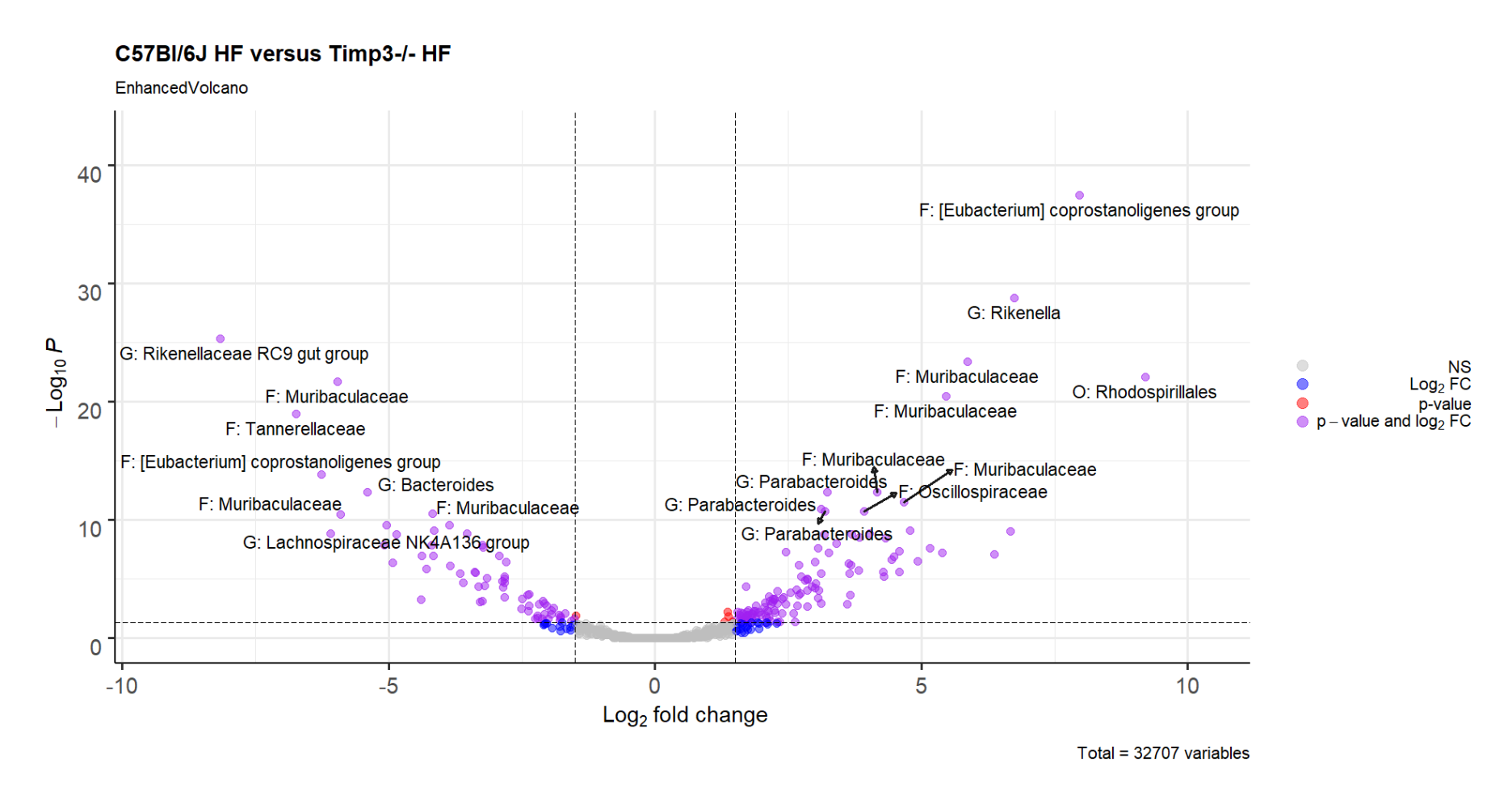


Figure 4.21 Volcano plot displaying the fold change of genera within the *Timp3*-/- high-fat group compared to the C57Bl/6J high-fat group at seven weeks of age, identified by DESeq2. Grey points indicate non-significant ASVs. Red points indicate ASVs with a p-value lower than 0.01, blue points indicate ASCVs with a Log2 fold change more than +/-2 and purple points indicate ASVs that meet both these requisites. The 20 most significant ASVs are labelled.

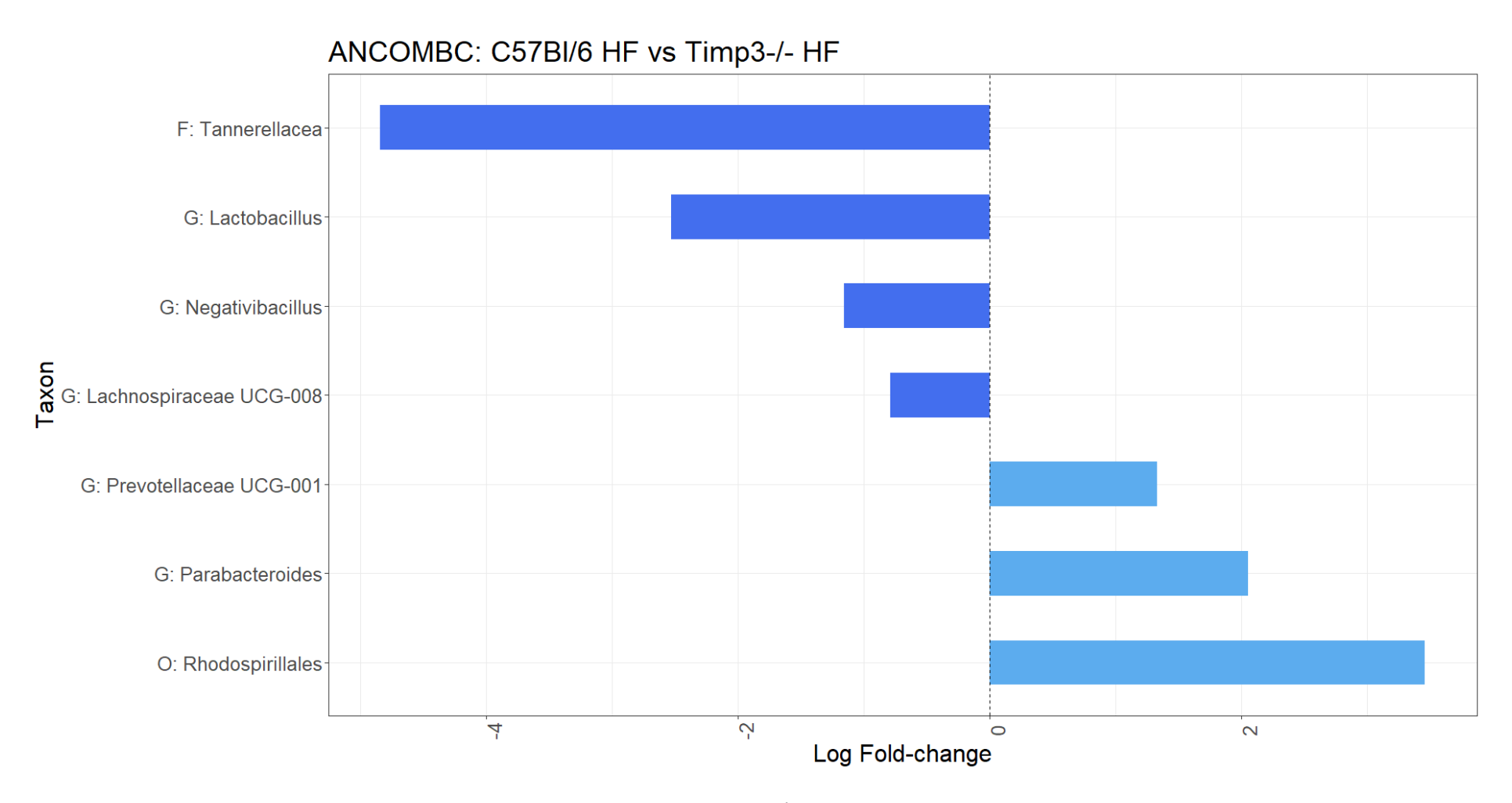


Figure 4.22 Bar plot displaying the fold change of significant genera within the *Timp3*-/- high-fat group compared to the C57BI/6J high-fat group with all ages combined, identified by ANCOM-BC. Significance level was set at p = 0.01.

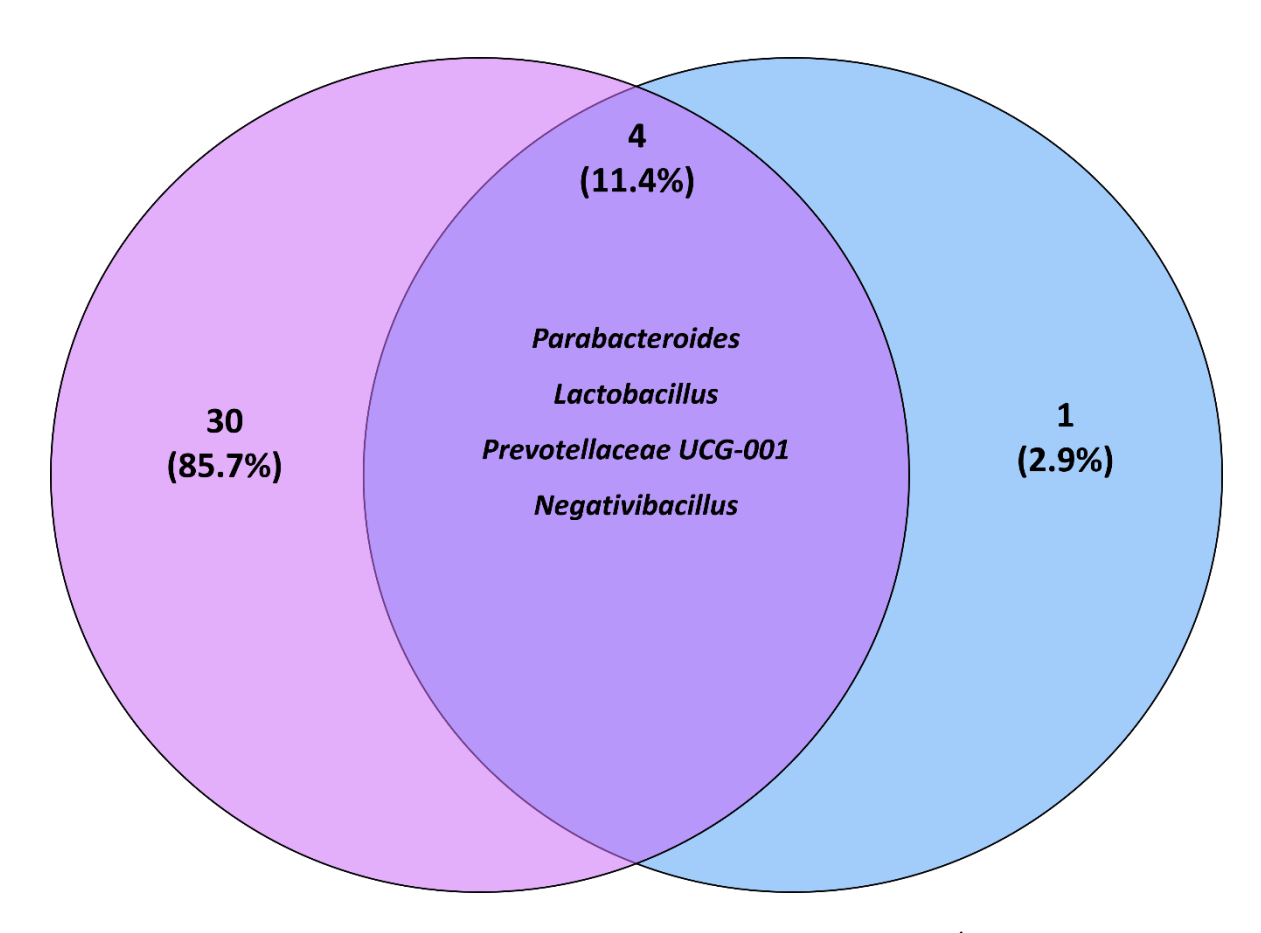


Figure 4.23 Venn diagram displaying the percentage of ASVs identified in *Timp3*-/- high-fat, compared to C57BI/6J high-fat, by DESeq2 and ANCOM-BC, with common genera between methods listed.

4.4.4 Differential Abundance Summary

The most significantly altered genera in both DESEq2 and ANCOM-BC analysis are presented in **Table 4.1**. A total of 21 genera were identified, most in response to HFD. The remaining significant ASVs identified can be found in **Appendix E**.

Table 4.1 Summary table of selected genera identified in differential abundance analysis. Genera listed are those which presented significant differences between the genotypes. Arrows represent increase (♠) or decrease (▶) in abundance.

Phylum	Genus	High-fat (v chow)		<i>Timp3^{-/-}</i> (v C57Bl/6J)	
		C57BI/6J	Timp3 ^{-/-}	Chow	High-fat
Bacteroidota	Parabacteroides	A	<u> </u>		
Bacillota	Lactobacillus	<u> </u>	<u>↑</u>	<u> </u>	↑
Bacteroidota	Prevotellaceae UCG-001	Ψ	Ψ	^	^
Bacillota	Negativibacillus				Ψ
Mycoplasmota	Anaeroplasma	Ψ	Ψ	^	
Bacillota	[Eubacterium] siraeum group		Ψ	^	
Bacillota	Ruminococcus		Ψ	^	
Bacteroidota	Rikenella			^	
Bacillota	Turicibacter			^	
Bacillota	Roseburia			^	
Bacteroidota	Odoribacter			^	
Bacillota	Christensenellaceae R-7 group		Ψ	^	
Bacillota	[Eubacterium] xylanophilum group		Ψ	^	
Bacillota	Candidatus Stoquefichus		Ψ	^	
Bacillota	Marvinbryantia	Ψ	Ψ	^	
Bacteroidota	Alloprevotella	^		4	
Bacillota	Romboutsia	^		^	

4.4.5 Measures of Microbial Activity within the *Timp3*-/- Mouse

4.4.5.1 Expression of Toll-like Receptor 4

Mean fold change and SEM for expression of toll-like receptor 4 (Trl4) in liver and colon samples from $Timp3^{-/-}$ mice on C and HF diets, and controls, at 5, 7, 10, 15 and 17 weeks old are shown in **Figures 4.24 and 4.25**, respectively. One-way ANOVA with Tukey's multiple comparisons was used to test for differences between $\Delta\Delta$ ct values. No significant changes in expression were seen in either tissue type.

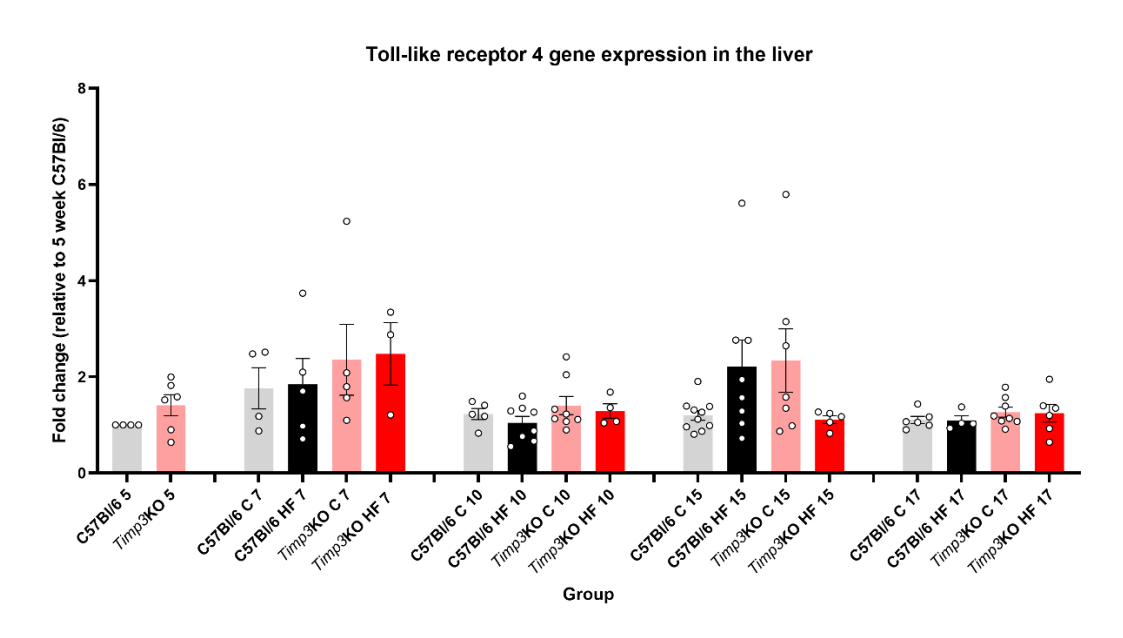


Figure 4.24 *Tlr4* gene expression in the liver of *Timp3*-/- male mice at ages 5, 10, 15 and 17 weeks old, following high-fat diet from 5 weeks. Mean fold change ± SEM from RT-qPCR gene expression in male *Timp3*-/- liver samples on chow (C) and high-fat (F) diets, and C57BI/6 controls. n=3-10 biological samples per group. Data are normalised to 5-week-old C57BI/6 and *β-actin* and *Gapdh* internal control genes. One-way ANOVA with multiple comparisons used to test for differences.

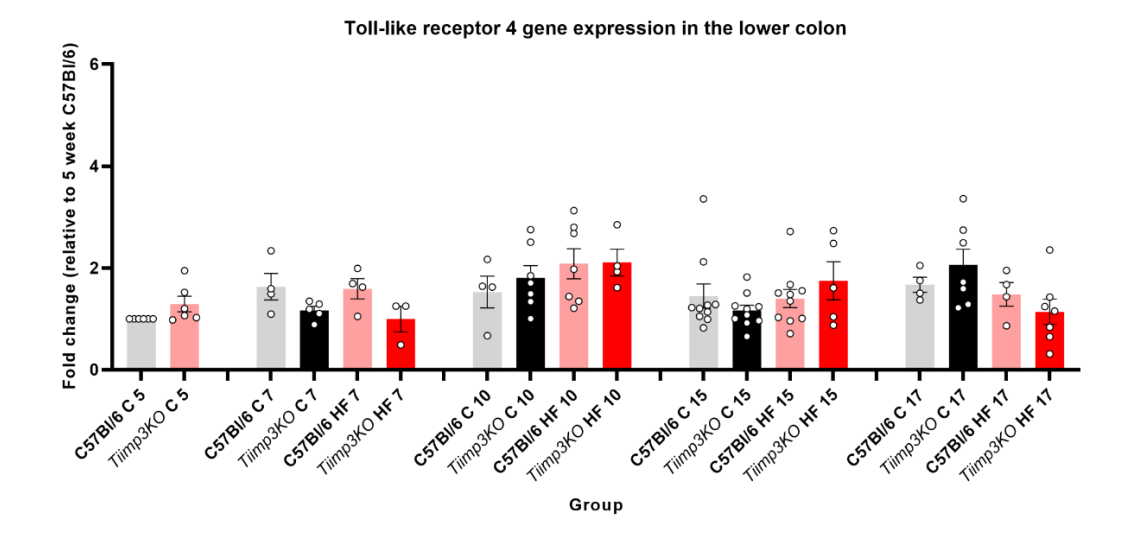


Figure 4.25 *Tlr4* gene expression in lower colon of *Timp3*-/- male mice at ages 5, 10, 15 and 17 weeks old, following high-fat diet from 5 weeks. Mean fold change ± SEM from RT-qPCR gene expression in male *Timp3*-/- liver samples on chow (C) and high-fat (F) diets, and C57Bl/6 controls. n=3-10 biological samples per group. Data are normalised to 5-week-old C57Bl/6 and *β-actin* and *Gapdh* internal control genes. One-way ANOVA with multiple comparisons used to test for differences.

4.5 Discussion

The mouse digestive tract comprises the mouth, oesophagus, stomach, duodenum, jejunum, ileum (small intestine), cecum, colon and rectum (large intestine). Each section of the digestive tract has a distinct microbial composition. Most studies investigating the mouse gut microbiome use either colon content or faecal samples. Human colon content is obviously difficult to sample and therefore faecal samples are more widely used. However, faecal microbiota samples are not necessarily representative of the flora within the colon which may impact application of study findings. The cecum (first section of the colon) is more densely populated with bacteria than the small intestine and is the major site of gut bacterial fermentation, producing short-chain fatty acids, free fatty acids, and secondary bile acids, among other products. Along the colon, bacterial fermentation continues, particularly in the upper colon. By the time faeces is excreted, microbial density increases 100-fold and the proportions of specific bacteria within the faeces differ greatly to those seen in the cecum or colon. In this study, colon content was analysed to capture a more accurate picture of bacteria involved in fermentation processes (Brown et al., 2018; Lyra et al., 2012; Marteau et al., 2001).

4.5.1 Overall community composition

Colon content samples were taken from mice aged between 5 and 15 weeks old in order to investigate the development of the *Timp3*-/- gut microbiota. Previous studies have demonstrated significant changes due to aging within humans and mice (Langille et al., 2014; Yatsunenko et al., 2012). In this study, however, age conferred negligible differences to the gut microbiota. This could be due to a dominating effect of diet and genotype. Therefore, experimental groups were analysed with all ages combined. However, plots per age group can be found in **Appendix E.**

Overall community structure, as measured by beta diversity metrics, was more similar between genotypes although diet caused huge community divergence. When measuring alpha diversity variation, the addition of HFD again had a significant effect. In this case, the HFD groups had overall a significantly decreased number of observed species, diversity, richness, and evenness across all indices. The *Timp3*-/- chow group showed decreased species number and richness compared to the WT chow, however, no difference was seen between the two genotypes under HFD. This suggests that although the absence of *Timp3*-/- causes distinct changes to the gut microbial composition, its effect could be masked by the HFD, causing communities to homogenise. The decreases in beta and alpha diversity under HFD conditions is concurrent with current literature (Chan et al., 2016; Heisel et al., 2017).

4.5.2 Differential abundance analysis

Following the changes seen in overall community structure, differential abundance analysis was used to identify significantly different genera in the experimental groups. Most genera identified belong to the Firmicutes (Bacillota) phylum. Increased Firmicutes abundance is associated with obesity (Koliada et al., 2017; Olivia Maurine Jasirwan et al., 2021; Riva et al., 2017). Naturally, on a chow diet, *Timp3*-/- mice have increased abundance of many of these *Firmicutes*. This might indicate a predisposition to diet-induced obesity.

Out of the most significantly different genera, *Parabacteroides* was increased in the *Timp3*-/-mouse and under HFD conditions. Members of this genus are recognised as potentially probiotic and confer host benefits via SCFA production and bile acid metabolism. Although some studies have reported increased abundance in obesity and diabetes (Wu et al., 2010), many have reported a negative association with these diseases (Lee et al., 2018; Wang et al., 2019). In this study, the increase in this genus under HFD suggests positive association with obesity. This increase may be due to diet composition, however, as the bacteria are also enriched in mice on a ketogenic diet (high fat, low carbohydrate) in epilepsy models (Olson et al., 2018). They are known to have a dichotomous role in host metabolism.

In agreement with current literature, the probiotic *Lactobacillus* genus is decreased in HFD *Timp3*^{-/-}. The *Timp3*^{-/-} mouse has lower abundance of these bacteria compared to the wild-type.

Prevotellaceae UCG 001 is naturally more abundant in the *Timp3*-/-mouse but decreased under HFD conditions. Members of *Prevotellaceae* are seen to decrease in abundance in obesity models and are associated with a healthy metabolic phenotype which supports what was seen in this study. However, members of this group are known to produce succinate which is considered pro-inflammatory and linked to cardiovascular diseases (Osuna-Prieto et al., 2021). Although serum butyrate was decreased in these mice, other SCFAs including succinate were not measured. Thus, it could be worth measuring succinate specifically in future studies to evaluate the implications of *Prevotellaceae* UCG 001 abundance.

Two *Eubacterium* groups were among the most significantly different genera identified by differential abundance analysis, *Eubacterium siraeum* and *Eubacterium xylanophilum*. Both were naturally increased in the *Timp3*-/- mouse but subsequently decreased under HFD, resulting in comparable levels to the WT HFD mice. Decreased abundance in obesity is seen in mice and humans (Jones et al., 2019; Wei et al., 2021).

The pattern shown by the *Eubacterium* groups (enriched in the *Timp3*-/- mouse but reversed under HFD) is also seen in the following groups: *Ruminococcus, Rikenella, Turicibacter, Roseburia, Odoribacter* and *Christensenellaceae* R7. Where differences in these groups are seen between chow diet groups, none are seen between mice on HFD. This further suggests the high-fat diet has a larger effect than genotype on gut microbiome composition and may even negate some effects of the *Timp3* gene deletion. Members of these genera are associated with healthy metabolic phenotypes and have decreased abundance in obesity. Increased abundance in the *Timp3*-/- chow group may be linked to their naturally lower body weight and energy expenditure.

Among the genera identified in the differential abundance analysis, *Oscilibacter*, *Lachnospiraceae* UCG 004, *Lachnospiraceae* NK4A136 and *Roseburia* are known butyrate producers. At this study endpoint, butyrate concentration in the blood plasma was measured and showed a significant decrease in the *Timp3*-/- HF group only, suggesting the combined effect of the genotype and HF diet caused a change in gut microbial composition leading to altered bacterial metabolism. Butyrate, a SCFA, is the major energy source of intestinal epithelial cells and lack of butyrate is linked to colitis (Chapman et al., 1994; Hague et al., 1996). Many murine studies show that butyrate improves metabolic syndrome and reduces development of NAFLD by improving gut-barrier integrity and modifying the gut microbiome composition, including decreasing abundance of *Rikenellaceae* and *Bilophila* species and increasing *Akkermansia*, *Roseburia* and *Coriobacteriaceae* (F. Gao et al., 2019; Ye et al., 2018; Zhou et al., 2017).

The expression of toll-like receptor 4 (*Tlr4*), which recognises bacterial endotoxin, was measured in the liver and colon at multiple ages. Although no significant differences were seen in this study, other studies have shown *Tlr4* plays a role in inflammation during obesity and liver fibrosis, and its expression can be decreased with butyrate supplementation (Kang et al., 2017; K. A. Kim et al., 2012; Ren et al., 2022).

4.6 Strengths and limitations

Colon content was sampled in this study to assess the *Timp3*-/- gut flora. Studies investigating gut microbial communities also often use faecal samples. Since each section of the gastrointestinal (GI) tract has a distinct microbial flora, results obtained in this study may not be comparable to other published literature that sample different sites. In addition, by focusing on the colon content only, potential important information from other sites in the GI tract may have been excluded. For these reasons, it may be useful to sample different areas of the gut in future research.

Many experiments which use diet-induced obesity models only study the endpoint. Here, the use of a longitudinal study allowed the analysis of the development of the mouse microbiome over the period of which HF diet was administered. However, to maintain alignment with the three Rs of animal research (replacement, reduction, and refinement), sample number was kept to a necessary minimum. Age groups were combined in order to mitigate the effect of a low sample size, however the high variability of the microbiome at younger ages may have impacted the identification of genera that are significant in the older age group. Future studies could use an increased sample number to confirm this data.

4.7 Conclusions

In conclusion, this study showed that the *Timp3*-/- gut microbiome composition is significantly different to the WT. On chow diet, the *Timp3*-/- had decreased abundance of three bacterial genera, *Oscilibacter, Parasutterella* and *Erysipelatoclostridium* associated with metabolic health, and increased abundance of three genera, *Rikenellaceae* RC9 gut group, *Rikenella*, and *Prevotellaceae* UCG 001, associated with obesity. Differences initially seen in the *Timp3*-/- mouse are diminished under HFD conditions, and characteristics of the microbiota become more similarto the WT HFD effect. This suggests that the HF diet effect overpowers the effect of the

Chapter 4

Timp3-/-, rather than producing a combined effect which exacerbates DIO. Although, the *Timp3*-/- HFD group alone showed significantly decreased plasma butyrate, indicating there is some compounding effect of *Timp3* and HFD in bacterial metabolism.

Chapter 5 Effects of *Timp3* Deletion on Cardiovascular Function in Mice

5.1 Introduction

Diagnosing factors for metabolic syndrome (MetS) overlap with risk factors for cardiovascular disease (CVD), and MetS can lead to the development of CVDs (Powell et al., 2010). The integrity of blood vessel structure is highly important in CVD pathology, as changes in the vasculature can lead to several pathologies, including hypertension and vascular distension (Golledge & Norman, 2010; Kalra & Shanahan, 2012). Changes in the vascular extracellular matrix (ECM) are also highly implicated in the pathology of CVD (Chistiakov et al., 2013). One such component of the ECM, TIMP3, is associated with atherosclerosis and other CVDs (Cardellini et al., 2009; Fan et al., 2014; Stöhr et al., 2015; Zhabyeyev et al., 2018).

Preliminary data from the Pender lab group, Clinical and Experimental Sciences, Faculty of Medicine, University of Southampton, shows that female *Timp3*-/- mice kept in specific pathogen-free housing have a shorter life span and elevated blood pressure compared to the female C57Bl/6J mice. The vasoactivity of the aorta and the detailed composition of the aorta ECM, in the absence of TIMP3, has yet to be determined. Therefore, this chapter aims to investigate the effect of *Timp3* deletion in female mice on aorta ECM and on the contractility of the aorta.

5.2 Aims and Hypothesis

The aim of this study was to investigate the effect of *TIMP3* deletion in the female mouse aorta, in relation to its contractility and ECM composition, in comparison to age-matched female C57BI/6J control mice. Both these mouse genotypes were kept in a specific pathogen-free (SPF) environment.

The hypothesis was that the deletion of *TIMP3* in female mice will result in dysfunctional cardiovascular function and impaired aorta contractile and relaxation responses, due to alteration in the ECM structure of the aorta.

Specific objectives were as follows:

- Investigate the effect of a high-fat diet on the phenotype (body weight, fat depot weights and blood pressure) and the functional responses and reactivity of isolated aortas by myography from 16-week-old female Timp3^{-/-} mice kept in SPF.
- 2. Characterise and compare the phenotype (body weight, fat depot weights and blood pressure) and the functional responses and reactivity of isolated aortas by myography between the chow-fed 16-week-old and 30-week-old female *Timp3*-/- mice kept in SPF.
- 3. Examine the morphology of the aorta of the 30-week-old female *Timp3*-/mice on using histological techniques and label-free second-harmonic
 generation microscopy and two-photon-excitation autofluorescence
 (TPEF) microscopy.
- 4. Determine the gene expression levels of metalloproteinases (Mmp2, Mmp9, and Mmp12), collagens (Col1 and Col3) and glucose transporter 1 (Glut1) in aortas of the 30-week-old chow-fed SPF-housed female Timp3^{-/-} mice

5.3 Methods

To investigate vascular function, female *Timp3*-/-and C57BI/6J wild-type mice were used at 16 and 30 weeks old with subgroups in the 16-week-old group that were given the HF diet from 5 weeks of age. All mice were house in a specific-pathogen free environment with ad-libitum access to food and water.

In this study, plethysmography, wire myography, and histological techniques were used to investigate blood pressure, vasoactivity and histology of the aorta, respectively, in female *Timp3*-/-mice. A portion of the wire myography experiments and aorta staining and imaging were carried out with the assistance of a CUHK summer student, Eileen Li from the Chinese University of Hong Kong. A BMedSci project student Rhiannon Nielsen also assisted with the myography in the 16-week-old groups.

A custom-built multiphoton imaging setup was used for second harmonic generation (SHG) and two-photon excitation fluorescence (TPEF) imaging (Bionanophotonics group, Institute for Life Sciences, University of Southampton, UK). Details can be found in **Chapter 2.14**. The microscope objective used for all images was 20x/0.5. The tiled images were acquired using Scanlmage 2016b and were later stitched together during analysis in Fiji. Using Fiji, SHG images were thresholded using the Triangle method and TPEF using the default method. The pixel area of collagen and elastin within each section was quantified for analysis. Details can be found in **Chapter 2.16**.

Individual collagen fibre extraction and analysis were performed using CT-FIRE v3.0 (Laboratory for Optical and Computational Instrumentation, LOCI) (Bredfeldt et al., 2014). This program identifies four fibre properties. Width is the average width along the fibre length in pixels. Angle is the fibre angle with respect to the horizontal axis (ranging between 0-180 degrees). Length is the distance of the fibre from end to end in pixels. Straightness is the distance between the two endpoints of the fibre divided by the fibre length and ranges between 0-1.

Expression of *Mmp2*, *Mmp9*, *Mmp12*, *Col1*, *Col3* and *Glut1* genes within the 30-week aorta was measured using RT-qPCR.

Statistical analysis was conducted in GraphPad Prism v9.4.1, using unpaired t-test or 2-way ANOVA where appropriate.

5.4 Results

- 5.4.1 Effects of a high fat diet in 16-week-old *Timp3-/-* female mice
- 5.4.1.1 Effect of a high fat diet on body weight, gonadal, retroperitoneal, inguinal, and intrascapular brown fat in 16-week-old *Timp3*^{-/-} female mice

Total body weight, heart weight and various fat depot weights (expressed as a percent of total body weight) of $Timp3^{-/-}$ female mice at 16 weeks old on chow (C) and high-fat (HF) diets, and their C57Bl/6J controls, are shown in **Figure 5.1**. The addition of a high-fat diet caused increases in total body weight, gonadal, inguinal, and retroperitoneal fat depot weights between the chow groups and their high-fat fed counterparts in $Timp3^{-/-}$ mice. Body weight was significantly increased in the $Timp3^{-/-}$ (**Figure 5.1 (a) c d** p < 0.05). An increase in gonadal, inguinal, and retroperitoneal fat depot weight was also seen in C57Bl/6J mice on HF diet (**Figure 5.1 (d), (e)** and **(f)**, p < 0.0001, p < 0.01 and p < 0.05, respectively). Significant differences between the two genotypes were not observed in any measured category, nor were any significant differences seen between any groups in heart or iBAT weight.

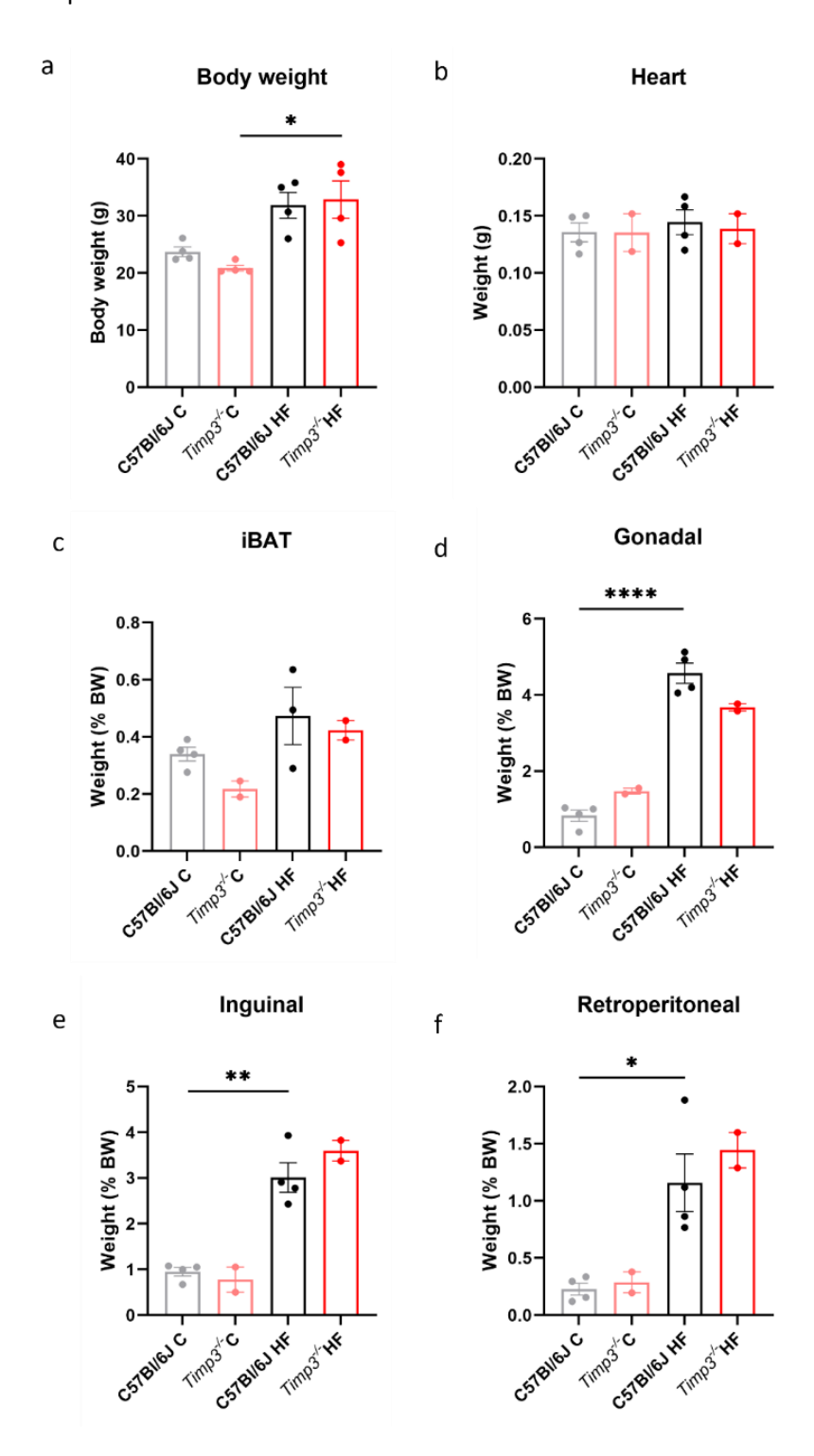


Figure 5.1 Body weight, heart weight and fat depot weights in 16-week-old *Timp3*-/- and C57Bl/6J female mice on either a standard chow or high fat diet. Body and heart weights (a and b, respectively) and fat depot weights (c-f, expressed as a percentage of total body weight) of female *Timp3*-/- and C57Bl/6J control mice at 16 weeks old, on either chow (C) or high-fat (HF) diet. iBAT, intrascapular brown adipose tissue. n = 2-4 per group. Values are means ± SEM, expressed as a percentage of total body weight. Tukey's multiple comparisons was used to test for differences. *p<0.05, **p<0.01, ****p<0.0001.

5.4.1.2 Effect of a high fat diet on a ortic function in 16-week-old *Timp3-/-* female mice

Myography results of the passive and active responses generated by aorta tissue from 16 week-old *Timp3*-/- and C57BI/6J female mice fed a standard chow (C) or HF diet are shown in **Figure 5.2**. Noradrenaline (NA) works to constrict blood vessels, whereas carbachol (Cch) and sodium nitroprusside (SNP) work to relax the vessels (Benham and Tsien, 1988; Bolton et al., 1984; Bolton and Clapp, 1986; Kreye et al., 1975). Myography measures the contraction or relaxation response of the blood vessel, in this care the aorta, to these drugs. No significant changes were observed between any of the groups in response to mechanical stretching or the administered drugs.

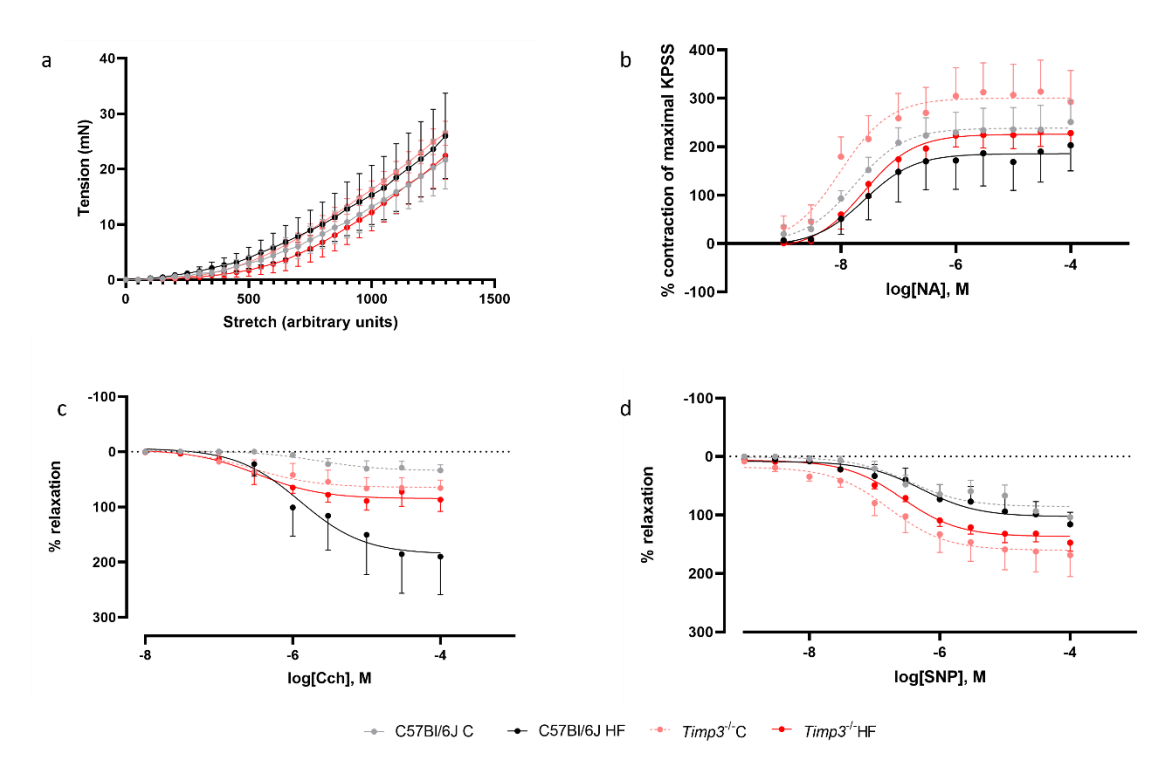


Figure 5.2 Tension generated during myography by aortic tissues taken from 16-week-old

Timp3^{-/-} and C57BI/6 female mice on either a standard chow (C) or high fat (HF)

diet. (a) tension generated in response to mechanical, incremental stretching; (b)

contraction generated in response to the cumulative concentration of noradrenaline

(NA); (c) relaxation generated in response to the cumulative concentration of

carbachol (CCh); and (d) relaxation generated in response to the cumulative

concentration of sodium nitroprusside (SNP). Values are means ± SEM, n = 4-10 per

group. Tukey's multiple comparisons was used to test for differences.

- 5.4.2 Phenotype and cardiovascular function in 30-week-old *Timp3*^{-/-} female mice
- 5.4.2.1 Comparison in body weight, gonadal, retroperitoneal, inguinal and intrascapular brown fat between the 30- and 16-week-old chow-fed *Timp3-/-* female mice

A comparison of the body weight, heart weight and the weights of the various fat depots between the chow-fed *Timp3*-/- and C57BI/6J mice at 16 vs 30 weeks of age are shown in Figure 5.3. At 30 weeks old, the *Timp3*-/- mice had significantly lower body weight (**Figure 5.3a**) and gonadal fat weight (**Figure 5.3d**) compared to the C57BI/6J WT controls (both at p<0.01). Otherwise, no significant differences were seen in the heart weight (**Figure 5.3b**), iBAT (**Figure 5.3c**), inguinal and retroperitoneal fat (**Figures 5.3e & f**).

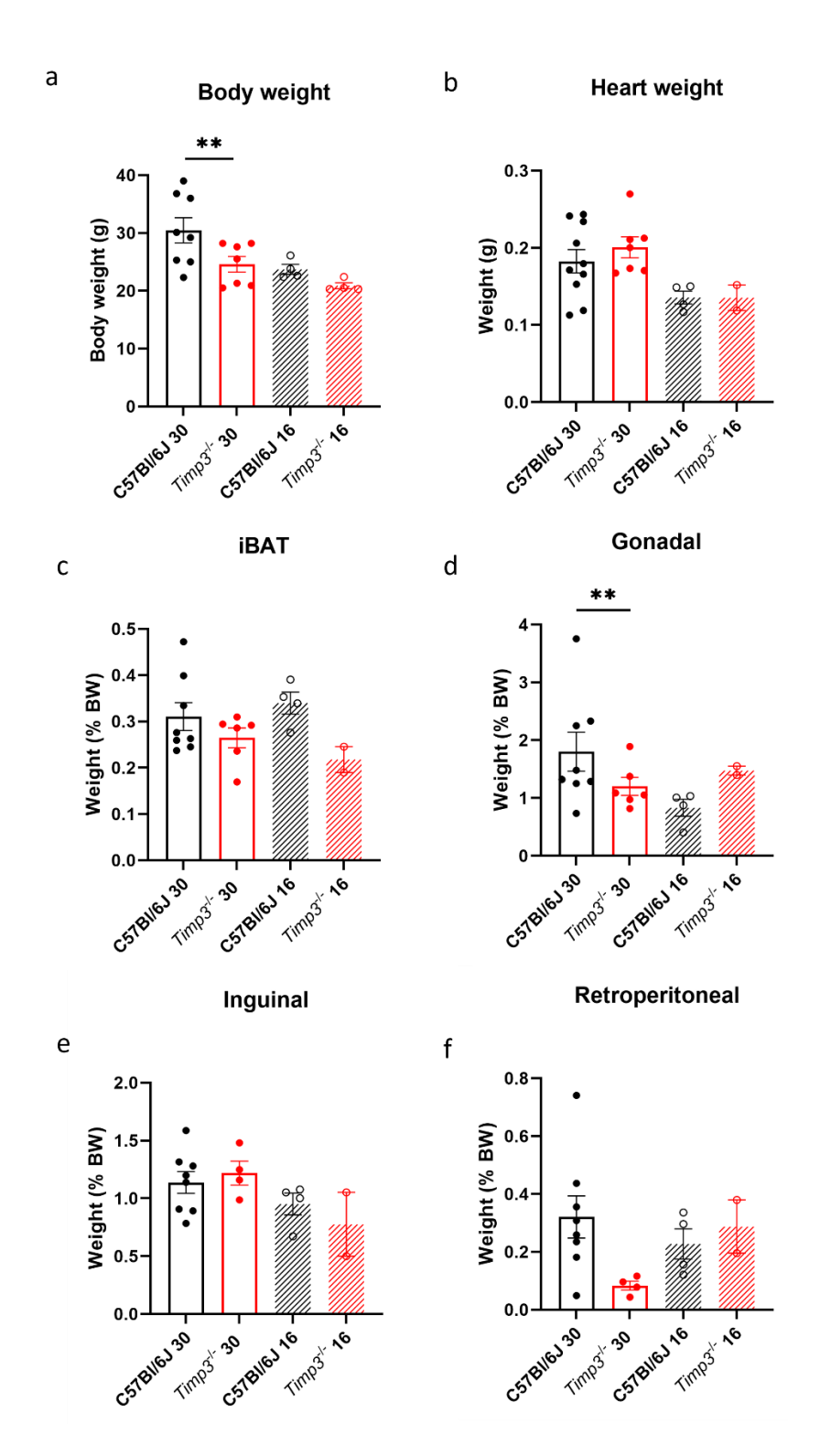


Figure 5.3 Body weight, heart weight and fat depot weights in 30- and 16-week-old *Timp3-/-* and C57BI/6J female mice. Total body and heart weights (a & b, respectively) and fat depot weights (c-f, expressed as a percentage of total body weight) in 30 and 16-week-old female *Timp3-/-* and C57BI/6J control mice on chow diet. Values are means ± SEM, n = 2-8 per group. Tukey's multiple comparisons was used to test for differences between means. **p<0.01.

5.4.2.2 Blood pressure and heart rate in 30-week-old *Timp3*^{-/-} female mice

The heart rate, systolic and diastolic blood pressure are shown in Figure 5.4. The heart rates were similar between the 30-week-old $Timp3^{-/-}$ females and the age matched C57Bl/6J WT controls on a similar chow diet (**Figure 5.4a** heart rate: $Timp3^{-/-}$ 665.4 \pm 16.38 vs WT 686.1 \pm 16.63 beats per minute). In the other hand, systolic and diastolic blood pressure in these 30-week-old $Timp3^{-/-}$ females were significantly elevated compared to age-matched C57Bl/6J WT controls (**Figure 5.4b** systolic blood pressure: $Timp3^{-/-}$ 107.4 \pm 4.75 vs WT 85.4 \pm 3.9 mmHg, p<0.01; **Figure 5.4c** diastolic blood pressure: $Timp3^{-/-}$ 84.3 \pm 3.9 vs WT 61.3 \pm 5.64 mmHg, p<0.01).

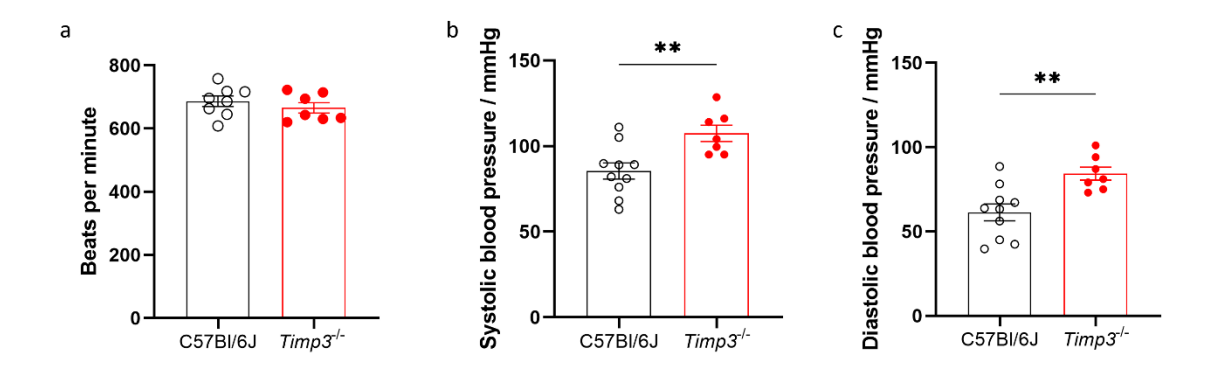


Figure 5.4 Heart rate and blood pressure in 30-week-old $Timp3^{-/-}$ female mice. Mean heart rate, systolic and diastolic blood pressure (a-c, respectively) in 30-week-old female chowfed $Timp3^{-/-}$ and C57Bl/6J control mice measured by plethysmography. Values are means \pm SEM, n = 7-10 per group. Unpaired two-tailed Student t-test was used to test differences between means. **p<0.01

Following the observed increase in blood pressure, Timp3-/- heart weight as a proportion of body weight was tested (**Figure 5.5** $Timp3^{-/-}$ mean 0.829 % ±0.063 versus C57Bl/6J 0.623 % ±0.083; p = 0.076). Although $Timp3^{-/-}$ heart weight was increased, the difference was not significant.

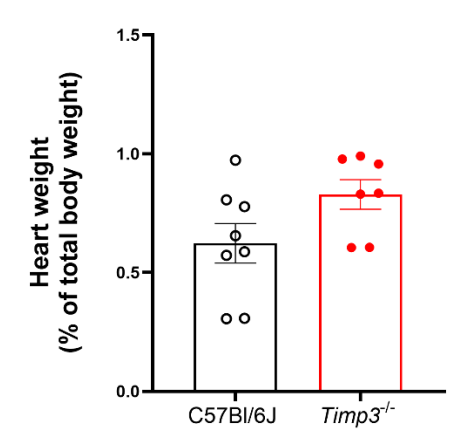


Figure 5.5 Heart weight in the 30-week-old female *Timp3-/-* **mouse, as a proportion of total body weight.** Mean heart weight expressed as a percentage of total body weight ± SEM in aged female *Timp3-/-* mice on chow diet, and C57BI/6J controls. n=7-8 biological samples per group. Two-tailed unpaired Student's t-test was used to test for differences (p = 0.0756).

5.4.2.3 Aortic function in 30-week-old *Timp3*^{-/-} female mice

Myography results of the tension generated in 30-week-old *Timp3*-/- and C57Bl/6J aorta, in response to selected drugs is shown in **Figure 5.5**. In response to mechanical stretching, there was no significant difference in the tension generated between the 30-week-old female *Timp3*-/- and C57Bl/6J control aorta tissues (**Figure 5.5a**) but there was significant difference between these two mouse groups in active responses (**Figure 5.5b & c**). In response to noradrenaline (NA), the *Timp3*-/- aortas had a significantly reduced contraction response compared to aortas from the C57Bl/6J controls (**Figure 5.5b**, p<0.05), as well as a significantly reduced relaxation response to carbachol (CCh) (**Figure 5.5c**, p<0.05). No significant difference in relaxation was seen in response to sodium nitroprusside (SNP) (**Figure 5.5d**).

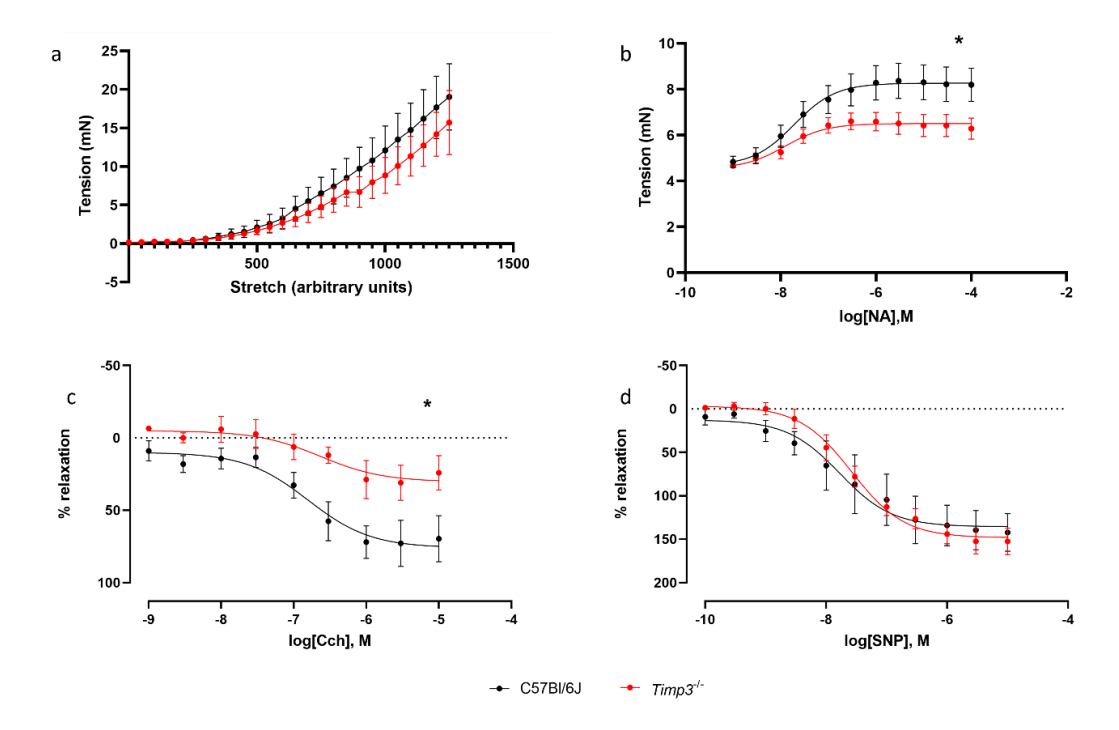


Figure 5.6 Tension generated during myography by aortic tissues taken from 30-week-old female *Timp3*-/- and C57BI/6 control mice on standard chow diet. (a) tension generated in response to mechanical, incremental stretching; (b) contraction generated in response to the cumulative concentration of noradrenaline (NA); (c) relaxation generated in response to the cumulative concentration of carbachol (CCh); and (d) relaxation generated in response to the cumulative concentration of sodium nitroprusside (SNP). Values are means ± SEM, n = 4-10. Unpaired two-tailed Student t-test was used to test for differences. *p<0.05

5.4.2.4 Comparison of aortic function between the 30- and 16-week-old *Timp3*-/- female mice

Myography results of the comparison in the tension generated by the aortas taken from 16-and 30-week-old *Timp3*-/- and C57Bl/6J female mice are shown in Figure 5.6. In response to mechanical stretching, no significant differences were observed in aortas from the four mouse groups (Figure 5.6a). However, the addition of NA resulted in significantly decreased contraction response in the aortas from the 30-week-old *Timp3*-/- female mice compared to the aortas from the 16-week-old *Timp3*-/- females (Figure 5.6b, p<0.01). No significant difference in contraction response to NA was observed between the aortas from the 16- and 30-week-old C57Bl/6J mice. On the other hand, the addition of CCh resulted in a significant increased relaxation of the aortas from the 30-week C57Bl/6J mice compared to the aortas from their 16-week counterparts (Figure 5.6c, p<0.05). No significant difference in relaxation in response to CCh was observed in aortas from the 16- and 30-week-old *Timp3*-/- female mice. Further, the addition of SNP resulted in

significantly reduced relaxation in aortas from the 30-week-old C57Bl/6J compared to the aortas from the 16-week-old C57Bl/6J mice (Figure 5.6d, p<0.05). No significant difference in relaxation in response to SNP was observed in aortas from the 16- and 30-week-old *Timp3*-/- female mice

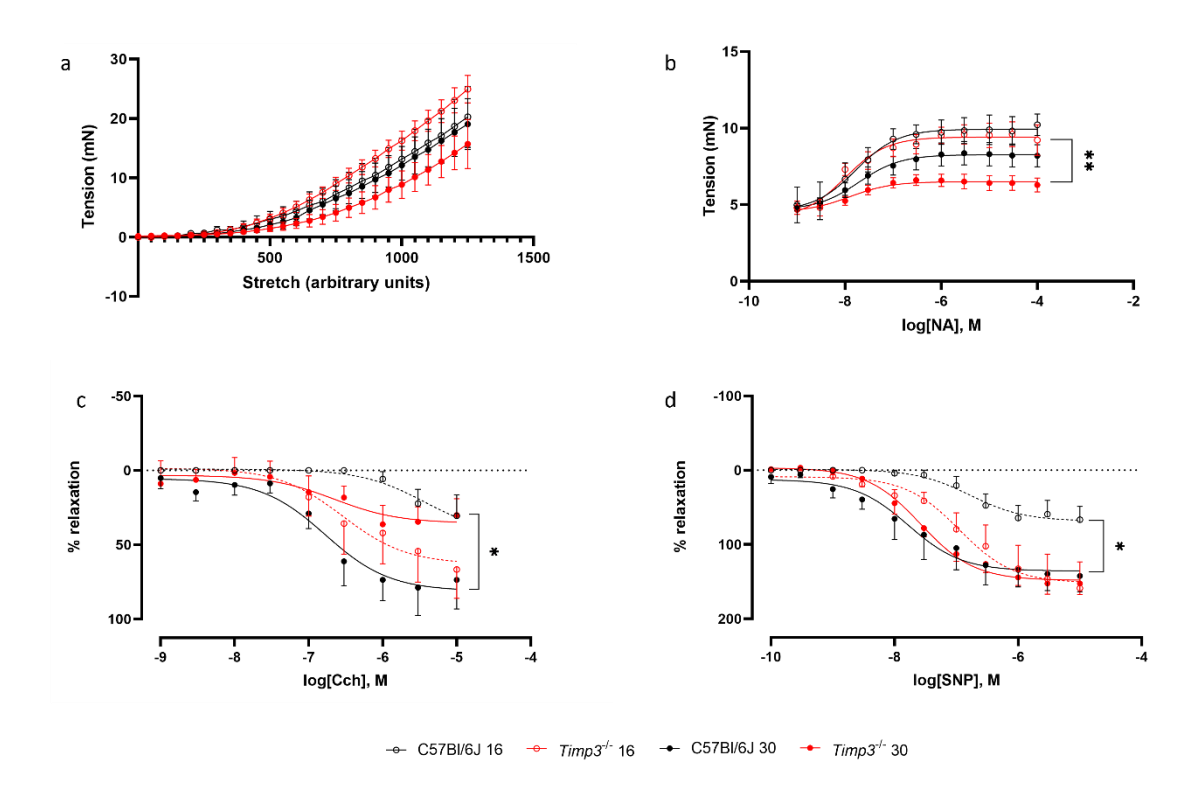


Figure 5.7 Tension generated during myography by aortic tissue in 16- and 30-week-old female *Timp3*^{-/-} and C57BI/6 female mice on chow diet. (a) tension generated in response to mechanical, incremental stretching; (b) contraction generated in response to the cumulative concentration of noradrenaline (NA); (c) relaxation generated in response to the cumulative concentration of carbachol (CCh); and (d) relaxation generated in response to the cumulative concentration of sodium nitroprusside (SNP). Values are means ± SEM, n = 4-10. Tukey's multiple comparisons was used to test for differences. *p<0.05, **p<0.01.

5.4.3 Morphology and structure of the aortas taken from 30-week-old *Timp3*^{-/-} female mice

5.4.3.1 Aortic wall width

Haematoxylin and eosin (H&E) stained sections of aortas taken from 30-week-old female *Timp3*^{-/-} and C57BI/6J control mice on chow diet were used to measure total aorta width and tunica media (smooth-muscle cell containing) width (Figure 5.7). No significant differences were found in aortic wall width between the 30-week-old *Timp3*^{-/-} and C57BI/6J female mice.

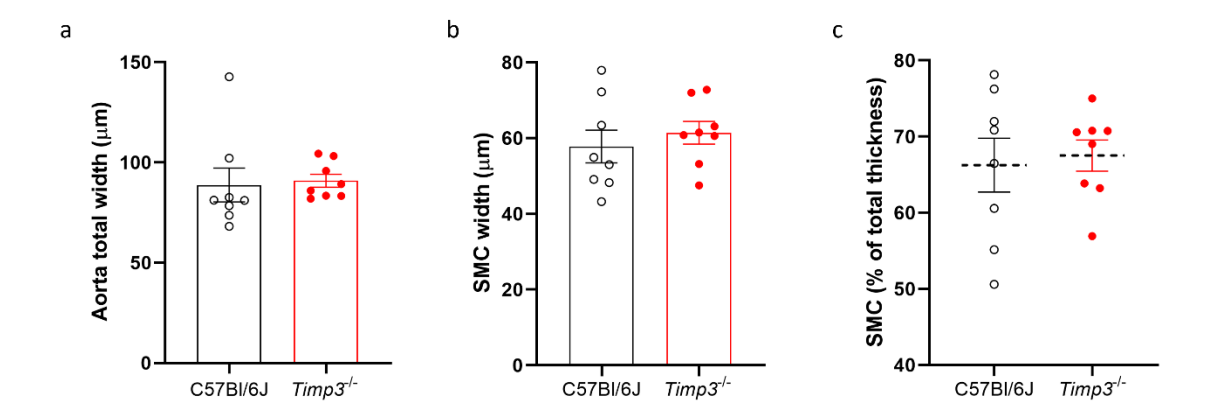


Figure 5.8 Total wall width and smooth-muscle cell layer width of the aortas taken from 30-week-old female *Timp3*-/- female and C57Bl/6J control mice. (a) total aorta wall width; (b) tunica media width; and (c) tunica media width as a proportion of the total aorta wall width. Measurements taken from H&E stained aorta sections using ImageJ. Values are mean ± SEM. n = 8. Unpaired two-tailed Student t-test was used to test for differences.

5.4.3.2 Measurement of collagen content within the cross-section of aortas by light and polarised-light microscopy

Sirius Red stained sections of the aortas from 30-week-old *Timp3*-/- and C57Bl/6J controls mice on chow diet were used to determine the collagen content of the aortas (**Figure 5.8**). In the representative figure (**Figure 5.8b**), the tunica adventitia is stained dark pink due to the high presence of collagen, tunica media and intima with comparatively less collagen is stained light pink. Following image analysis of the stained sections, there was a significantly increased pixel area of stained collagen in the aortas from the *Timp3*-/- female mice compared to C57Bl/6J animals (p<0.05).

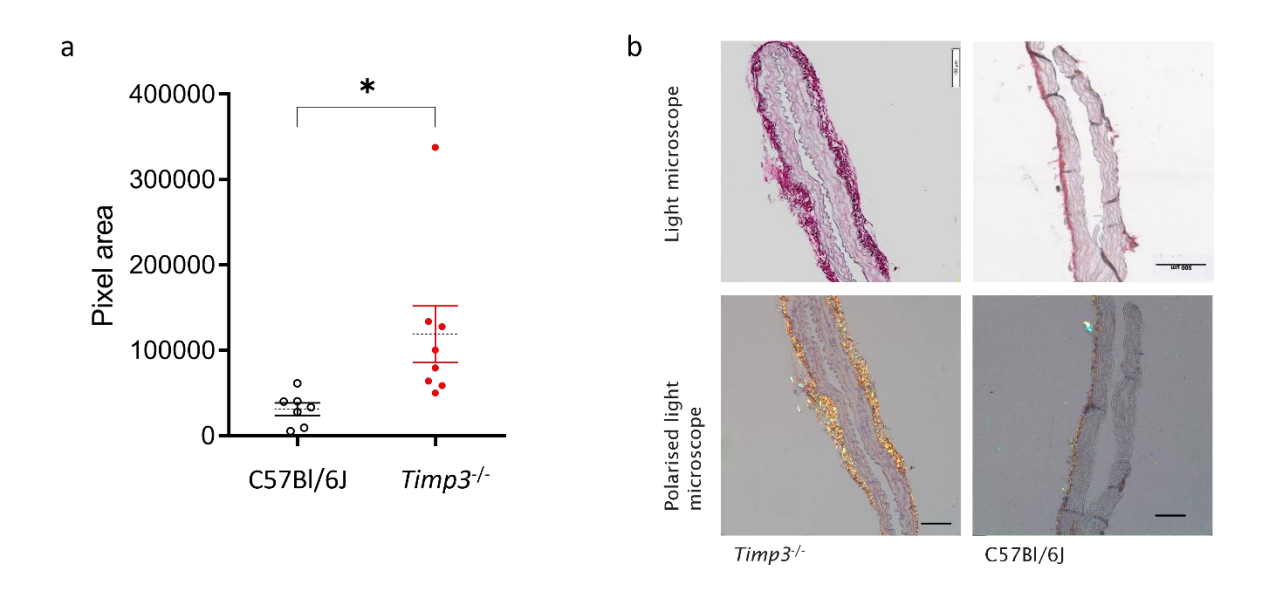


Figure 5.9 Collagen content within Sirius Red stained aorta taken from 30-week-old *Timp3*-/female mice. (a) total pixel area of stained collagen fibres in the aortas from *Timp3*-/and C57BI/6J WT control female mice; (b) representative images of Sirius Red stained
aorta from 30-week-old female *Timp3*-/- and C57BI/6J control mice under light and
polarised-light microscopes. Measurements were made using ImageJ. Values are
mean ± SEM. Unpaired two-tailed Student t-test was used to test for differences.
*p<0.05

5.4.3.3 Measurement of collagen and elastin content within the cross-section of the aorta by second-harmonic generation (SHG) and two-photon-excitation autofluorescence (TPEF) microscopy

To further investigate the impact of *Timp3* gene deletion on the distribution of collagen and elastin within the cross-section of aortas from 30-week-old female *Timp3*-/- and C57BI/6J control mice, second-harmonic generation (SHG) and two-photon-excitation autofluorescence (TPEF) microscopy were used to visualise individual fibres. **Figure 5.9** shows representative images of SHG and TPEF signals. Original SHG signal is shown as magenta in the left-most panels, highlighting the collagen fibres. The original TPEF signal is shown as green, highlighting the elastin structures. Within the middle panels, fibre extraction output from CT-FIRE is shown. Here, CT-FIRE highlights individual collagen fibres in various colours and overlays them onto the SHG signal to show how each fibre is orientated within the context of the whole tissue section. In the left-most panels, a magnified section of the collagen fibre overlay is shown.

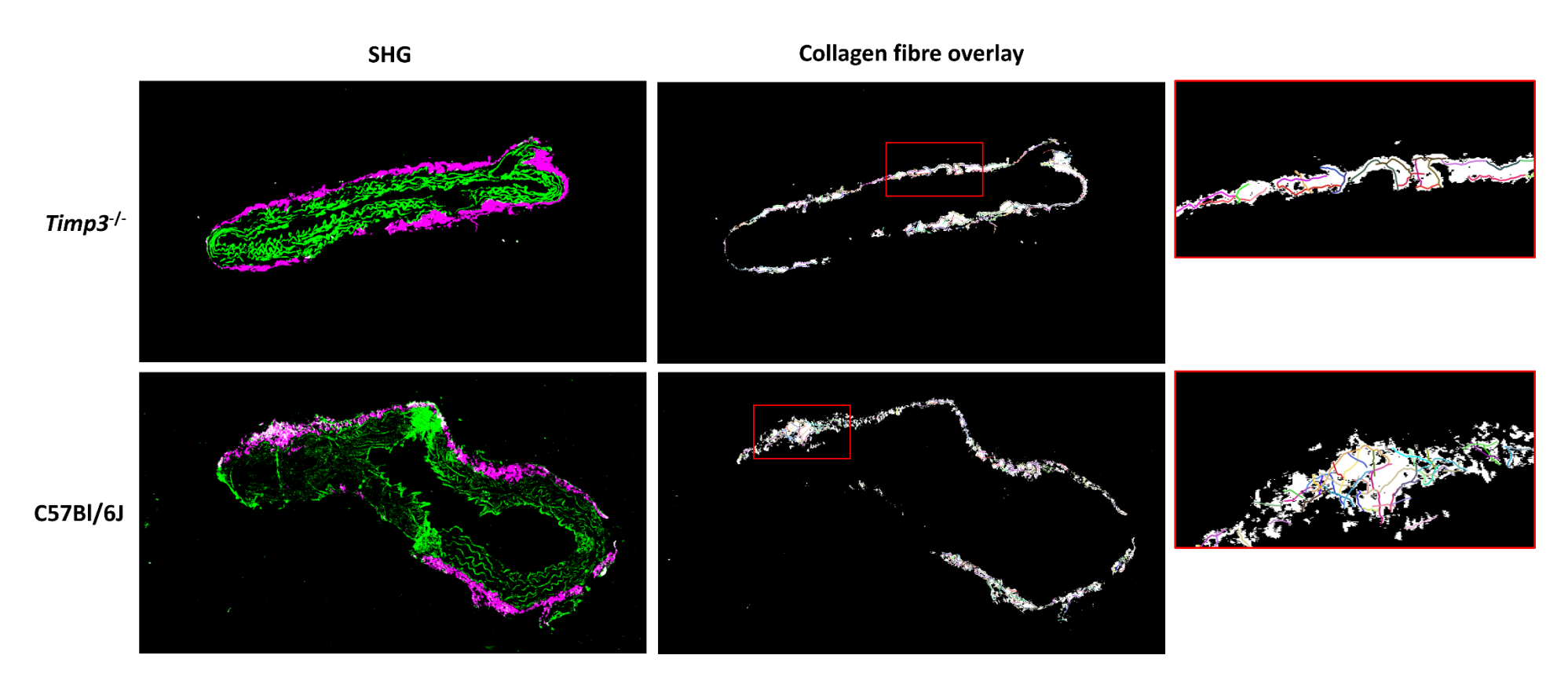


Figure 5.10 Representative SHG and TPEF cross-section images of the aortas and individual fibre extraction output from CT-FIRE. Magenta signal is second-harmonic generation (SHG), highlighting collagen molecules (left panels). The green signal is two-photon-excited autofluorescence (TPEF), highlighting elastin molecules. Collagen fibre extraction output from CT-FIRE (middle panels) is overlaid onto the SHG signal and red boxes indicate the section magnified within the rightmost panels. Within the magnified sections, in the right panels, detail of individual collagen fibres can be seen, identified by each coloured line.

Chapter 5

The distribution of individual collagen parameter results from CT-FIRE analysis of the aortas are shown in **Figure 5.10**. Both C57BI/6J and *Timp3*^{-/-} aorta follow the same patterns: fibre length and straightness show left and right skewed distributions, respectively; fibre width follows a normal distribution and fibre angle follows a multimodal distribution.

The frequency of the fibres in the *Timp3*-/- aorta appear increased compared to the C57Bl/6J. Following this, average fibre parameter data were plotted for each sample, including total fibres identified (Figure 5.11). Although the mean of total collagen fibres in the Timp3-/- group is higher, there was no significant difference. Of the five parameters measured, the only significant difference was seen in straightness, where *Timp3*-/- fibres were straighter than the C57Bl6/J (**Figure 5.11d**, p<0.05).

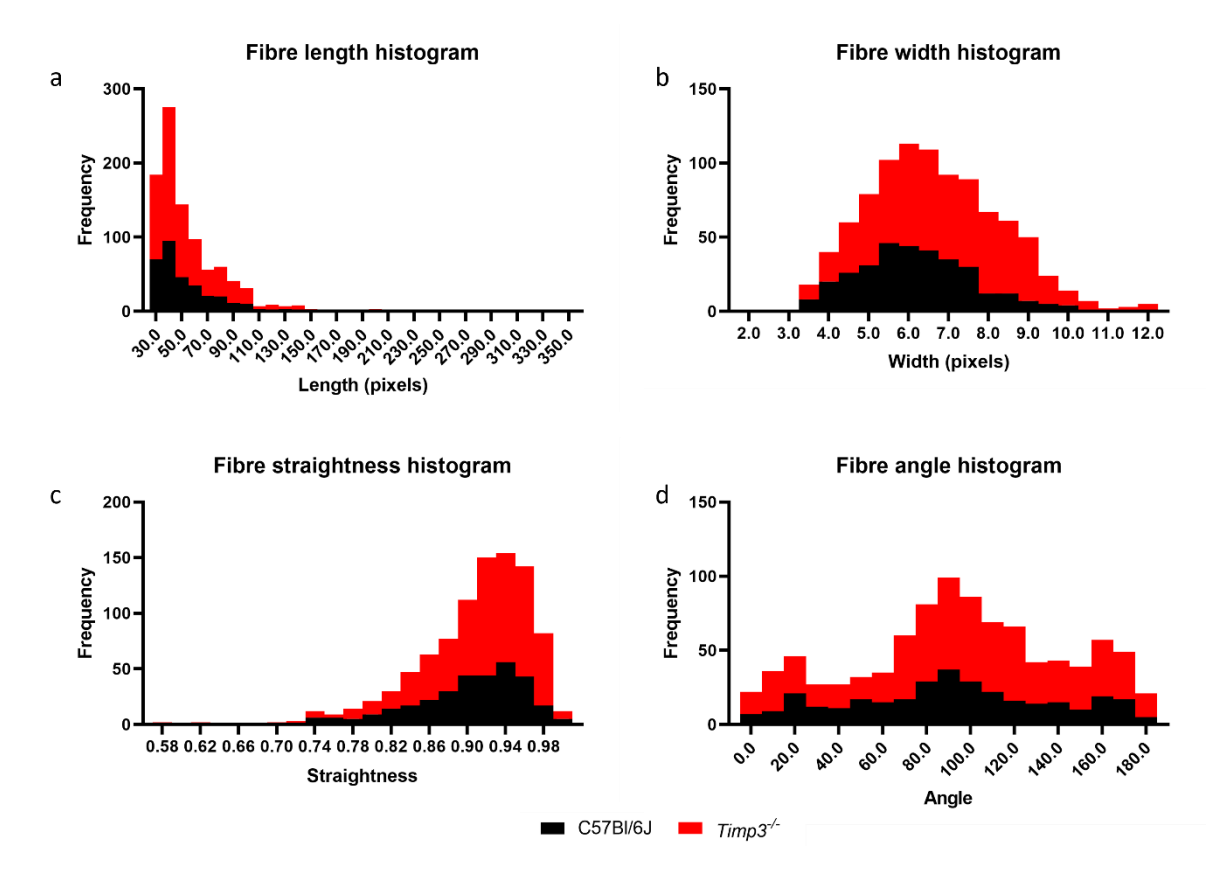


Figure 5.11 Distribution of collagen fibre parameter results from CT-FIRE analysis in cross sections of aortas taken from the 30-week-old female *Timp3*-/- aorta and C57BI/6J control mice. (a) collagen fibre length; (b) collagen fibre width; (c) collagen fibre straightness; and (d) collagen fibre angle. n = 5-6 per group.

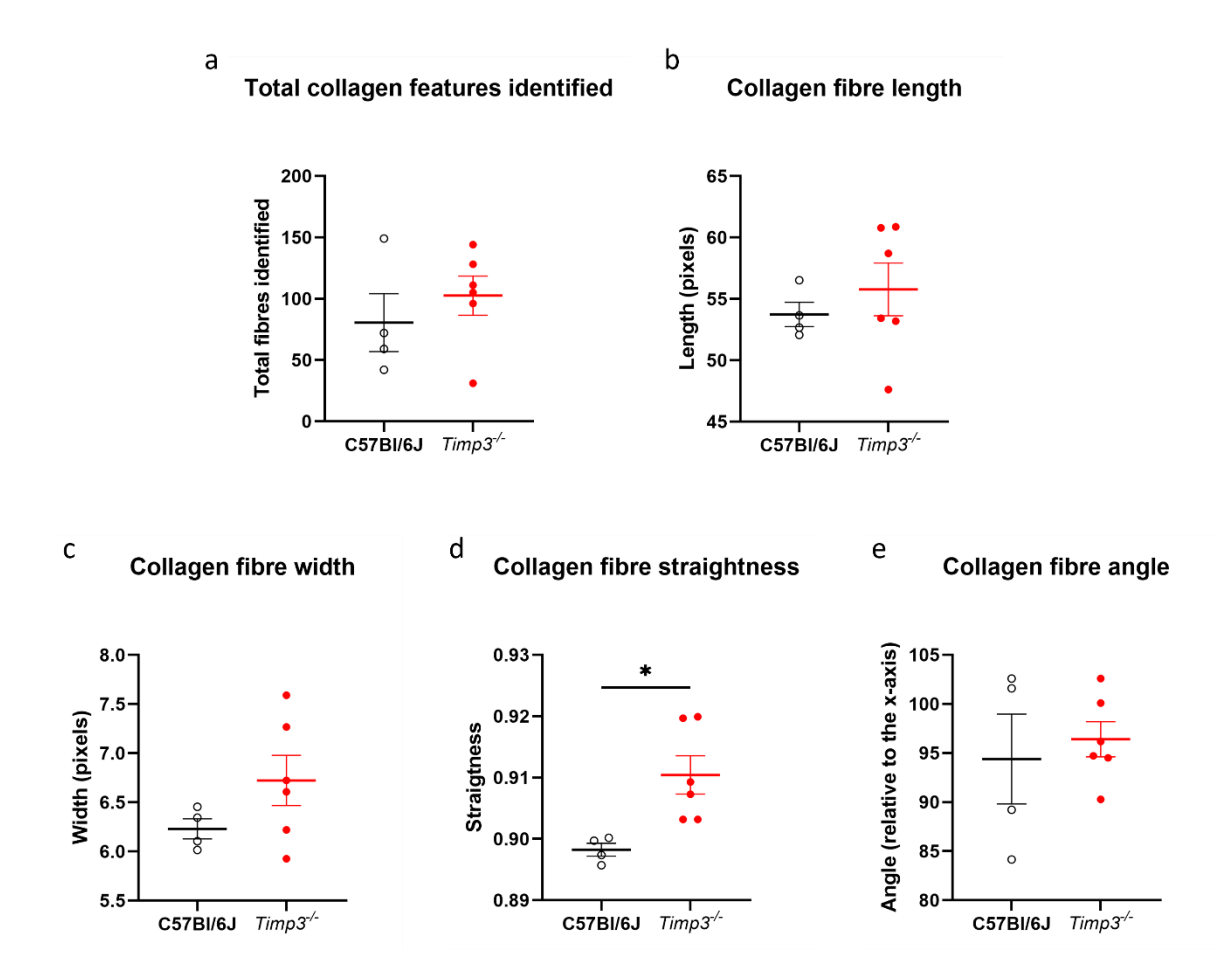


Figure 5.12 Collagen fibre analysis of the cross-section of the aorta taken from 30-week-old

Timp3^{-/-} female mice. Analysis of collagen fibre parameters in 30-week-old female $Timp3^{-/-}$ and C57BI/6J control mice that was measured using CT-FIRE. (a) fibres detected; (b) fibre width in pixels; (c) fibre length in pixels; d) fibre straightness; (e) fibre angle; and (f) representative SHG images used in CT-FIRE analysis. Plots represent mean \pm SEM. n = 4-6. Unpaired two-tailed Student t-test was used to test for differences. *p<0.05

Overall collagen and elastin content, calculated as the total pixel area, as a proportion of the total aorta and as a ratio, from SHG and TPEF images of aorta samples taken from 30-week-old female *Timp3*-/- and C57BI/6J mice are shown in **Figure 5.12**. No significant differences were found in all the parameters between the aortas from 30-week-old female *Timp3*-/- and C57BI/6J mice.

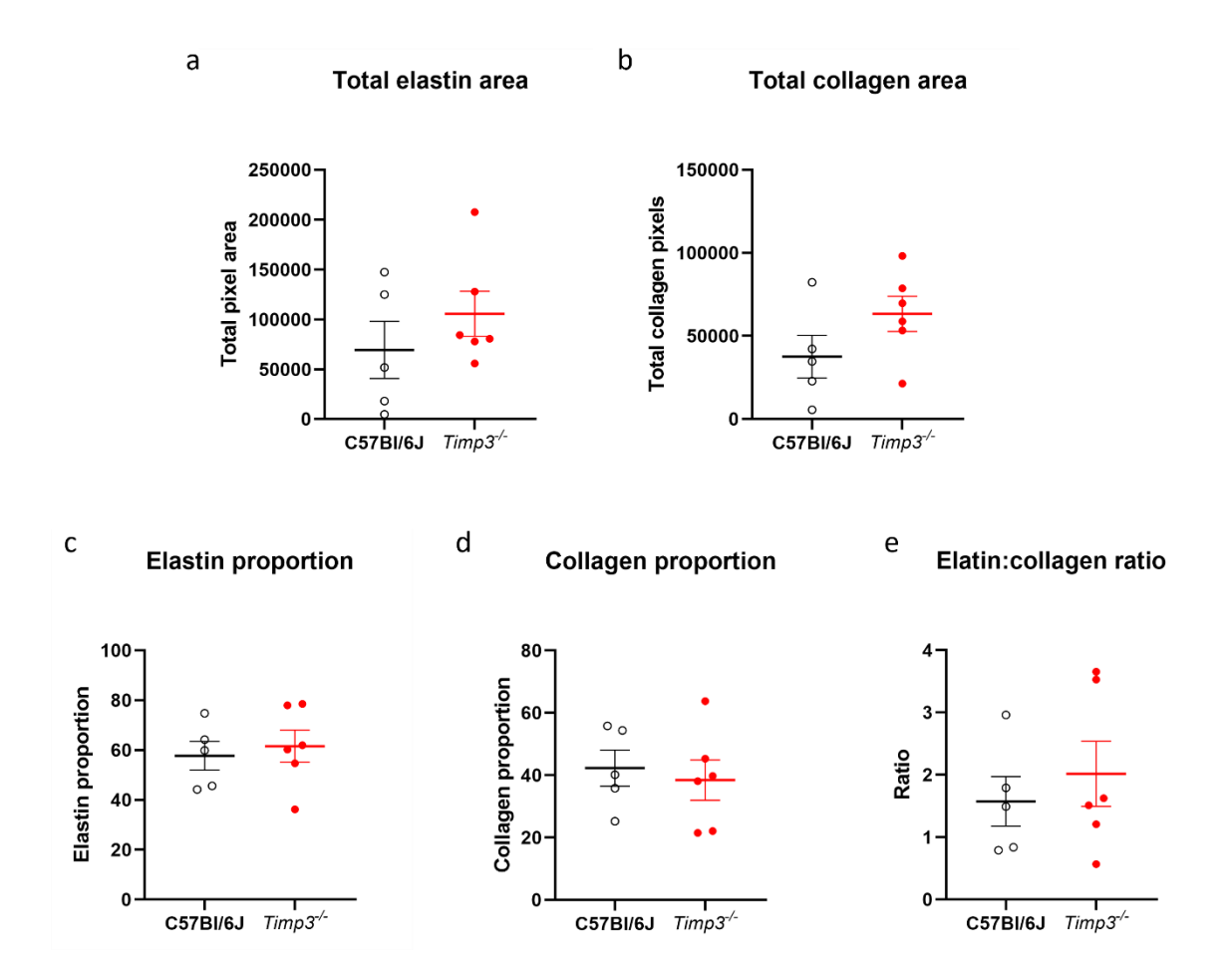


Figure 5.13 Total collagen and elastin content of the cross-section of the aorta taken from 30-week-old *Timp3*-/- female mice. Analysis of total collagen and elastin content within *Timp3*-/- female mice at 30 weeks old, and C57Bl/6J controls measured using ImageJ.

(a) total elastin pixel area; (b) total collagen pixel area; (c) elastin content as a proportion of total aorta area; (d) collagen content as a proportion of total aorta area; and (e) elastin to collagen ratio. Plots represent mean ± SEM. n = 4-6. Unpaired two-tailed Student t-test was used to test for differences.

Chapter 5

Correlation analysis was further used to test the relationships between these fibre parameters (**Figure 5.13**). Within the *Timp3*^{-/-} aorta, collagen fibre width is significantly positively correlated (p<0-05) to length, whereas width is negatively correlated within the C57Bl/6J but is not significant. (**Figure 5.13a**).

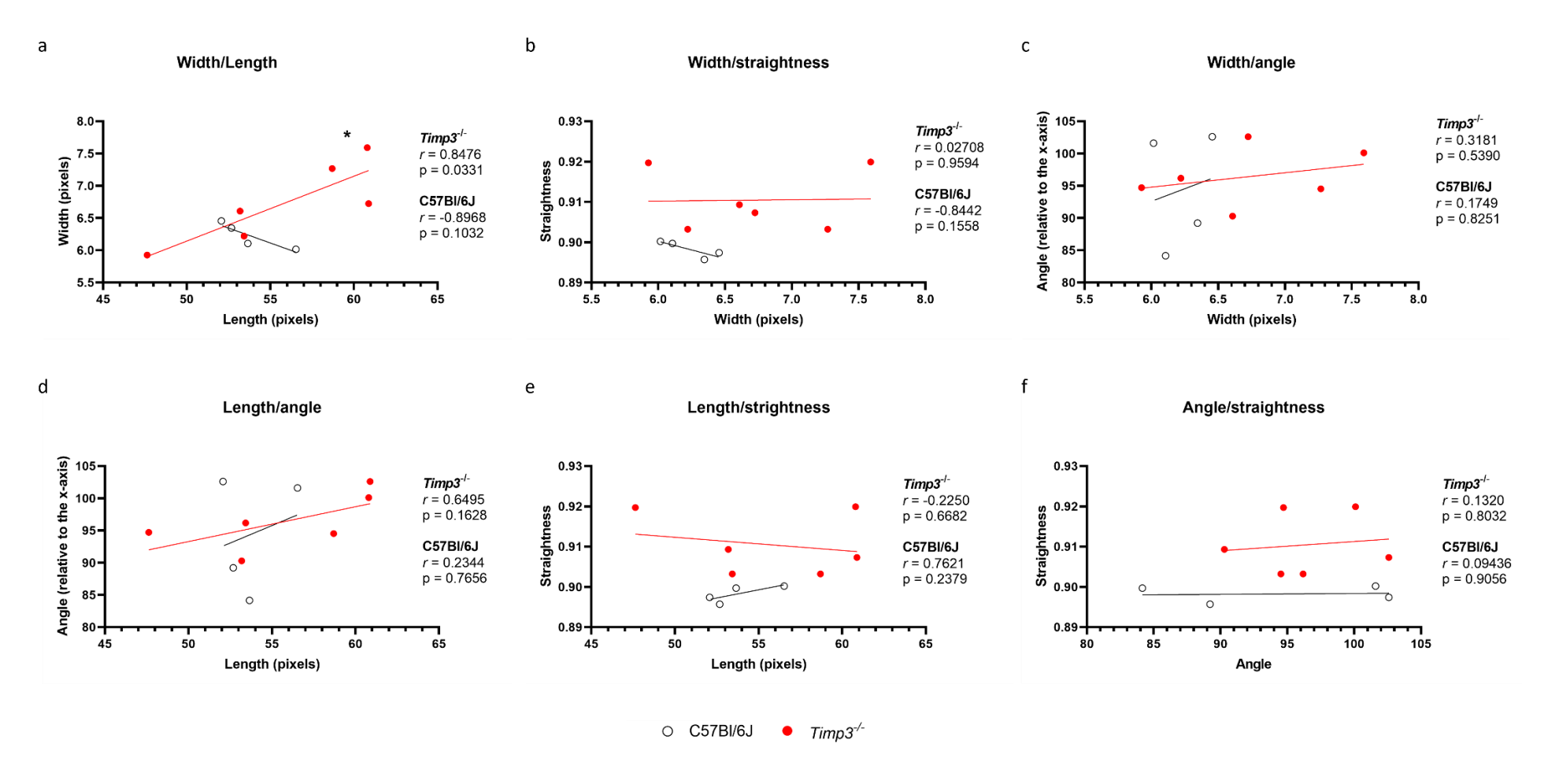


Figure 5.14 Figure 5.13 Correlation analysis of collagen fibre parameters within the cross-section of the aortas taken from *Timp3-/-* female mice. (a) fibre width and length; (b) fibre width and straightness; (c) fibre width and angle; (d) fibre length and angle; (e) fibre length and straightness; and (f) fibre angle and straightness.

5.4.4 Gene expression in the aorta samples taken from 30-week-old *Timp3*^{-/-} female mice

The expression levels of various genes involved in aortic function in aorta samples taken from 30-week-old $Timp3^{-/-}$ and C57Bl/6J controls mice are shown in Figure 5.14. $Timp3^{-/-}$ mice have significantly higher levels of expression of the Mmp2 gene in the aorta compared to the C57Bl/6J group (Figure 5.14a, p<0.05). Otherwise, no significant changes in expression were seen across the other genes between the two groups, although there was a trend towards increasing levels in Mmp9 in the aortas from $Timp3^{-/-}$ mice. Δ

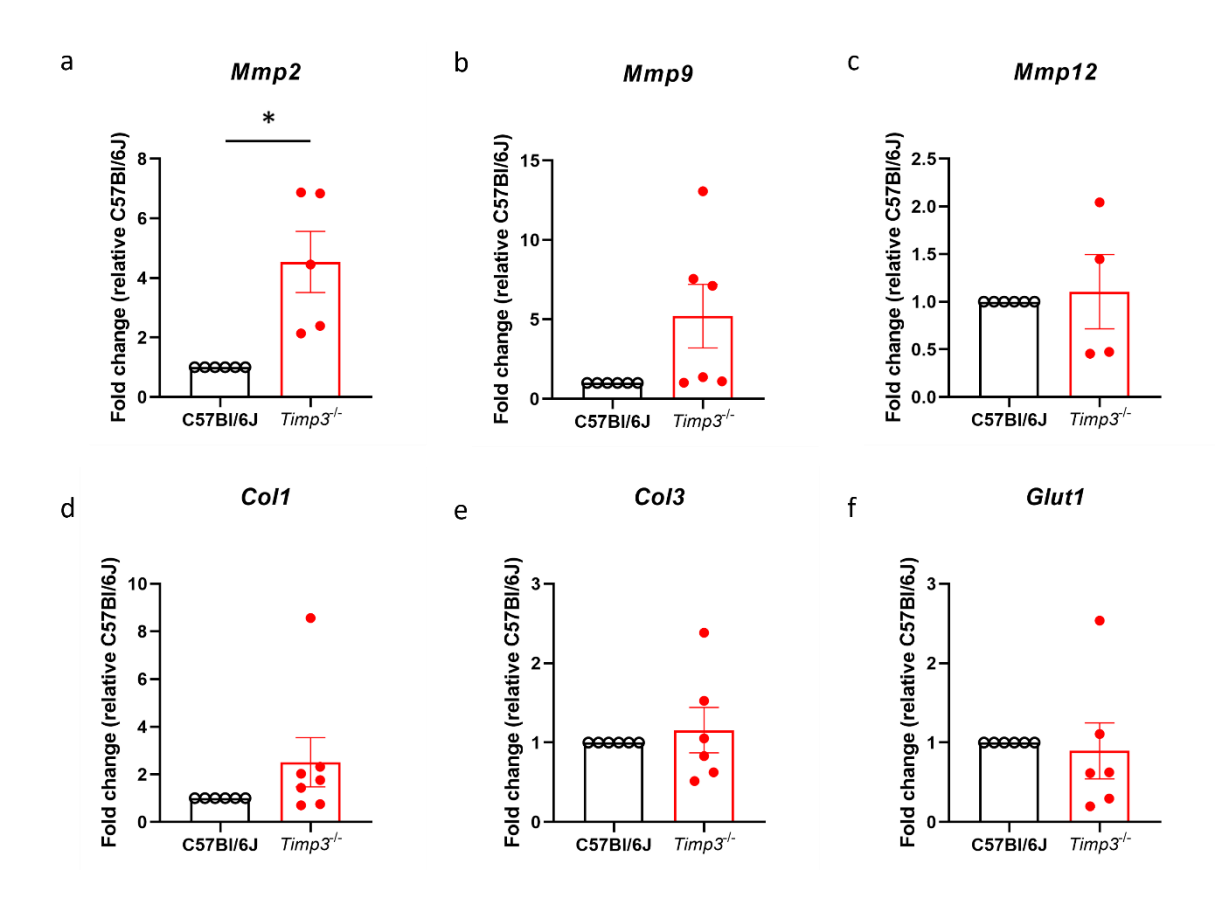


Figure 5.15 Mmp2, Mmp12, Col1, Col3 and Glut1 gene expression in aorta tissue taken from 30-week-old $Timp3^{-/-}$ female mice on chow diet. Mean fold change \pm SEM (normalised to aorta samples taken from 30-week-old chow-fed female C57Bl/6 control mice) from RT-qPCR gene expression in aorta samples taken from 30-week-old female $Timp3^{-/-}$ mice on chow diet. n=4-6 biological samples per group. Unpaired two-tailed Student t-test was used to test for differences. Statistical analysis was conducted using $\Delta\Delta$ ct values, normalised to θ -actin and Gapdh internal control genes. *p<0.05.

5.5 Discussion

Aging alone increases the risk of cardiovascular pathologies including hypertension, stroke, and atherosclerosis. As an aging population, the impact of aging on cardiovascular disease (CVD) is becoming more pertinent. Additionally, although men have higher rate of CVD, women often have worse outcomes for certain pathologies such as AAA (Bilson et al., 2022; Li et al., 2022; Lo et al., 2013; Lucà et al., 2022). Distinct sex differences in cardiovascular function and CVD progression exist but despite this, many animal studies in CVD research utilise males only. This could be due to several reasons such as to minimise the number of animals used, to enable comparisons with published literature or to avoid introducing extra variables related to sex differences. This means that much research may not be translatable to half of our population. Therefore, it is important to expand our knowledge in this area.

The aorta is the largest artery in the human body, directly connected to the left ventricle via the aortic valve, supplying blood flow to the rest of the body. Therefore, it is critically important that the aorta maintains appropriate pressure and flow of blood. The principal structures within the aorta extracellular matrix (ECM) are collagen and elastin, providing the tensile strength and elasticity required to withstand the high pressure from blood ejected from the left ventricle (McCullagh et al., 1980; Silver et al., 2001).

Since female *Timp3-/-* mice have a reduced lifespan compared to the wild type, their vulnerability to the ageing process makes them a useful model to study.

The high-fat (HF) diet resulted in significant increase in body weight along with increased weight of white-adipose tissue depots in the female *Timp3*-/- and C57Bl/6J mice at 16 weeks of age as this HF diet is well-known to cause diet induced obesity in the C57Bl/6J mouse. However, the increase in body weight and adiposity, as a consequence of HF feeding, were similar between the two genotypes. At 30 weeks old and maintained on the standard chow diet, *Timp3*-/- mice had a significantly lower body weight and gonadal fat weight compared to age-matched C57Bl/6J control mice. Thus, the body weight trajectory and adiposity in these female *Timp3*-/- female mice were stunted from 16 weeks of age onwards, suggesting that this might be due to *Timp3* deletion.

Of all collagen fibre parameters analysed using SHG microscopy, only straightness showed a significant increase within the *Timp3*-/- aorta. *Timp3*-/- fibres also showed increased angle, width and length although did not reach significance. Changes in collagen fibre orientation and morphology are associated with vascular pathology. Watson et al used SHG imaging to find that collagen fibres within ApoE mice on western diet were oriented at a different angle, highlighting a role for atherosclerosis and diet in collagen remodelling (Watson et al., 2016). Many other studies

show collagen deposition and fibre thickness is increased in atherosclerosis and aging (Lacolley et al., 2020; Sawabe, 2010).

Fibrillar collagens type I and III make up most of the aorta wall and type IV is the main collagen present in the basal membrane and around VSMCs (Tsamis et al., 2013; Vouyouka et al., 2001). Collagen fibrils assemble into thick, highly organised fibre bundles that provide strength and shock-absorption. These fibres exist in a "wavy" or undulating shape. This allows lengthening of the collagen fibre in response to pressure to effectively disperse energy or store it as elastic energy for subsequent recoil of the vessel wall. This mechanical response protects the vascular tissue from stress and reduces damage (Kesson & Atkins, 2005). As the Timp3^{-/-} collagen fibres are straighter, they are presumably closer to their maximal length and therefore may not be able stretch effectively to accommodate mechanical stress generated by pulse pressure. This could cause damage to ECM structures and aberrant remodelling, resulting in a stiffer vessel. Increased expression of the gelatinase, Mmp2, in this study supports the inference that the Timp3-/- aorta undergoes maladaptive remodelling. Matrix metalloproteinase 2 is constitutively expressed by the endothelium and VSMCs, and primarily degrades collagen type IV, although it also has affinity for other collagens and elastin (Monaco et al., 2006; Zeng et al., 1999). Increased MMP2 activity is a marker of hypertension, atherosclerosis, and abdominal aortic aneurysm (AAA) (Petersen et al., 2000; Yasmin et al., 2005). Expression of another gelatinase, Mmp9, was upregulated in the Timp3^{-/-} aorta although it did not reach significance. Both Mmp2 and Mmp9 are associated with excessive ECM degradation, including elastin degradation, in vascular pathology. In Timp3^{-/-} aorta, no change was seen in the expression of collagens I and III, which suggests the rate of ECM degradation may exceed the rate of repair, further contributing to aberrant remodelling. Glucose transporter 1 is associated with hypertension and can cause reduction in VSMC contractility via glucose uptake (Adhikari et al., 2011; Gnudi & Raij, 2006). However, no difference in gene expression was seen in this model, suggesting Timp3-mediated vessel dysfunction is not linked to metabolism.

Matrix metalloproteinase 2 also plays a role in the phenotypic switching of VSMCs from contractile to synthetic. The synthetic phenotype reduces expression of contractile proteins and is associated with vascular pathologies, including hypertension (Belo et al., 2015). Contractile proteins in the VSMCs are essential for responding to physiological stimuli, to control vascular tone and thus blood pressure. Osteopontin expression is a marker of synthetic VSMCs and therefore could be measured in the *Timp3*-/- aorta to determine the phenotype of the smooth muscle (H. Gao et al., 2012).

The *Timp3*^{-/-} aorta had impaired response in NA-induced constriction. Impaired blood vessel constriction ordinarily equates to reduced blood pressure. However, the *Timp3*^{-/-} mice have significantly increased blood pressure compared to the WT. Furthermore, increased vessel constriction is typically seen in hypertension. In this study, *Timp3*^{-/-} aorta had reduced constriction response to noradrenaline in myography. Since noradrenaline acts on VSMCs via alpha adrenergic receptors, the hypertension seen in these mice is likely mediated by a different mechanism (Strosberg, 1993). Future studies could investigate the impaired adrenergic signalling, for example by measuring receptor gene expression, and could examine other mechanisms of vascular constriction, such as the angiotensin pathway. Organisation of the ECM also impacts contractility of VSMCs. Smooth muscle cells are tethered to the ECM via adhesion molecules such as integrins which connect the actin cytoskeleton to collagen, mediating transduction of mechanical signals between the cell and surrounding matrix (Tang & Gerlach, 2017). Therefore, one could investigate whether altered the collagen fibre morphology seen in *Timp3*^{-/-} mice contributes to the impaired VSMC contraction response.

Regarding vasodilation, *Timp3*^{-/-} aorta tissue responded normally to SNP-induced relaxation but had impaired response to carbachol (Cch, which mimics the action of acetylcholine). In both pathways, nitric oxide (NO) causes vasodilation via soluble guanylate cyclase and cyclic GMP, leading to calcium ion efflux from the VSMCs and subsequent relaxation (Hottinger et al., 2014; Khurana et al., 2004). However, whereas SNP is a direct NO donor to VSMCs, Cch must first activate NO production by endothelial cells for diffusion into smooth muscle (SNP induced relaxation is endothelium-independent, whereas Cch induced relaxation is endothelium-dependent). The myography results therefore indicate impaired NO pathway signalling in the endothelium, but not VSMCs. Future studies could investigate components of the endothelial NO pathway, such as muscarinic acetylcholine receptor expression, to determine which part of the NO pathway is contributing to endothelial dysfunction in the *Timp3*-/- mouse.

Defective aorta function and hypertension leads to reduced blood flow which the heart will have to compensate for, in order to maintain adequate supply to the body. Prolonged hypertension and increased workload on the heart ultimately leads to left ventricular hypertrophy (LVH) (Katholi & Couri, 2011; Ruilope & Schmieder, 2008). Patients with LVH have increased risk of heart failure and myocardial infarction (Bornstein et al., 2023; Y. H. Kim et al., 2018).

As mentioned previously, the *Timp3*-/- female mice exhibit premature death without any obvious symptoms leading up to the event. Sudden cardiac death (SCD) is a similar phenomenon that occurs in the human population, the risk of which is greatly increased in cases of LVH (Shenasa & Shenasa, 2017; Yun et al., 2021). Incidence of SCD within the female population

increases with age (Skjelbred et al., 2022). Heart weight was measured in the aged *Timp3*-/- mice and although increase in the mean raw weight and weight proportional to body weight were increased, neither reached statistical significance. This may be because although these mice are aged, they are not old and roughly equal an age of between 30-40 years in humans, therefore may only be in the early stages of cardiovascular pathology. Despite non-significant heart weight, it would be useful to examine its histology and left ventricular wall thickness in future studies as this may show significant differences.

5.6 Strengths and Limitations

The reduced life span and sudden death of the female *Timp3*-/- mouse makes it a great model to study the effects of aging in cardiovascular disease. As mentioned previously, much cardiovascular research uses male only animal models which could reduce the translatability of findings due to sex differences. This study therefore helps fill a much-needed gap in female-specific research. Of course, this would mean also that these findings may not be applicable to processes in males. Future investigations could include the study of the male *Timp3*-/-cardiovascular phenotype, which in addition to improving translatability, could help elucidate how sex differences propagate differences in disease development.

The mice used in this study were 30 weeks old. Aging increases risk of cardiovascular disease in humans, especially in post-menopausal women. Although clear vascular phenotype was seen in these mice, it may be more beneficial to study progression at later ages. However, in the *Timp3*-/- mouse specifically, this is practically and ethically difficult due to premature death.

Due to the scarcity of aorta tissue, the tissue used in myography was subsequently used for histological analysis. This may have introduced structural changes that affected the morphological analysis. However, since all samples were subjected to myography, any changes would have been present in all samples, thus reducing any potential confounding effect. The use of SHG in this study allowed highly detailed analysis of individual collagen fibres which is not possible with traditional histological techniques. Histological staining may also introduce artefacts due to the staining process. As SHG imaging is label-free there is no risk of this. Collagen fibre straightness, measured using CT-FIRE, takes an average measurement using the distance between the two fibre endpoints. It does not consider waviness within the individual fibre which is shown to have implications for aorta function (Niestrawska et al., 2022). Future studies could also investigate this parameter.

5.7 Conclusions

Aged *Timp3*^{-/-} female mice exhibit hypertension and impaired aorta function. A summary of findings is shown in **Figure 5.16**. Diminished response to the vasoactive compounds NA and Cch indicates issues in the adrenergic and NO signalling pathways in smooth muscle and endothelium, respectively. Findings from SHG imaging suggest that this may be in part due to erroneous collagen or ECM remodelling, which is corroborated by increased expression of *Mmp2* in the aorta. Similar findings in the young *Timp3*^{-/-} mice were not seen, supporting the age-dependent role of *Timp3* in aorta dysfunction.

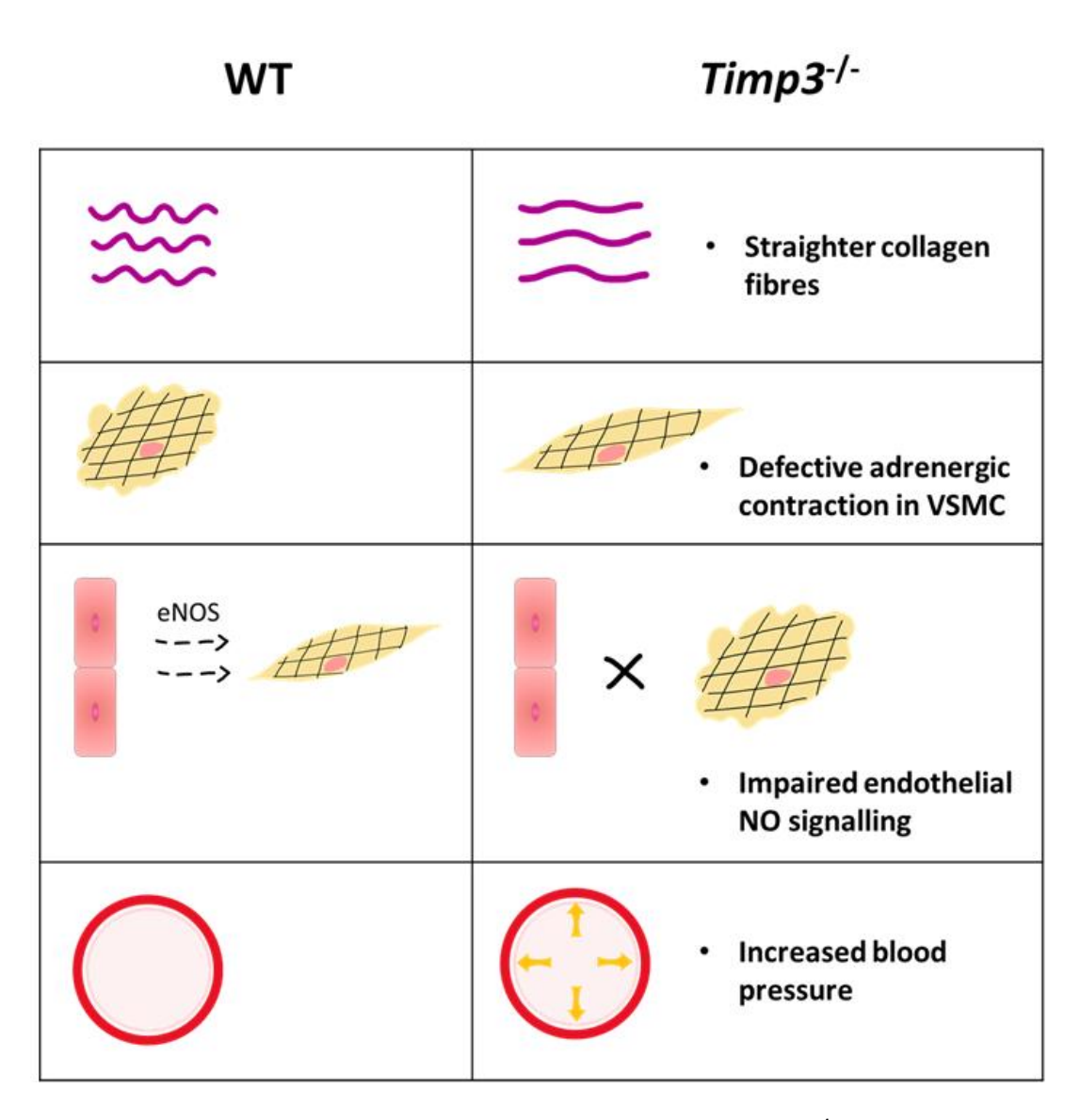


Figure 5.16 Summary table of results, seen in the aged female *Timp3-¹*-aorta (right column) compared to the WT control (left column). eNOS: Nitric oxide synthase; NO: Nitric oxide

Chapter 6 Conclusion

The aim of this project was to determine the impact of TIMP3 in the development of metabolic disease, using a diet-induced obesity (DIO) model. Particular interest was given to the gut microbial composition, cardiovascular function, and energy homeostasis. Using a *Timp3*-/- DIO mouse model to achieve this aim, progression of obesity and metabolic syndrome (MetS) parameters were measured, gut bacterial taxa identified, and aorta structure and function investigated. Male mice were followed from weaning to young adult age to study energy metabolism and the gut microbiome, whereas female mice were observed at two time points – young adult and mature adult – to study the aorta. A variety of techniques were employed for sample analysis including molecular studies, whole genome sequencing, myography and imaging.

Firstly, this project found that *Timp3* knock-out does effect development of DIO. Altered energy metabolism was observed within these mice, despite being less obese than the C57BI/6J controls. Altered energy metabolism was indicated by increased retroperitoneal fat depot and iBAT depot weights, alongside increased plasma adiponectin, and elevated *Srebf1c* and decreased *AdipoR1* expression. Altered adiponectin signalling indicated reduced sensitivity to adiponectin. Retroperitoneal fat is particularly important because it is an indicator of abdominal obesity. Changes in energy metabolism also effected the energy expenditure of *Timp3*-/- mice, measured via indirect calorimetry. In the juvenile *Timp3*-/- mouse, energy expenditure follows a significantly different pattern to the wild-type controls. What's more, the RER follows an altered pattern that may be propagated via dysregulated circadian rhythm.

Circulating levels of plasma butyrate were decreased in the *Timp3*-/- mouse under HFD conditions, indicating that the gut microbiota may play a role in the *Timp3*-/- energy metabolism in DIO. Subsequently, the gut microbiota was investigated using 16s rRNA sequencing. Here, it was observed that abundance of the butyrate-producing bacteria *Oscilibacter*, *Parasutterella* and *Erysipelatoclostridium* are decreased in the *Timp3*-/- which likely impacts the observed alteration in plasma butyrate. Additionally, the addition of HFD diminished the gut microbial community differences seen in the *Timp3*-/- mouse and beta diversity measurements indicated that *Timp3* knock-out in combination with HFD had less of an effect than either variable independently.

Finally, this study found that *Timp3* knock-out leads to aorta dysfunction via aberrant remodelling of the vessel extracellular matrix. This was evidenced by reduced aortic relaxation and constriction responses in myography, alongside altered collagen fibre morphology, observed using Second Harmonic Generation Microscopy and increased *Mmp2* gene expression.

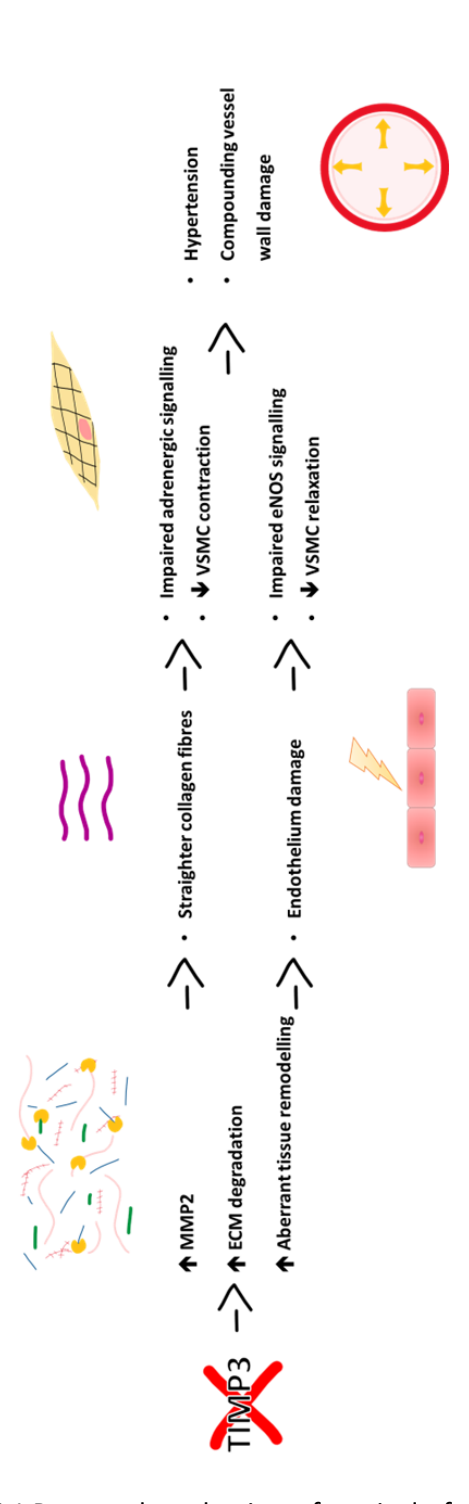


Figure 6.1 Proposed mechanism of aortic dysfunction in the Timp3-/- female mice

6.1 Future work

- Conduct molecular and histological studies in other tissues involved in energy
 homeostasis. This project focused on the liver where limited effects of the *Timp3* knockout were seen. Observed differences in these mice may be affected by other tissues such
 as adipose.
- Investigate DIO in *Timp3*^{-/-} mice raised in a conventional mouse room. Mice in this study were housed in a specific-pathogen free environment. Cleanliness of environment impacts the gut microbiome composition and therefore raising *Timp3*^{-/-} in a conventional mouse room may further impact development of obesity.
- Investigate the gut microbiota in *Timp3*-/- female mice. The gut microbiome plays a role in development of cardiovascular diseases and may be important in this mouse model. For example, male *Timp3*-/- mice had increased abundance of *Prevotellaceae* which produce succinate, a SCFA related to CVD.
- Investigate alternative mechanisms of vasoconstriction in the *Timp3*-/- females such as the Ang II pathway to elucidate the progression of hypertension.
- Investigate vascular function in older *Timp3*-/- female mice as findings may be more translatable to our ageing population.

Appendix A

A.1 Supplementary Material

Table A. 1 List of mouse gene primers used in SYBR green RT-qPCR and their details.

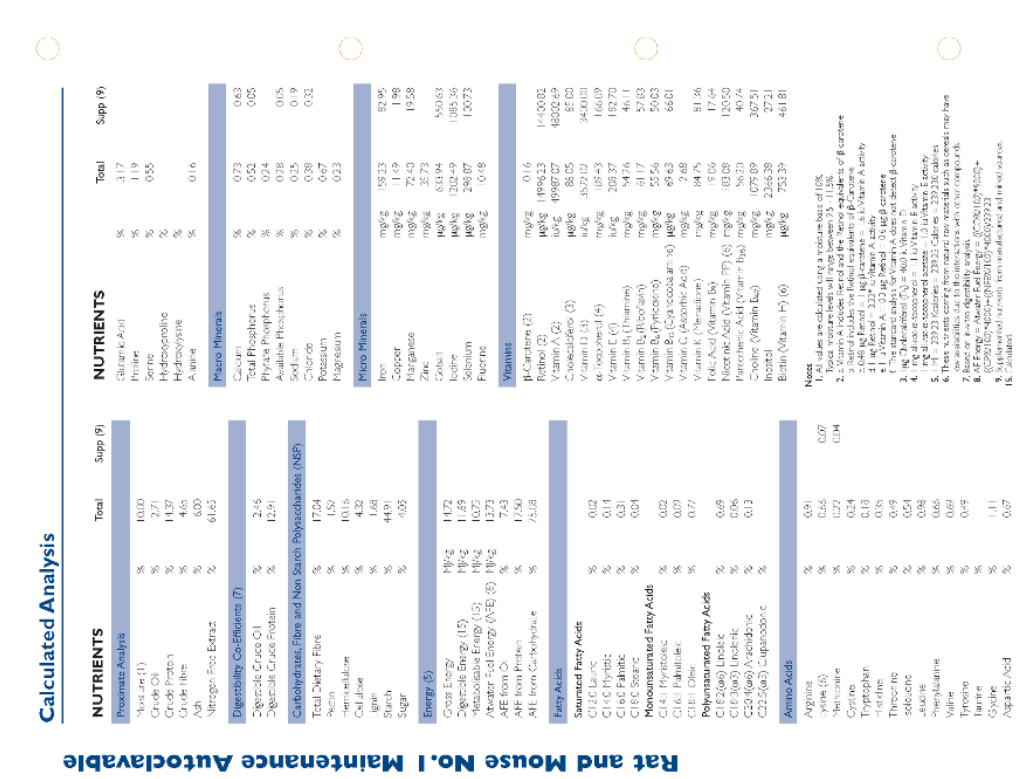
Gene	Supplier	Forward sequence (5'-3')	Reverse sequence (3'-5')
name			
Gapdh	Sigma	ATGGTGAAGGTCGGTGTGAAC	TTGATGTTAGTGGGGTCTCGC
	Aldrich		
β-actin	Sigma	GTGACGTTGACATCCGTAAAGA	GCCGGACTCATCGTACTCC
	Aldrich		
Mmp2	Sigma	CCAGATACCTGCACCACCTT	CTTGGTTCTCCTCCATCCAG
	Aldrich		
Мтр9	Sigma	GCAGAGGCATACTTGTACCG	TGATGTTATGATGGTCCCACTTG
	Aldrich		
Mmp12	Sigma	AACACTACTGGAGGTATGATG	CTGCATCAATTTTAGGCTTG
	Aldrich		
Mmp13	Sigma	TGTTTGCAGAGCACTACTTGAA	CAGTCACCTCTAAGCCAAAGAAA
	Aldrich		
Mmp28	Sigma	CCATCACTGTAGGGAGTTAC	CATCTTTTCTGTAGTGGACG
	Aldrich		
Tnf-α	Sigma	ATGAGCACAGAAAGGATGATC	TACAGGCTTGTCACTCGAATT
	Aldrich		
Irs1	Sigma	AGTTAGTAGAACCAAGCATTAAACAC	TGAGGAAGAGACTGAACCATCA
	Aldrich		
Irs2	Sigma	ACCGACTTGGTCAGCGAAG	CACGAGCCCGTAGTTGTCAT
	Aldrich		
Glut2	Sigma	ACTTGGAAGGATCAAAGCAATGT	CAGTCCTGAAATTAGCCCACAA
	Aldrich		

Appendix A

Gene name	Supplier	Forward sequence (5'-3')	Reverse sequence (3'-5')
Glut4	Sigma Aldrich	GTGACTGGAACACTGGTCCTA	CCAGCCACGTTGCATTGTAG
Fxr	Sigma Aldrich	TGGGCTCCGAATCCTCTTAGA	TGGTCCTCAAATAAGATCCTTGG
Сур7а1	Sigma Aldrich	GGGATTGCTGTGGTAGTGAGC	GGTATGGAATCAACCCGTTGTC
Srebf1c	Sigma Aldrich	TGACCCGGCTATTCCGTGA	CTGGGCTGAGCAATACAGTTC
Tlr4	Sigma Aldrich	GCCTTTCAGGGAATTAAGCTCC	GATCAACCGATGGACGTGTAAA
Adipor1	Sigma Aldrich	CCTCCTGGATAGGGTCGGT	CTTCCTGTGATGGTGGACACTTAG
Adipor2	Sigma Aldrich	GTCGGAAGGAGGGTCAACT	GTTGGTGCCCTTTTCTGAGC
1116	Sigma Aldrich	CCTTCCAGGATGAGGACATGA	TGAGTCACAGAGGATGGGCTC

Appendix B

Chow Diet Composition B.1



INGREDIENTS

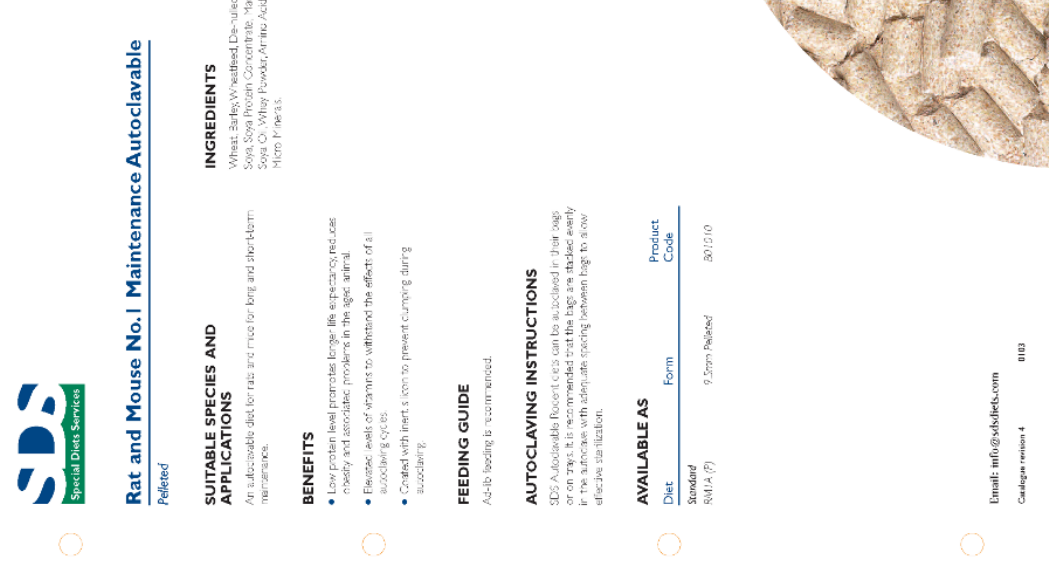
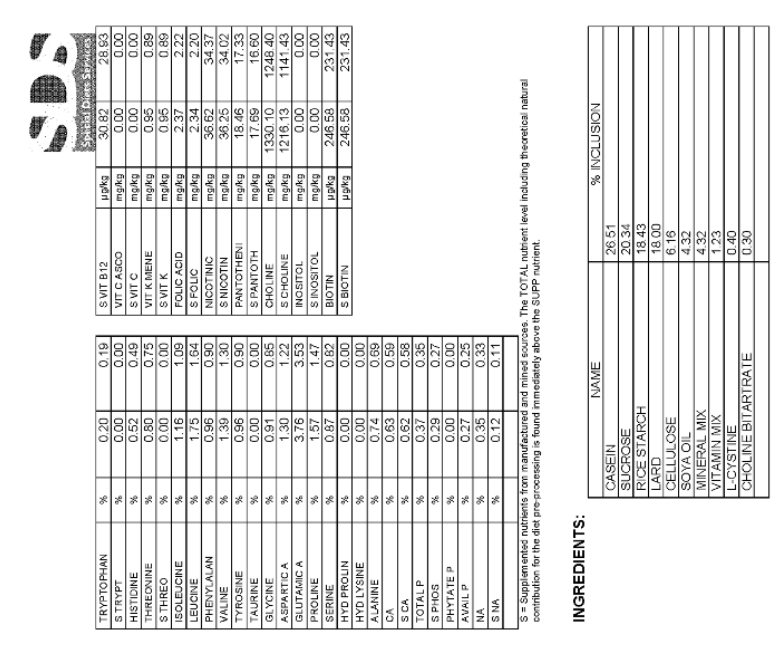


Figure B. 1 Chow diet composition from Special diet Services (SDS)

B.2 High-fat diet composition



FRESH 10% H2O		6 0.28 0.26	0.19	0.45	0.44	0.08	90:0	58.86	52.92	L	7.43	13.29	11.96 11.23	68.90	37.09		00:00	kg 254.59 238.95	kg 254.59 238.95	197.20	197.20	kg 1.24 1.16		kg 4931.57 4628.65	kg 4931.57 4628.65		ка 7863.40 7380.39	kg 1232.89 1157.16		kg 100.64 94.46		96.39	96.39	96.39 7.36 7.25	96.39 7.36 7.25 6.37	96.39 7.36 7.25 6.37 5.92	96.39 7.36 7.25 6.37 5.92 8.65
888	8 8 8	28 28 3	8		g	*	%	mg/kg	mg/kg	mg/kg	mg/kg	mg/kg	mg/kg	mg/kg	mg/kg	ража	palkg	pakg	раже	L	ряжа	mg/kg		iu/kg 4	iu/kg 4		iu/kg 72	iu/kg 13		in/kg	in No.	- Francisco	mg/kg	mg/kg mg/kg	mg/kg mg/kg	mg/kg mg/kg mg/kg	mg/kg mg/kg mg/kg
		70	SCL	×	SK	MG	SMG	Æ	SE	8	scu	NN	SMN	NZ	SZN	00	sco	_	- 10	35	S SE	L		VITA	SVITA		VIT D3	S VIT D3		VITE	L	u = 5 o	VIT B1 THI	VIT B1 THI	SVIT B1 THI SVIT B1	SVITE VIT B1 THI SVIT B1 SVIT B2	SVITE SVITE VITEZRE SVITEZ VITESPYR
10% H2O	100.00	10.00	21.22	21.56	4.22	4.15	37.90		0000	0.11	5.56	00:00	14.88	21.27		19.05	17.47	16.13	4287.75		0.02	0.03	90.9	3.53	0.37	0.01	0.00	0.03	0.29	404	1.80		0.69	1.37	137	137	0.00 0.00 0.53
FRESH	100.00	4.11	22.61	22.97	4.50	4.42	40.38		00.00	0.12	5.92	00.0	15.85	22.66		20.30	18.61	17.19	4568.36		0.02	0.03	6.46	3.76	0.39	0.01	0.00	0.03	0.31	4.30	1.92		0.73	1.46	0.00	0.73 0.00 0.57	0.73 0.00 0.57 0.00
	×	×	×	%	%	*	×		%	ž	%	ş	%	ν,		MJ/kg	MJ/kg	MJ/kg	kcalkg		7%	×	×	ž	8	*	*	8	37	8	×		%	8 8	8 8 8	* * * *	8 8 8 8 8
		2	OIL	PROTEIN	FIBRE					TUULOSE	OSE					ENERGY	BLE .	LISABLE	1GY		OLEIC	OLEIC	9 OLEIC	m C)	3 Sic	9 ONIC	3 ODONIC	URIC	YRISTIC	VUMITIC	FEARIC		E	ш		I I	E SIN

This information is intended as a guide only. For actual data we recommend that analysis work is carried out to confirm the nutrient parameters precisely

Figure B. 2 High-fat diet composition from special diet services.

DIET FORMULATION AND SPECIFICATION DATA

BASIC DIET INFORMATION:

CALCULATED ANALYSIS:

Appendix C



SCOTTISH ACCREDITATION BOARD

This is to certify that

Rachel Meadows

has successfully achieved the learning outcomes of the following modules as required under UK and EU training frameworks.

MODULES: L (EU1 Legislation), E1 (EU2 Ethics)

PILA (EU3.1 Basic Biology (theory), EU4 Animal Care, Health & Management (theory), EU5 Recognition of PSD, EU7 Minimally Invasive Procedures (theory), EU3.2 Basic Biology (practical), EU8 Minimally Invasive Procedures (skills))

K (EU6.1 Humane Killing (theory), EU6.2 (skills))

PILB (EU20 Anaesthesia – Minor Procedures)

TRAINING IN (list animal/types species of PILA):

Mouse

Training organised by: CHARLES RIVER UK LTD

Certificate Number: BE3993

Date: 18th January 2019

ean Wilson

Signature 1 For Course Organiser Signature 2
For Scottish Accreditation Board

Please note, this Certificate allows you to apply for a Licence, but it is <u>not</u> a licence to perform procedures under the Animals (Scientific Procedures) Act 1986.

References to EU Modules relates to requires arising from Directive 2010/63/EU – further information can be obtained at:

http://ec.europa.eu/environment/chemicals/lab_animals/pdf/Endorsed_E-T.pdf

Appendix D

Timp3 expression in 15 week males

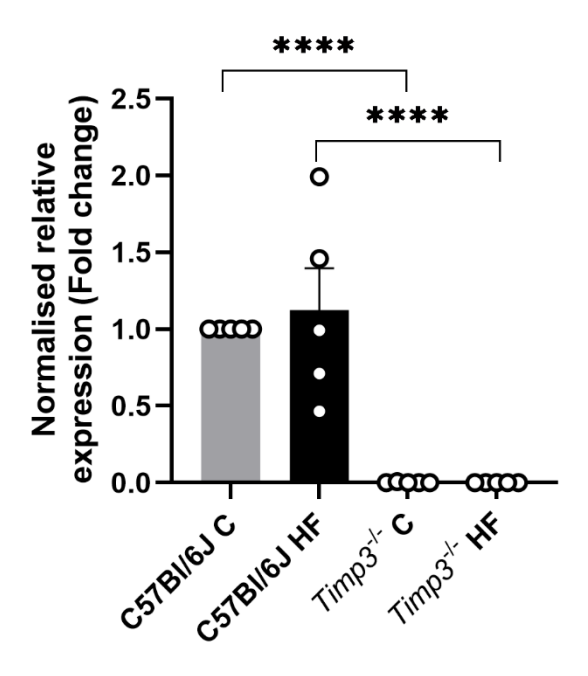


Figure D. 1 *Timp3* gene expression in liver tissue of *Timp3*-/- mice, at 15 weeks of age, on chow (C) and high-fat (HF) diet. Mean fold change \pm SEM (normalised to chow-fed C57BI/6J control samples, and internal control genes θ act and θ from RT-qPCR gene expression in male θ fiver samples on chow and high-fat diet, and C57BI/6J controls. n=5 biological samples per group. Unpaired two-tailed Student's t-test was used to test for differences. Statistical analysis was conducted using ddct values.

**** = p < 0.0001.

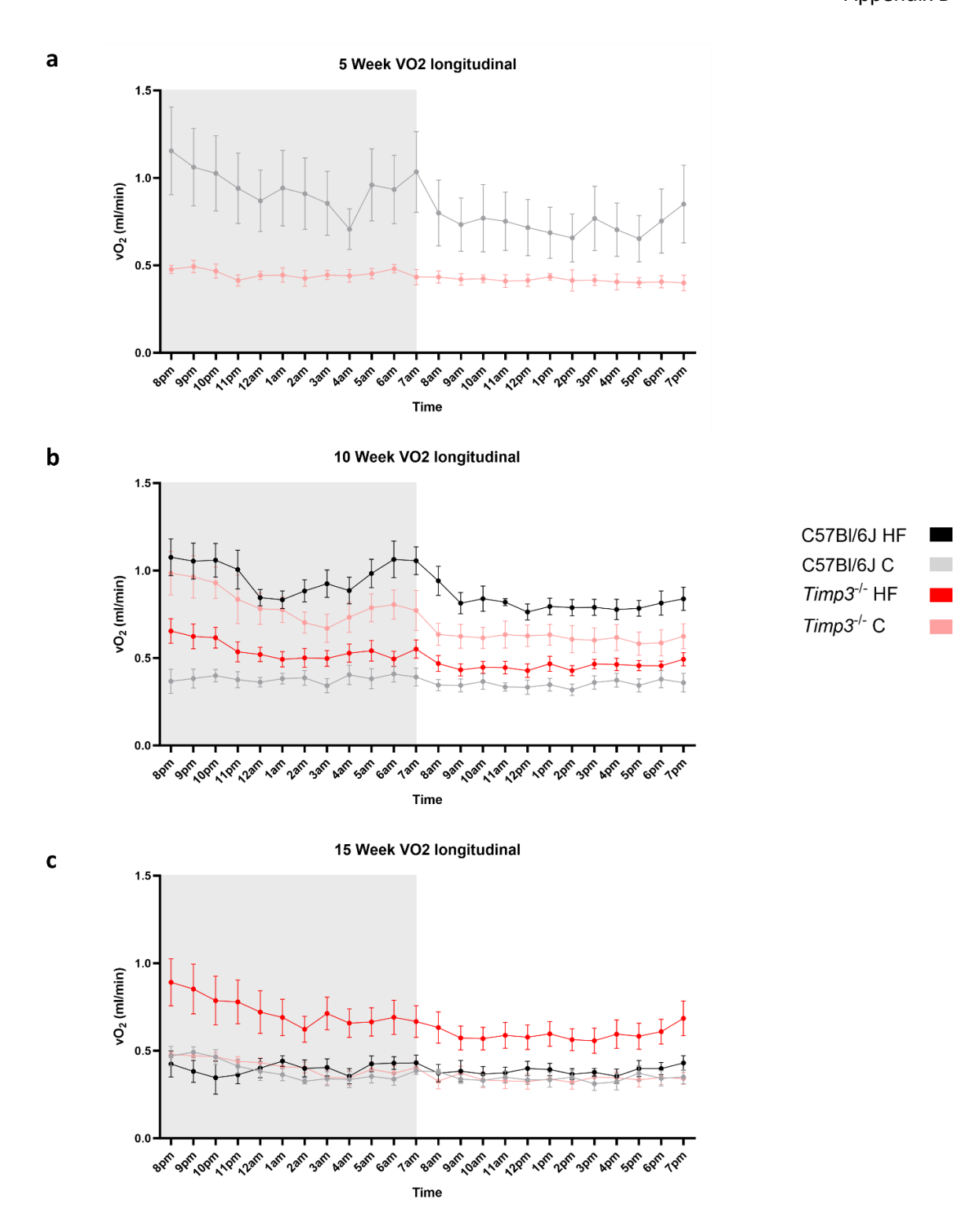


Figure D. 2 Oxygen consumption of *Timp3*-/- mice, across a 24hr period at three ages, on chow (C) and high-fat (HF) diet. Mean oxygen consumption expressed as millilitres per minute ±SEM in male *Timp3*-/- mice on chow and high-fat diet, and C57BI/6J controls, at 5 weeks (a), 10 weeks (b) and 15 weeks (c) of age. n=4-10 biological samples per group. Shaded area indicates the dark period within the animal house (from 7pm to 7am).

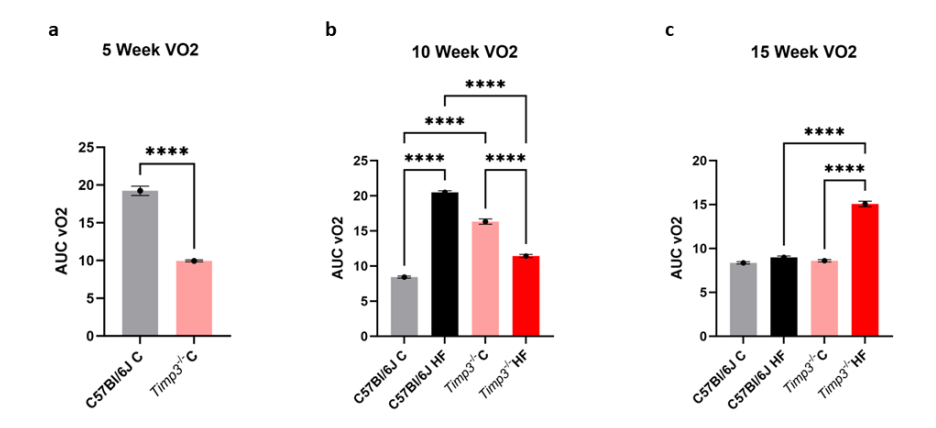
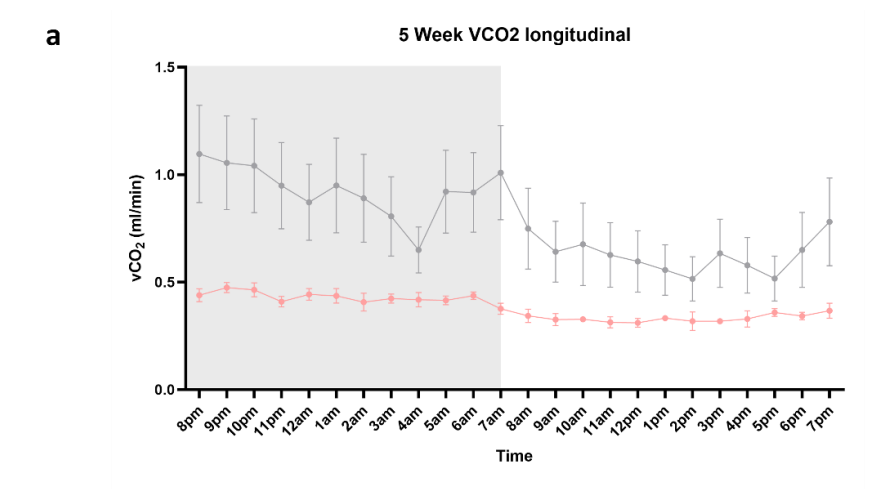
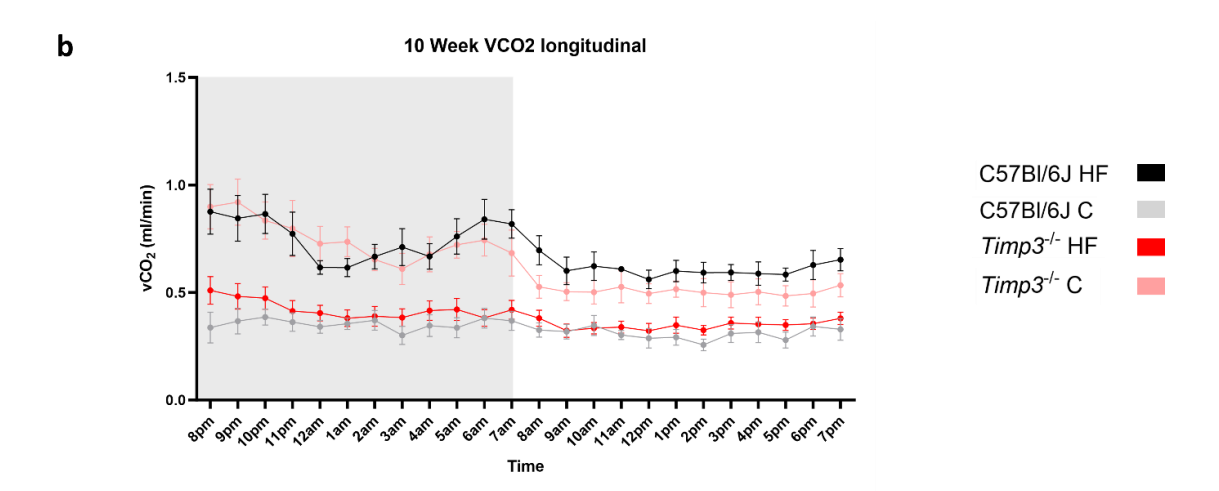


Figure D. 3 Area under the curve of oxygen consumption of $Timp3^{-/-}$ mice. Bar chart shows area under the curve of oxygen consumption in male $Timp3^{-/-}$ mice on chow and high-fat diet, and C57BI/6J controls. Tukey's comparisons was used to test for differences.

**** = p < 0.0001.





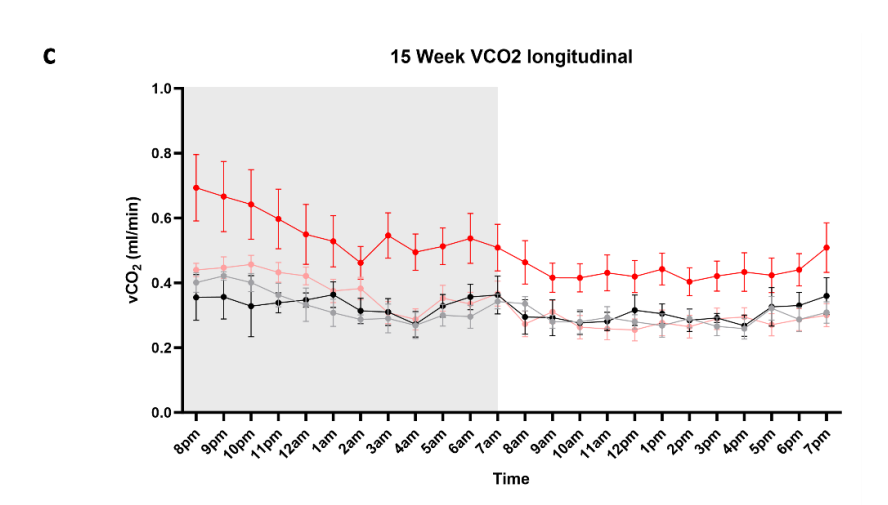


Figure D. 4 Carbon dioxide production of *Timp3*^{-/-} mice, across a 24hr period at three ages, on chow (C) and high-fat (HF) diet. Mean carbon dioxide production expressed as millilitres per minute ±SEM in male *Timp3*^{-/-} mice on chow and high-fat diet, and C57Bl/6J controls, at 5 weeks (a), 10 weeks (b) and 15 weeks (c) of age. n=4-10 biological samples per group. Shaded area indicates the dark period within the animal house (from 7pm to 7am).

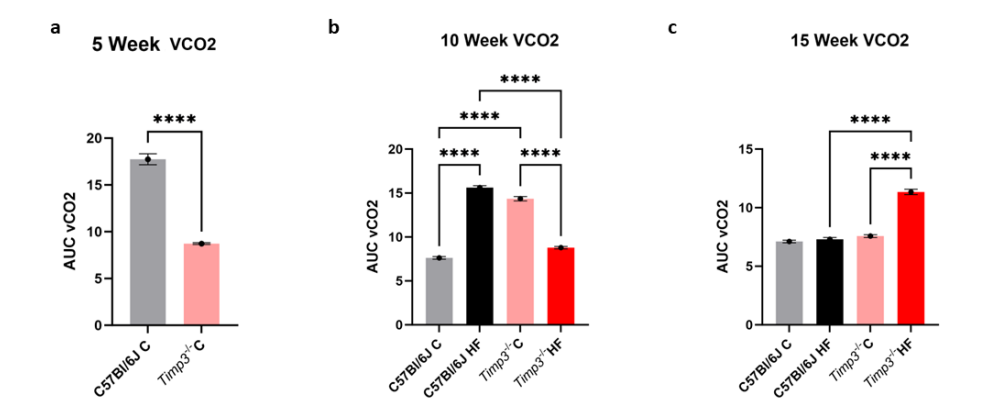
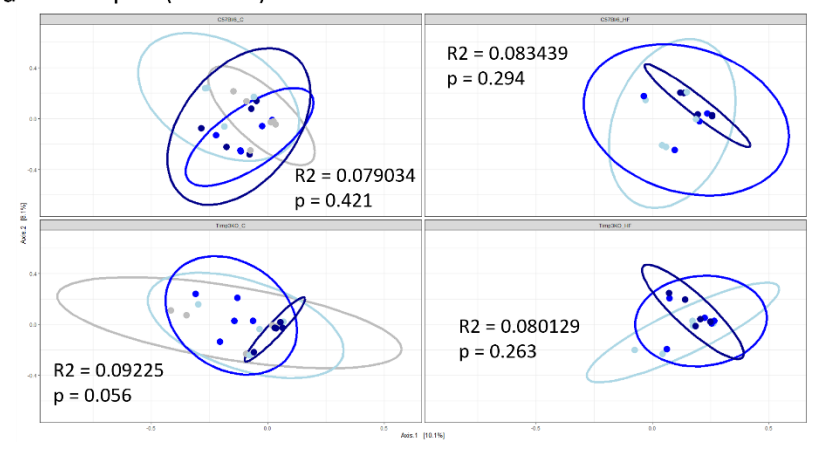


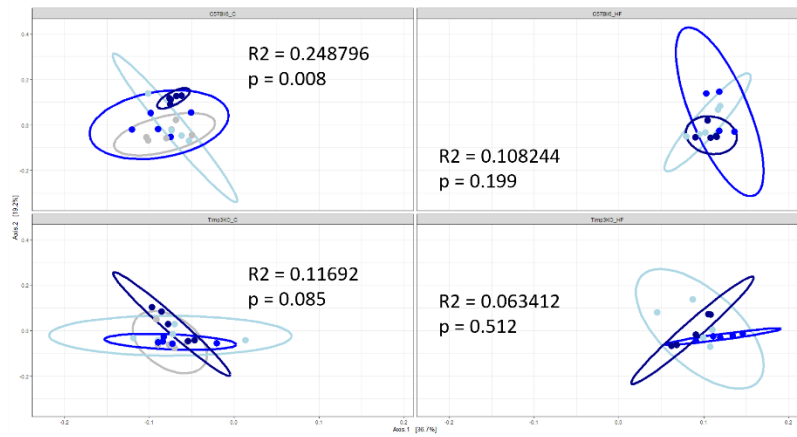
Figure D. 5 Area under the curve of carbon dioxide production of $Timp3^{-/-}$ mice. Bar chart shows area under the curve of carbon dioxide production in male $Timp3^{-/-}$ mice on chow and high-fat diet, and C57BI/6J controls. Tukey's comparisons was used to test for differences. **** = p < 0.0001.

Appendix E

a PCoA plot (UniFrac) - Rarefied Data



c PCoA plot (Weighted UniFrac) – Rarefied Data



e PCoA plot (Bray-Curtis) - Rarefied Data

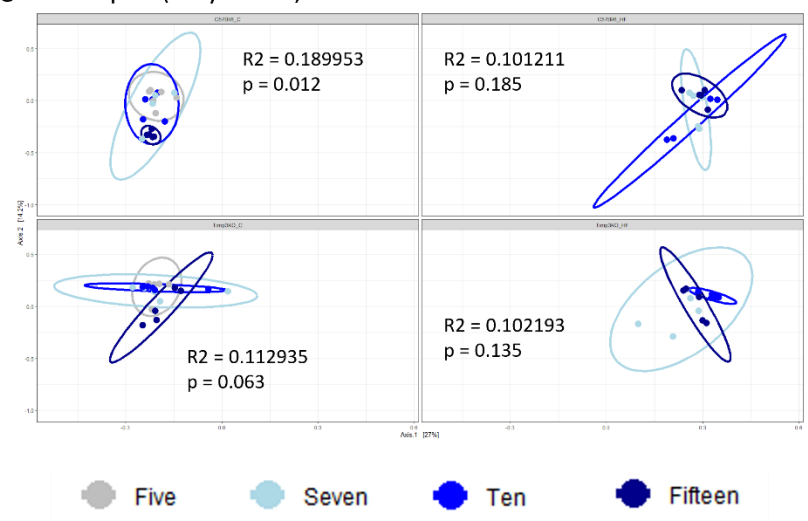


Figure E. 1 PCoA plots using different beta diversity distances in rarefied data, for each experimental group and differentiating between ages seven, ten and fifteen. (a) plot with Bray-Curtis distance; (b) plot with unweighted UniFrac distance; (c) plot with weighted UniFrac distance.

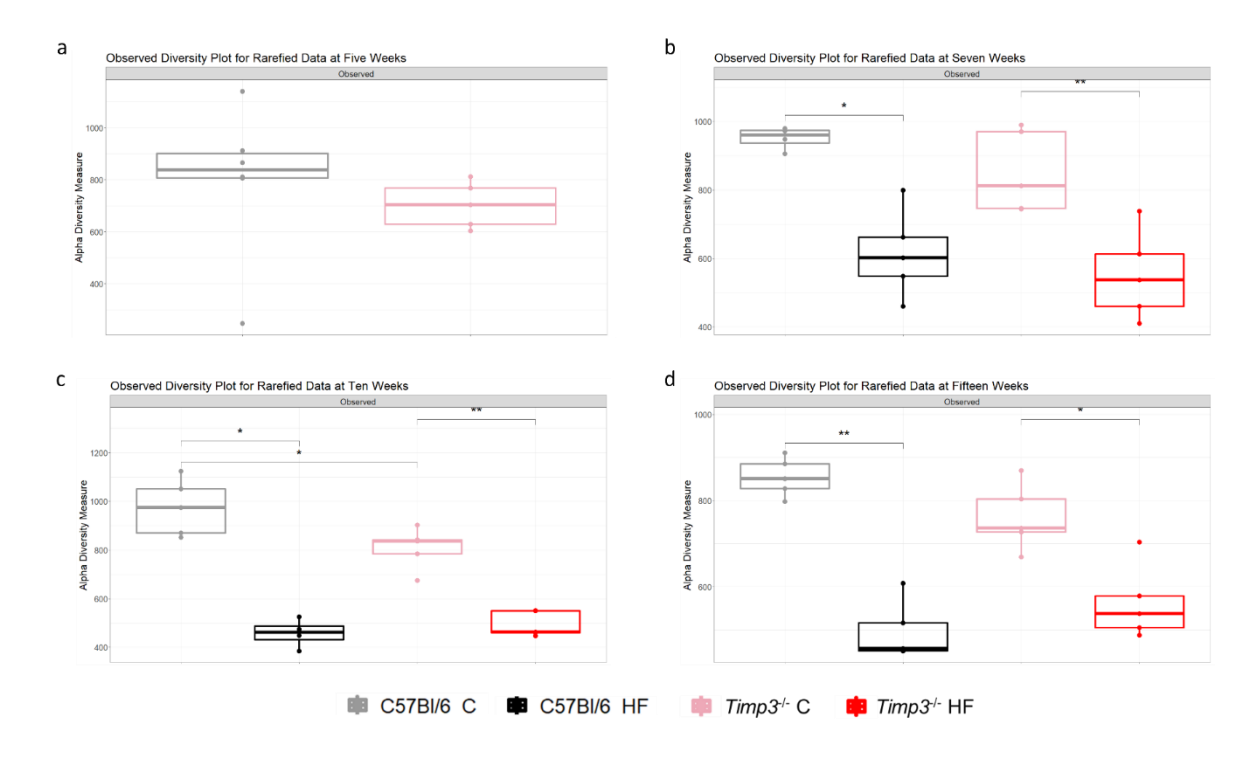


Figure E. 2 Observed alpha diversity box plots at age five (a), seven (b), ten (c), fifteen (d) weeks using rarefied abundance data. Wilcox test was used to test for differences between groups. n = 4-6 samples per group. * = p < 0.05, ** = p < 0.01.

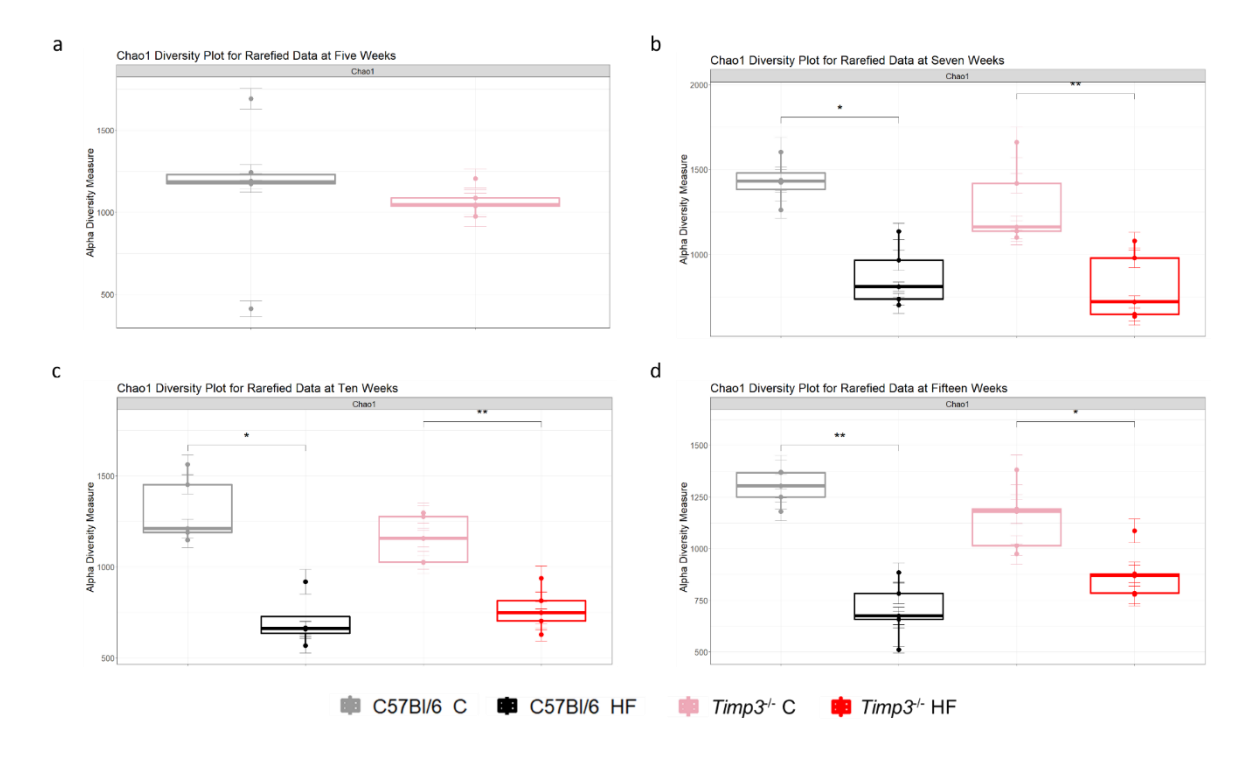


Figure E. 3 Chao1 alpha diversity box plots at age five (a), seven (b), ten (c), fifteen (d) weeks

using rarefied abundance data. Wilcox test was used to test for differences between
groups. n = 4-6 samples per group.

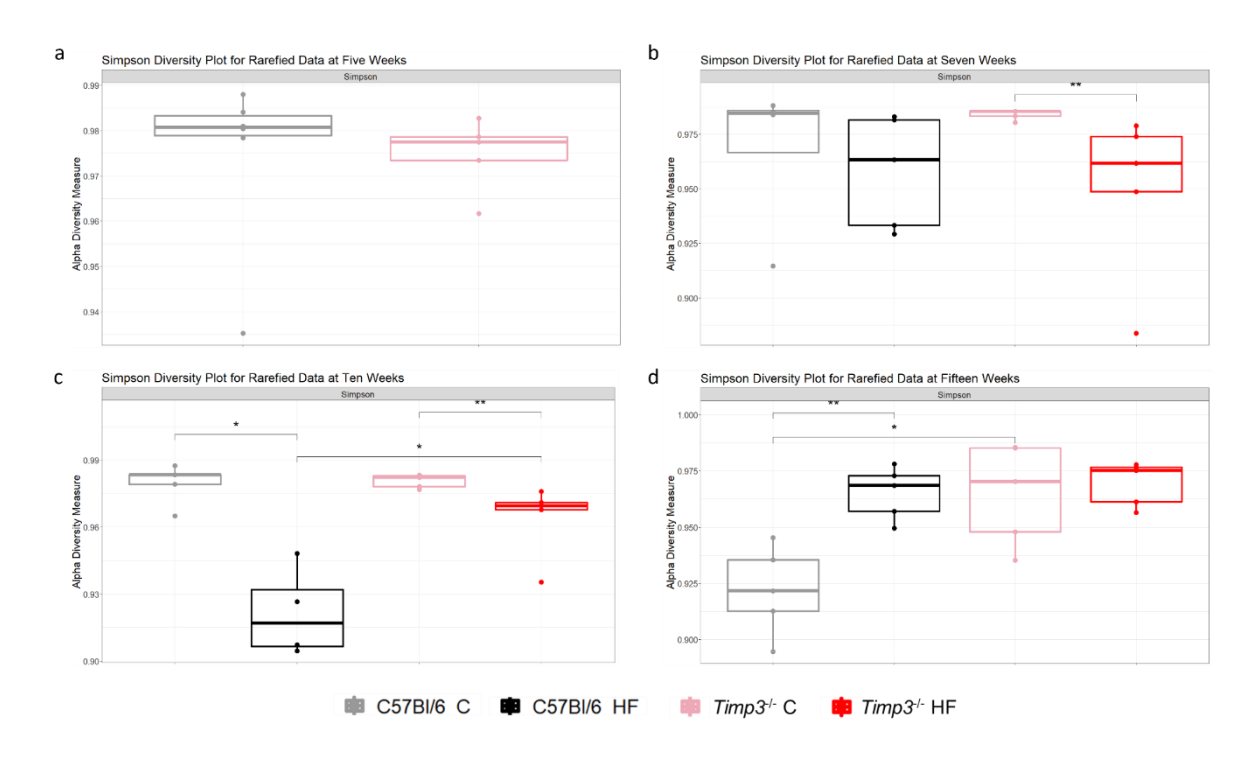


Figure E. 4 Simpson alpha diversity box plots at age five (a), seven (b), ten (c), fifteen (d) weeks using rarefied abundance data. Wilcox test was used to test for differences between groups. n = 4-6 samples per group. * = p < 0.05.

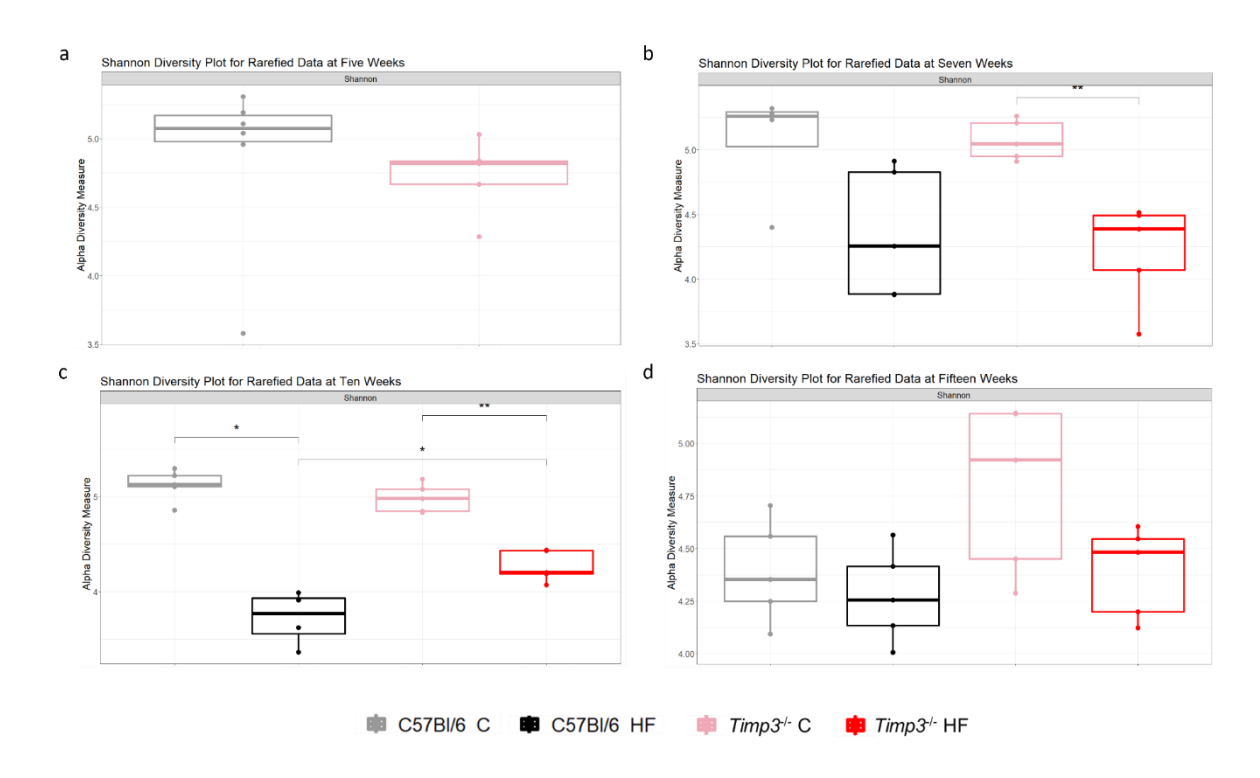


Figure E. 5 Shannon alpha diversity box plots at age five (a), seven (b), ten (c), fifteen (d) weeks using rarefied abundance data. Wilcox test was used to test for differences between groups. n = 4-6 samples per group. * = p < 0.05.

Appendix E

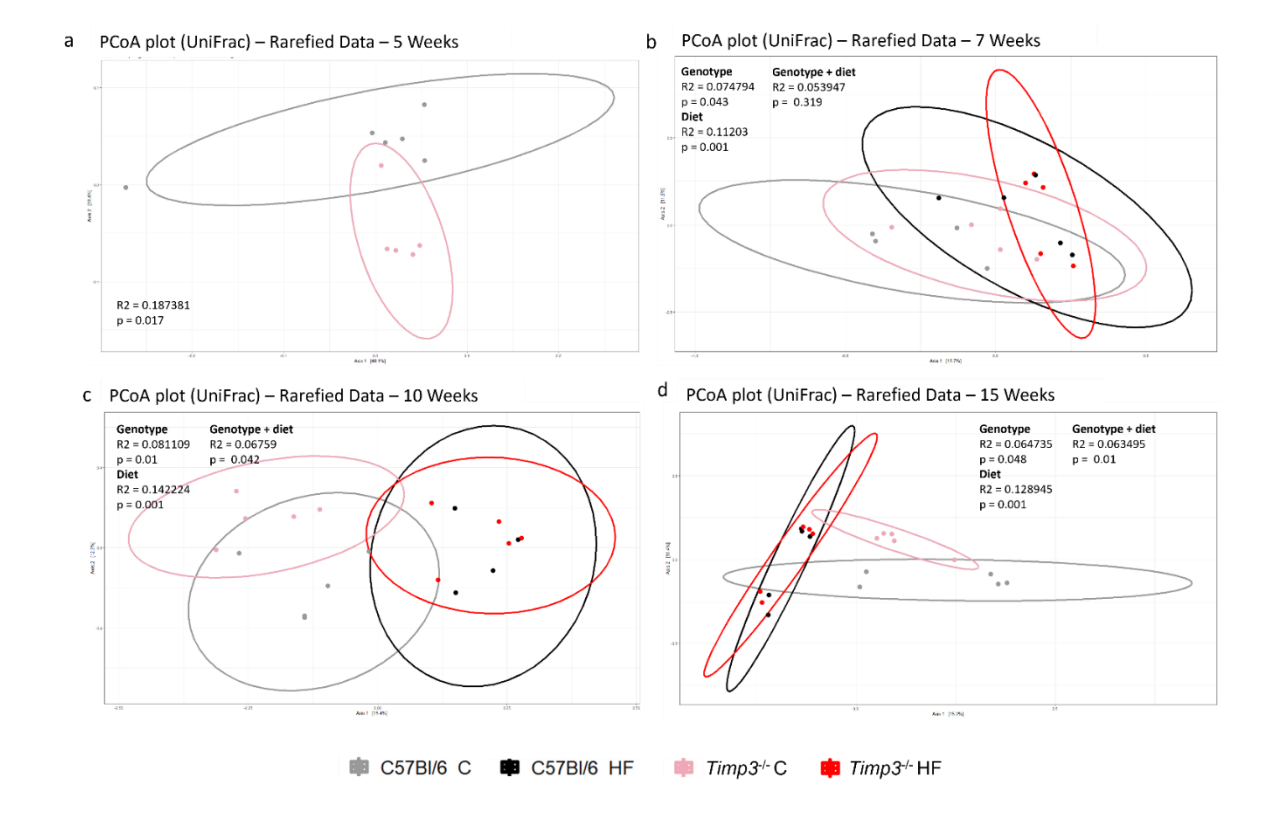


Figure E. 6 PCoA plots based on the UniFrac diversity metric, using rarefied data, at 5 (a), 7 (b), 10 (c) and 15 (d) weeks. PERMANOVA was used to test for differences. Ellipses represent 95% CI.

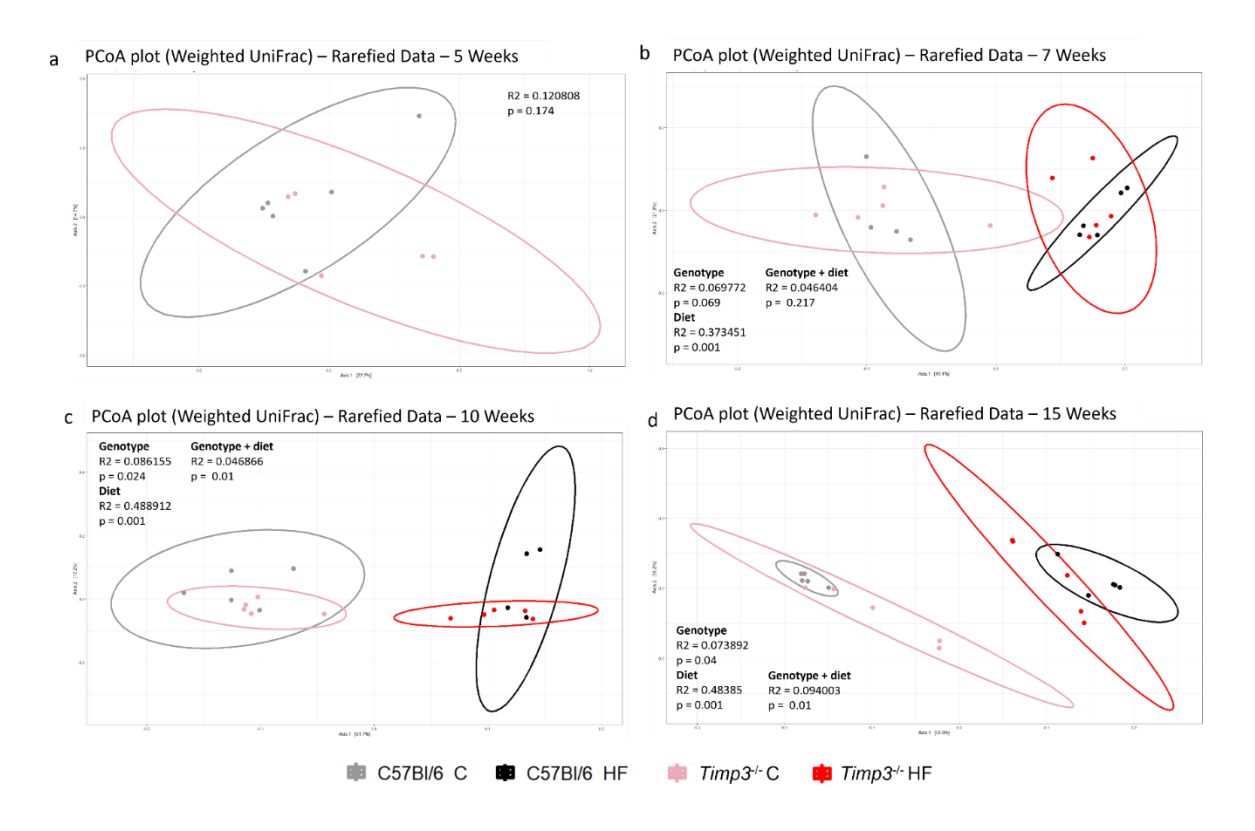


Figure E. 7 PCoA plots based on the weighted UniFrac diversity metric, using rarefied data, at 5 (a), 7 (b), 10 (c) and 15 (d) weeks. PERMANOVA was used to test for differences.

Ellipses represent 95% CI.

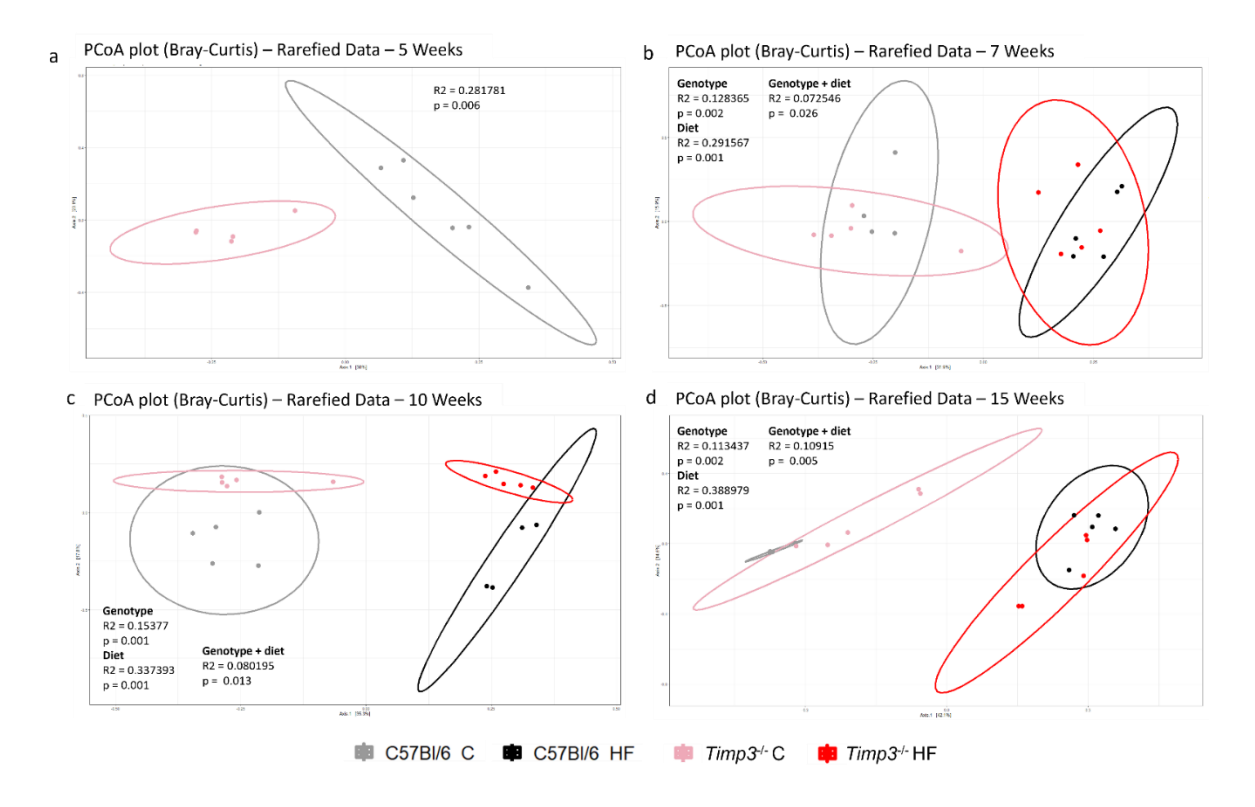


Figure E. 8 PCoA plots based on the Bray-Curtis diversity metric, using rarefied data, at 5 (a), 7 (b), 10 (c) and 15 (d) weeks. PERMANOVA was used to test for differences. Ellipses represent 95% CI.

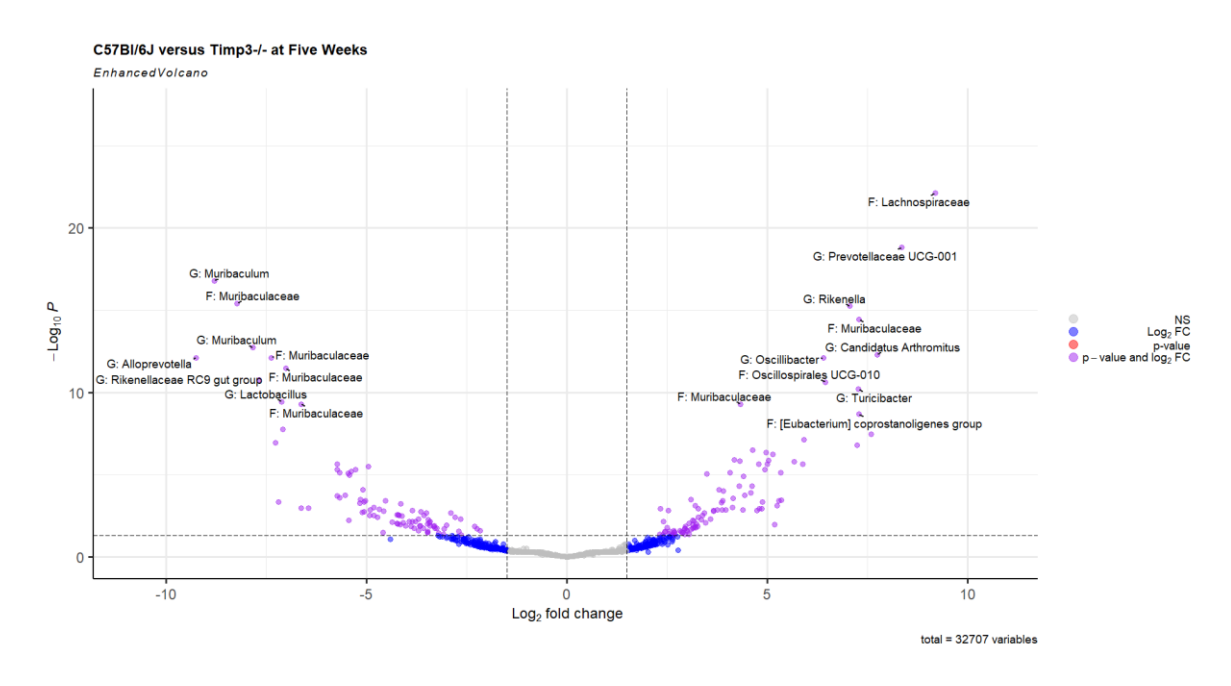


Figure E. 9 Volcano plot displaying the fold change of genera within the *Timp3*^{-/-} chow group compared to the C57BI/6J chow group at five weeks of age, identified by DESeq2.

Grey points indicate non-significant ASVs. Red points indicate ASVs with a p-value

lower than 0.01, blue points indicate ASCVs with a Log2 fold change more than +/-2 and purple points indicate ASVs that meet both these requisites. The 20 most significant ASVs are labelled.

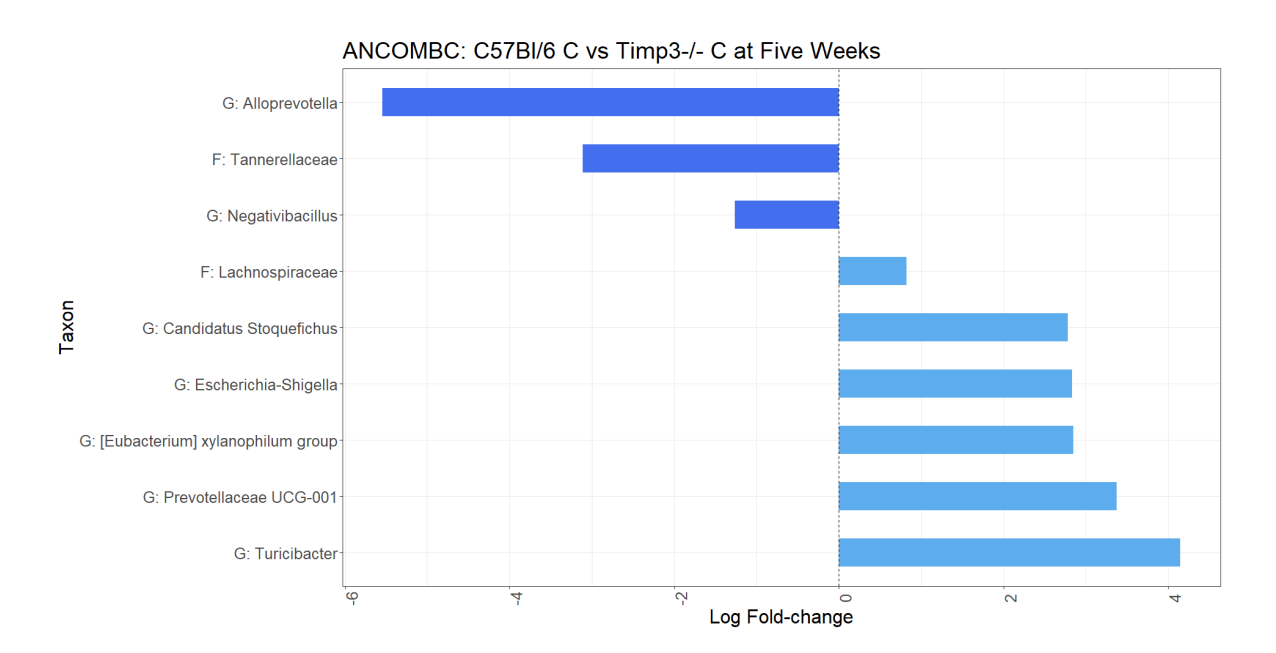


Figure E. 10 Bar plot displaying the fold change of significant genera within the *Timp3*-/- chow group compared to the C57BI/6J chow group at five weeks of age, identified by ANCOM-BC. Significance level was set at p = 0.01.

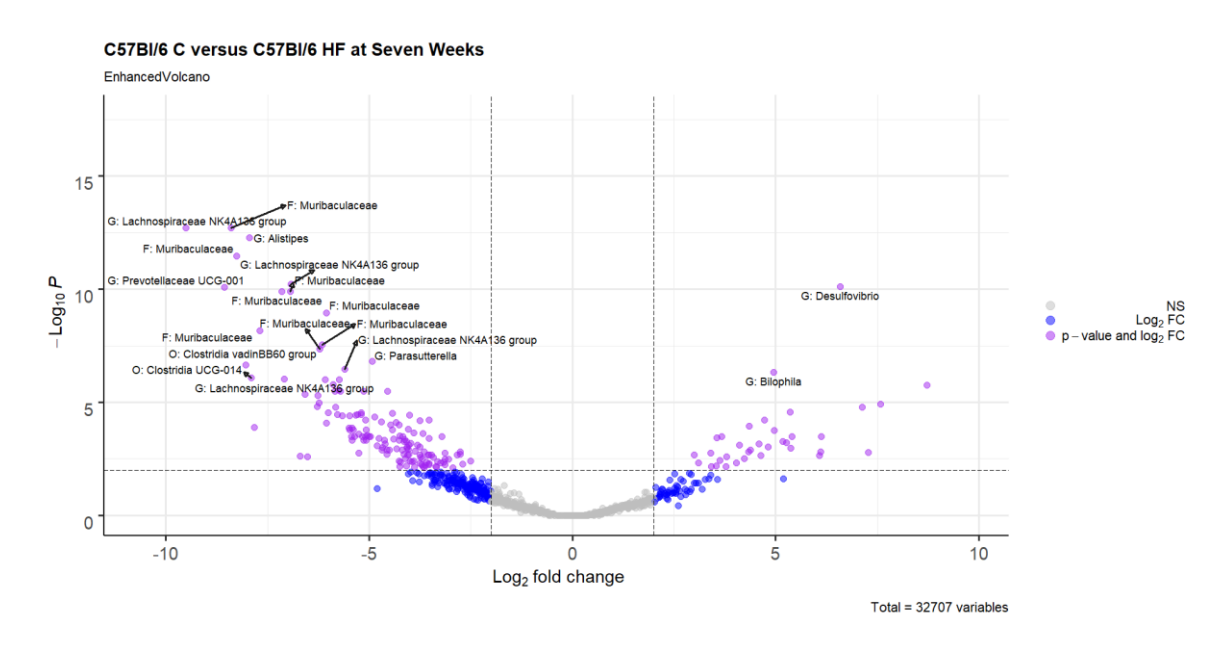


Figure E. 11 Volcano plot displaying the fold change of genera within the C57Bl/6J high fat group compared to the C57Bl/6J chow group at seven weeks of age, identified by DESeq2.

Grey points indicate non-significant ASVs. Red points indicate ASVs with a p-value

Appendix E

lower than 0.01, blue points indicate ASCVs with a Log2 fold change more than +/-2 and purple points indicate ASVs that meet both these requisites. The 20 most significant ASVs are labelled.

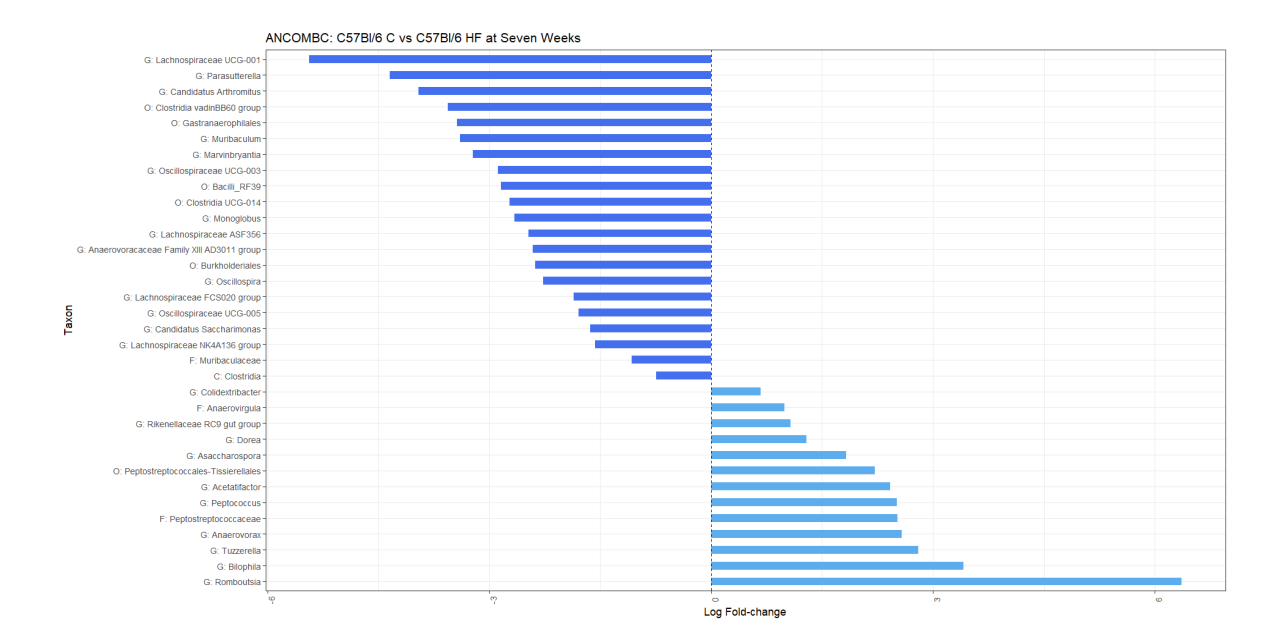


Figure E. 12 Bar plot displaying the fold change of significant genera within the C57Bl/6J high-fat group compared to the C57Bl/6J chow group at seven weeks of age, identified by ANCOM-BC. Significance level was set at p = 0.01.

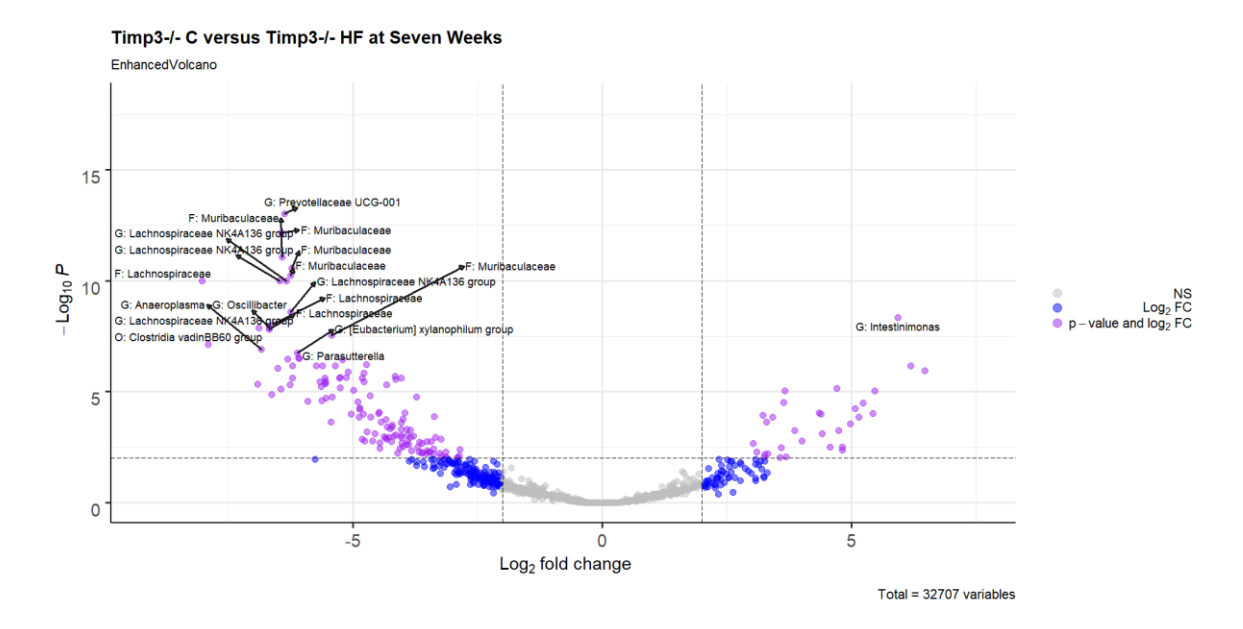


Figure E. 13 Volcano plot displaying the fold change of genera within the *Timp3-/-* high-fat group compared to the *Timp3-/-* chow group at seven weeks of age, identified by DESeq2.

Grey points indicate non-significant ASVs. Red points indicate ASVs with a p-value lower than 0.01, blue points indicate ASCVs with a Log2 fold change more than +/-2 and purple points indicate ASVs that meet both these requisites. The 20 most significant ASVs are labelled.

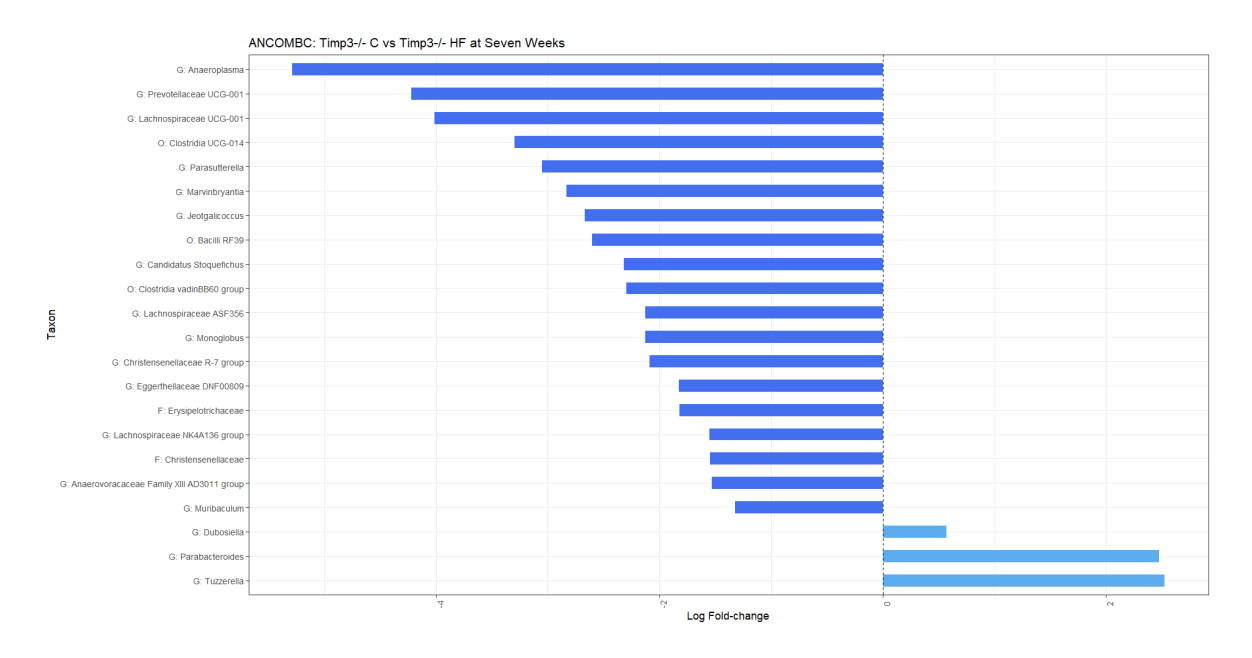


Figure E. 14 Bar plot displaying the fold change of significant genera within the *Timp3*^{-/-} high-fat group compared to the *Timp3*^{-/-} chow group at seven weeks of age, identified by ANCOM-BC. Significance level was set at p = 0.01.

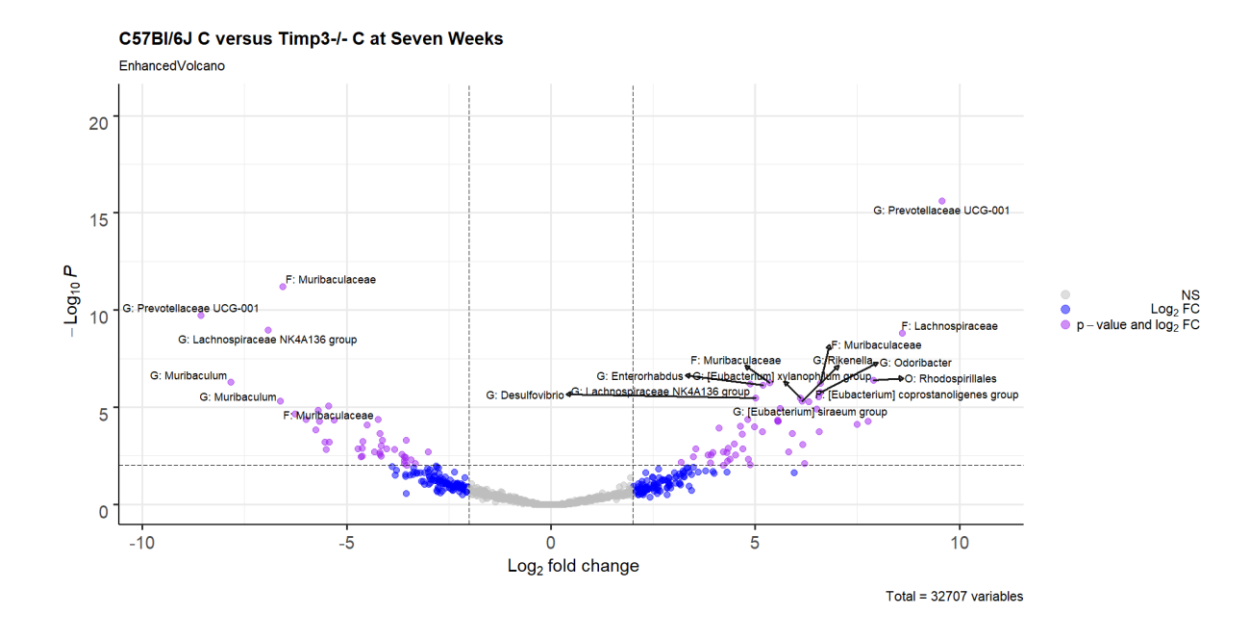


Figure E. 15 Volcano plot displaying the fold change of genera within the *Timp3*-/- chow group compared to the C57Bl/6J chow group at seven weeks of age, identified by DESeq2.

Grey points indicate non-significant ASVs. Red points indicate ASVs with a p-value lower than 0.01, blue points indicate ASCVs with a Log2 fold change more than +/-2 and purple points indicate ASVs that meet both these requisites. The 20 most significant ASVs are labelled.

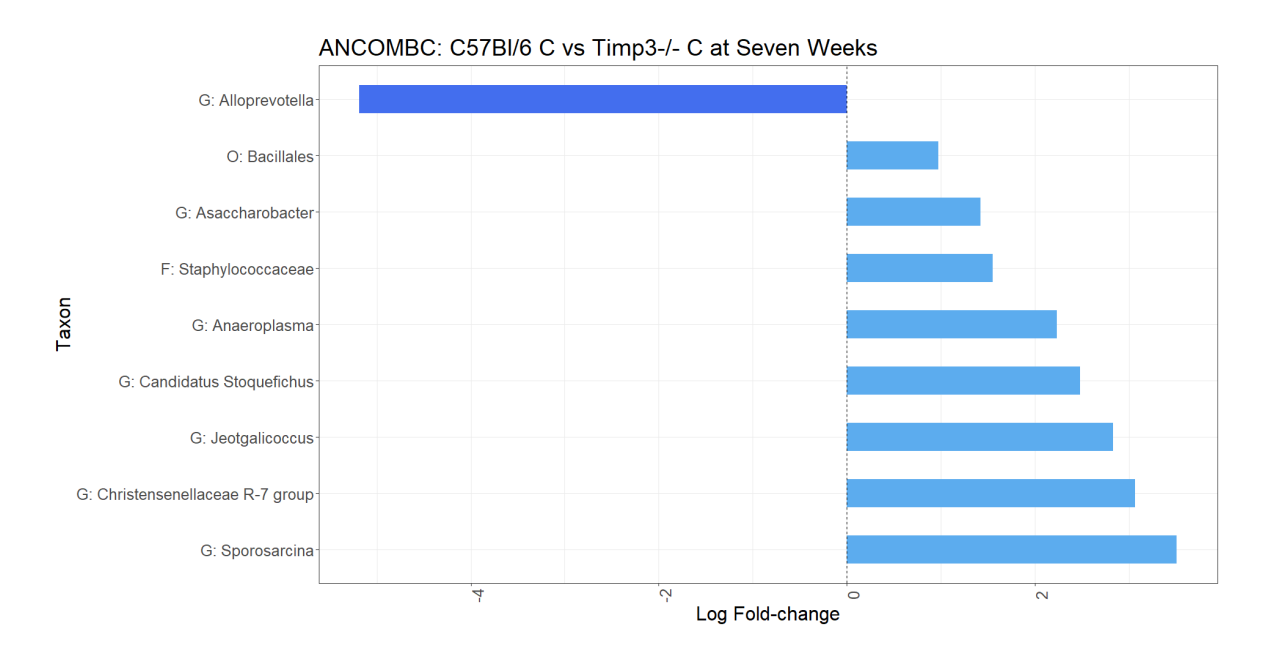


Figure E. 16 Bar plot displaying the fold change of significant genera within the *Timp3*-/- chow group compared to the C57Bl/6J chow group at seven weeks of age, identified by ANCOM-BC. Significance level was set at p = 0.01.

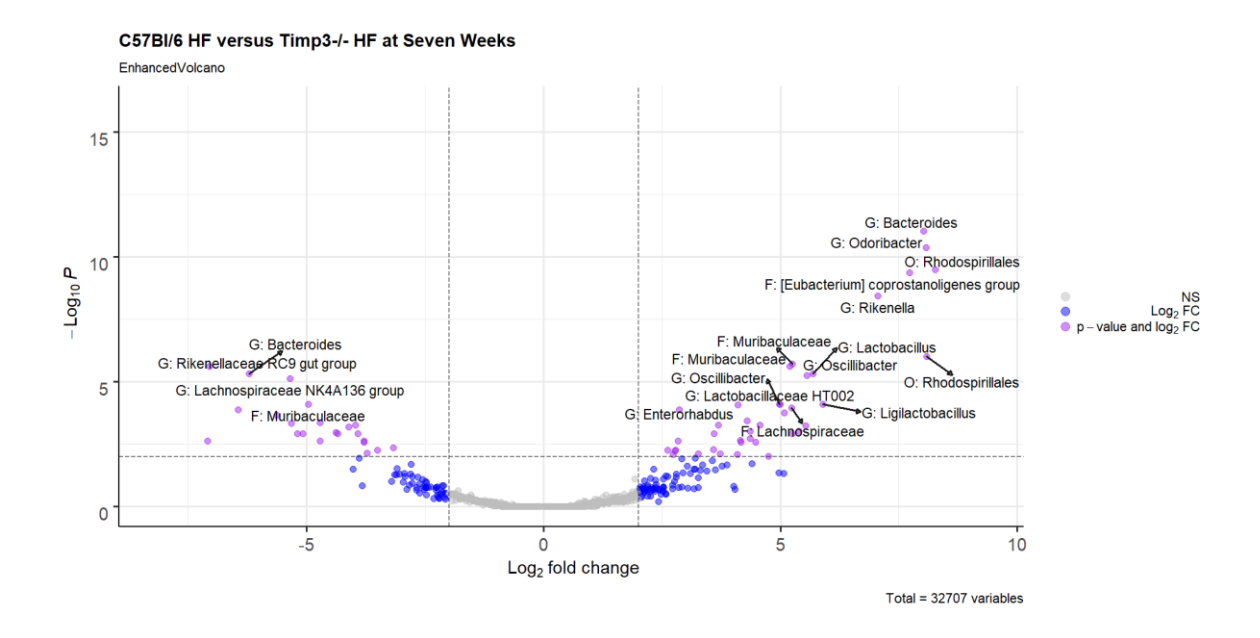


Figure E. 17 Volcano plot displaying the fold change of genera within the *Timp3*-/- high-fat group compared to the C57BI/6J high-fat group at seven weeks of age, identified by DESeq2. Grey points indicate non-significant ASVs. Red points indicate ASVs with a p-value lower than 0.01, blue points indicate ASCVs with a Log2 fold change more than +/-2 and purple points indicate ASVs that meet both these requisites. The 20 most significant ASVs are labelled.

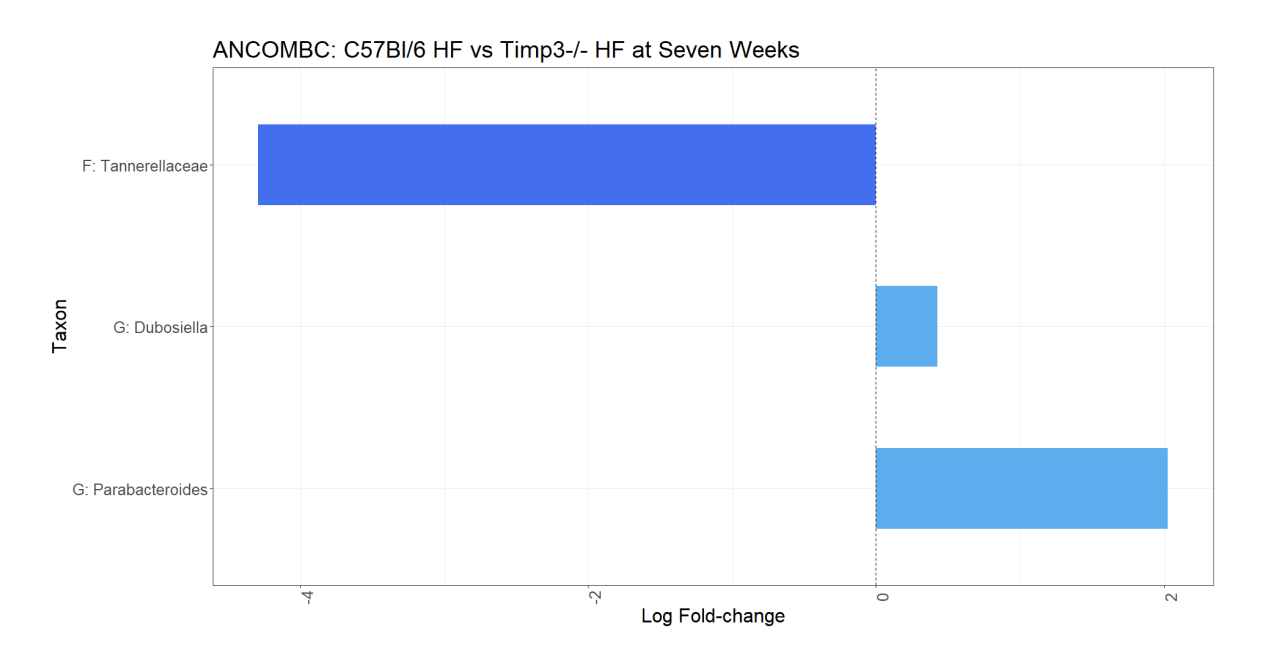


Figure E. 18 Bar plot displaying the fold change of significant genera within the *Timp3*-/- high-fat group compared to the C57BI/6J high-fat group at seven weeks of age, identified by ANCOM-BC. Significance level was set at p = 0.01.

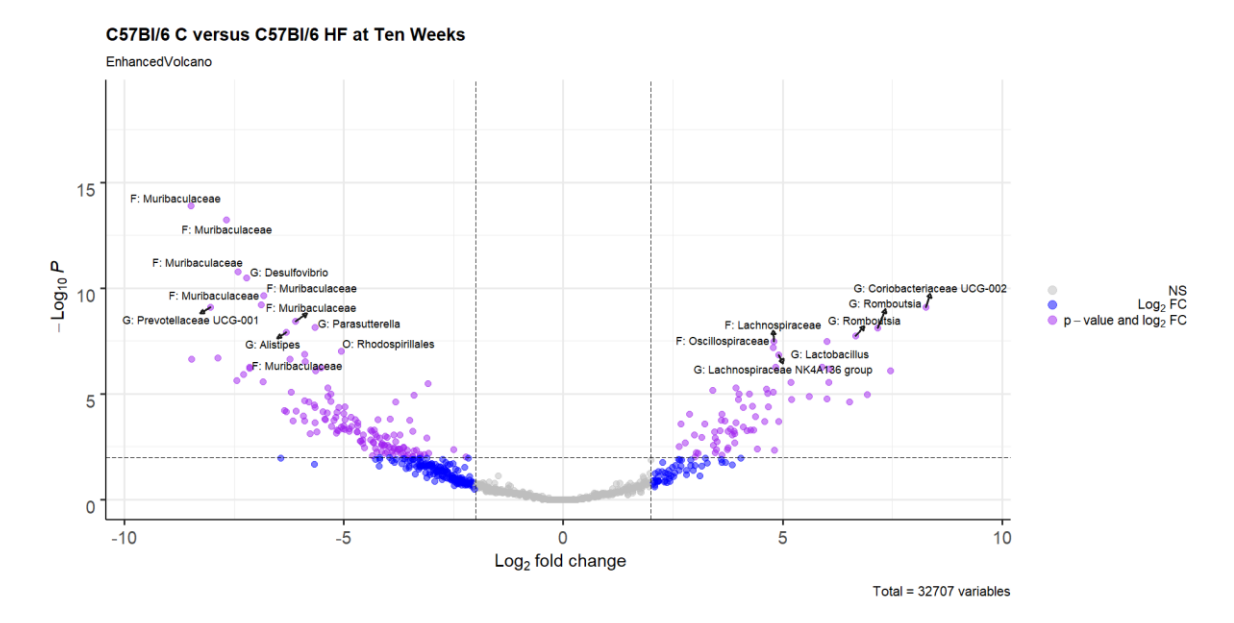


Figure E. 19 Volcano plot displaying the fold change of genera within the C57Bl/6J high fat group compared to the C57Bl/6J chow group at ten weeks of age, identified by DESeq2.

Grey points indicate non-significant ASVs. Red points indicate ASVs with a p-value lower than 0.01, blue points indicate ASCVs with a Log2 fold change more than +/-2 and purple points indicate ASVs that meet both these requisites. The 20 most significant ASVs are labelled.

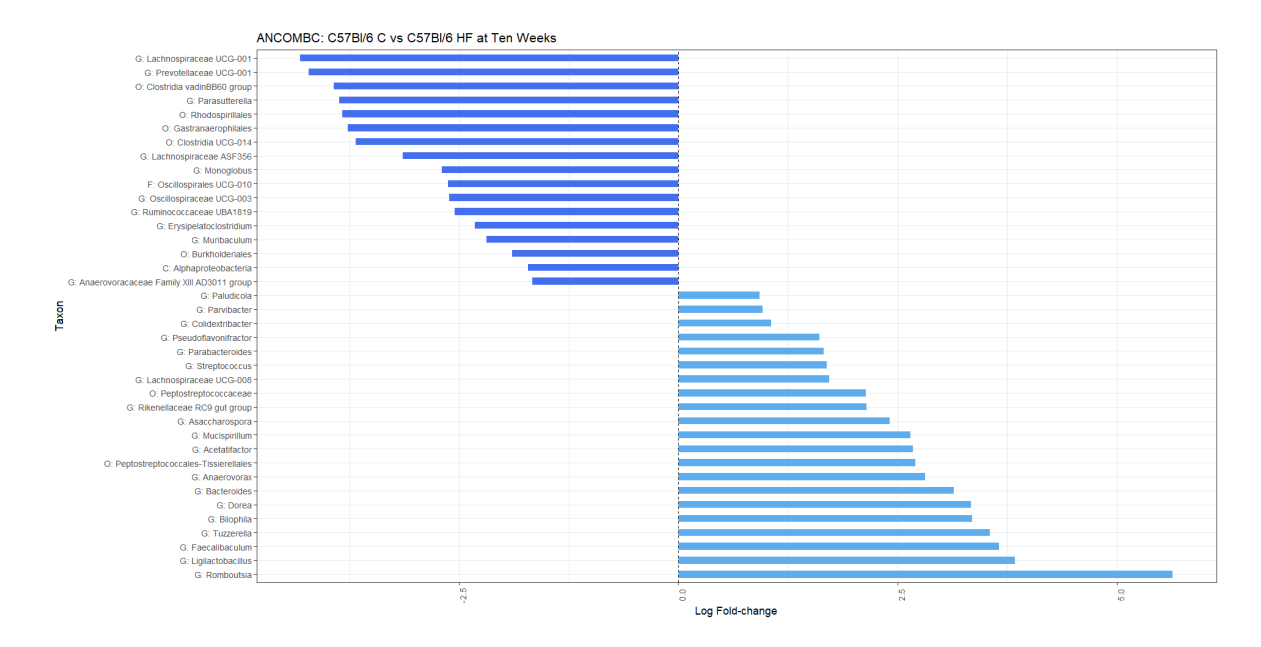


Figure E. 20 Bar plot displaying the fold change of significant genera within the C57Bl/6J high-fat group compared to the C57Bl/6J chow group at ten weeks of age, identified by ANCOM-BC. Significance level was set at p = 0.01.

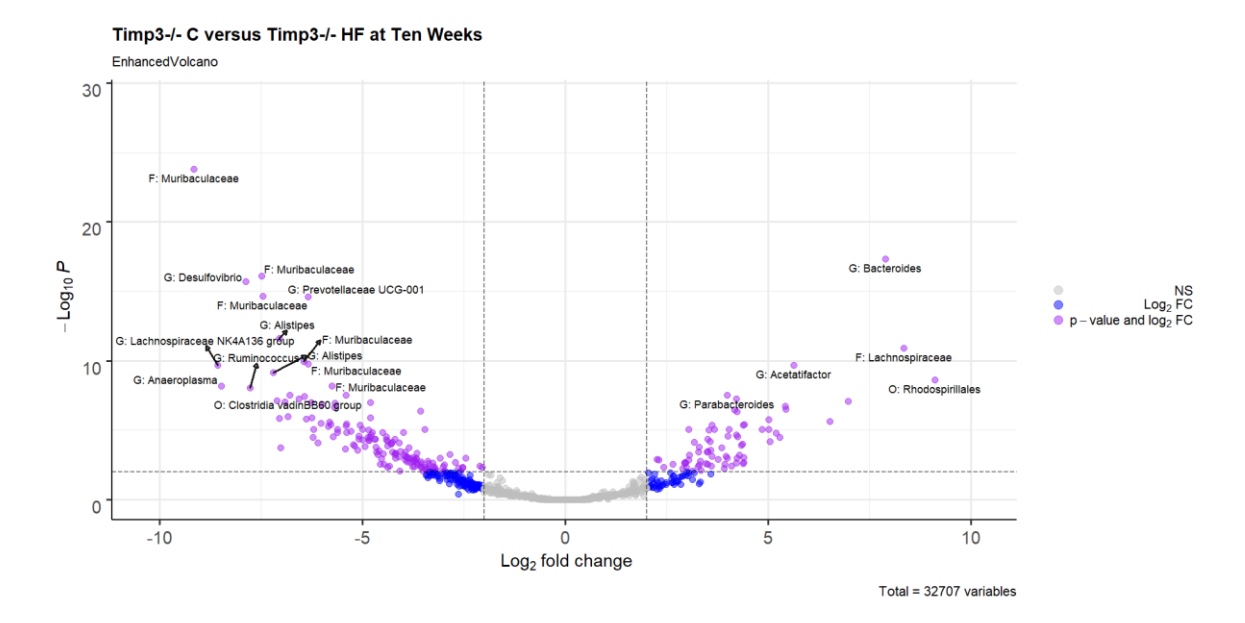


Figure E. 21 Volcano plot displaying the fold change of genera within the *Timp3-/-* high-fat group compared to the *Timp3-/-* chow group at ten weeks of age, identified by DESeq2.

Grey points indicate non-significant ASVs. Red points indicate ASVs with a p-value lower than 0.01, blue points indicate ASCVs with a Log2 fold change more than +/-2 and purple points indicate ASVs that meet both these requisites. The 20 most significant ASVs are labelled.

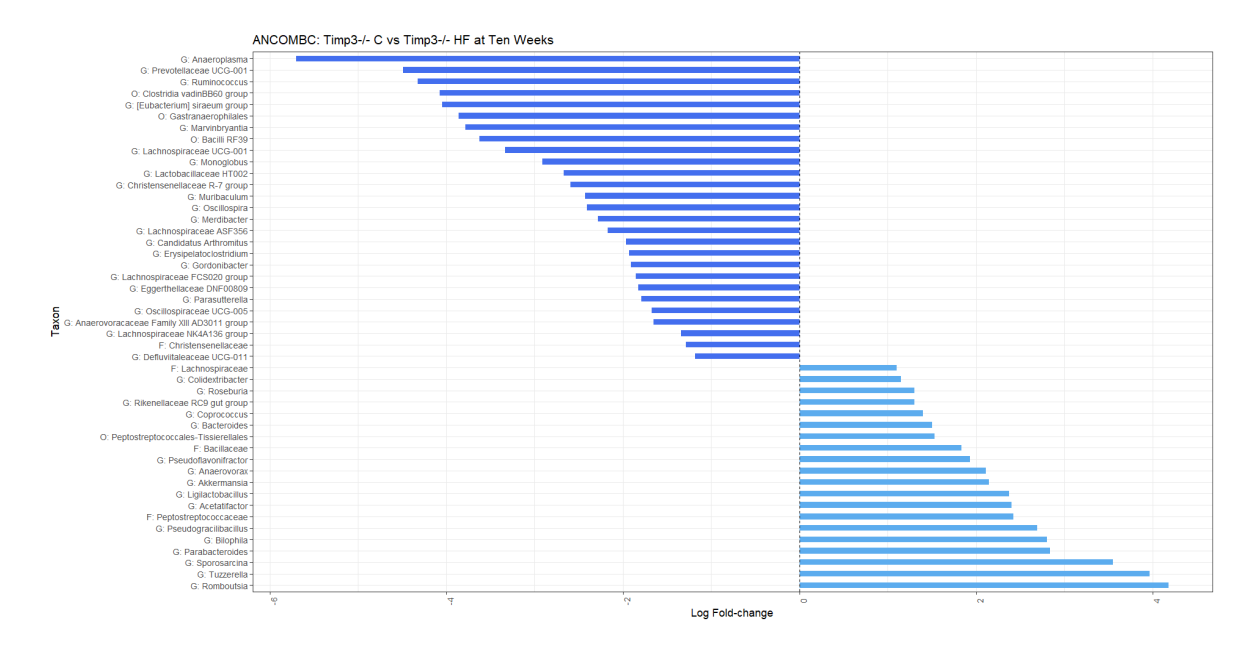


Figure E. 22 Bar plot displaying the fold change of significant genera within the *Timp3*^{-/-} high-fat group compared to the *Timp3*^{-/-} chow group at ten weeks of age, identified by ANCOM-BC. Significance level was set at p = 0.01.

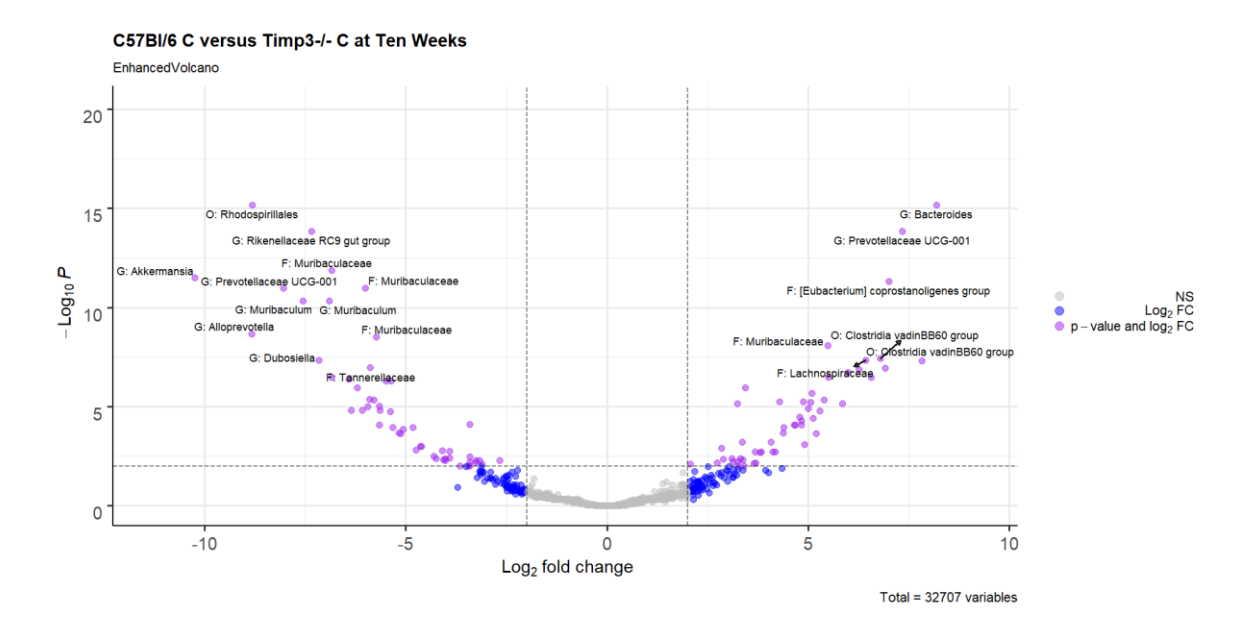


Figure E. 23 Volcano plot displaying the fold change of genera within the *Timp3*-/- chow group compared to the C57Bl/6J chow group at ten weeks of age, identified by DESeq2.

Grey points indicate non-significant ASVs. Red points indicate ASVs with a p-value lower than 0.01, blue points indicate ASCVs with a Log2 fold change more than +/-2 and purple points indicate ASVs that meet both these requisites. The 20 most significant ASVs are labelled.

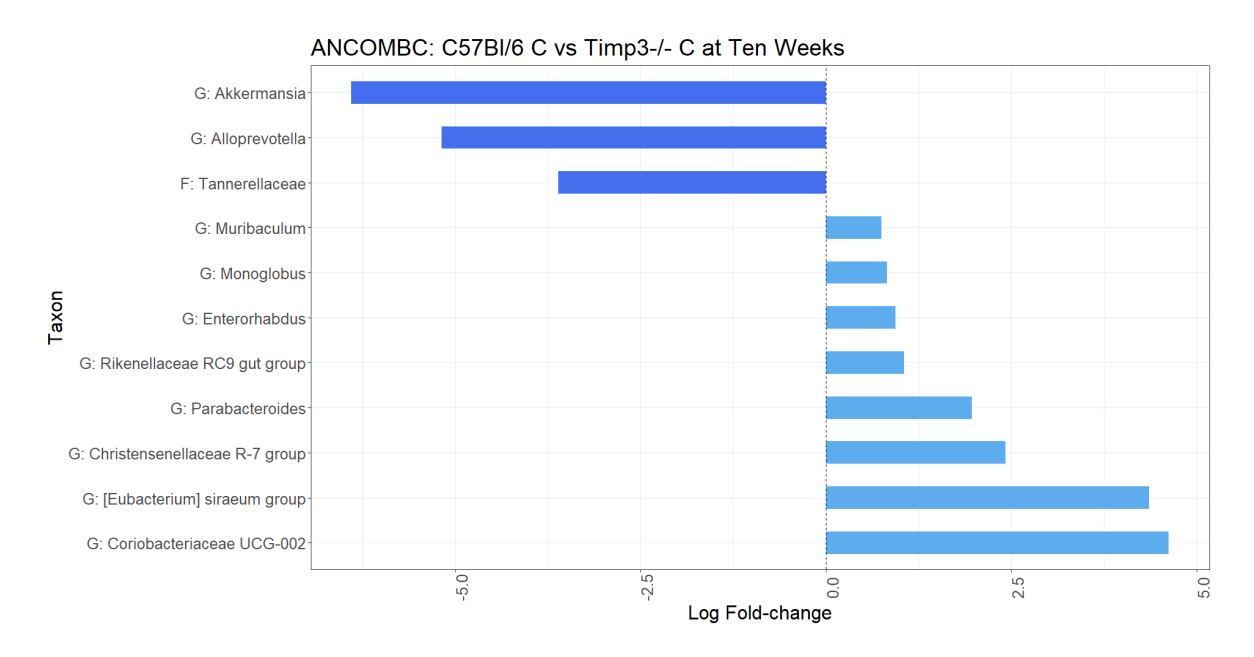


Figure E. 24 Bar plot displaying the fold change of significant genera within the $Timp3^{-/-}$ chow group compared to the C57Bl/6J chow group at ten weeks of age, identified by ANCOM-BC. Significance level was set at p = 0.01.

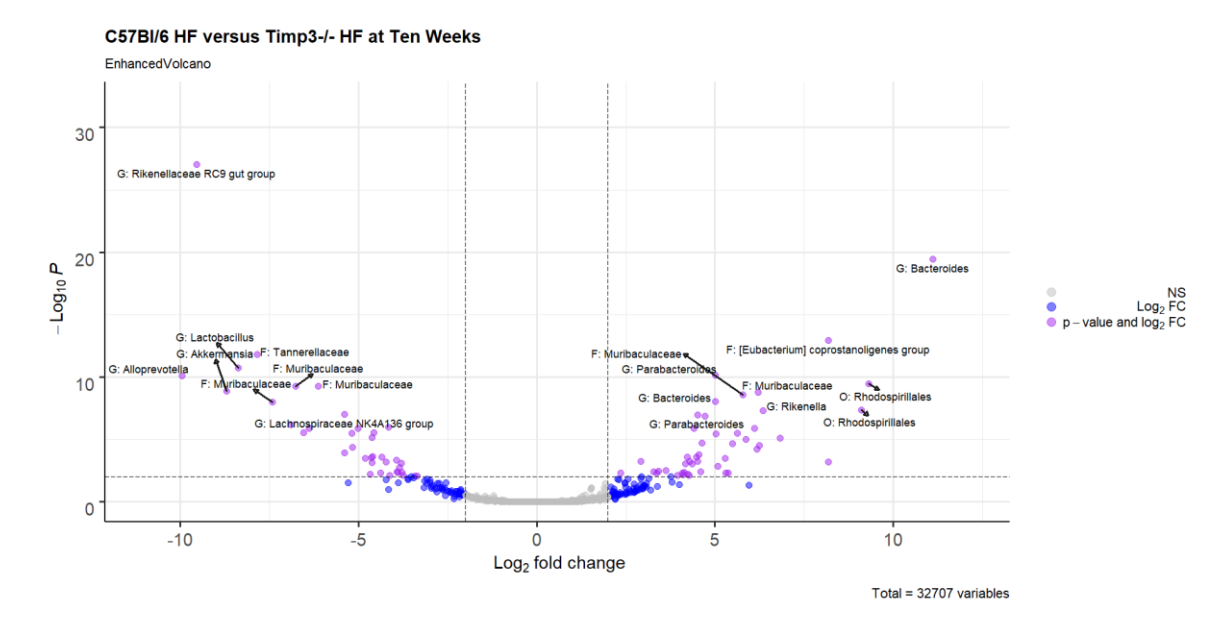


Figure E. 25 Volcano plot displaying the fold change of genera within the *Timp3-/-* high-fat group compared to the C57BI/6J high-fat group at ten weeks of age, identified by DESeq2. Grey points indicate non-significant ASVs. Red points indicate ASVs with a p-value lower than 0.01, blue points indicate ASCVs with a Log2 fold change more than +/-2 and purple points indicate ASVs that meet both these requisites. The 20 most significant ASVs are labelled.

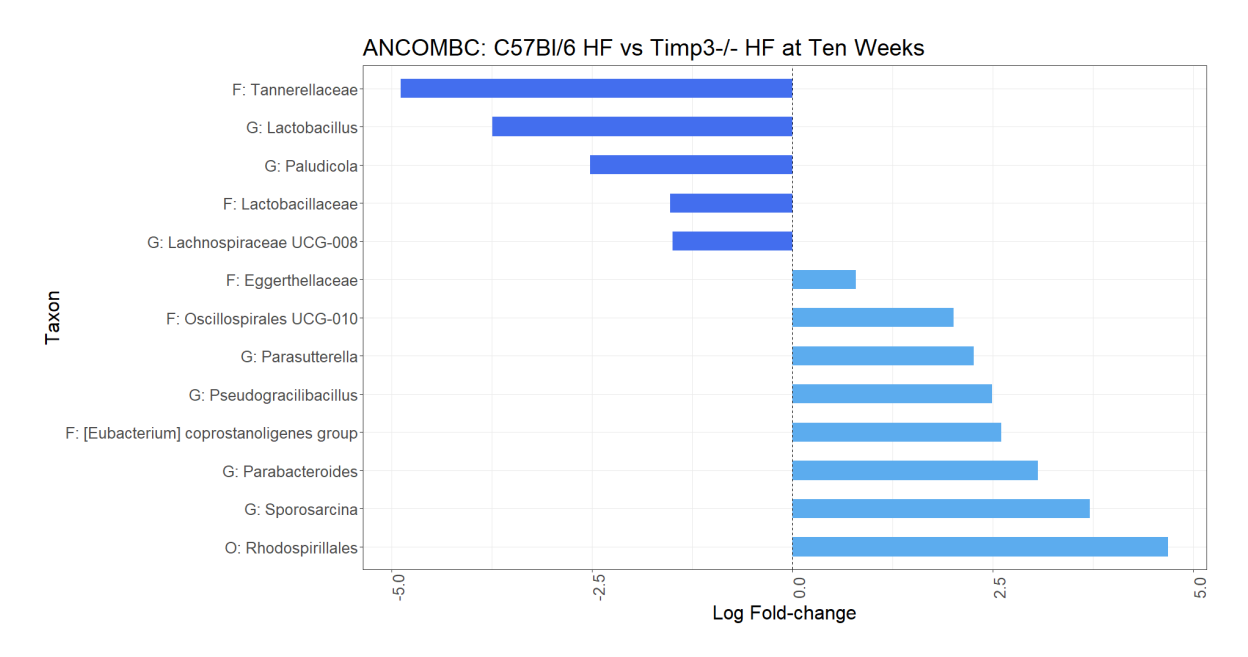


Figure E. 26 Bar plot displaying the fold change of significant genera within the *Timp3*-/- high-fat group compared to the C57BI/6J high-fat group at ten weeks of age, identified by ANCOM-BC. Significance level was set at p = 0.01.

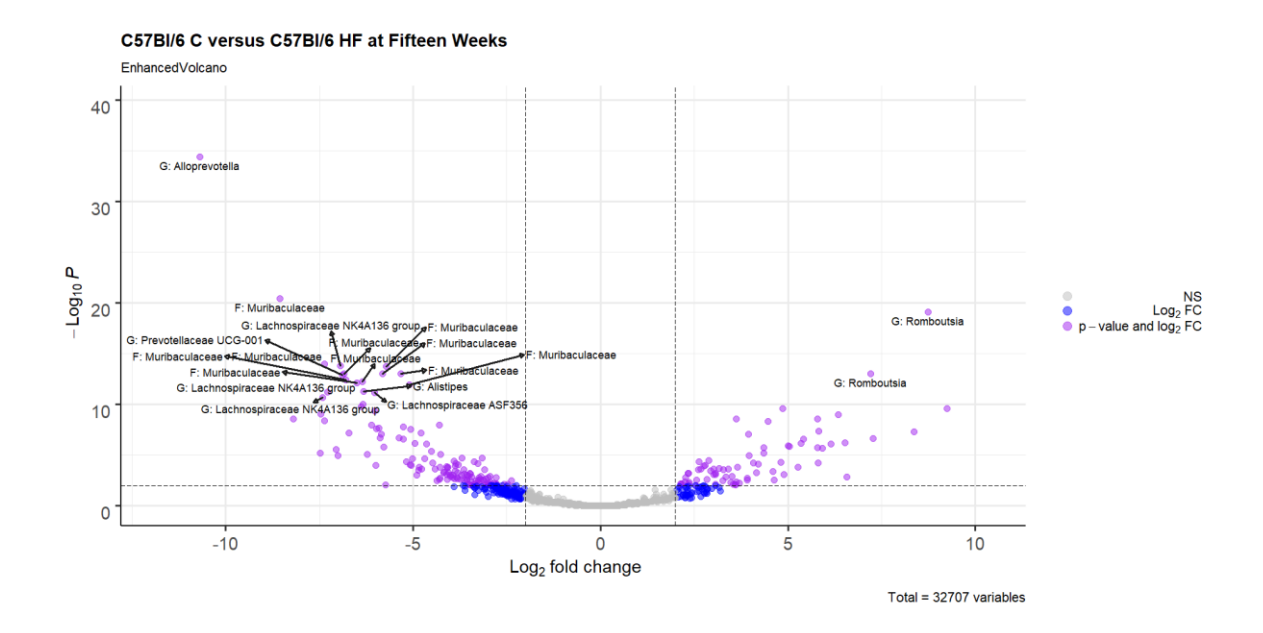


Figure E. 27 Volcano plot displaying the fold change of genera within the C57Bl/6J high fat group compared to the C57Bl/6J chow group at fifteen weeks of age, identified by DESeq2. Grey points indicate non-significant ASVs. Red points indicate ASVs with a p-value lower than 0.01, blue points indicate ASCVs with a Log2 fold change more than +/-2 and purple points indicate ASVs that meet both these requisites. The 20 most significant ASVs are labelled.

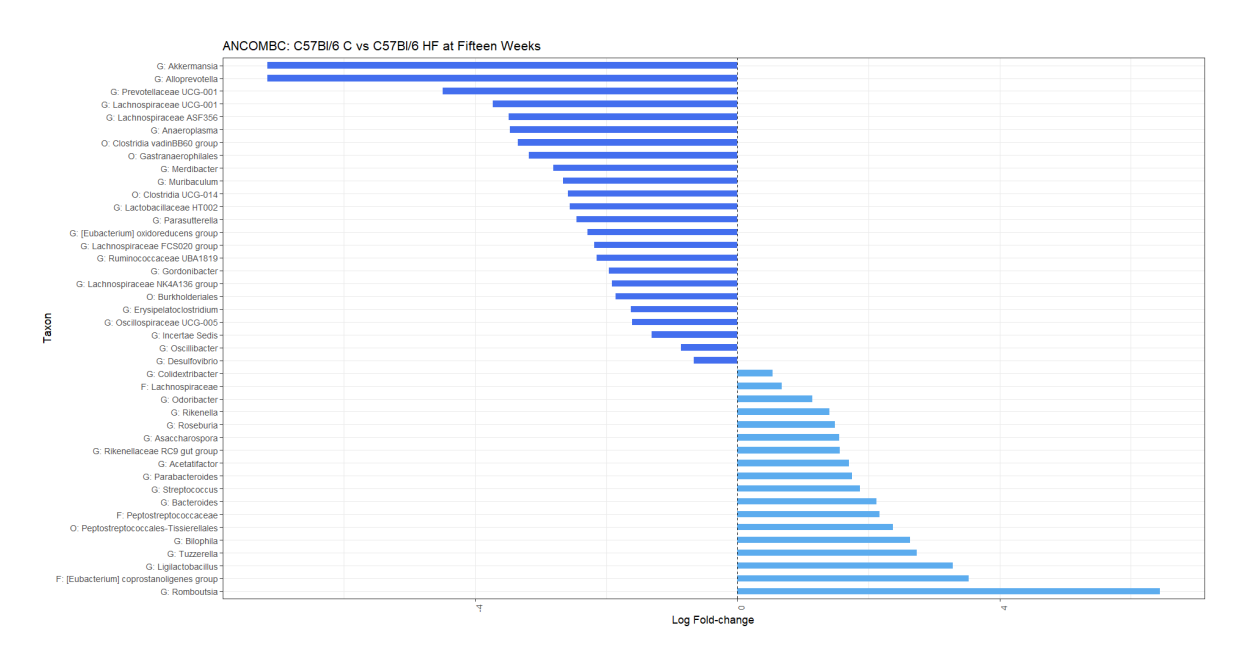


Figure E. 28 Bar plot displaying the fold change of significant genera within the C57Bl/6J high-fat group compared to the C57Bl/6J chow group at fifteen weeks of age, identified by ANCOM-BC. Significance level was set at p = 0.01.

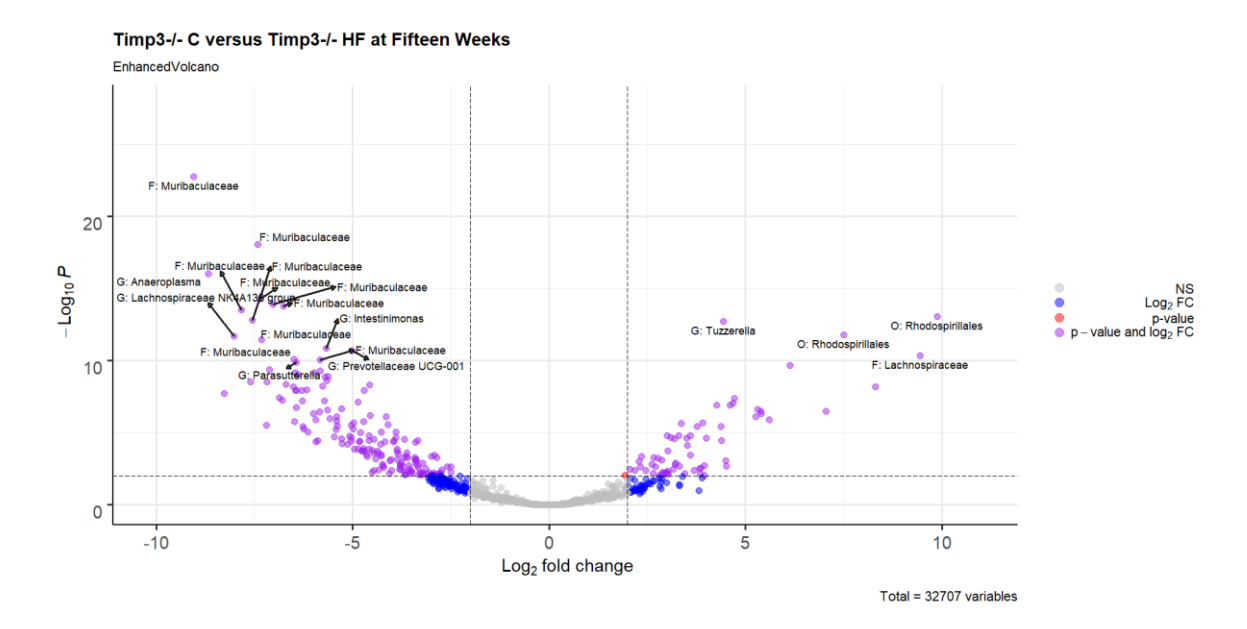


Figure E. 29 Volcano plot displaying the fold change of genera within the *Timp3*-/- high-fat group compared to the *Timp3*-/- chow group at seven weeks of age, identified by DESeq2.

Grey points indicate non-significant ASVs. Red points indicate ASVs with a p-value lower than 0.01, blue points indicate ASCVs with a Log2 fold change more than +/-2 and purple points indicate ASVs that meet both these requisites. The 20 most significant ASVs are labelled.

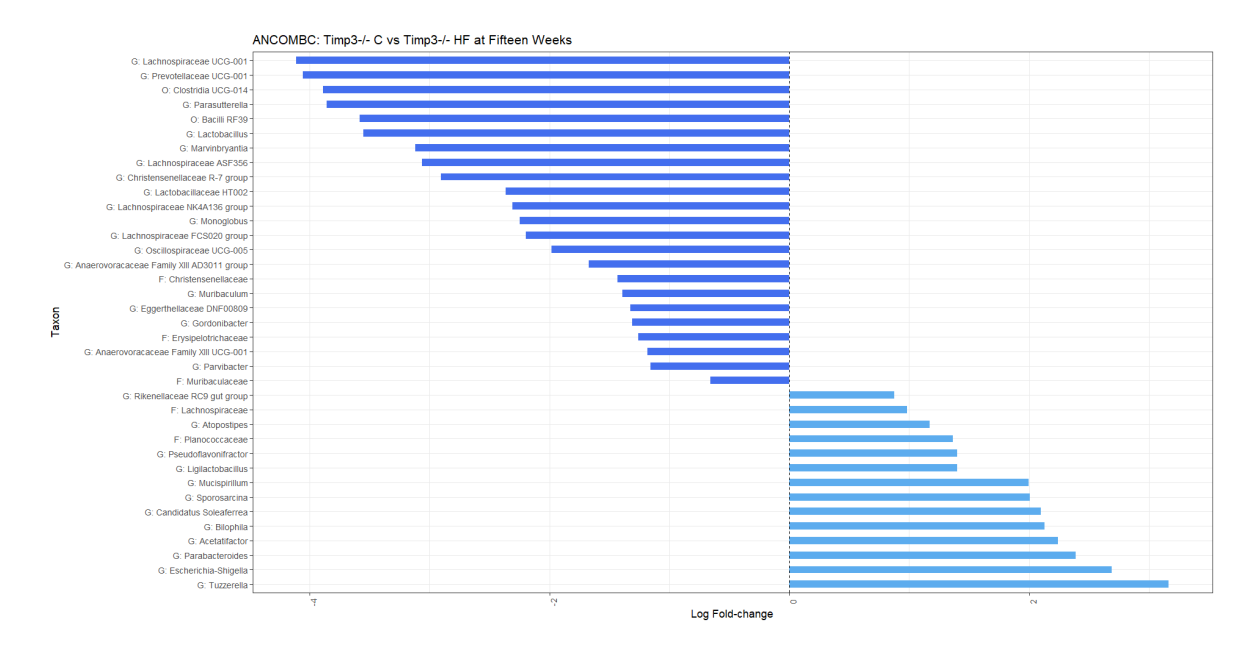


Figure E. 30 Bar plot displaying the fold change of significant genera within the *Timp3*^{-/-} high-fat group compared to the *Timp3*^{-/-} chow group at fifteen weeks of age, identified by ANCOM-BC. Significance level was set at p = 0.01.

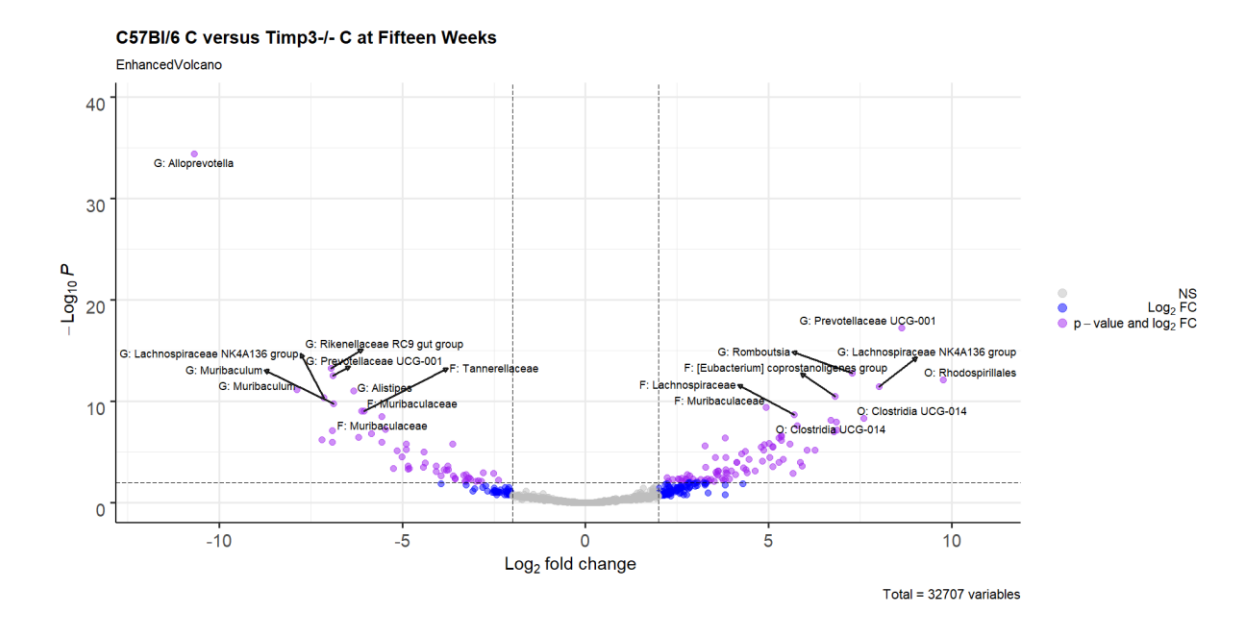


Figure E. 31 Volcano plot displaying the fold change of genera within the *Timp3*-/- chow group compared to the C57Bl/6J chow group at fifteen weeks of age, identified by DESeq2. Grey points indicate non-significant ASVs. Red points indicate ASVs with a p-value lower than 0.01, blue points indicate ASCVs with a Log2 fold change more than +/-2 and purple points indicate ASVs that meet both these requisites. The 20 most significant ASVs are labelled.

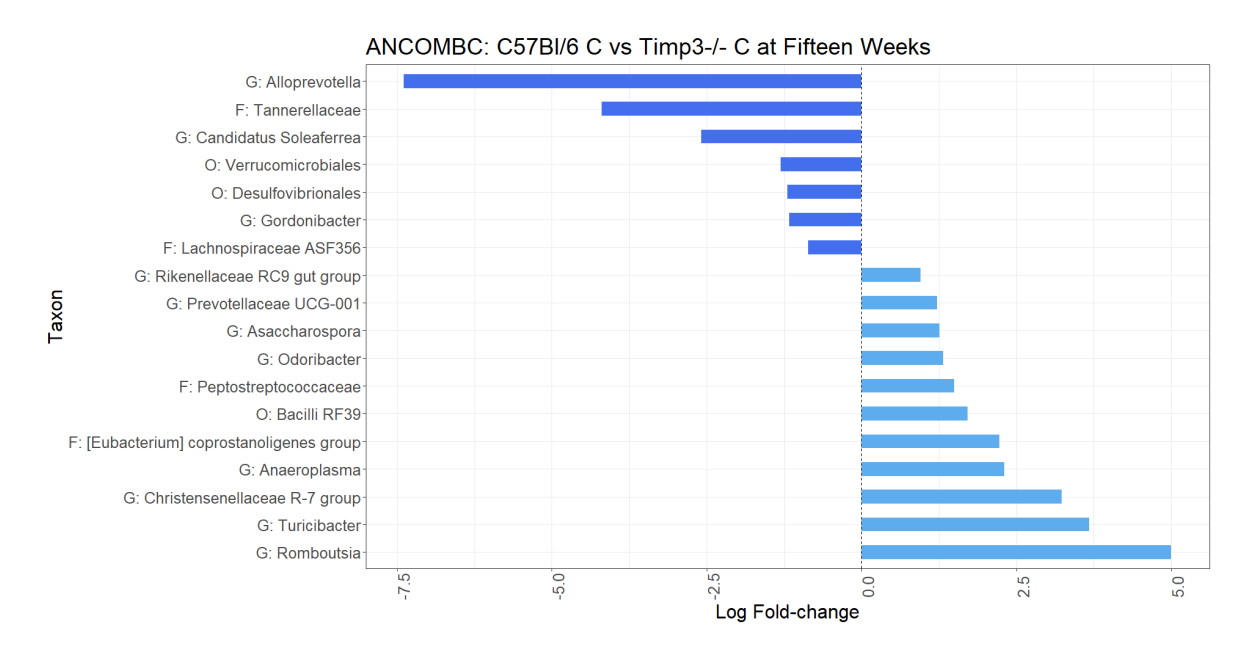


Figure E. 32 Bar plot displaying the fold change of significant genera within the *Timp3*^{-/-} chow group compared to the C57Bl/6J chow group at fifteen weeks of age, identified by ANCOM-BC. Significance level was set at p = 0.01.

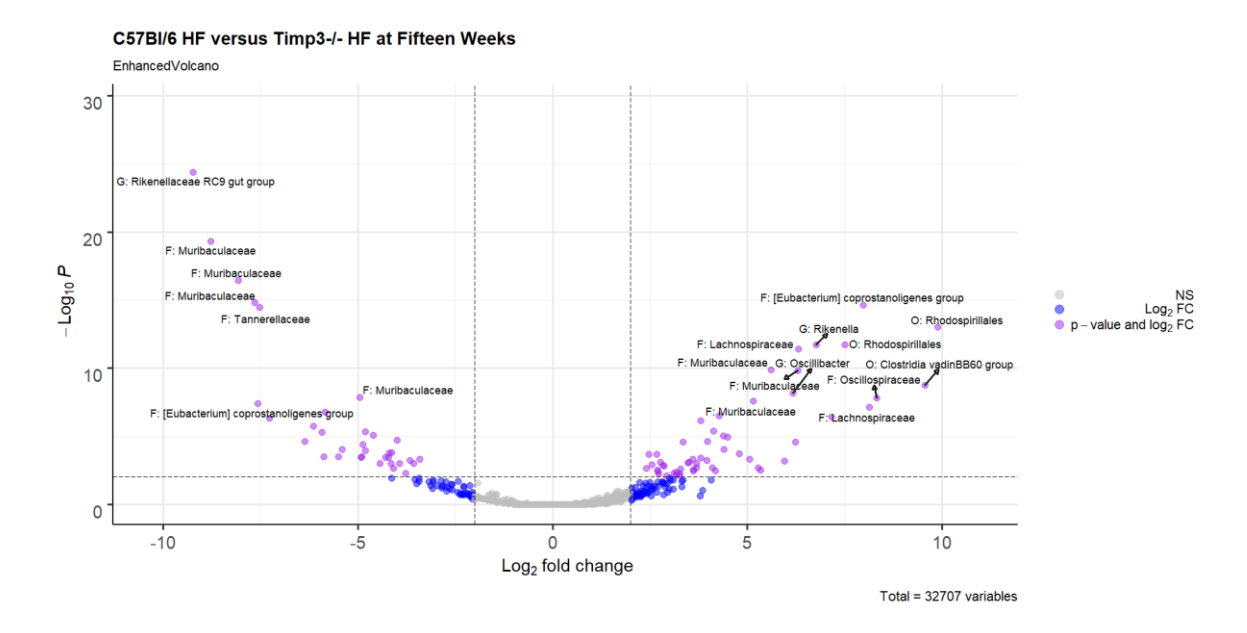


Figure E. 33 Volcano plot displaying the fold change of genera within the *Timp3*-/- high-fat group compared to the C57Bl/6J high-fat group at fifteen weeks of age, identified by DESeq2. Grey points indicate non-significant ASVs. Red points indicate ASVs with a p-value lower than 0.01, blue points indicate ASCVs with a Log2 fold change more than +/-2 and purple points indicate ASVs that meet both these requisites. The 20 most significant ASVs are labelled.

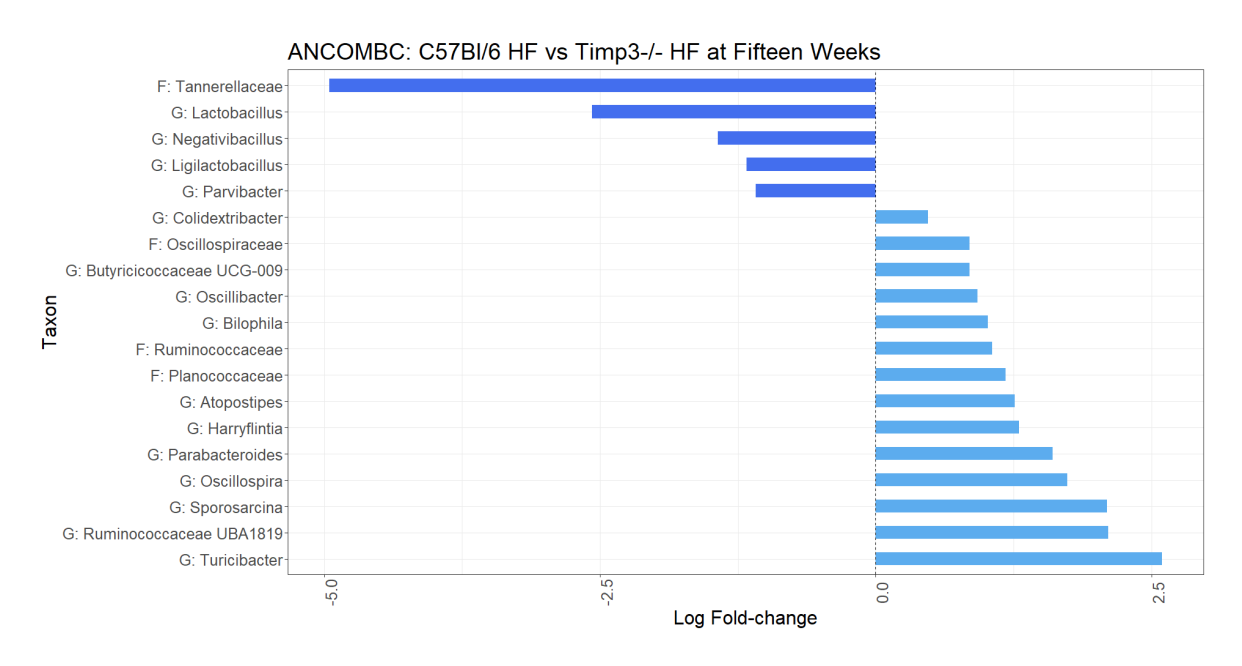


Figure E. 34 Bar plot displaying the fold change of significant genera within the *Timp3-/-* high-fat group compared to the C57BI/6J high-fat group at fifteen weeks of age, identified by ANCOM-BC. Significance level was set at p = 0.01.

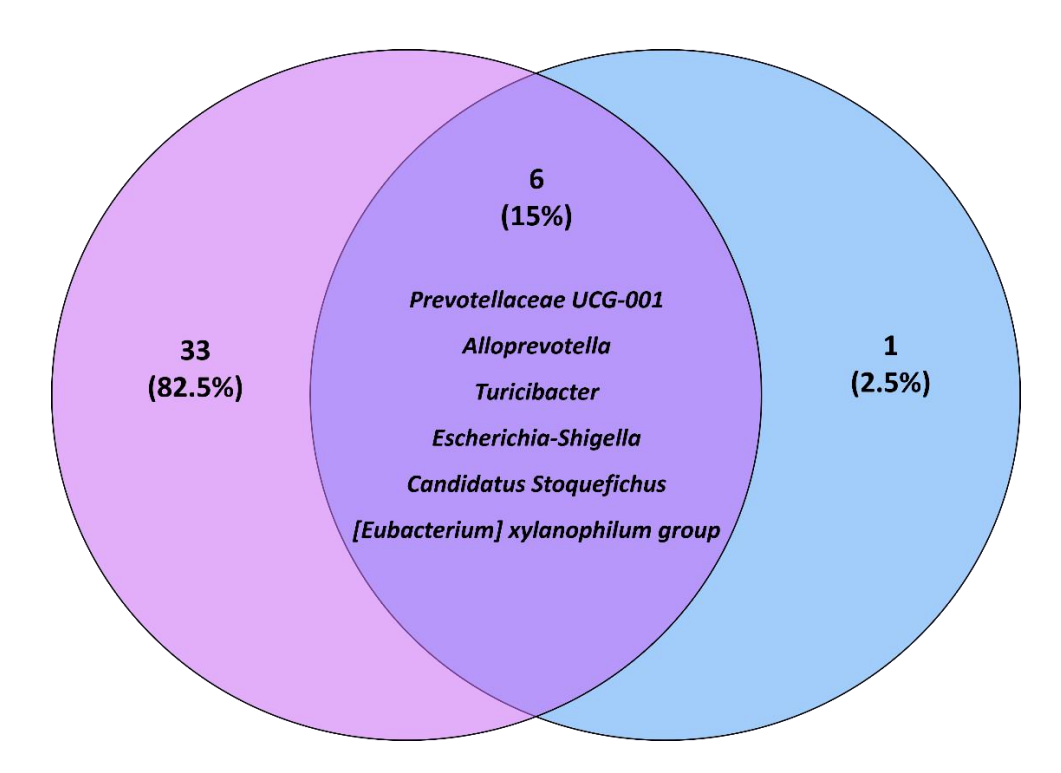


Figure D. 6 Venn diagram displaying the percentage of ASVs identified at 5 weeks of age, in *Timp3*-/- compared to C57BI/6J on chow diet, by DESeq2 and ANCOM-BC, with common genera listed.

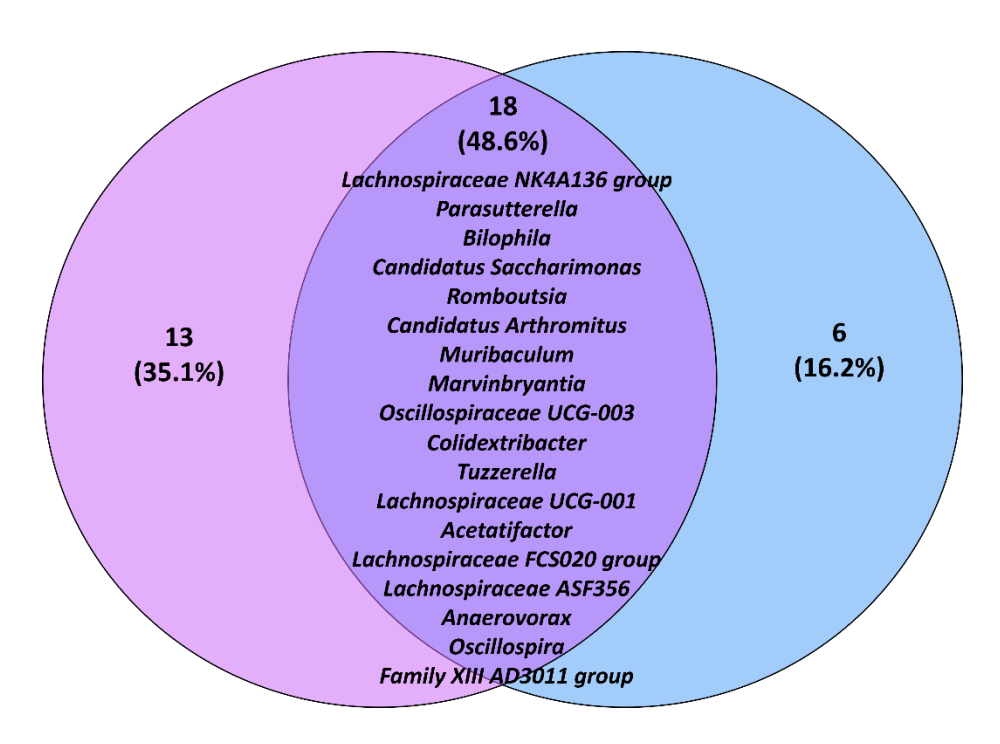


Figure D. 7 Venn diagram displaying the percentage of ASVs identified at 7 weeks of age, in C57bl/6J HF compared to C57Bl/6J C, by DESeq2 and ANCOM-BC, with common genera listed.

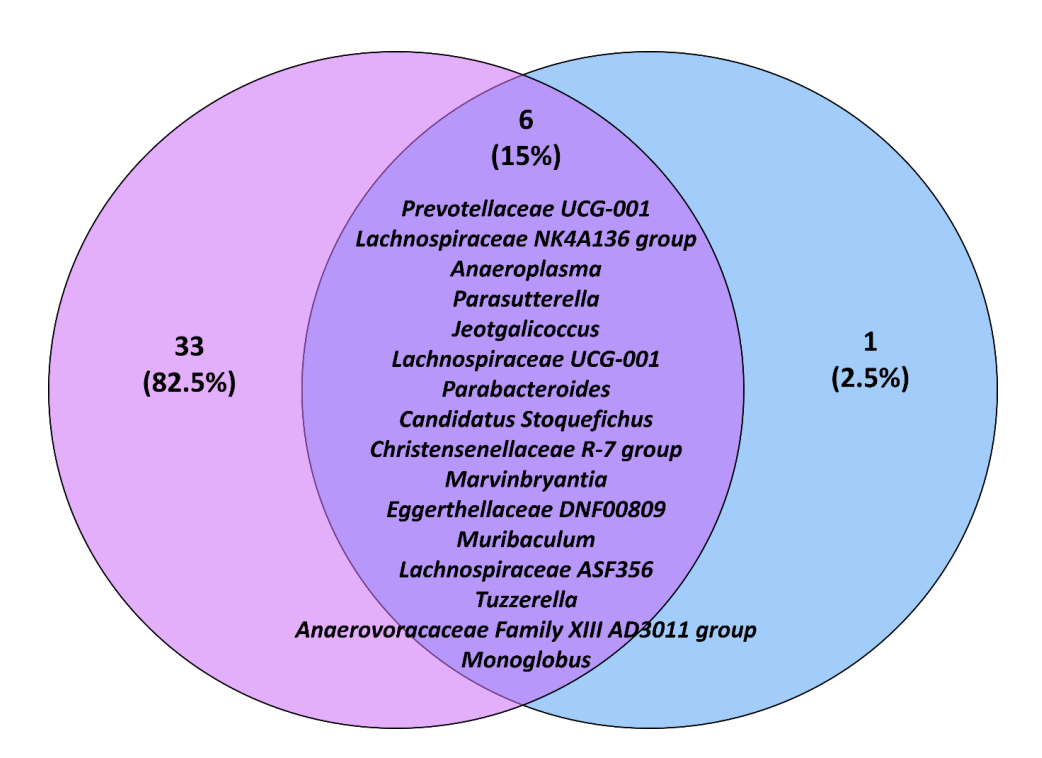


Figure D. 8 Venn diagram displaying the percentage of ASVs identified at 7 weeks of age, in *Timp3*^{-/-} HF compared to *Timp3*^{-/-} C, by DESeq2 and ANCOM-BC, with common genera listed.

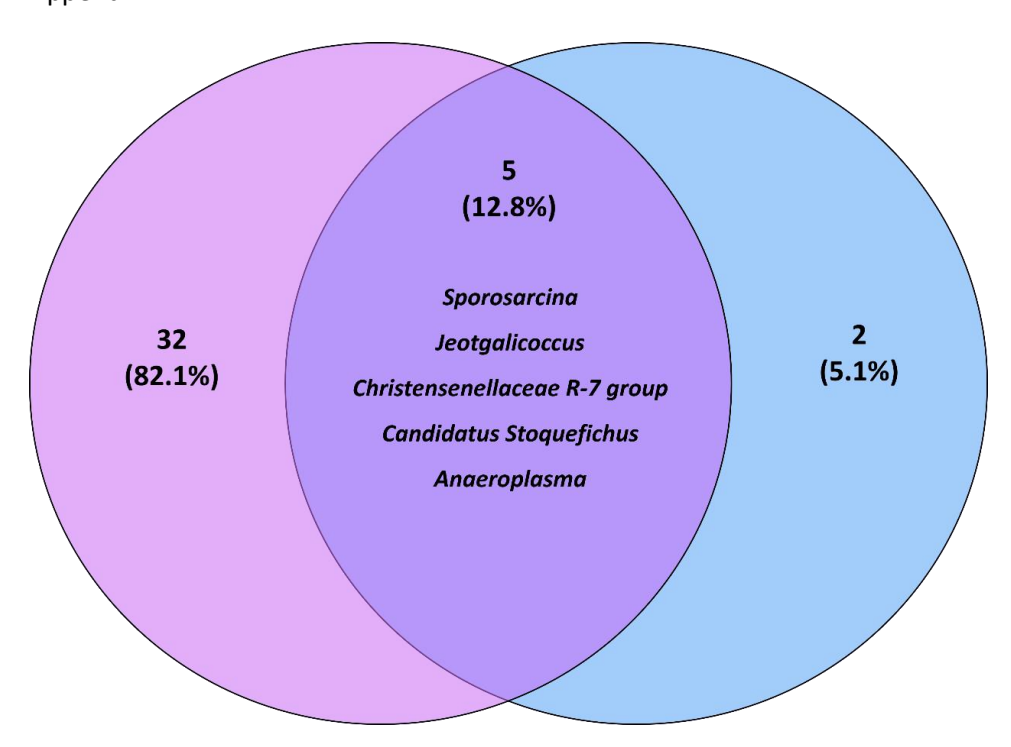


Figure D. 9 Venn diagram displaying the percentage of ASVs identified at 7 weeks of age, in *Timp3*^{-/-} compared to C57BI/6J on chow diet, by DESeq2 and ANCOM-BC, with common genera listed.

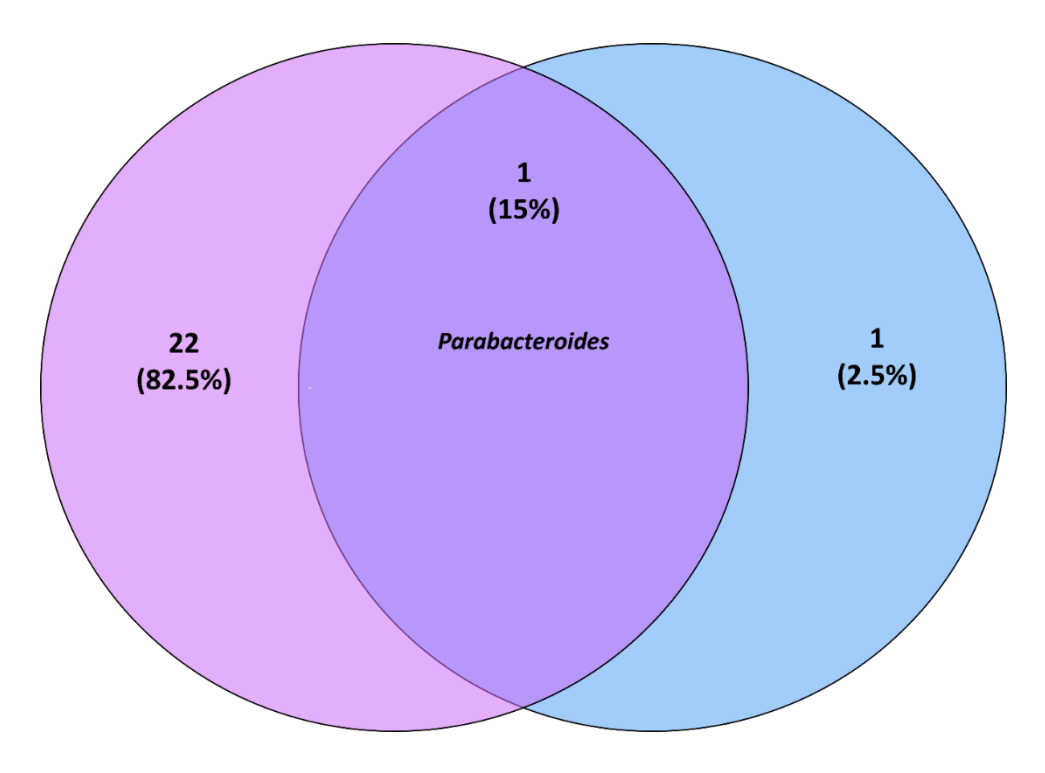


Figure D. 10 Venn diagram displaying the percentage of ASVs identified at 7 weeks of age, in *Timp3*-/- compared to C57BI/6J on high-fat diet, by DESeq2 and ANCOM-BC, with common genera listed.

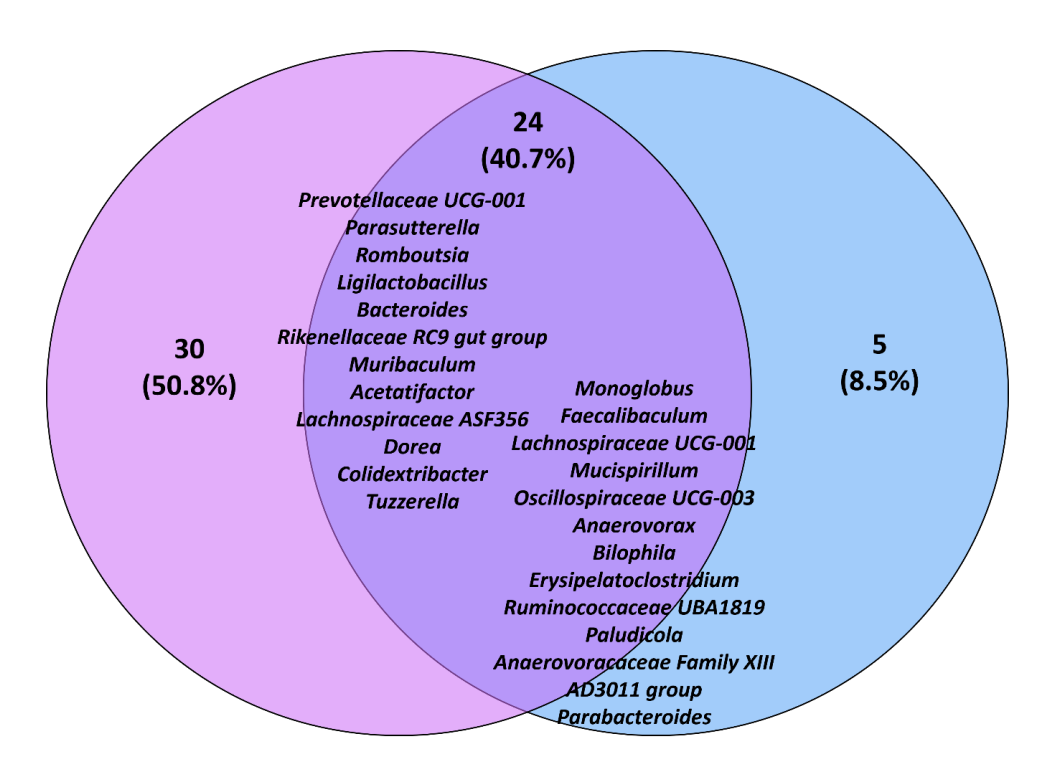


Figure D. 11 Venn diagram displaying the percentage of ASVs identified at 10 weeks of age, in C57BI/6J HF compared to C57BI/6J C, by DESeq2 and ANCOM-BC, with common genera listed.

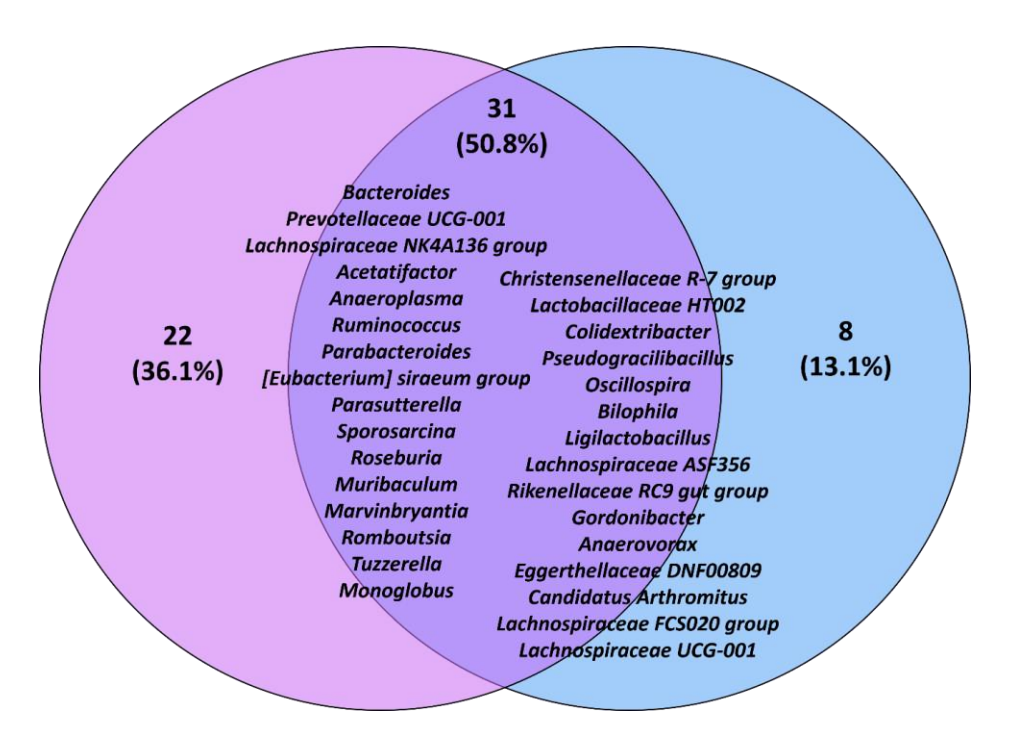


Figure D. 12 Venn diagram displaying the percentage of ASVs identified at 10 weeks of age, in Timp3^{-/-} HF compared to Timp3^{-/-} C, by DESeq2 and ANCOM-BC, with common genera listed.

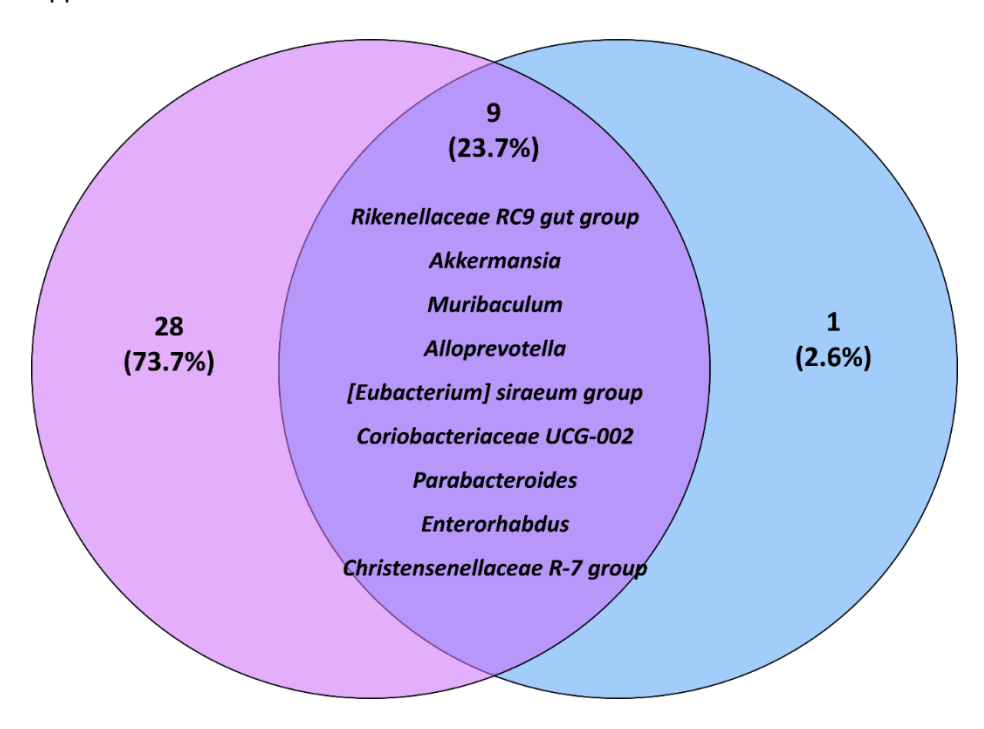


Figure D. 13 Venn diagram displaying the percentage of ASVs identified at 10 weeks of age, in Timp3^{-/-} compared to C57BI/6J on chow diet, by DESeq2 and ANCOM-BC, with common genera listed.

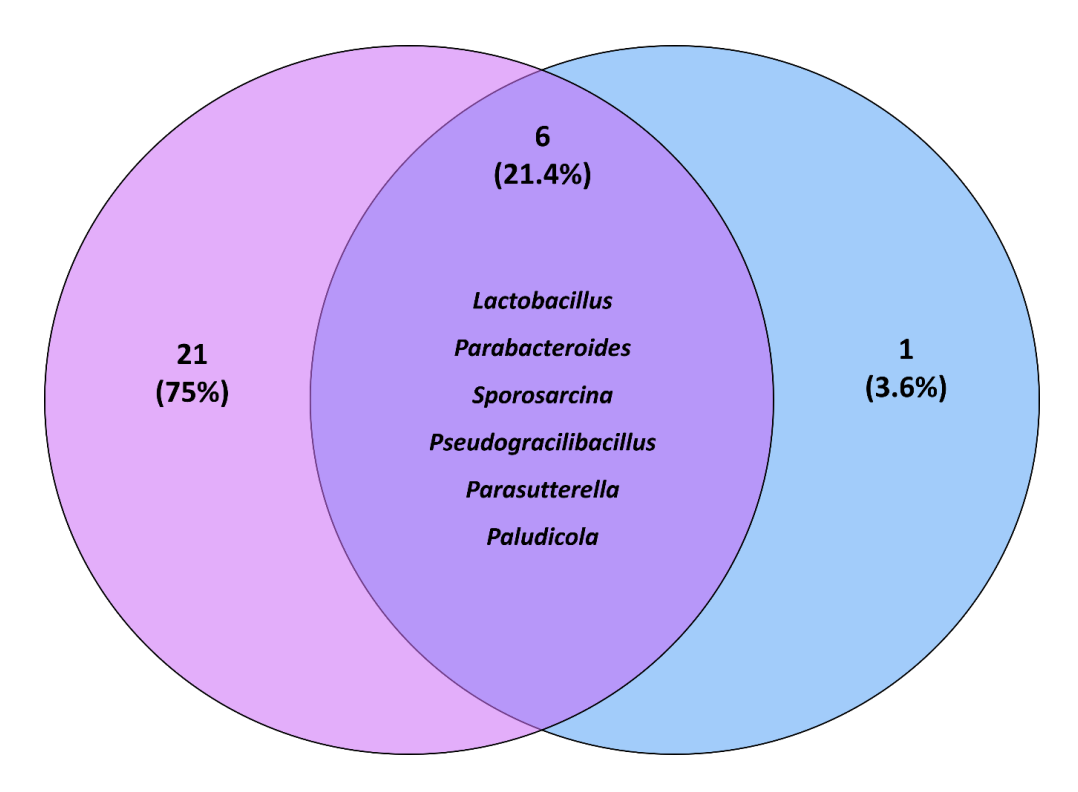


Figure D. 14 Venn diagram displaying the percentage of ASVs identified at 10 weeks of age, in *Timp3*-/- compared to C57BI/6J on high-fat diet, by DESeq2 and ANCOM-BC, with common genera listed.

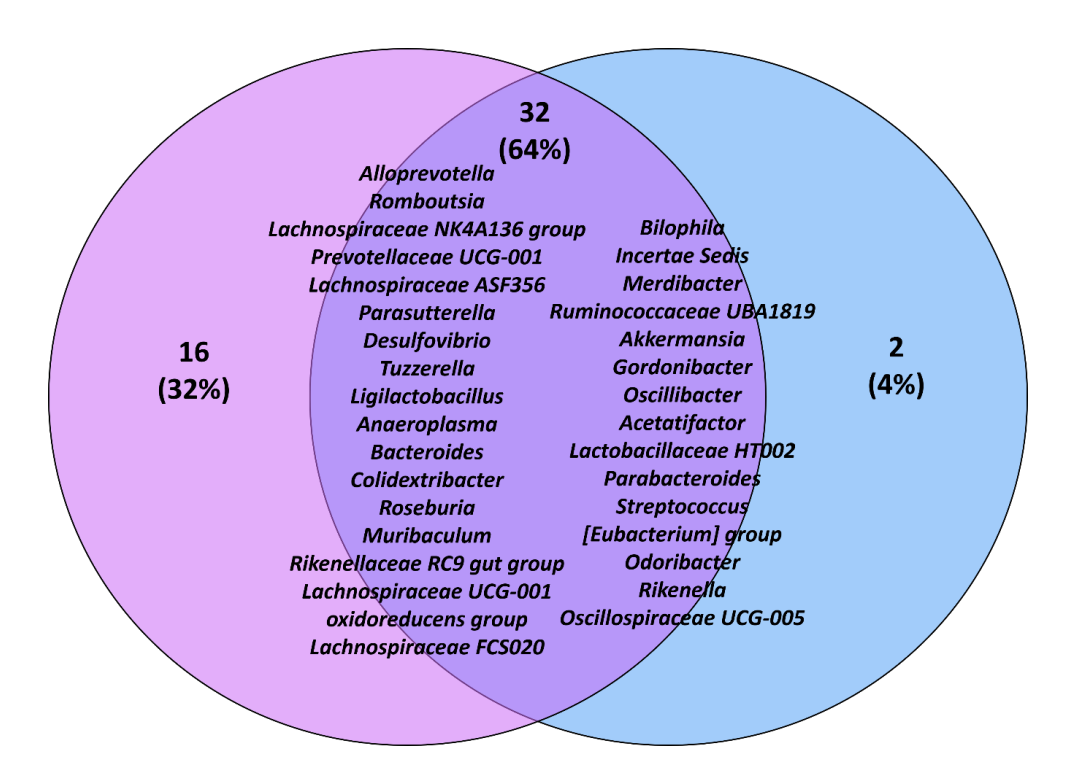


Figure D. 15 Venn diagram displaying the percentage of ASVs identified at 15 weeks of age, in C57BI/6J HF compared to C57BI/6J C, by DESeq2 and ANCOM-BC, with common genera listed.

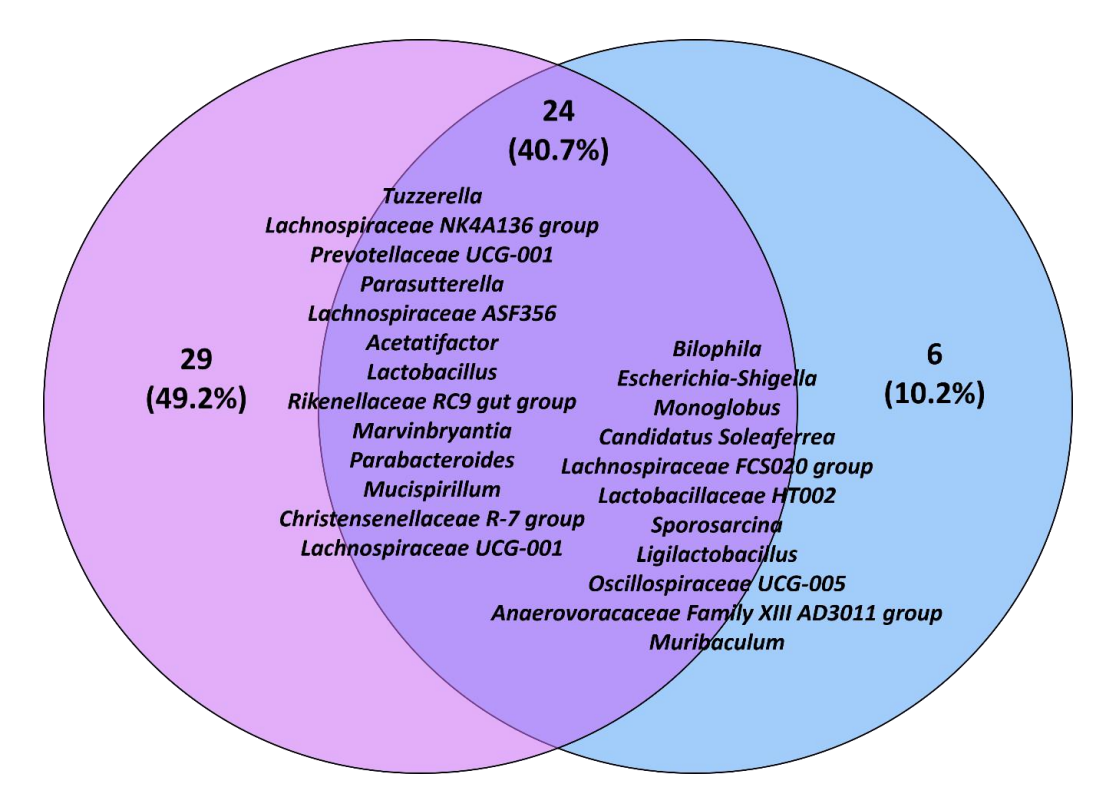


Figure D. 16 Venn diagram displaying the percentage of ASVs identified at 15 weeks of age, in Timp3^{-/-} HF compared to Timp3^{-/-} C, by DESeq2 and ANCOM-BC, with common genera listed.

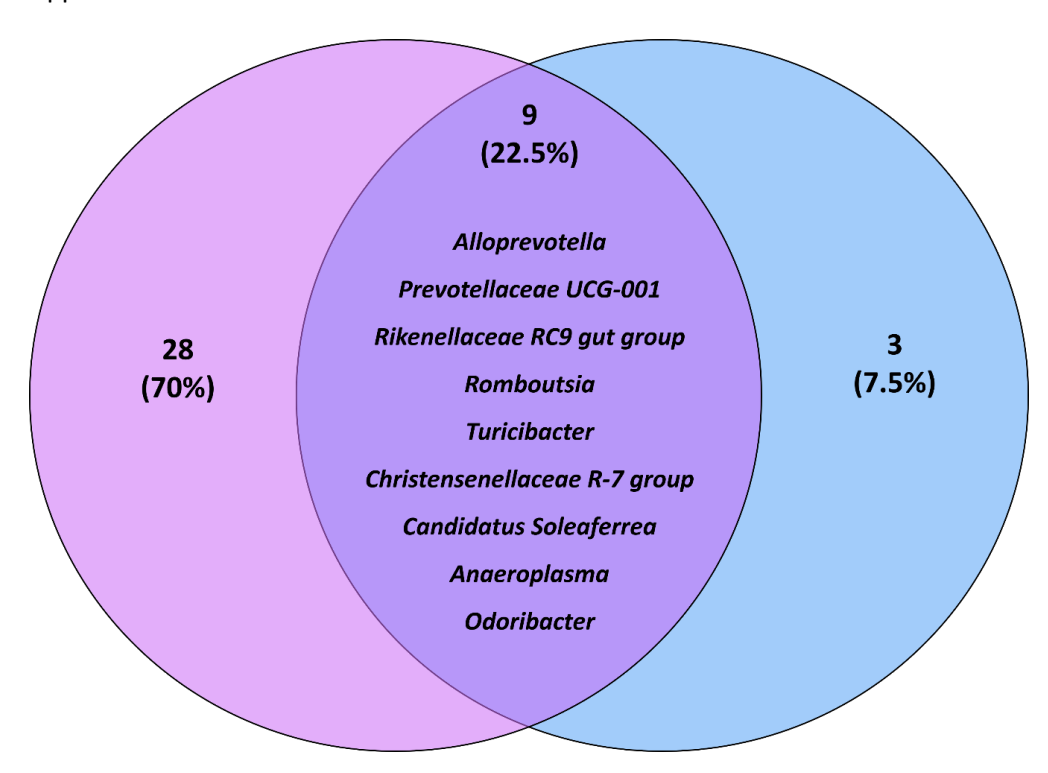


Figure D. 17 Venn diagram displaying the percentage of ASVs identified at 15 weeks of age, in Timp3^{-/-} compared to C57BI/6J on chow diet, by DESeq2 and ANCOM-BC, with common genera listed.

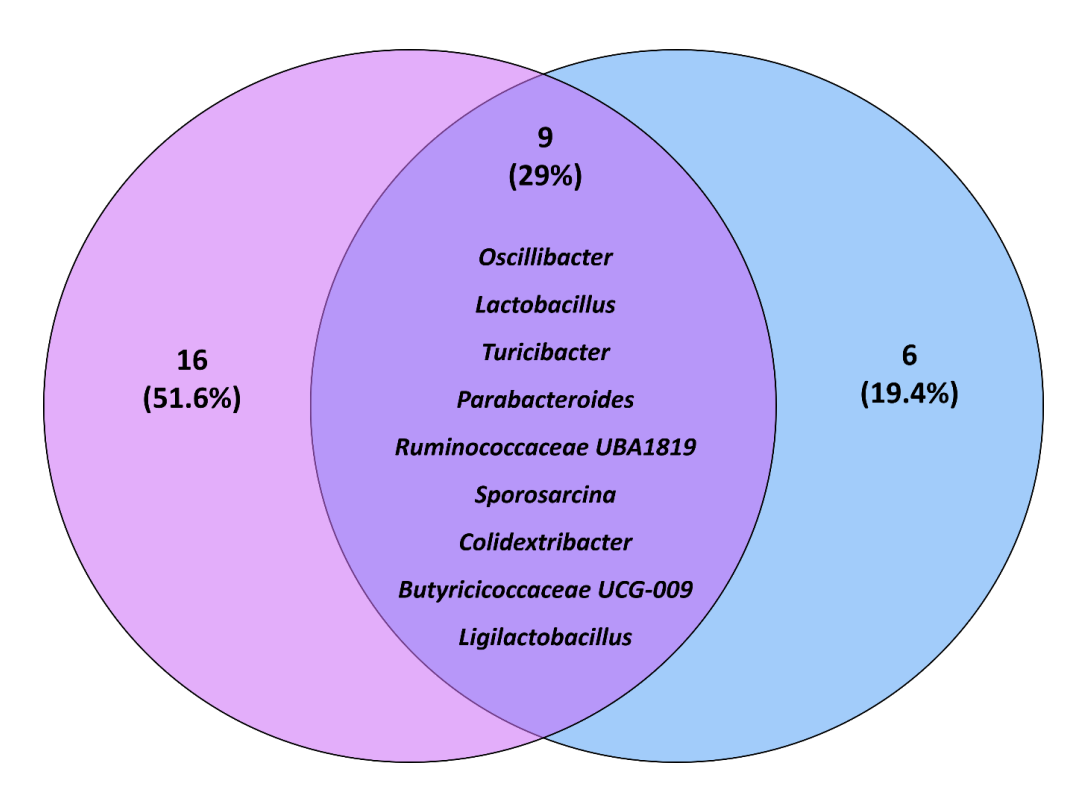


Figure D. 18 Venn diagram displaying the percentage of ASVs identified at 15 weeks of age, in Timp3^{-/-} compared to C57Bl/6J on high-fat, by DESeq2 and ANCOM-BC, with common genera listed.

Table D. 1 Summary table of remaining genera identified in differential abundance analysis. Genera listed are those which presented significant differences between the genotypes. Arrows represent increase (♠) or decrease (♦) in abundance.

	Genus	High-fat (v chow)		<i>Timp3^{-/-}</i> (v C57Bl/6J)	
Phylum		C57BI/6J	Timp3 ^{-/-}	Chow	High-fat
Bacillota	Lachnospiraceae NK4A136 group				
Bacillota	Tuzzerella	^	^		
Bacillota	Colidextribacter	^	^		
Bacillota	Lachnospiraceae UCG-001	\	Ψ		
Bacillota	Candidatus Arthromitus	\	Ψ		
Bacillota	Lachnospiraceae ASF356	4	Ψ		
Bacillota	Lachnospiraceae FCS020 group	Ψ	Ψ		
Bacillota	Dorea	↑			
unknown	Candidatus Saccharimonas	Ψ			
Bacillota	Ruminococcaceae UBA1819	Ψ			
Bacillota	[Eubacterium] oxidoreducens group	Ψ			
Bacteroidota	Rikenellaceae RC9 gut group	^	^		
Actinomycetota	Enterorhabdus		Ψ		
Bacillota	Monoglobus	Ψ	Ψ		
Thermodesulfobacteriota	Bilophila	^	^		
Bacteroidota	Bacteroides	^	1		
Bacteroidota	Muribaculum	Ψ	Ψ		
Actinomycetota	Gordonibacter	Ψ	Ψ		
Actinomycetota	Eggerthellaceae DNF00809	Ψ	Ψ		
Bacillota	Acetatifactor	^	1		
Bacillota	Merdibacter	V	V		

		High-fat (v chow)		Timp3 ^{-/-} (v C57BI/6J)	
Phylum	Genus		,		
		C57BI/6J	Timp3 ^{-/-}	Chow	High-fat
Deferribacteres	Mucispirillum		^		
Bacillota	Oscillospiraceae UCG-003	Ψ	Ψ		
Bacillota	Limosilactobacillus		Ψ		
Bacillota	Erysipelatoclostridium	Ψ	Ψ		
Bacillota	Anaerovorax	^	^		
Bacillota	Oscillospiraceae UCG-005	Ψ	Ψ		
Bacillota	Lactobacillaceae HT002	Ψ	Ψ		
Bacillota	Harryflintia	^	^		
Bacillota	Butyricicoccus	Ψ	Ψ		
Bacillota	Anaerovoracaceae Family XIII AD3011 group	Ψ	Ψ		
Bacillota	Oscillibacter	Ψ			
Bacillota	Lachnospiraceae A2	Ψ			
Bacillota	Faecalibaculum	^			
Bacillota	Peptococcus	^			
Bacillota	Ligilactobacillus	^			

ADA. (2018). Classification and diagnosis of diabetes: Standards of medical care in Diabetesd2018. In *Diabetes Care* (Vol. 41, pp. S13–S27). American Diabetes Association Inc. https://doi.org/10.2337/dc18-S002

Adhikari, N., Basi, D. L., Carlson, M., Mariash, A., Hong, Z., Lehman, U., Mullegama, S., Weir, E. K., & Hall, J. L. (2011). Increase in GLUT1 in Smooth Muscle Alters Vascular Contractility and Increases Inflammation in Response to Vascular Injury. *Arteriosclerosis, Thrombosis, and Vascular Biology*, 31(1), 86–94. https://doi.org/10.1161/ATVBAHA.110.215004

Alberti, K. g. m. m., Eckel, R. H., Grundy, S. M., Zimmet, P. Z., Cleeman, J. I., Donato, K. A., Fruchart, J.-C., James, W. P. T., Loria, C. M., & Smith, S. C. (2009). Harmonizing the Metabolic Syndrome. *Circulation*, *120*(16), 1640–1645. https://doi.org/10.1161/CIRCULATIONAHA.109.192644

Alves-Bezerra, M., & Cohen, D. E. (2017). Triglyceride metabolism in the liver. *Comprehensive Physiology*, 8(1), 1–8. https://doi.org/10.1002/cphy.c170012

Belo, V. A., Guimarães, D. A., & Castro, M. M. (2015). Matrix Metalloproteinase 2 as a Potential Mediator of Vascular Smooth Muscle Cell Migration and Chronic Vascular Remodeling in Hypertension. *Journal of Vascular Research*, *52*(4), 221–231. https://doi.org/10.1159/000441621

Bilson, J., Sethi, J. K., & Byrne, C. D. (2022). Non-alcoholic fatty liver disease: A multi-system disease influenced by ageing and sex, and affected by adipose tissue and intestinal function. *Proceedings of the Nutrition Society*, *81*(2), 146–161.

https://doi.org/10.1017/S0029665121003815

Bornstein, A. B., Rao, S. S., & Marwaha, K. (2023). Left Ventricular Hypertrophy. In *StatPearls* [Internet]. StatPearls Publishing. https://www.ncbi.nlm.nih.gov/books/NBK557534/

Bray, J. R., & Curtis, J. T. (1957). An Ordination of the Upland Forest Communities of Southern Wisconsin. *Ecological Monographs*, *27*(4), 325–349. https://doi.org/10.2307/1942268

Bredfeldt, J. S., Liu, Y., Pehlke, C. A., Conklin, M. W., Szulczewski, J. M., Inman, D. R., Keely, P. J., Nowak, R. D., Mackie, T. R., & Eliceiri, K. W. (2014). Computational segmentation of collagen fibers from second-harmonic generation images of breast cancer. *Journal of Biomedical Optics*, *19*(1), 016007. https://doi.org/10.1117/1.JBO.19.1.016007

Brown, K., Abbott, D. W., Uwiera, R. R. E., & Inglis, G. D. (2018). Removal of the cecum affects intestinal fermentation, enteric bacterial community structure, and acute colitis in mice. *Gut Microbes*, *9*(3), 218–235. https://doi.org/10.1080/19490976.2017.1408763

Caleyachetty, R., Barber, T. M., Mohammed, N. I., Cappuccio, F. P., Hardy, R., Mathur, R., Banerjee, A., & Gill, P. (2021). Ethnicity-specific BMI cutoffs for obesity based on type 2 diabetes risk in England: A population-based cohort study. *The Lancet Diabetes & Endocrinology*, *9*(7), 419–426. https://doi.org/10.1016/S2213-8587(21)00088-7

Chakraborti, C. K. (2015). Role of adiponectin and some other factors linking type 2 diabetes mellitus and obesity. *World Journal of Diabetes*. https://doi.org/10.4239/wjd.v6.i15.1296

Chan, Y. K., Brar, M. S., Kirjavainen, P. V., Chen, Y., Peng, J., Li, D., Leung, F. C. C., & El-Nezami, H. (2016). High fat diet induced atherosclerosis is accompanied with low colonic bacterial diversity and altered abundances that correlates with plaque size, plasma A-FABP and cholesterol: A pilot study of high fat diet and its intervention with Lactobacillus rhamnosus GG (LGG) or telmisartan in ApoE-/- mice. *BMC Microbiology*, *16*(1), 1–13. https://doi.org/10.1186/s12866-016-0883-4

Chapman, M. A., Grahn, M. F., Boyle, M. A., Hutton, M., Rogers, J., & Williams, N. S. (1994). Butyrate oxidation is impaired in the colonic mucosa of sufferers of quiescent ulcerative colitis. *Gut*, *35*(1), 73–76. https://doi.org/10.1136/gut.35.1.73

Chiang, J. Y. L., & Ferrell, J. M. (2020). Up to date on cholesterol 7 alpha-hydroxylase (CYP7A1) in bile acid synthesis. *Liver Research*, *4*(2), 47–63. https://doi.org/10.1016/j.livres.2020.05.001

Choe, S. S., Huh, J. Y., Hwang, I. J., Kim, J. I., & Kim, J. B. (2016). Adipose Tissue Remodeling: Its Role in Energy Metabolism and Metabolic Disorders. *Frontiers in Endocrinology*, *7*, 30. https://doi.org/10.3389/fendo.2016.00030

Clarke, M., Mitchell, K. W., Goodship, J., McDonnell, S., Barker, M. D., Griffiths, I. D., & McKie, N. (2001). Clinical features of a novel TIMP-3 mutation causing Sorsby's fundus dystrophy: Implications for disease mechanism. *The British Journal of Ophthalmology*, *85*(12), 1429–1431. https://doi.org/10.1136/BJO.85.12.1429

Cox, K. H., & Takahashi, J. S. (2019). *Circadian clock genes and the transcriptional architecture of the clock mechanism*. https://doi.org/10.1530/JME-19-0153

Cui, H., López, M., & Rahmouni, K. (2017). The cellular and molecular bases of leptin and ghrelin resistance in obesity. *Nature Reviews Endocrinology*, *13*(6), 338–351. https://doi.org/10.1038/nrendo.2016.222

Dewing, Carare, Lotery, & Ratnayaka. (2019). The Diverse Roles of TIMP-3: Insights into Degenerative Diseases of the Senescent Retina and Brain. *Cells*, *9*(1), 39. https://doi.org/10.3390/cells9010039

Eichner, J. E., Dunn, S. T., Perveen, G., Thompson, D. M., Stewart, K. E., & Stroehla, B. C. (2002). Apolipoprotein E Polymorphism and Cardiovascular Disease: A HuGE Review. *American Journal of Epidemiology*, *155*(6), 487–495. https://doi.org/10.1093/aje/155.6.487

Faul, F., Erdfelder, E., Buchner, A., & Lang, A.-G. (2009). Statistical power analyses using G*Power 3.1: Tests for correlation and regression analyses. *Behavior Research Methods*, *41*(4), 1149–1160. https://doi.org/10.3758/BRM.41.4.1149

Faul, F., Erdfelder, E., Lang, A.-G., & Buchner, A. (2007). G*Power 3: A flexible statistical power analysis program for the social, behavioral, and biomedical sciences. *Behavior Research Methods*, 39(2), 175–191. https://doi.org/10.3758/BF03193146

Feingold, K. R. (2021). Introduction to Lipids and Lipoproteins. In *Endotext [Internet]*. MDText.com, Inc. https://www.ncbi.nlm.nih.gov/books/NBK305896/

Folco, E. J., Rocha, V. Z., López-llasaca, M., & Libby, P. (2009). Adiponectin inhibits pro-inflammatory signaling in human macrophages independent of interleukin-10. *Journal of Biological Chemistry*. https://doi.org/10.1074/jbc.M109.019786

Gao, F., Lv, Y. W., Long, J., Chen, J. M., He, J. M., Ruan, X. Z., & Zhu, H. B. (2019). Butyrate improves the metabolic disorder and gut microbiome dysbiosis in mice induced by a high-fat diet. *Frontiers in Pharmacology*, *10*, 1040. https://doi.org/10.3389/FPHAR.2019.01040/BIBTEX

Gao, H., Steffen, M. C., & Ramos, K. S. (2012). Osteopontin regulates α-smooth muscle actin and calponin in vascular smooth muscle cells. *Cell Biology International*, *36*(2), 155–161. https://doi.org/10.1042/CBI20100240

Gnudi, L., & Raij, L. (2006). The link between Glut-1 and hypertension in diabetic nephropathy. Current Hypertension Reports, 8(1), 79–83. https://doi.org/10.1007/s11906-006-0044-5

Haas, J. T., & Biddinger, S. B. (2009). Dissecting the role of insulin resistance in the metabolic syndrome. *Current Opinion in Lipidology*. https://doi.org/10.1097/MOL.0b013e32832b2024

Hague, A., Butt, A. J., & Paraskeva, C. (1996). The role of butyrate in human colonic epithelial cells: An energy source or inducer of differentiation and apoptosis? *Proceedings of the Nutrition Society*, *55*(3), 937–943. https://doi.org/10.1079/PNS19960090

Heindel, J. J., Blumberg, B., Cave, M., Machtinger, R., Mantovani, A., Mendez, M. A., Nadal, A., Palanza, P., Panzica, G., Sargis, R., Vandenberg, L. N., & vom Saal, F. (2017). Metabolism disrupting chemicals and metabolic disorders. *Reproductive Toxicology*, *68*, 3–33. https://doi.org/10.1016/J.REPROTOX.2016.10.001

Heisel, T., Montassier, E., Johnson, A., Al-Ghalith, G., Lin, Y.-W., Wei, L.-N., Knights, D., & Gale, C. A. (2017). High-Fat Diet Changes Fungal Microbiomes and Interkingdom Relationships in the Murine Gut. *mSphere*, *2*(5), 10.1128/msphere.00351-17. https://doi.org/10.1128/msphere.00351-17

Hottinger, D. G., Beebe, D. S., Kozhimannil, T., Prielipp, R. C., & Belani, K. G. (2014). Sodium nitroprusside in 2014: A clinical concepts review. *Journal of Anaesthesiology Clinical Pharmacology*, *30*(4), 462. https://doi.org/10.4103/0970-9185.142799

Jäkel, L., Kuiperij, H. B., Gerding, L. P., Custers, E. E. M., Van Den Berg, E., Jolink, W. M. T., Schreuder, F. H. B. M., Küsters, B., Klijn, C. J. M., & Verbeek, M. M. (2020). Disturbed balance in the expression of MMP9 and TIMP3 in cerebral amyloid angiopathy-related intracerebral haemorrhage. *Acta Neuropathologica Communications*, 8(1), 1–14. https://doi.org/10.1186/s40478-020-00972-z

Jo, J., Gavrilova, O., Pack, S., Jou, W., Mullen, S., Sumner, A. E., Cushman, S. W., & Periwal, V. (2009). Hypertrophy and/or hyperplasia: Dynamics of adipose tissue growth. *PLoS Computational Biology*, *5*(3). https://doi.org/10.1371/journal.pcbi.1000324

Jonas, A., & Phillips, M. C. (2008). CHAPTER 17—Lipoprotein structure. In D. E. Vance & J. E. Vance (Eds.), *Biochemistry of Lipids, Lipoproteins and Membranes (Fifth Edition)* (pp. 485–506). Elsevier. https://doi.org/10.1016/B978-044453219-0.50019-2

Jones, R. B., Alderete, T. L., Kim, J. S., Millstein, J., Gilliland, F. D., & Goran, M. I. (2019). High intake of dietary fructose in overweight/obese teenagers associated with depletion of Eubacterium and Streptococcus in gut microbiome. *Gut Microbes*, *10*(6), 712–719. https://doi.org/10.1080/19490976.2019.1592420

Kamei, M., & Hollyfield, J. G. (1999). TIMP-3 in Bruch's Membrane: Changes during Aging and in Age-Related Macular Degeneration. *Investigative Ophthalmology & Visual Science*, *40*(10), 2367–2375.

Kang, H. H., Kim, I. K., Lee, H. in, Joo, H., Lim, J. U., Lee, J., Lee, S. H., & Moon, H. S. (2017). Chronic intermittent hypoxia induces liver fibrosis in mice with diet-induced obesity via

TLR4/MyD88/MAPK/NF-kB signaling pathways. *Biochemical and Biophysical Research Communications*, 490(2), 349–355. https://doi.org/10.1016/j.bbrc.2017.06.047

Katholi, R. E., & Couri, D. M. (2011). Left Ventricular Hypertrophy: Major Risk Factor in Patients with Hypertension: Update and Practical Clinical Applications. *International Journal of Hypertension*, 2011(1), 495349. https://doi.org/10.4061/2011/495349

Kesson, M., & Atkins, E. (2005). Chapter 2—Soft tissues of the musculoskeletal system. In M. Kesson & E. Atkins (Eds.), *Orthopaedic Medicine (Second Edition)* (pp. 33–54). Butterworth-Heinemann. https://doi.org/10.1016/B978-075065563-7.50008-4

Khurana, S., Chacon, I., Xie, G., Yamada, M., Wess, J., Raufman, J.-P., & Kennedy, R. H. (2004). Vasodilatory effects of cholinergic agonists are greatly diminished in aorta from M3R-/- mice. *European Journal of Pharmacology*, *493*(1–3), 127–132. https://doi.org/10.1016/j.ejphar.2004.04.012

Kim, K. A., Gu, W., Lee, I. A., Joh, E. H., & Kim, D. H. (2012). High Fat Diet-Induced Gut Microbiota Exacerbates Inflammation and Obesity in Mice via the TLR4 Signaling Pathway. *PLoS ONE*. https://doi.org/10.1371/journal.pone.0047713

Kim, Y. H., Her, A.-Y., Choi, B. G., Choi, S. Y., Byun, J. K., Baek, M. J., Ryu, Y. G., Park, Y., Mashaly, A., Jang, W. Y., Kim, W., Choi, J. Y., Park, E. J., Na, J. O., Choi, C. U., Lim, H. E., Kim, E. J., Park, C. G., Seo, H. S., & Rha, S.-W. (2018). Impact of left ventricular hypertrophy on long-term clinical outcomes in hypertensive patients who underwent successful percutaneous coronary intervention with drug-eluting stents. *Medicine*, *97*(35), e12067. https://doi.org/10.1097/MD.00000000000012067

Kohsaka, A., Laposky, A. D., Ramsey, K. M., Estrada, C., Joshu, C., Kobayashi, Y., Turek, F. W., & Bass, J. (2007). High-Fat Diet Disrupts Behavioral and Molecular Circadian Rhythms in Mice. *Cell Metabolism*, *6*(5), 414–421. https://doi.org/10.1016/J.CMET.2007.09.006

Koliada, A., Syzenko, G., Moseiko, V., Budovska, L., Puchkov, K., Perederiy, V., Gavalko, Y., Dorofeyev, A., Romanenko, M., Tkach, S., Sineok, L., Lushchak, O., & Vaiserman, A. (2017). Association between body mass index and Firmicutes/Bacteroidetes ratio in an adult Ukrainian population. *BMC Microbiology*. https://doi.org/10.1186/s12866-017-1027-1

Kruit, J. K., Groen, A. K., van Berkel, T. J., & Kuipers, F. (2006). Emerging roles of the intestine in control of cholesterol metabolism. *World Journal of Gastroenterology: WJG*, *12*(40), 6429–6439. https://doi.org/10.3748/wjg.v12.i40.6429

Lackey, D. E., Burk, D. H., Ali, M. R., Mostaedi, R., Smith, W. H., Park, J., Scherer, P. E., Seay, S. A., McCoin, C. S., Bonaldo, P., & Adams, S. H. (2014). Contributions of adipose tissue architectural and tensile properties toward defining healthy and unhealthy obesity. *American Journal of Physiology-Endocrinology and Metabolism*. https://doi.org/10.1152/ajpendo.00476.2013

Lacolley, P., Regnault, V., & Laurent, S. (2020). Mechanisms of Arterial Stiffening. *Arteriosclerosis, Thrombosis, and Vascular Biology*, 40(5), 1055–1062.

https://doi.org/10.1161/ATVBAHA.119.313129

Langton, K. P., McKie, N., Smith, B. M., Brown, N. J., & Barker, M. D. (2005). Sorsby's fundus dystrophy mutations impair turnover of TIMP-3 by retinal pigment epithelial cells†. *Human Molecular Genetics*, *14*(23), 3579–3586. https://doi.org/10.1093/hmg/ddi385

Lear, S. A., James, P. T., Ko, G. T., & Kumanyika, S. (2010). Appropriateness of waist circumference and waist-to-hip ratio cutoffs for different ethnic groups. *European Journal of Clinical Nutrition*, *64*(1), 42–61. https://doi.org/10.1038/ejcn.2009.70

Lee, H., Lee, Y., Kim, J., An, J., Lee, S., Kong, H., Song, Y., Lee, C.-K., & Kim, K. (2018). Modulation of the gut microbiota by metformin improves metabolic profiles in aged obese mice. *Gut Microbes*, *9*(2), 155–165. https://doi.org/10.1080/19490976.2017.1405209

Li, B., Eisenberg, N., Witheford, M., Lindsay, T. F., Forbes, T. L., & Roche-Nagle, G. (2022). Sex Differences in Outcomes Following Ruptured Abdominal Aortic Aneurysm Repair. *JAMA Network Open*, *5*(5), e2211336. https://doi.org/10.1001/jamanetworkopen.2022.11336

Lin, D., Chun, T. H., & Kang, L. (2016). Adipose extracellular matrix remodelling in obesity and insulin resistance. *Biochemical Pharmacology*, *119*, 8–16. https://doi.org/10.1016/j.bcp.2016.05.005

Lin, H., & Peddada, S. D. (2020). Analysis of compositions of microbiomes with bias correction. *Nature Communications 2020 11:1, 11*(1), 1–11. https://doi.org/10.1038/s41467-020-17041-7

Liu, T., Chen, J.-M., Zhang, D., Zhang, Q., Peng, B., Xu, L., & Tang, H. (2021). ApoPred: Identification of Apolipoproteins and Their Subfamilies With Multifarious Features. *Frontiers in Cell and Developmental Biology*, 8. https://www.frontiersin.org/articles/10.3389/fcell.2020.621144

Lo, R. C., Bensley, R. P., Hamdan, A. D., Wyers, M., Adams, J. E., & Schermerhorn, M. L. (2013). Gender differences in abdominal aortic aneurysm presentation, repair, and mortality in the Vascular Study Group of New England. *Journal of Vascular Surgery*, *57*(5), 1261-1268.e5. https://doi.org/10.1016/j.jvs.2012.11.039

Love, M. I., Huber, W., & Anders, S. (2014). Moderated estimation of fold change and dispersion for RNA-seq data with DESeq2. *Genome Biology*, *15*(12), 1–21. https://doi.org/10.1186/S13059-014-0550-8/FIGURES/9

Lozupone, C., & Knight, R. (2005). UniFrac: A New Phylogenetic Method for Comparing Microbial Communities. *Applied and Environmental Microbiology*, *71*(12), 8228–8235. https://doi.org/10.1128/AEM.71.12.8228-8235.2005

Lucà, F., Abrignani, M. G., Parrini, I., Fusco, S. A. D., Giubilato, S., Rao, C. M., Piccioni, L., Cipolletta, L., Passaretti, B., Giallauria, F., Leone, A., Francese, G. M., Riccio, C., Gelsomino, S., Colivicchi, F., & Gulizia, M. M. (2022). Update on Management of Cardiovascular Diseases in Women. *Journal of Clinical Medicine*, *11*(5). https://doi.org/10.3390/jcm11051176

Lutshumba, J., Liu, S., Zhong, Y., Hou, T., Daugherty, A., Lu, H., Guo, Z., & Gong, M. C. (2018). Deletion of BMAL1 in Smooth Muscle Cells Protects Mice From Abdominal Aortic Aneurysms. *Arteriosclerosis, Thrombosis, and Vascular Biology*, *38*(5), 1063–1075. https://doi.org/10.1161/ATVBAHA.117.310153

Lyra, A., Forssten, S., Rolny, P., Wettergren, Y., Lahtinen, S. J., Salli, K., Cedgård, L., Odin, E., Gustavsson, B., & Ouwehand, A. C. (2012). Comparison of bacterial quantities in left and right colon biopsies and faeces. *World Journal of Gastroenterology : WJG*, *18*(32), 4404–4411. https://doi.org/10.3748/wjg.v18.i32.4404

Maachi, M., Piéroni, L., Bruckert, E., Jardel, C., Fellahi, S., Hainque, B., Capeau, J., & Bastard, J. P. (2004). Systemic low-grade inflammation is related to both circulating and adipose tissue TNFα, leptin and IL-6 levels in obese women. *International Journal of Obesity*. https://doi.org/10.1038/sj.ijo.0802718

Makki, K., Froguel, P., & Wolowczuk, I. (2013). Adipose Tissue in Obesity-Related Inflammation and Insulin Resistance: Cells, Cytokines, and Chemokines. *ISRN Inflammation*. https://doi.org/10.1155/2013/139239

Mansbach, C. M., & Siddiqi, S. A. (2010). The Biogenesis of Chylomicrons. *Annual Review of Physiology*, 72, 315–333. https://doi.org/10.1146/annurev-physiol-021909-135801

Marteau, P., Pochart, P., Doré, J., Béra-Maillet, C., Bernalier, A., & Corthier, G. (2001). Comparative Study of Bacterial Groups within the Human Cecal and Fecal Microbiota. *Applied and Environmental Microbiology*, *67*(10), 4939–4942. https://doi.org/10.1128/AEM.67.10.4939-4942.2001

McCullagh, K. G., Duance, V. C., & Bishop, K. A. (1980). The distribution of collagen types I, III and V (AB) in normal and atherosclerotic human aorta. *The Journal of Pathology*, *130*(1), 45–55. https://doi.org/10.1002/path.1711300107

Monaco, S., Sparano, V., Gioia, M., Sbardella, D., Di Pierro, D., Marini, S., & Coletta, M. (2006). Enzymatic processing of collagen IV by MMP-2 (gelatinase A) affects neutrophil migration and it is modulated by extracatalytic domains. *Protein Science*, *15*(12), 2805–2815. https://doi.org/10.1110/ps.062430706

Muir, L. A., Neeley, C. K., Meyer, K. A., Baker, N. A., Brosius, A. M., Washabaugh, A. R., Varban, O. A., Finks, J. F., Zamarron, B. F., Flesher, C. G., Chang, J. S., DelProposto, J. B., Geletka, L., Martinez-Santibanez, G., Kaciroti, N., Lumeng, C. N., & O'Rourke, R. W. (2016). Adipose tissue fibrosis, hypertrophy, and hyperplasia: Correlations with diabetes in human obesity. *Obesity*. https://doi.org/10.1002/oby.21377

Myant, N. B. (2014). The Biology of Cholesterol and Related Steroids. Butterworth-Heinemann.

Myeong, J. Y., Gha, Y. L., Chung, J. J., Young, H. A., Seung, H. H., & Jae, B. K. (2006). Adiponectin increases fatty acid oxidation in skeletal muscle cells by sequential activation of AMP-activated protein kinase, p38 mitogen-activated protein kinase, and peroxisome proliferator-activated receptor{alpha}. *Diabetes*. https://doi.org/10.2337/db05-1322

Myers, M. G., Leibel, R. L., Seeley, R. J., & Schwartz, M. W. (2010). Obesity and leptin resistance: Distinguishing cause from effect. *Trends in Endocrinology and Metabolism: TEM, 21*(11), 643–651. https://doi.org/10.1016/j.tem.2010.08.002

Nguyen, N. T., Nguyen, X. M. T., Lane, J., & Wang, P. (2011). Relationship between obesity and diabetes in a US adult population: Findings from the national health and nutrition examination survey, 1999-2006. *Obesity Surgery*. https://doi.org/10.1007/s11695-010-0335-4

Olivia Maurine Jasirwan, C., Muradi, A., Hasan, I., Simadibrata, M., & Rinaldi, I. (2021). Correlation of gut Firmicutes/Bacteroidetes ratio with fibrosis and steatosis stratified by body mass index in patients with non-alcoholic fatty liver disease. *Bioscience of Microbiota, Food and Health*, 40(1), 50–58. https://doi.org/10.12938/BMFH.2020-046

Olson, C. A., Vuong, H. E., Yano, J. M., Liang, Q. Y., Nusbaum, D. J., & Hsiao, E. Y. (2018). The Gut Microbiota Mediates the Anti-Seizure Effects of the Ketogenic Diet. *Cell*, *174*(2), 497. https://doi.org/10.1016/j.cell.2018.06.051

Osuna-Prieto, F. J., Martinez-Tellez, B., Ortiz-Alvarez, L., Di, X., Jurado-Fasoli, L., Xu, H., Ceperuelo-Mallafré, V., Núñez-Roa, C., Kohler, I., Segura-Carretero, A., García-Lario, J. V., Gil, A., Aguilera, C. M., Llamas-Elvira, J. M., Rensen, P. C. N., Vendrell, J., Ruiz, J. R., & Fernández-Veledo, S. (2021). Elevated plasma succinate levels are linked to higher cardiovascular disease risk factors in young adults. *Cardiovascular Diabetology*, *20*(1), 151. https://doi.org/10.1186/s12933-021-01333-3

Park, S., Kim, K., Bae, I.-H., Lee, S. H., Jung, J., Lee, T. R., & Cho, E.-G. (2018). TIMP3 is a CLOCK-dependent diurnal gene that inhibits the expression of UVB-induced inflammatory cytokines in human keratinocytes. *FASEB Journal : Official Publication of the Federation of American Societies for Experimental Biology*, *32*(3), 1510–1523. https://doi.org/10.1096/fj.201700693R

Petersen, E., Gineitis, A., Wågberg, F., & Ängquist, K.-A. (2000). Activity of Matrix Metalloproteinase-2 and -9 in Abdominal Aortic Aneurysms. Relation to Size and Rupture. *European Journal of Vascular and Endovascular Surgery*, *20*(5), 457–461. https://doi.org/10.1053/ejvs.2000.1211

Powell, E. E., Jonsson, J. R., & Clouston, A. D. (2010). Metabolic factors and non-alcoholic fatty liver disease as co-factors in other liver diseases. In *Digestive Diseases* (Vol. 28, Issue 1, pp. 186–191). International Diabetes Federation. https://doi.org/10.1159/000282084

Public Health England. (2017). *Health matters: Obesity and the food environment—GOV.UK*. Gov.Uk. https://www.gov.uk/government/publications/health-matters-obesity-and-the-food-environment/health-matters-obesity-and-the-food-environment--2

Qi, J. H., Bell, B., Singh, R., Batoki, J., Wolk, A., Cutler, A., Prayson, N., Ali, M., Stoehr, H., & Anand-Apte, B. (2019). Sorsby Fundus Dystrophy Mutation in Tissue Inhibitor of Metalloproteinase 3 (TIMP3) promotes Choroidal Neovascularization via a Fibroblast Growth Factor-dependent Mechanism. *Scientific Reports*, *9*(1), 1–14. https://doi.org/10.1038/s41598-019-53433-6

Ren, Y., Wang, R., Yu, J., Bao, T., Liu, Y., Bai, Z., Wang, T., Li, Y., Zhang, X., Wang, H., & Yang, S. (2022). Butyrate ameliorates inflammation of alcoholic liver disease by suppressing the LPS-TLR4-NF-κB/NLRP3 axis via binding GPR43-β-arrestin2. *Journal of Functional Foods*, *99*, 105351. https://doi.org/10.1016/j.jff.2022.105351

Ridlon, J. M., Kang, D.-J., & Hylemon, P. B. (2006). Bile salt biotransformations by human intestinal bacteria. *Journal of Lipid Research*, *47*(2), 241–259. https://doi.org/10.1194/jlr.R500013-JLR200

Riva, A., Borgo, F., Lassandro, C., Verduci, E., Morace, G., Borghi, E., & Berry, D. (2017). Pediatric obesity is associated with an altered gut microbiota and discordant shifts in Firmicutes populations. *Environmental Microbiology*. https://doi.org/10.1111/1462-2920.13463

Ruilope, L. M., & Schmieder, R. E. (2008). Left Ventricular Hypertrophy and Clinical Outcomes in Hypertensive Patients. *American Journal of Hypertension*, *21*(5), 500–508. https://doi.org/10.1038/ajh.2008.16

Rustan, A., & Drevon, C. (2005). *Fatty Acids: Structures and Properties*. https://doi.org/10.1038/npg.els.0003894

Santoro, A., Mattace Raso, G., & Meli, R. (2015). Drug targeting of leptin resistance. *Life Sciences*. https://doi.org/10.1016/j.lfs.2015.05.012

Sarkar, A., Ye, A., & Singh, H. (2016). On the role of bile salts in the digestion of emulsified lipids. *Food Hydrocolloids*, *60*, 77–84. https://doi.org/10.1016/j.foodhyd.2016.03.018

Sawabe, M. (2010). Vascular aging: From molecular mechanism to clinical significance. *Geriatrics & Gerontology International*, *10*(s1), S213–S220. https://doi.org/10.1111/j.1447-0594.2010.00603.x

Schoettl, T., Fischer, I. P., & Ussar, S. (2018). Heterogeneity of adipose tissue in development and metabolic function. *The Journal of Experimental Biology*. https://doi.org/10.1242/jeb.162958

Shenasa, M., & Shenasa, H. (2017). Hypertension, left ventricular hypertrophy, and sudden cardiac death. *International Journal of Cardiology*, *237*, 60–63.

https://doi.org/10.1016/j.ijcard.2017.03.002

Silver, F. H., Horvath, I., & Foran, D. J. (2001). Viscoelasticity of the vessel wall: The role of collagen and elastic fibers. *Critical Reviews in Biomedical Engineering*, *29*(3), 279–301. https://doi.org/10.1615/critrevbiomedeng.v29.i3.10

Skjelbred, T., Rajan, D., Svane, J., Lynge, T. H., & Tfelt-Hansen, J. (2022). Sex differences in sudden cardiac death in a nationwide study of 54 028 deaths. *Heart*, *108*(13), 1012–1018. https://doi.org/10.1136/heartjnl-2021-320300

Snijder, M. B., Visser, M., Dekker, J. M., Goodpaster, B. H., Harris, T. B., Kritchevsky, S. B., De Rekeneire, N., Kanaya, A. M., Newman, A. B., Tylavsky, F. A., & Seidell, J. C. (2005). Low subcutaneous thigh fat is a risk factor for unfavourable glucose and lipid levels, independently of high abdominal fat. The Health ABC Study. *Diabetologia*. https://doi.org/10.1007/s00125-004-1637-7

Strosberg, A. D. (1993). Structure, function, and regulation of adrenergic receptors. *Protein Science*, *2*(8), 1198–1209. https://doi.org/10.1002/pro.5560020802

Tang, D. D., & Gerlach, B. D. (2017). The roles and regulation of the actin cytoskeleton, intermediate filaments and microtubules in smooth muscle cell migration. *Respiratory Research*, *18*(1), 54. https://doi.org/10.1186/s12931-017-0544-7

Tsamis, A., Krawiec, J. T., & Vorp, D. A. (2013). Elastin and collagen fibre microstructure of the human aorta in ageing and disease: A review. *Journal of the Royal Society Interface*, *10*(83). https://doi.org/10.1098/rsif.2012.1004

Turek, F. W., Joshu, C., Kohsaka, A., Lin, E., Ivanova, G., McDearmon, E., Laposky, A., Losee-Olson, S., Easton, A., Jensen, D. R., Eckel, R. H., Takahashi, J. S., & Bass, J. (2005). Obesity and Metabolic Syndrome in Circadian Clock Mutant Mice. *Science*, *308*(5724), 1043–1045. https://doi.org/10.1126/science.1108750

Vouyouka, A. G., Pfeiffer, B. J., Liem, T. K., Taylor, T. A., Mudaliar, J., & Phillips, C. L. (2001). The role of type I collagen in aortic wall strength with a homotrimeric [α 1(I)]3 collagen mouse model. *Journal of Vascular Surgery*, *33*(6), 1263–1270. https://doi.org/10.1067/mva.2001.113579

Wang, K., Liao, M., Zhou, N., Bao, L., Ma, K., Zheng, Z., Wang, Y., Liu, C., Wang, W., Wang, J., Liu, S. J., & Liu, H. (2019). Parabacteroides distasonis Alleviates Obesity and Metabolic Dysfunctions via Production of Succinate and Secondary Bile Acids. *Cell Reports*, *26*(1), 222-235.e5. https://doi.org/10.1016/j.celrep.2018.12.028

Watson, S. R., Liu, P., Peña, E. A., Sutton, M. A., Eberth, J. F., & Lessner, S. M. (2016). Comparison of Aortic Collagen Fiber Angle Distribution in Mouse Models of Atherosclerosis Using Second-Harmonic Generation (SHG) Microscopy. *Microscopy and Microanalysis*, *22*(1), 55–62. https://doi.org/10.1017/S1431927615015585

Wei, J., Zhao, Y., Zhou, C., Zhao, Q., Zhong, H., Zhu, X., Fu, T., Pan, L., Shang, Q., & Yu, G. (2021). Dietary Polysaccharide from Enteromorpha clathrata Attenuates Obesity and Increases the Intestinal Abundance of Butyrate-Producing Bacterium, Eubacterium xylanophilum, in Mice Fed a High-Fat Diet. *Polymers*, *13*(19), Article 19. https://doi.org/10.3390/polym13193286

Westergaard, H., & Dietschy, J. M. (1976). The mechanism whereby bile acid micelles increase the rate of fatty acid and cholesterol uptake into the intestinal mucosal cell. *The Journal of Clinical Investigation*, *58*(1), 97–108. https://doi.org/10.1172/JCI108465

Wilcox, G. (2005). Insulin and Insulin Resistance. *Clinical Biochemist Reviews*, 26(2), 19–39.

Wu, X., Ma, C., Han, L., Nawaz, M., Gao, F., Zhang, X., Yu, P., Zhao, C., Li, L., Zhou, A., Wang, J., Moore, J. E., Cherie Millar, B., & Xu, J. (2010). Molecular Characterisation of the Faecal Microbiota

in Patients with Type II Diabetes. *Current Microbiology, 61*(1), 69–78. https://doi.org/10.1007/s00284-010-9582-9

Yasmin, null, Wallace, S., McEniery, C. M., Dakham, Z., Pusalkar, P., Maki-Petaja, K., Ashby, M. J., Cockcroft, J. R., & Wilkinson, I. B. (2005). Matrix Metalloproteinase-9 (MMP-9), MMP-2, and Serum Elastase Activity Are Associated With Systolic Hypertension and Arterial Stiffness.

Arteriosclerosis, Thrombosis, and Vascular Biology, 25(2), 372–378.

https://doi.org/10.1161/01.ATV.0000151373.33830.41

Ye, J., Lv, L., Wu, W., Li, Y., Shi, D., Fang, D., Guo, F., Jiang, H., Yan, R., Ye, W., & Li, L. (2018). Butyrate Protects Mice Against Methionine—Choline-Deficient Diet-Induced Non-alcoholic Steatohepatitis by Improving Gut Barrier Function, Attenuating Inflammation and Reducing Endotoxin Levels. *Frontiers in Microbiology*, *9*.

https://www.frontiersin.org/articles/10.3389/fmicb.2018.01967

Yun, M., Li, S., Yan, Y., Sun, D., Guo, Y., Fernandez, C., Bazzano, L., He, J., Zhang, T., & Chen, W. (2021). Blood Pressure and Left Ventricular Geometric Changes: A Directionality Analysis. *Hypertension*, 78(5), 1259–1266. https://doi.org/10.1161/HYPERTENSIONAHA.121.18035

Zeng, Z.-S., Cohen, A. M., & Guillem, J. G. (1999). Loss of basement membrane type IV collagen is associated with increased expression of metalloproteinases 2 and 9 (MMP-2 and MMP-9) during human colorectal tumorigenesis. *Carcinogenesis*, *20*(5), 749–755.

https://doi.org/10.1093/carcin/20.5.749

Zhou, D., Pan, Q., Xin, F.-Z., Zhang, R.-N., He, C.-X., Chen, G.-Y., Liu, C., Chen, Y.-W., & Fan, J.-G. (2017). Sodium butyrate attenuates high-fat diet-induced steatohepatitis in mice by improving gut microbiota and gastrointestinal barrier. *World Journal of Gastroenterology*, *23*(1), 60–75. https://doi.org/10.3748/wjg.v23.i1.60